N d'ordre : 4862

THÈSE

PRÉSENTÉE A

L'UNIVERSITÉ BORDEAUX I

ÉCOLE DOCTORALE DES SCIENCES CHIMIQUES

Par
Jean-Marcel ATEBA MBA

POUR OBTENIR LE GRADE DE

DOCTEUR

SPÉCIALITÉ : PHYSICO-CHIMIE DE LA MATIÈRE CONDENSÉE

New Transition Metal Fluorophosphates as Positive Electrode Materials for Li-ion Batteries

---

Thèse dirigée par :

Mme **Laurence CROGUENNEC**	Chargée de Recherche CNRS HDR, ICMCB – CNRS, Pessac
M. **Christian MASQUELIER**	Professeur, LRCS - Université Picardie Jules Verne (UPJV), Amiens

Soutenue le 4 octobre 2013 devant la commission d'examen formée par :

Mme **Laurence CROGUENNEC**	Chargée de Recherche CNRS HDR, ICMCB - CNRS	Examinateur
Mme **Marie-Liesse DOUBLET**	Directrice de recherche CNRS, ICG - Université de Montpellier	Rapporteur
M. **Helmut EHRENBERG**	Professeur Dr, KIT - Karlsruhe Institute of Technology	Examinateur
M. **Eric LE FUR**	Maître de Conférences HDR, ENSCR, Rennes	Rapporteur
M. **Mario MAGLIONE**	Directeur de Recherche CNRS, ICMCB - CNRS	Président
M. **Christian MASQUELIER**	Professeur, LRCS - UPJV, Amiens	Examinateur
Mme **Maria-Rosa PALACIN**	Directrice de recherche, ICMAB - CSIC, Barcelone	Examinateur
M. **Nadir RECHAM**	Maître de Conférences, LRCS - UPJV, Amiens	Examinateur

RESUME DE LA THESE

Synthèses de $LiMPO_4X$

La voie céramique a été utilisée pour synthétiser les matériaux $LiMPO_4X$ (avec M = V, Fe, Ti et X = O ou F) dont les diagrammes de diffraction des rayons X sont donnés à la figure 1. $LiVPO_4O$ a été obtenu pour la première fois par une voie céramique en une seule étape. $LiVPO_4F$ a été quant à lui obtenu par une voie céramique en deux étapes, la première étape consiste en la synthèse de VPO_4 tandis que la seconde étape consiste en un traitement à haute température du mélange VPO_4 : LiF, dans un tube d'or scellé pour éviter toute sublimation et ainsi la formation de la phase α-$Li_3V_2(PO_4)_3$. Les deux phases $LiFePO_4F$ et $LiTiPO_4F$ ont été obtenues en présence de LiF, qui est ensuite éliminées par un lavage de la poudre à l'eau froide.

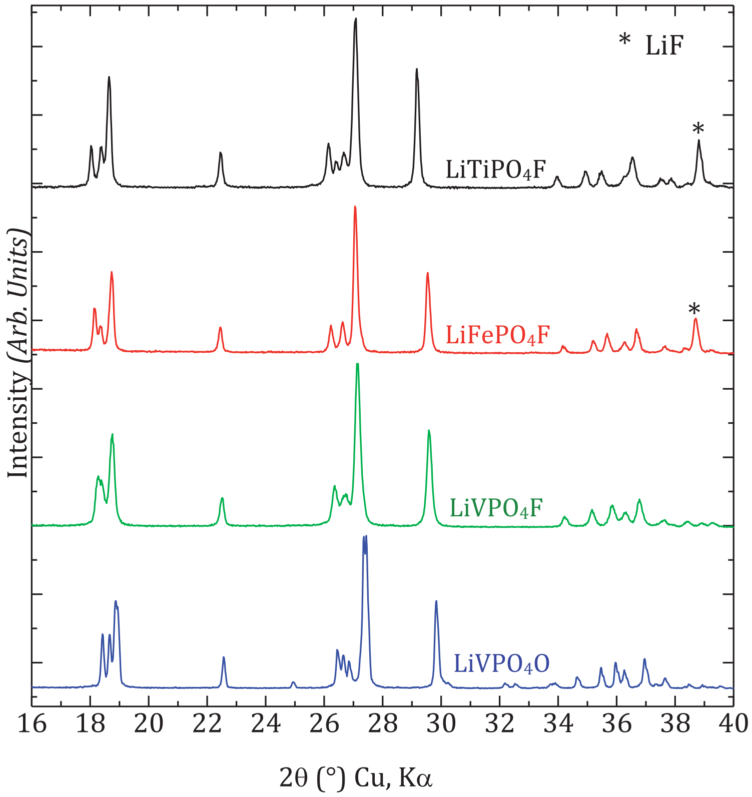

Figure 1: Diagrammes de diffraction des rayons X des phases étudiées

Nous avons observé la dégradation de $LiTiPO_4F$ durant un vieillissement à l'air et un lavage à l'eau. Cette dégradation conduit à la formation de deux nouvelles phases: l'une cristallise dans le groupe d'espace $P\bar{1}$ tandis que la seconde cristallise dans le groupe d'espace *Cc*.

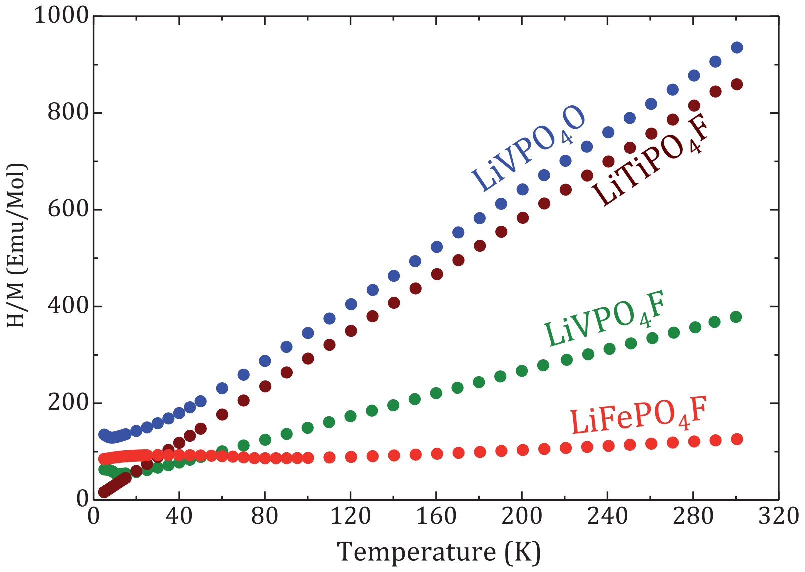

Figure 2: Dépendance du rapport H/M avec la température pour LiMPO$_4$X

La composition chimique et plus particulièrement les teneurs en Li, M (avec M = Ti, V et Fe) et P dans LiMPO$_4$F ont été confirmées par des dosages ICP. Des analyses CHNS ont montré que la teneur en H était négligeable dans les deux matériaux LiFePO$_4$F et LiTiPO$_4$F. La variation de la susceptibilité magnétique à basse température (Figure 2) indique un comportement antiferromagnétique avec des températures de Néel respectivement de 9 K, 13 K et 80 K pour LiVPO$_4$F, LiVPO$_4$O et LiFePO$_4$F. De plus, la susceptibilité à haute température a permis de confirmer le degré d'oxydation de chaque métal de transition (Fe^{3+}, V^{3+}, V^{4+}, dont les configurations électroniques sont respectivement $t_{2g}^3e_g^2$, $t_{2g}^2e_g^0$ et $t_{2g}^1e_g^0$). Sur la base des analyses menées en spectroscopie Mössbauer nous avons également pu confirmer le degré d'oxydation et l'environnement octaédrique des ions Fe^{3+} dans LiFePO$_4$F.

Structures de LiMPO$_4$X (avec X = O et F)

La caractérisation structurale complète des phases LiMPO$_4$X a pu être réalisée en combinant des études en diffraction des rayons X et des neutrons ainsi qu'en spectroscopie RMN. Les phases LiMPO$_4$X cristallisent dans une structure de type Tavorite et sont iso-structurales au minéral LiFePO$_4$OH. La figure 3 représente les longueurs de liaisons le long des chaines dans chacune des structures. Le volume de la maille élémentaire de LiVPO$_4$O est deux fois plus grand que celui de LiMPO$_4$F. Nous avons ainsi observé alternativement une liaison longue (2.21 Å et 2.17 Å) et une liaison courte (1.62 Å et 1.71 Å) le long des chaines de LiVPO$_4$O (les liaisons longues étant de type vanadyle) alors que pour LiFePO$_4$F et LiVPO$_4$F, nous avons observé des distances M–F de

1.98 Å. Dans la structure de $LiTiPO_4F$, nous avons observé des distances de 2.01 Å et 1.94 Å telles que la distance moyenne est de 1.98 Å.

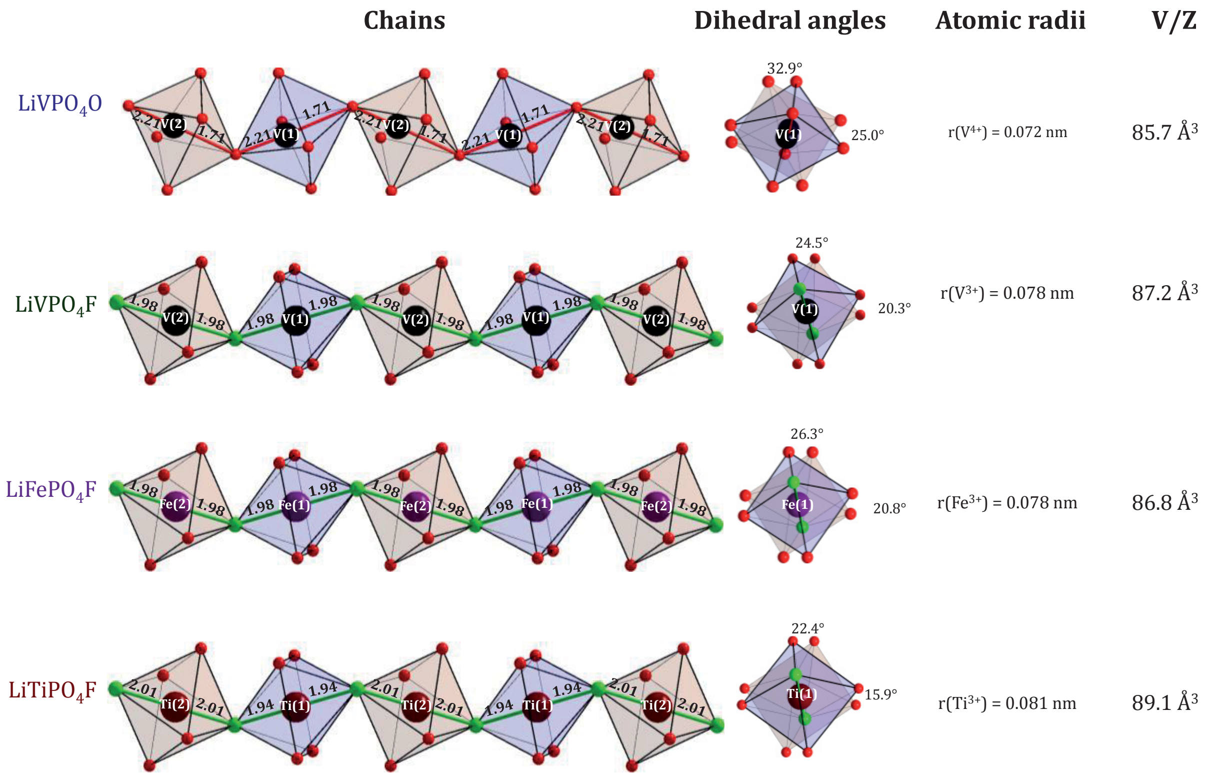
Chains
Dihedral angles
Atomic radii
V/Z
LiVPO4O
2.21
V(2)
1.71
V(1)
32.9°
25.0°
r(V4+) = 0.072 nm
85.7 Å3
LiVPO4F
1.98
24.5°
20.3°
r(V3+) = 0.078 nm
87.2 Å3
LiFePO4F
Fe(2)
Fe(1)
26.3°
20.8°
r(Fe3+) = 0.078 nm
86.8 Å3
LiTiPO4F
2.01
1.94
Ti(2)
Ti(1)
22.4°
15.9°
r(Ti3+) = 0.081 nm
89.1 Å3

Figure 3: comparaison des chaines [MO_4X_2], des angles diédraux, des rayons ioniques des métaux de transition et des rapports V/Z dans $LiMPO_4X$ (M = V, Fe, Ti et X = O ou F)

L'évolution du ratio V/Z est en bon accord avec celle des rayons ioniques des métaux de transition. En effet, V/Z augmente avec le rayon ionique. Les contraintes stériques induites par la présence des ions Li^+ dans les tunnels sont illustrées par les angles diédraux.

Un seul site de lithium est observé dans les structures $LiVPO_4F$ et $LiFePO_4F$, les ions Li^+ sont coordonnés par 4 atomes d'oxygène et 1 atome de fluor, formant un pentaèdre distordu très similaire dans les deux structures ($\delta = 6.00 \cdot 10^{-3}$ dans $LiVPO_4F$ et $\delta = 6.51 \cdot 10^{-3}$ dans $LiFePO_4F$). La spectroscopie RMN MAS du ^7Li réalisées pour les deux échantillons révèle un signal fin déplacé de 117 ppm pour $LiVPO_4F$ et de 203 ppm pour $LiFePO_4F$, ces déplacements sont en bon accord avec l'augmentation du nombre d'électrons non-appariés dans les orbitales t_{2g} (2 pour V^{3+} et 3 pour Fe^{3+}). Le signal RMN MAS du ^7Li de $LiVPO_4F$ présente un épaulement qui n'a pas été attribué à une impureté mais à des defaults structuraux qui ne sont pas détectés par diffraction des rayons X et des neutrons.

Les deux sites du Li présents dans la structure de $LiVPO_4O$ son entourés de cinq atomes d'oxygènes (formant des pentaèdres distordus) et sont séparés de 3.44 Å. Etonnamment, le spectre de RMN MAS du ^7Li montre un seul signal centré à 71 ppm. Les deux sites du Li sont significativement différents (*i.e.* avec des distances V-O et angles O-V-O différents), l'observation d'un signal unique n'était pas attendue. Néanmoins, des calculs réalisés en DFT ont montré que les deux signaux sont en fait attendus proches, du fait d'un transfert très similaire de densité de spins des ions vanadium paramagnétiques vers les deux types de noyaux Li. Par conséquent, dans les conditions de mesures utilisées, les deux contributions ne peuvent pas être séparées. Une autre explication pour ce signal unique pourrait être une grande mobilité entre les deux sites du Li bien qu'ils sont séparés de 3.44 Å. Des mesures à haut champ et à grande vitesse de rotation permettraient très certainement de séparer ces deux signaux. La localisation du Li dans $LiTiPO_4F$ n'a pas pu être effectuée car les données de diffraction des neutrons n'étaient pas de qualité suffisante. Néanmoins, la RMN MAS du ^7Li NMR a montré qu'il a trois signaux de RMN suggérant la présence de trois sites/environnement du lithium dans la structure.

Un signal fortement déplacé est observé pour le fluor en RMN MAS du ^{19}F (à -1500 ppm) pour $LiVPO_4F$. Aucun signal n'est observé pour $LiFePO_4F$ car il est probablement fortement déplacé en ppm, les ions Fe^{3+} possèdent en effet plus d'électrons non appariés que les ions V^{3+}. Néanmoins, (étonnamment) aucun signal n'est observé pour $LiTiPO_4F$ alors que Ti^{3+} possède moins de spins que V^{3+}.

La structure magnétique de $LiVPO_4F$ et $LiFePO_4F$ a été déterminée par un affinement Rietveld des données de diffraction des neutrons enregistrées à basse température. Les moments magnétiques portés par les métaux dans chacun de ces matériaux sont anti-parallèles le long des chaines et anti-parallèles entre les chaines. Les moments magnétiques résultants sont respectivement 1.22 μ_B et 3.92 μ_B pour $LiVPO_4F$ et $LiFePO_4F$.

Pour $LiVPO_4O$, les mesures magnétiques révèlent une transition magnétique à une température de 9 K entre un ordre paramagnétique et un ordre antiferromagnétique. Pourtant, aucune transition magnétique n'est observée en diffraction des neutrons à basse température, probablement du fait de la transparence du vanadium aux neutrons et de la configuration électronique de V^{4+} (t_{2g}^1 e_g^0) qui possède uniquement un électron célibataire. Dans le cas de $LiVPO_4F$, seulement deux pics supplémentaires de très faibles intensités sont observés. Il n'est donc pas étonnant que la transition magnétique ne soit pas observée pour $LiVPO_4O$.

Comportement électrochimique de $LiMPO_4X$

Le comportement électrochimique de $LiMPO_4X$ a été étudié *vs.* Li^+/Li et comparé à celui d'autres phosphates. Nous avons toujours observé des potentiels relativement élevés pour les couples redox mis en jeu. A titre d'exemple, $LiVPO_4F$ présente un potentiel de 4.22 V, le plus élevé jamais observé pour le couple redox V^{4+}/V^{3+} dans les phosphates de vanadium. Lors de l'extraction du Li^+ de $LiVPO_4F$ (qui conduit à la formation de VPO_4F) une phase intermédiaire a été mise en évidence pour la composition $Li_{0.67}VPO_4F$. Celle-ci est clairement observée par diffraction des rayons X et cristallise dans le groupe d'espace $P\overline{1}$. La désintercalation du lithium de $Li_{0.67}VPO_4F$ conduit ensuite à la formation de VPO_4F qui cristallise dans le groupe d'espace $C2/c$. Par contre, lors de la réintercalation de lithium dans VPO_4F la formation de la phase intermédiaire $Li_{0.67}VPO_4F$ n'est pas observée, comme montré par diffraction des rayons X *in situ*, mais seules les deux phases VPO_4F et $LiVPO_4F$ sont présentes. Tous les processus mis en jeu reposent sur des mécanismes biphasés.

$LiVPO_4F$ peut également intercaler un autre lithium dans sa structure hôte et conduire ainsi à la formation de Li_2VPO_4F via un mécanisme biphasé. Li_2VPO_4F cristallise dans le groupe d'espace $C2/c$ et s'est révélée être très instable. Les deux phases VPO_4F et Li_2VPO_4F sont homéotypes de $LiVPO_4F$. Les états d'oxydation des ions vanadium dans ces phases ont été confirmés par des mesures magnétiques. La structure de $Li_{0.67}VPO_4F$ n'a pas pu être déterminée.

Les mauvaises performances électrochimiques de $LiVPO_4O$ (cyclabilité limités, grande polarisation…) ont été attribuées à des particules de grandes tailles et fortement agglomérées. L'extraction du Li^+ de $LiVPO_4O$ conduit à la formation de VPO_4O via un processus biphasé, et le couple redox V^{5+}/V^{4+} est observé à 3.95 V *vs.* Li^+/Li. Nous avons démontré pour la première fois que $LiVPO_4O$ peut accepter un ion lithium supplémentaire dans sa structure et conduire ainsi à la formation de Li_2VPO_4O dans laquelle le degré d'oxydation du vanadium est +3. Le couple redox V^{4+}/V^{3+} est observé à un potentiel moyen de 2.3 V *vs.* Li^+/Li pour le système $LiVPO_4O \Leftrightarrow Li_2VPO_4O$ alors qu'il est observé à 4.2 V *vs.* Li^+/Li pour le système $LiVPO_4F \Leftrightarrow VPO_4F$. Cette différence peut être le résultat de la présence alternée de liaisons longues V–O et courtes V=O dans la structure de $LiVPO_4O$.

L'insertion/extraction de Li^+ dans la structure de $LiVPO_4O$ a lieu réversiblement via la formation de deux phases intermédiaires, $Li_{1.5}VPO_4O$ et $Li_{1.75}VPO_4O$, jamais rapportées précédemment dans la littérature.

La courbe électrochimique de $LiFePO_4F$ est caractérisée par un potentiel de l'ordre de 2.8 V *vs.* Li^+/Li. Une oxydation du Fe^{3+} en Fe^{4+} est suggérée par celle-ci, mais ceci n'est clairement pas possible à un potentiel aussi bas. Cette signature particulière a été attribuée à une dégradation de la phase lors de son broyage à l'air à l'aide d'un broyeur Spex.

L'étude des propriétés électrochimiques de $LiTiPO_4F$ a montré que le potentiel observé pour le couple redox Ti^{4+}/Ti^{3+} est de l'ordre de 3 V *vs.* Li^+/Li. La désintercalation/intercalation de Li^+ de la structure de $LiTiPO_4F$ démontre une bonne rétention de capacité et une faible polarisation tandis que l'intercalation/désintercalation du Li^+ se traduit par une perte rapide de capacité et une forte polarisation.

L'étude des propriétés électrochimiques du matériau $LiTiPO_4F$ lavé à l'eau froide révèle des propriétés complètement différentes de celle de $LiTiPO_4F$ non lavé, avec l'apparition de deux pseudo-plateaux de potentiel : l'un à 3.0 V et l'autre à 1.7 V vs. Li^+/Li. Dans chaque domaine de potentiel, seulement 0.5 Li peuvent être échangés en bon accord avec un degré d'oxydation moyen pour le titane proche de 3.5 (*i.e.* $Ti^{3+}/Ti^{4+} \sim 1/1$). La signature électrochimique de l'échantillon vieilli un an à l'air ne démontre pas de capacité lors de la première extraction du Li, en bon accord avec la seule présence de titane tétravalent dans le matériau.

Contents

General Introduction

1. General Introduction 5
2. Rechargeable Li-ion Batteries 8
3. Positive Electrode Materials 10
4. Tavorite Materials 12
5. The Aim of This Thesis 15

Chapter I : SYNTHESIS AND CRYSTAL STRUCTURE OF $LiVPO_4F$ AND $LiVPO_4O$

I-1. Introduction 23
I-2. CERAMIC SYNTHESIS OF $LiVPO_4F$ AND $LiVPO_4O$ 24
    I-2a. One-step Ceramic Synthesis of $LiVPO_4F$ 24
    I-2b. Two-Step Ceramic Route for the Synthesis of $LiVPO_4F$ 26
        i- Synthesis of the intermediate phase: C-VPO_4 26
        ii- Synthesis of $LiVPO_4F$ 28
    I-2c. Synthesis of $LiVPO_4O$ 30
    I-2d. Morphology and Magnetic Behavior of $LiVPO_4X$ (X = O/F) 31
    I-2e. Summary and Conclusion 34
I-3. CRYSTAL AND MAGNETIC STRUCTURES OF $LiVPO_4F$ 34
    I-3a. The Crystal structure of $LiVPO_4F$ 35
    I-3b. NMR Study of $LiVPO_4F$ 40
    I-3c. Magnetic structure of $LiVPO_4F$ 44
    I-3d. Conclusion and Summary 46
I-4. CRYSTAL STRUCTURE AND NMR STUDY OF $LiVPO_4O$ 47
    I-4a. Crystal structure of $LiVPO_4O$ 47
    I-4b. NMR Study of LiVPO4O 51
I-5. Conclusion and summary of this chapter 53

Chapter II : ELECTROCHEMICAL BEHAVIOR OF $LiVPO_4X$ (X = O or F)

II-1. Introduction 61

II-2. ELECTRODES PREPARATION AND BATTERIES CONFIGURATION 64

II-3. ELECTROCHEMICAL BEHAVIOR OF $LiVPO_4F$ 66

  II-3a. Reversible Li+ insertion into $LiVPO_4F$ (V^{3+}/V^{2+} couple) 66
  II-3b. Reversible Li+ extraction from $LiVPO_4F$ (V^{4+}/V^{3+} couple) 69
  II-3c. Crystal Structures of Li_xVPO_4F (x = 2, 0.67, 0) 77
    i- Crystal Structure of VPO_4F 78
    ii- Hypothesis on the structure of $Li_{0.67}VPO_4F$ 80
    iii- Structure of Li_2VPO_4F 81
    iv- Comparative NMR Study of Li_xVPO_4F *phases (with* x *= 1, 0.67 and 0)* 84

  II-3d. Conclusion 86

II-4. ELECTROCHEMICAL BEHAVIOR OF $LiVPO_4O$ 88

  II-4a. Reversible Li^+ insertion into $LiVPO_4O$ (V^{3+}/V^{4+} couple) 89
  II-4b. Reversible Li^+ extraction from $LiVPO_4O$ (V^{4+}/V^{5+} couple) 92

II-5. Conclusions and summary of this chapter 97

Chapter III : SYNTHESIS, CRYSTAL STRUCTURE AND ELECTROCHEMICAL PROPERTIES OF $LiFePO_4F$

III-1. Introduction 107

III-2. SYNTHESIS OF $LiFePO_4F$ 109

  III-2a. Iono-thermal Synthesis 110
  III-2b. One-step Ceramic Synthesis 112
  III-2c. Mössbauer spectroscopy and Magnetic properties of $LiFePO_4F$ 113
  III-2d. Conclusion 115

III-3. CRYSTAL AND MAGNETIC STRUCTURES OF $LiFePO_4F$ 116

  III-3a. Crystal structure of $LiFePO_4F$ 116
  III-3b. NMR measurements 121

III-3c. Magnetic structure of $LiFePO_4F$ 124

III-4. ELECTROCHEMICAL PROPERTIES OF $LiFePO_4F$ 127

III-5. Conclusion and summary of this chapter 134

Chapter IV : SYNTHESIS, CRYSTAL STRUCTURE AND ELECTROCHEMICAL PROPERTIES OF $LiTiPO_4F$

IV-1. Introduction 143

IV-2. STUDY OF THE PHASE $LiTiPO_4F$ 144

IV-2a. Synthesis of $LiTiPO_4F$ 144
IV-2b. Chemical composition and magnetic behavior of $LiTiPO_4F$ 145
IV-2c. Crystal Structure of $LiTiPO_4F$ 146

IV-3. WASHING AND AGING EFFECT ON $LiTiPO_4F$ 150

IV-3a. Effect of aging in air on $LiTiPO_4F$ 150
IV-3b. Effect of washing on $LiTiPO_4F$ 154
IV-3c. Conclusion and summary 157

IV-4. ELECTROCHEMICAL BEHAVIOR OF $LiTiPO_4F$ 157

IV-5. Conclusion and summary of this chapter 160

GENERAL CONCLUSION, SUMMARY AND PERSPECTIVES

GENERAL CONCLUSION, SUMMARY AND PERSPECTIVES 165

ANNEXE 177

Figures Captions 189

Tables Captions 201

INTRODUCTION

Contents

1. General Introduction 5

2. Rechargeable Li-ion Batteries 8

3. Positive Electrode Materials 10

4. Tavorite Materials 12

5. The Aim of This Thesis 15

1. General Introduction

A country's energy consumption is directly related to both its economic output and the individual well-being of its citizens. Both the growth of population and the desire to maintain growth while raising standards of living result in increased energy consumption as a society develops. In 2008, the world population of 6.7 billion inhabitants consumed a total amount of energy of 132,000 TWh[1]. This energy consumption is steadily increasing from 74,000 TWh in 1973 to 137,000 TWh in 2010 (Figure 1). The recent projections estimate that our energy consumption will reach 160,000 TWh in 2040 with a world population of 9 billion[2]. Another important factor that deeply influences the increase of energy consumption is the quality of life. Indeed due to their development, the so call "third world countries" now aspire to live in the same way as the so call "developed countries".

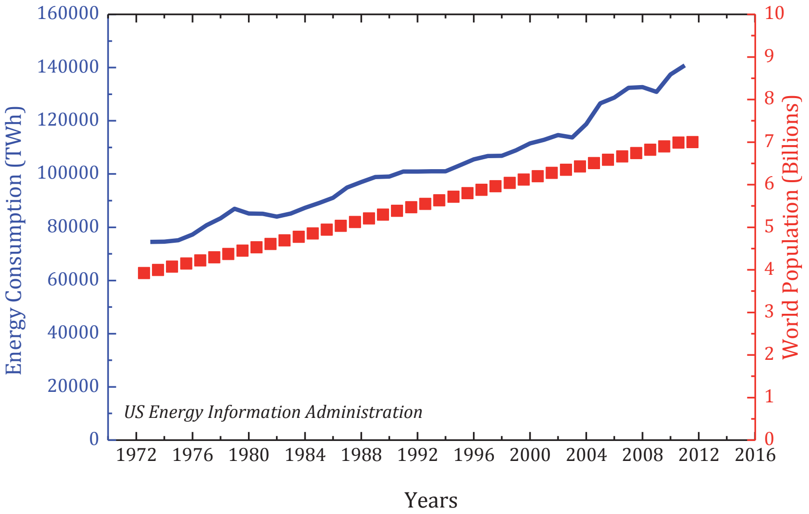

Figure 1 : World total final consumption and world population from 1973 to 2011

In order to satisfy our energetic demand, we are using two kinds of energy sources: *non-renewable energy* (energy produced once by nature which cannot be reproduced or generated but can only be depleted) and *renewable energy* (energy top up by nature which can be reproduced or regenerated only by nature and which is considered as being infinite). Non-renewable energy represents 95% of energy consumed nowadays (Nuclear power included). However, non-renewable energies present two main drawbacks:

- It gets inevitably exhausted, and regarding its definition it is consumed faster than its generation. Current state of the non-renewable energies confirmed its depleting. As an example, the current reserve of oil (which represents 48% of energy now consumed mainly for transportation) remaining is 54 years (this is an average value which deeply depends on the region see Figure 2)[3]. The second most consumed non-renewable energy is natural gas (20% of total energy consumed in 2010), but according to the specialists the natural gas in our disposition cannot stand over 60 years if the production trend is maintained. Another example can be seen through the coal reserve which can stand for 110 years. In the light of the foregoing, it becomes clear that most of the non-renewable energies mostly used as energy resources today will probably disappear in the next century.

---

[1] International Energy Agency, *Key World Energy Statistic 2012*
[2] US Energy Information Administration

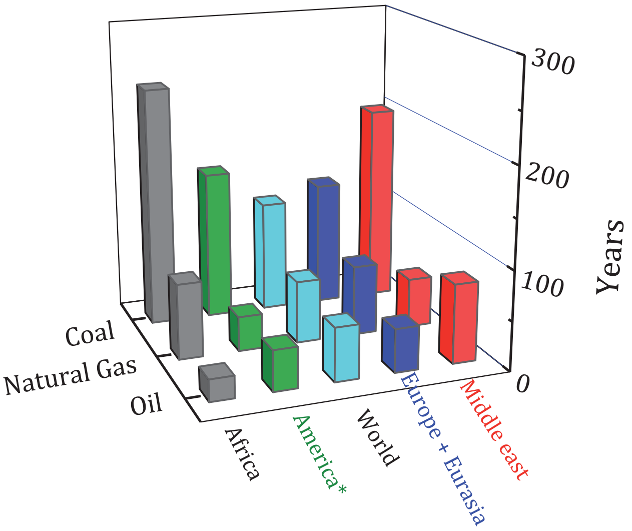

Figure 2: Primary Energy reserves by regions (America referred to North and Latin America). The values are given in R/P ratio i.e. amount of known resource/amount used per year

- Another major drawback of the non-renewable energies is their impact on the climate changes. Indeed despite the Kyoto Protocol and a wealth of good intentions, emissions of greenhouse gases continued to increase in recent years. We face a global environmental crisis that is expected to include the increase of temperatures over lands and in oceans, rising sea levels, more acidification of the oceans, increased floodings as well as droughts, and as a result the extinction of many species. The climate-energy crisis could cause major disruptions to ecosystems, the availability of fresh water, farming … Even nuclear power which has been considered as a reliable source of electricity in many countries for decades (an essential point for the mix of energy sources) has to face serious ecological problems as encountered in Fukushima in 2010.

With regard to what follows, it becomes obvious that *i)* we cannot continue to use exceedingly non-renewable energies while they are limited; *ii)* we cannot continue to pollute environment through an intensive use of non-renewable energies. To overcome the limitations of non-renewable energies, many countries have turned to renewable energies which are:

---

[3] BP Statistical Review of World Energy, June 2012 ; *bp.com/statisticalreview*

- Hydroelectric power: in terms of renewable resources, the share of hydroelectric power has remained constant, as concerns have grown about its social and environmental consequences. This energy represents 80-90 % of the renewable energy consumed today.

- Solar energy: utilization of solar energy on a terawatt can be a cost effective solution in large-scale, environmental friendly and a solution to the growing global demand for energy. Solar technologies can contribute to significant reductions of carbon emissions and pollution of the environment and includes conventional photovoltaic solar cells and solar thermal concentration…

- Wind energy: Wind energy has evolved significantly in the last decades. In 2010, the installed capacity was 0.2 terawatts and is expected to reach 1.5 terawatts by 2020. In addition, the cost of production is now nearly comparable to that of conventional electricity generation technologies.

Most of renewable energy sources are dependent to short-term weather conditions (geothermal, hydro, biomass, wind …), and are therefore variable (vary over relatively short time period) and uncertain (there are not completely predictable). Thus, renewable energy is not often correlated with normal demand patterns for electricity and large-scale deployment of renewable energy creates challenges for grid operators to maintain reliable service. To prevent blackout particularly during peak energy demand, a storage system is required to balance and to regulate electricity production and consumption.

Although other options are available, the most flexible energy-storage schemes are batteries and capacitors, since they can be located almost everywhere and often are maintenance-free, readily, scalable and portable.

The batteries are well above other forms of electrical energy storage system and their size is flexible into different formats varying from coin cell to megawatt load-leveling applications. Alessandro Volta is well known as being the first who developed in 1800 the first battery, a cell consisting of alternate disks of zinc and copper separated by cardboard with an electrolyte of a brine solution.

With the invention of lead-acid battery by Gaston Planté in 1859, the secondary batteries well known as rechargeable batteries, began to be attractive. In 1899, Waldermar Jungner developed the nickel cadmium battery and a year later, Thomas Edison invented nickel-iron battery as energy source for electric vehicles.

In 2000, a quarter of batteries sold were Li-ion batteries and almost half were Ni-MH batteries. Last year, those statistics were inversed. Indeed the secondary battery sales statistics by volume indicates that almost 60% of the batteries sold were Li-ion[4]. This attractiveness of Li-ion batteries are due to higher volumetric energy storage capability (see Figure 3) and lower cost of Li-ion batteries. As an example, higher-energy and lower-cost Li-ion batteries are already operational in hybrid electric buses, in electric cars and in fully electric vehicles.

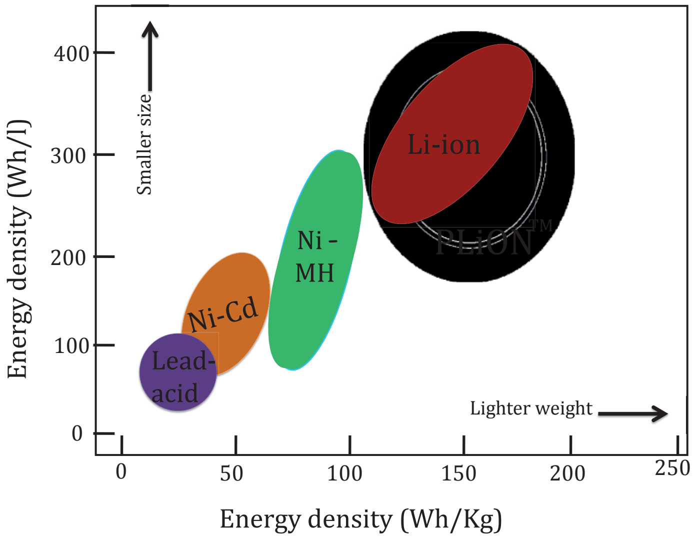

Figure 3: Energy densities of different well-known electrochemical batteries

2. Rechargeable Li-ion Batteries

A rechargeable Li-ion battery is an electrochemical storage device composed of a “negative” host electrode and a “positive” host electrode. Both electrodes are immersed in an ionic conductor (electrical insulator), the electrolyte. As the battery is being **charged**, lithium ions (positively charged lithium atoms, illustrated in Figure 4 as green balls) migrate from the “positive” electrode through the electrolyte towards the “negative” electrode. The reverse process takes place upon the **discharge** process. Thus lithium ions shuttle back and forth between the two electrodes.

---

[4] Machinery statistics released by the Japan Ministry of Economy, Trade and Industry

Simultaneously with the migration of Li^+ ion, electrons migrate through an external circuit and consequently can be "recuperated" through electrical energy during discharge. Note that the "negative" electrode is also call **anode** (electrode in which chemical oxidation occurred during discharge) and the "positive" electrode **cathode** (electrode in which chemical reduction occurred during discharge).

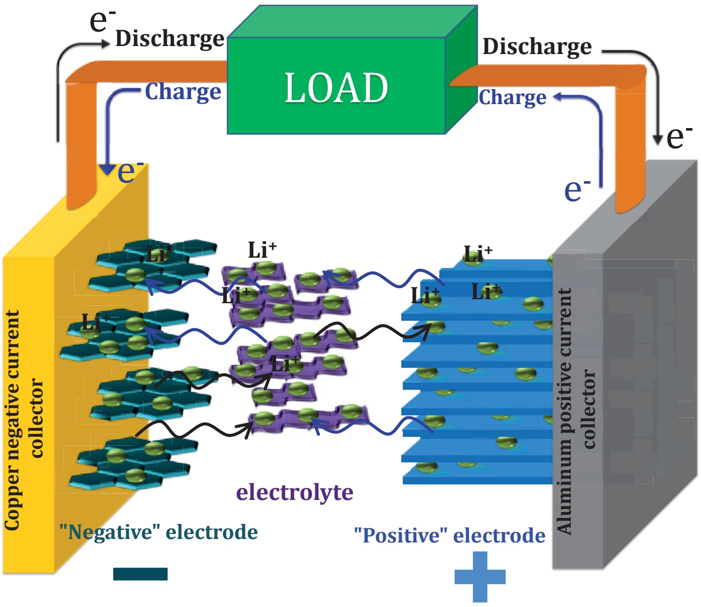
e-
Discharge
Charge
LOAD
Discharge
Charge
e-
e-
e-
Li+
Li+
Li+
Li+
Li+
Li+
Li+
Copper negative current collector
Aluminum positive current collector
electrolyte
"Negative" electrode
"Positive" electrode
−
+

Figure 4: A schematic representation of a Li-ion battery with graphite as negative insertion electrode material and an insertion compound as positive electrode material.

The chemical reaction, **insertion reaction**, occurring at the positive electrode can be summarized as shown here as an example for the well known intercalation compound $LiFePO_4$:

$$Li_xFePO_4 \underset{\text{Discharge}}{\overset{\text{Charge}}{\rightleftarrows}} FePO_4 + x\,Li^+ + x\,e^-$$

The two main feature of the Li-ion battery are: *i)* the **potential:** which depends on the nature of the two redox couples involved and on the difference in potential between them, but also on the advancement of the reactions; *ii)* the **capacity** which depends on the number of Li exchanged per metal.

According to the above equation, the electric charge transferred (linked to the mole of Li) during the charge or discharge process is $(96500/3600) \times x$ in A·h/mol. For the active material this leads to a specific capacity of $(26.8/M) \times x$ A·h/g (M being the molar mass of the active material). Therefore, the specific capacity can also be reported as the energy stored in the chemical reaction, expressed in volumetric basis by using the density or in gravimetric by using molar mass according to the followings:

Specific energy in gravimetric units: $E \times (26.8 \times x / M)$ in W·h/g

Specific energy in volumetric units: $E \times (26.8 \times x / M) \times d$ in W·h/l

With **E** the potential and *d* the density of the active material.

The energy of a Li-ion battery can consequently be improved by increasing the number of moles of Li exchanged which is usually below 1 per transition metal ion (but that can reach 3 for conversion reactions, not discussed here [1, 2]), by choosing an active material with a low molar mass and/or by choosing a positive electrode material which can operated at higher potential E.

3. Positive Electrode Materials

The choice of the positive electrode material is important for the optimization of the Li-ion battery. The ions-electrons duality is mandatory for the positive electrode used in the intercalation chemistry. Indeed the active material should possess both stable crystallographic structure which allows an intercalation/extraction of the Li^+ ions and a transition metal stable at different oxidation states (ability to be oxidized and/or reduced reversibly). There are varieties of active materials which can be classified according to their framework structure (Figure 5):

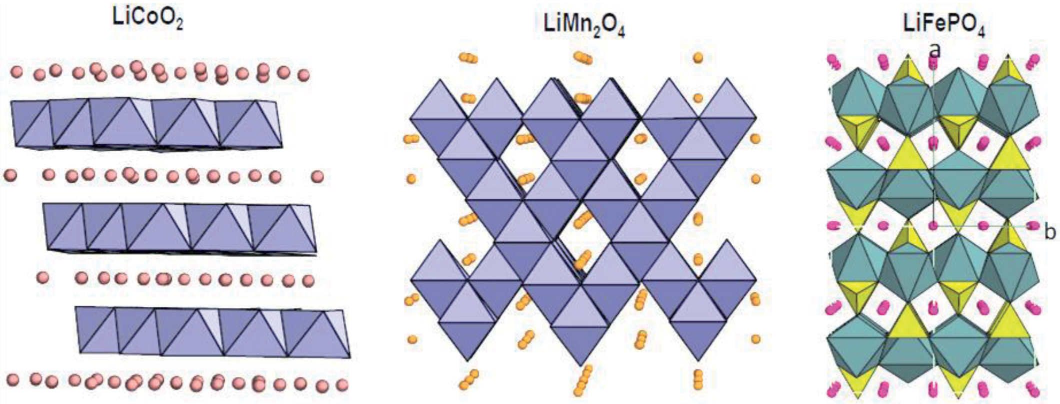

Figure 5: Schematic representation of the crystal structures of 2D $LiCoO_2$ (left), 3D $LiMn_2O_4$ (center) and polyanionic (here triphylite $LiFePO_4$) (right) [3]

Layered structures: The compounds are built up by layers of lithium lying between slabs of close-packed octahedra formed by the transition metal and oxygens. Their structure is therefore a bi-dimensional crystal structure from which lithium ions may be easily intercalated or extracted in a reversible manner. As an example one can mention $LiCoO_2$, first introduced by J.B. Goodenough [4], that remains the main material used as positive electrode in commercial lithium-ion batteries. We can also enumerate $LiNi_{1-y-z}Co_yAl_zO_2$, [5] and $LiCo_{1/3}Ni_{1/3}Mn_{1/3}O_2$ [6]. Overlithiated layered oxides (such as $Li_{1+x}Mn_{1-x}O_2$ with M being mainly Mn) exhibit high reversible capacities (> 200 mAh/g) after an "activation" process at high voltage (> 4.5 V vs. Li) [7, 8]. Due to irreversible structural instabilities (when the number of extracted lithium ions is high at the end of the charge process), irreversible migration of transition metals within the lithium layers may occur and lead to important capacity loss upon cycling. Moreover, a more dramatic effect is that in the charged state the transition metal ions, such as Ni or Co, are at the tetravalent state, an instable oxidation state so that any heating leads to metal reduction through oxygen loss.

Spinel structures: In order to overcome the drawbacks of the layered structures, J.B. Goodenough [9] and M.M. Thackeray [9-11] had envisioned the possibility to use a three-dimensional oxides such as the Spinel $LiMn_2O_4$. In such Spinel structure, MnO_6 octahedra are connected to each other through edge-sharing and define a three-dimensional network of conduction paths for lithium motion (Figure 5). Spinel $LiMn_2O_4$ exhibits an operating voltage of 4.1 V *vs.* Li^+/Li, and its high potential analogue, $Li[Ni_{1/2}Mn_{3/2}]O_4$, lies at about 4.7 V *vs.* Li^+/Li. Coupled with an elevated-potential negative electrode such as the Spinel $Li_4Ti_5O_{12}$, that latter system provides a route to develop a promising new generation of 12 V batteries [12]. These oxides (layered oxides and Spinel oxides) are reasonably good ionic and electronic conductors and lithium insertion/extraction proceeds while operating on the M^{4+}/M^{3+} redox couple, located between 4V and 5V *vs.* Li^+/Li.

Polyanionic frameworks: Besides those "simple" oxides (which may lead actually to quite complicated mixed cation arrangements and properties), three-dimensional frameworks built of transition metals and polyanions $(XO_4)^{n-}$ have become in the last fifteen years the subject of very intensive research worldwide since the discovery of the electrochemically active $LiFePO_4$ [13, 14]. Despite the "weight penalty" (smaller theoretical gravimetric capacity) arising from the presence of polyanion groups such as $(PO_4)^{3-}$, $(SiO_4)^{4-}$, $(SO_4)^{2-}$ etc. the positive attributes of such materials are as follows:

- ✓ Very stable frameworks provide long term structural stability, essential for extensive cycling and safety issues

- ✓ The chemical nature of the polyanion allows the monitoring of a given $M^{n+}/M^{(n-1)+}$ redox couple, through the **inductive effect** introduced by Goodenough [15, 16] and gives rise to higher values *vs.* Li than in oxides

- ✓ An immense variety of atomic arrangements and crystal structures adopted with an extreme versatility towards cation and anion substitutions for a given structural type

Among polyanionic-based materials, one might enumerate: NASICON structure ($A_xMM'(XO_4)_3$); Olivine structure $LiMPO_4$; more "exotic" structures such as hydrated phosphates, diphosphates, alluaudites, silicates, borates… and new promising materials derivated from the Tavorite structure $A_xM(XO_4)Y$.

4. Tavorite Materials

The name Tavorite was known 67 years ago since the first discovery of this mineral by Dr. Elysiário Távora Filho (Brazilian professor of Mineralogy at the Federal University of Rio de Janiero) [17]. The first study of the Tavorite mineral was performed by M.L. Lindberg et al. [18] who proposed the chemical formula of $LiFePO_4OH$ (with Fe ion at the trivalent state), similar to the Montebrasite $LiAlPO_4OH$ (which was discovered in Montebras in ~1870, (Creuse, France) [19]). Note that the description of the Tavorite structure ($LiFePO_4OH$) is exactly the same as that of the Amblygonite structure (first described by Prof. Johann Friedrich August Breithaupt – German mineralogist), which chemical formula consisted of $LiAlPO_4F$. Amblygonite and Tavorite are therefore isostructural and both differ from the Montebrasite structure. Indeed Montebrasite mineral crystallizes in the monoclinic system with the space group of *C2/c*, on the contrary to the Tavorite structure which crystallizes in the triclinic system with the space group *P-1* (Figure 6).

The general chemical formula of Tavorite family is A_xMXO_4Y with A as alkaline ion, M as a transition metal or earth-alkaline metal, X as phosphorus or sulfur and Y as halide, hydroxide, oxygen, or a mixed of halide and hydroxide … V.I. Simonov and N.V. Belov [20] first described the crystal structure of the Tavorite compound. The structure is built up by $[MO_4Y_2]$ octahedra and $[PO_4]$ tetrahedra connected to each other through their corners by oxygen atoms. The octahedra chains of $-[\cdots YO_4MY-YO_4MY\cdots]-$ (Figure 6) are connected through the ligand Y and the chains are connected to each other through $[PO_4]$ tetrahedra by oxygen atoms. Two crystallographic sites were observed for the transition metal M (both at special Wyckoff position) and one crystallographic site for X (phosphorus or sulfur). The structure generates 3 tunnels (in three directions) within which the atom A lies. The number of Li sites and their precise localization were hypothetical in the Tavorite-type structure. Indeed V.I. Simonov and N.V. Belov [20], through their studies of the $LiAlPO_4(F_x,OH_{1-x})$ series, reported a large and extremely anisotropic displacement parameter for the Li atom and suggested that the site was split into two fractionally occupied positions. Note that Baur et al. [21] found no such splitting in the structure of Montebrasite $LiAlPO_4OH$. Later, during the study of the $LiAlPO_4(F_x,OH_{1-x})$ series (performed using single crystals), L.A. Groat et al. [22] confirmed the distribution of Li between two sites highly dependent on the amount of fluorine in the sample.

Note that the Montebrasite structure is very similar with the Tavorite / Amblygonite one, but slightly more distorted with only one site for the transition metal (Figure 6).

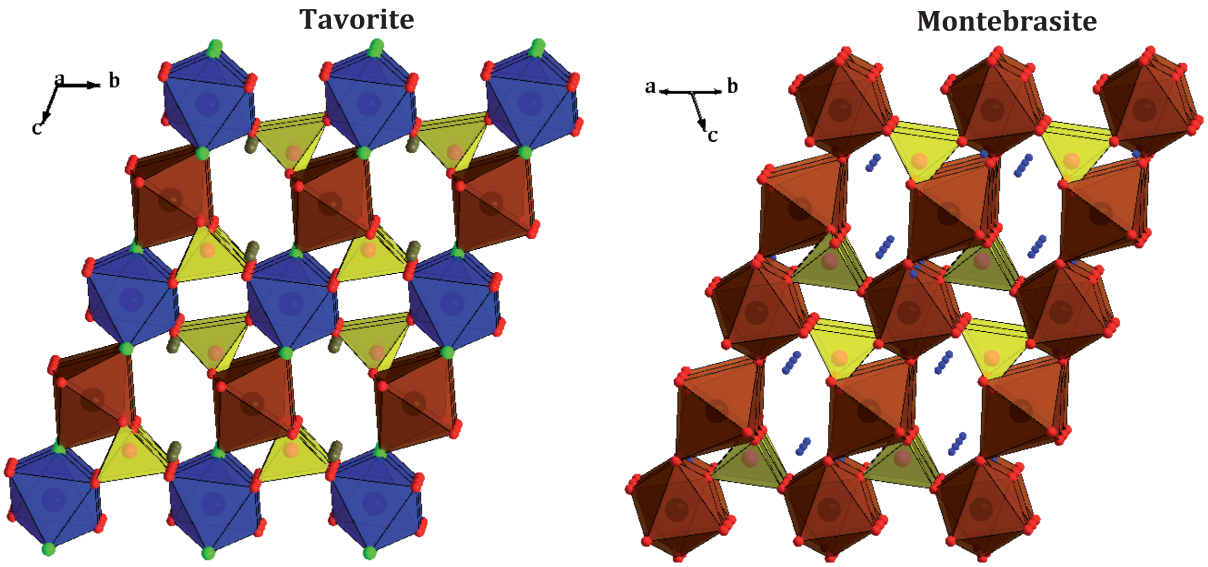
Tavorite

Montebrasite

Figure 6: Representation of the Tavorite (left) and Montebrasite (right) crystal structures. The blue and brown polyhedra are MO_4Y_2 octahedra and the yellow are XO_4 tetrahedra.

Four models of unit cells describing the Tavorite structure are reported in literature and gathered in Table 1. Figure 7 illustrates how these models are related to each other. The feature of model I, the most commonly used, is that $a_I < b_I < c_I$, $(\alpha_I, \beta_I) > 100°$, and $\gamma_I < 100°$. Model II derives from Model I through a simple permutation of the lattice parameters and angles: in other words, the generated "boxes" are identical. The volume of the unit-cell of Model III is twice bigger than those of Models I and II with complex transformation from one to the other ($a_{III} = a_I + b_I$, $b_{III} = c_I$, and $c_{III} = b_I - a_I$). One peculiar feature of Model IV, rarely used, is that at least one of the angles is lower than 70°, that is, far from a conventional description of a triclinic system. In this thesis the structure of the Tavorite will always be described in Model I so that the octahedra chains are running along the ***c*** axis. Note however that J. Barker et al. described the Tavorite-like $LiVPO_4F$ in Model I, but with the chains running along the longest diagonal of the primitive cell.

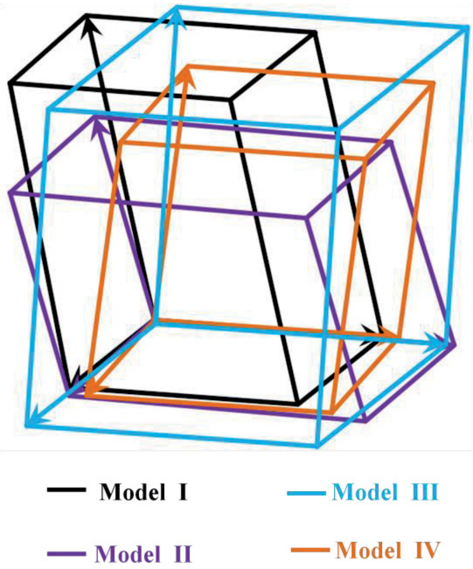

Figure 7: Illustration of geometrical relationships between the four models used in the literature to describe Tavorite-type structures.

Table 1 : Tavorite-like structures reported in the literature that adopt the space group $P\bar{1}$

	A	*b*	*c*	*α*	*B*	*γ*	V (Å)	*References*	MODEL
$FeSO_4\cdot H_2O$	5.176	5.176	7.608	107.57	107.57	93.65	182.55	*ICSD# 79162*	I
$LiMgSO_4F$	5.162	5.388	7.073	106.68	107.4	97.50	174.72	*ICSD# 281119*	I
$LiFeSO_4F$	5.174	5.494	7.222	106.52	107.21	97.791	182.44	*[23, 24]*	I
$LiCoSO_4F$	5.172	5.421	7.184	106.85	107.78	97.98	177.77	*ICSD# 167202*	I
$LiAlPO_4\cdot OH_{0.5}F_{0.5}$	5.060	5.160	7.080	109.87	107.5	97.9	159.78	*ICSD# 20577*	I
$LiAlPO_4F$	5.060	5.160	7.080	109.87	107.5	97.9	159.78	*ICSD# 48012*	I
$LiTiPO_4F$	5.199	5.314	7.243	106.97	108.26	97.655	176.09	*[20]*	I
$LiVPO_4F$	5.170	5.308	7.263	107.59	107.97	98.39	174.36	*This Work*	I
$LiFePO_4F$	5.155	5.304	7.261	107.35	107.85	98.618	174.24	*[20, 21]*	I
$LiFePO_4OH$	5.347	7.284	5.132	109.15	97.90	106.52	175.05	*ICSD# 167608*	II
Li_2FePO_4F	5.374	7.443	5.325	109.03	94.423	108.26	187.41	*[21]*	II
$LiTiPO_4O$	6.904	7.197	7.903	90.45	91.31	117.19	349.13	*ICSD# 39761*	III
$LiVPO_4O$	6.748	7.206	7.922	89.84	91.32	116.99	343.16	*ICSD# 20537*	III
$LiAlPO_4\cdot OH_{0.5}F_{0.5}$	5.184	7.155	5.040	112.12	97.80	67.88	160.43	*ICSD# 26513*	IV
$LiFePO_4\cdot(OH_{0.5},F_{0.5})$	5.138	5.307	7.422	67.48	67.72	81.98	172.99	*ICSD# 20808*	IV
$LiGaPO_4\cdot OH$	5.085	5.297	7.301	67.830	67.839	82.027	168.67	*ICSD# 250410*	IV

Tavorite based materials are becoming the subject of studies as positive materials for Li-ion batteries. Indeed the combination of "Tavorite" and "battery" introduced in "web of knowledge" gave a result of 30 articles, with 18 publications for only the year of 2012 (Figure 8). The tremendous increase of the number of citations also shows the huge interest of researchers for this new type of materials which was almost unknown 5 years ago as materials for Li-ion batteries. Note that ICMCB and LRCS published their first results on Tavorite-type materials for Li-ion batteries in 2010 [23-27].

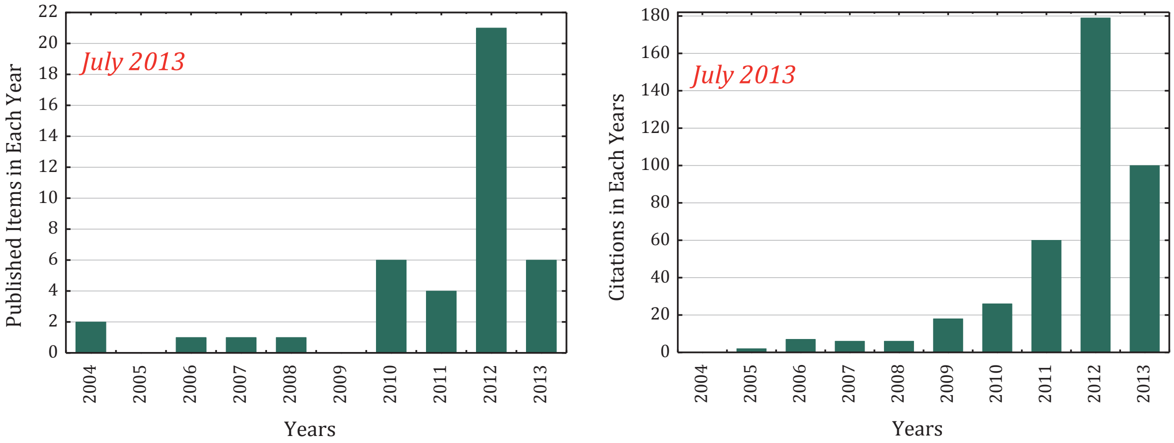

Figure 8: (left) Evolution of the number of articles published based on Tavorite system. (right) Evolution of the citations in each year. (Data recorded for the past 10 years in "web of knowledge")

5. The Aim of This Thesis

Fluoro-phosphate (and fluoro-sulphate) materials benefit in particular from the inductive effect of both phosphate (respectively sulphate) and F anions, which lowers the energy of a given $M^n/M^{n\text{-}1}$ redox couple, therefore leading to the increase of its potential vs. Li. As a result, lithium transition metal fluorophosphates is an appealing class of materials for Li-ion batteries as these Tavorite-type structures are capable to operate at very high potential compared to other phosphates ($Li_3V_2(PO_4)_3$, $LiFePO_4$ ...), hydroxyl phosphates ($LiFePO_4OH$ ...), oxyphosphates ($LiVPO_4O$, VPO_4O ...) ... Few (only 4 to our knowledge) structural families of lithium and sodium transition metal fluorophosphates have been reported before in the literature: $AMPO_4F$ (Figure 9), $A_3M_2(PO_4)_2F_3$ [28, 29] A_2MPO_4F [30, 31] and $A_5M(PO_4)_2F_2$ [32]. Note that the so-called fluorophosphates should be actually called fluoride phosphates as they combine phosphate and fluoride anions in the same framework and do not contain P-F type bonds.

Since the potential of a redox couple depend on the combination of the nature of the metal, the nature of the ligand and the nature of the crystalline structure, a large variety of Tavorite type material operate in a large range potential including 1.2 V to ~4.3 V vs. Li^+ (see Figure 9).

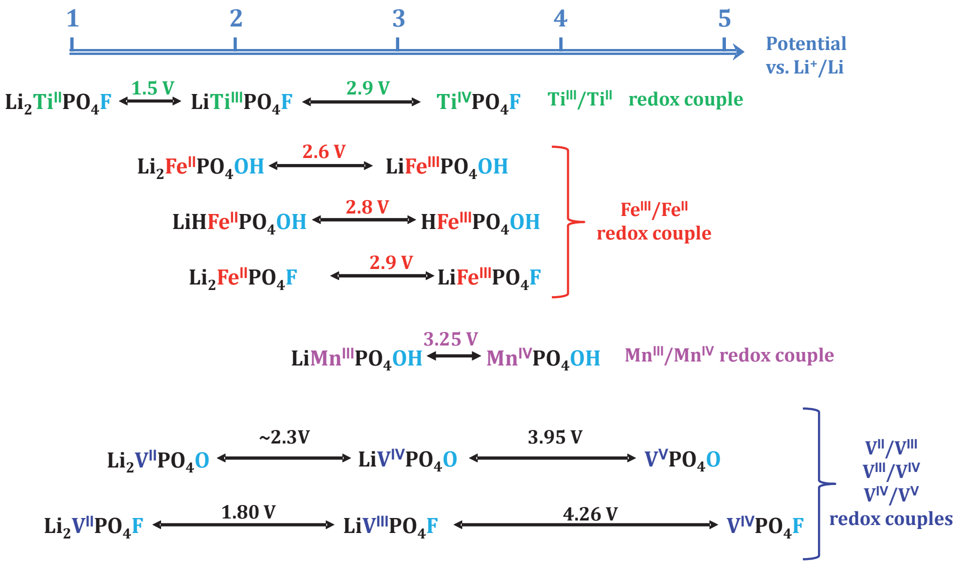
1
2
3
4
5
Potential vs. Li^+/Li
$Li_2Ti^{II}PO_4F$
1.5 V
$LiTi^{III}PO_4F$
2.9 V
$Ti^{IV}PO_4F$
Ti^{III}/Ti^{II} redox couple
$Li_2Fe^{II}PO_4OH$
2.6 V
$LiFe^{III}PO_4OH$
$LiHFe^{II}PO_4OH$
2.8 V
$HFe^{III}PO_4OH$
$Li_2Fe^{II}PO_4F$
2.9 V
$LiFe^{III}PO_4F$
Fe^{III}/Fe^{II} redox couple
$LiMn^{III}PO_4OH$
3.25 V
$Mn^{IV}PO_4OH$
Mn^{III}/Mn^{IV} redox couple
$Li_2V^{II}PO_4O$
~2.3V
$LiV^{IV}PO_4O$
3.95 V
$V^{V}PO_4O$
$Li_2V^{II}PO_4F$
1.80 V
$LiV^{III}PO_4F$
4.26 V
$V^{IV}PO_4F$
V^{II}/V^{III}
V^{III}/V^{IV}
V^{IV}/V^{V}
redox couples

Figure 9: Overview of redox couple potentials for the transition metal in Tavorite A_xMPO_4Y [3]

The crystal chemistry of Tavorite fluorophosphates, particularly the localization of the Li atom, was very ambiguous at the beginning of this work, due to the difficulty in obtaining single-phase samples exempt of impurities. Therefore, optimization of synthesis procedure and clarification of the crystal structures of $LiMPO_4F$ (M = V, Fe, Ti) were our priority. The prime focuses in this thesis are highlighted as follows:

- Preparation of high purity $LiMPO_4F$ via solid-state routes.
- Structural studies of $LiMPO_4F$ using X-ray and neutron diffraction, ^7Li, ^{31}P and ^{19}F MAS NMR.
- Magnetic behaviour and magnetic structure of $LiVPO_4F$ and $LiFePO_4F$ through the evolution of the magnetic susceptibility with temperature and neutron diffraction experiments performed at low temperature.
- Understanding the Li^+ extraction/insertion and insertion/extraction mechanism from/into $LiMPO_4F$.

References

1. Poizot, P.; Laruelle, S.; Grugeon, S.; Dupont, L. and Tarascon, J.M.; *From the Vanadates to 3d-Metal Oxides Negative Electrodes,* Ionics, **2000**, 6(5-6): p. 321-330.
2. Poizot, P.; Laruelle, S.; Grugeon, S.; Dupont, L. and Tarascon, J.M.; *Nano-sized transition-metaloxides as negative-electrode materials for lithium-ion batteries,* Nature, **2000**, 407(6803): p. 496-499.
3. Masquelier, C. and Croguennec, L.; *Polyanionic (Phosphates, Silicates, Sulfates) Frameworks as Electrode Materials for Rechargeable Li (or Na) Batteries,* Chemical Reviews, **2013**, 10.1021/cr3001862.
4. Mizushima, K.; Jones, P.C.; Wiseman, P.J. and Goodenough, J.B.; *LiXCOO2 "(0-less-Than-X-less-Than-Or-Equal-To-1) - A New Cathode Material for Batteries of High-Energy density* Materials Research Bulletin, **1980**, 15(6): p. 783-789.
5. Guilmard, M.; Pouillerie, C.; Croguennec, L. and Delmas, C.; *Structural and electrochemical properties of LiNi0.70Co0.15Al0.15O2,* Solid State Ionics, **2003**, 160(1-2): p. 39-50.
6. Ohzuku, T. and Makimura, Y.; *Layered lithium insertion material of LiCo1/3Ni1/3Mn1/3O2 for lithium-ion batteries,* Chemistry Letters, **2001**(7): p. 642-643.
7. Kropf, A.J.; Johnson, C.S.; Vaughey, J.T. and Thackeray, M.M.; *XAFS analysis of layered Li(x)Ni(0.5)Mn(0.5)O(2) (0 < x <= 2) electrodes for lithium batteries,* Physica Scripta, **2005**, T115: p. 274-277.
8. Lu, Z.H.; MacNeil, D.D. and Dahn, J.R.; *Layered cathode materials Li NixLi(1/3-2x/3)Mn(2/3-x/3) O-2 for lithium-ion batteries,* Electrochemical and Solid State Letters, **2001**, 4(11): p. A191-A194.
9. Goodenough, J.B.; Thackeray, M.M.; David, W.I.F. and Bruce, P.G.; *Lithium Insertion Extraction Reactions with Manganese Oxides,* Revue De Chimie Minerale, **1984**, 21(4): p. 435-455.
10. Thackeray, M.M.; David, W.I.F. and Goodenough, J.B.; *Structural Characterization of the Lithiated Iron-Oxides LiXFe3O4 and LiXFe2O3 (0-Less-Than-X-Less-Than-2),* Materials Research Bulletin, **1982**, 17(6): p. 785-793.
11. Thackeray, M.M.; Depicciotto, L.A.; David, W.I.F.; Bruce, P.G. and Goodenough, J.B.; *Structural Refinement of Delithiated LiVO2 by Neutron-Diffraction,* Journal of Solid State Chemistry, **1987**, 67(2): p. 285-290.
12. Imazaki, M.; Ariyoshi, K. and Ohzuku, T.; *An Approach to 12 V “Lead-Free” Batteries: Tolerance toward Overcharge of 2.5 V Battery Consisting of LTO and LAMO Batteries and Energy Storage: ,* J. Electrochem. Soc., **2009**, 156(10): p. A780-A786.
13. Padhi, A.K.; Nanjundaswamy, K.S. and Goodenough, J.B.; *Phospho-olivines as positive-electrode materials for rechargeable lithium batteries,* Journal of the Electrochemical Society, **1997**, 144(4): p. 1188-1194.
14. Padhi, A.K.; Nanjundaswamy, K.S.; Masquelier, C.; Okada, S. and Goodenough, J.B.; *Effect of structure on the Fe3+/Fe2+ redox couple in iron phosphates,* Journal of the Electrochemical Society, **1997**, 144(5): p. 1609-1613.
15. Manthiram, A. and Goodenough, J.B.; *Lithium Insertion into Fe2(Mo4)3 Frameworks - Comparison of M = W with M = Mo,* Journal of Solid State Chemistry, **1987**, 71(2): p. 349-360.
16. Manthiram, A. and Goodenough, J.B.; *Lithium Insertion into Fe2(SO4)3 Frameworks,* Journal of Power Sources, **1989**, 26(3-4): p. 403-408.
17. Filho, E.T., *Estudos brasileiros de geologia*. 1946: Fundação Getrilio Varpas.
18. Lindberg, M.L. and Pecora, W.T.; *Tavorite and Barbozalite, 2 New Phostate Minerals from Minas-Gerais, Brazil,* American Mineralogist, **1955**, 40(11-2): p. 952-966.
19. Cloizeaux, A.D., *On a New Locality of Amblygonite and on Montebrasite, A new Hydrated Aluminium and Lithium Phosphate*. 1874.

20. Simonov, V.I. and Belov, N.V.; *The Crystal Structure of Amblygonite,* Doklady Akademii Nauk Sssr, **1958**, 119(2): p. 354-356.
21. Baur, W.H.; *Die Kristallstruktur des Edelamblygonits LiAlPO4(OH,F),* Acta Crystallographica, **1959**, 12(12): p. 988-994.
22. Groat, L.A.; Chakoumakos, B.C.; Brouwer, D.H.; Hoffman, C.M.; Fyfe, C.A.; Morell, H. and Schultz, A.J.; *The amblygonite (LiAlPO(4)F)-montebrasite (LiAlPO(4)OH) solid solution: A combined powder and single-crystal neutron diffraction and solid-state (6)Li MAS, CP MAS, and REDOR NMR study,* American Mineralogist, **2003**, 88(1): p. 195-210.
23. Marx, N.; *Synthèse et Caractérisation de Nouveaux Phosphates Utilisés Comme Matériaux d'Electrode Positive pour Batteries au Lithium,* Univestité de Bordeaux 1, **2010**.
24. Marx, N.; Croguennec, L.; Carlier, D.; Bourgeois, L.; Kubiak, P.; Le Cras, F. and Delmas, C.; *Structural and Electrochemical Study of a New Crystalline Hydrated Iron(III) Phosphate FePO(4)center dot H(2)O Obtained from LiFePO(4)(OH) by Ion Exchange,* Chemistry of Materials, **2010**, 22(5): p. 1854-1861.
25. Marx, N.; Croguennec, L.; Carlier, D.; Wattiaux, A.; Le Cras, F.; Suard, E. and Delmas, C.; *The structure of tavorite LiFePO(4)(OH) from diffraction and GGA plus U studies and its preliminary electrochemical characterization,* Dalton Transactions, **2010**, 39(21): p. 5108-5116.
26. Recham, N.; Chotard, J.N.; Dupont, L.; Delacourt, C.; Walker, W.; Armand, M. and Tarascon, J.M.; *A 3.6 V lithium-based fluorosulphate insertion positive electrode for lithium-ion batteries,* Nature Materials, **2010**, 9(1): p. 68-74.
27. Recham, N.; Chotard, J.N.; Jumas, J.C.; Laffont, L.; Armand, M. and Tarascon, J.M.; *Ionothermal Synthesis of Li-Based Fluorophosphates Electrodes,* Chemistry of Materials, **2010**, 22(3): p. 1142-1148.
28. Le Meins, J.M.; Bohnke, O. and Courbion, G.; *Ionic conductivity of crystalline and amorphous Na3Al2(PO4)(2)F-3,* Solid State Ionics, **1998**, 111(1-2): p. 67-75.
29. Le Meins, J.M.; Courbion, G. and Greneche, J.M.; *Structural phase transitions evidenced by Mossbauer spectrometry in a ferric fluorophosphate: Na3Fe2(PO4)(2)F-3,* Hyperfine Interactions, **1999**, 122(3-4): p. 365-369.
30. Yakubovich, O.V.; Karimova, O.V. and Melnikov, O.K.; *The mixed anionic framework in the structure of Na-2{MnF PO4 },* Acta Crystallographica Section C-Crystal Structure Communications, **1997**, 53: p. 395-397.
31. Dutreilh, M.; Chevalier, C.; El-Ghozzi, M.; Avignant, D. and Montel, J.M.; *Synthesis and crystal structure of a new lithium nickel fluorophosphate Li-2 NiF(PO4) with an ordered mixed anionic framework,* Journal of Solid State Chemistry, **1999**, 142(1): p. 1-5.
32. Yin, S.C.; Herle, P.S.; Higgins, A.; Taylor, N.J.; Makimura, Y. and Nazar, L.F.; *Dimensional reduction: Synthesis and structure of layered Li5M(PO4)(2)F-2 (M = V, Cr),* Chemistry of Materials, **2006**, 18(7): p. 1745-1752.

Chapter I

SYNTHESIS AND CRYSTAL STRUCTURE OF $LiVPO_4F$ AND $LiVPO_4O$

Contents

I-1. Introduction 23

I-2. CERAMIC SYNTHESIS OF $LiVPO_4F$ AND $LiVPO_4O$ 24

- **I-2a. One-step Ceramic Synthesis of $LiVPO_4F$** 24
- **I-2b. Two-Step Ceramic Route for the Synthesis of $LiVPO_4F$** 26
  - ***i- Synthesis of the intermediate phase: C-VPO_4*** *26*
  - ***ii- Synthesis of $LiVPO_4F$*** *28*
- **I-2c. Synthesis of $LiVPO_4O$** 30
- **I-2d. Morphology and Magnetic Behavior of $LiVPO_4X$ (X = O/F)** 31
- **I-2e. Summary and Conclusion** 34

I-3. CRYSTAL AND MAGNETIC STRUCTURES OF $LiVPO_4F$ 34

- **I-3a. The Crystal structure of $LiVPO_4F$** 35
- **I-3b. NMR Study of $LiVPO_4F$** 40
- **I-3c. Magnetic structure of $LiVPO_4F$** 44
- **I-3d. Conclusion and Summary** 46

I-4. CRYSTAL STRUCTURE AND NMR STUDY OF $LiVPO_4O$ 47

- **I-4a. Crystal structure of $LiVPO_4O$** 47
- **I-4b. NMR Study of $LiVPO_4O$** 51

I-5. Conclusion and summary of this chapter 53

I-1. Introduction

The lithium vanadium fluorophosphate $LiVPO_4F$ was first synthesized by J. Barker et al. [1, 2] through a two-step ceramic process, the first step being a carbothermal reduction (CTR) process which leads to the formation of VPO_4. An excess of carbon was used over stoichiometric proportions in order to ensure a complete reduction of vanadium. Y. Li et al. [3] and Q. Zhang et al. [4] reported the synthesis of $LiVPO_4F$ using a two-step sol-gel process with the synthesis of $V_2O_5{\cdot}nH_2O$ as an intermediate phase. A pure phase of $LiVPO_4F$, as mentioned by several authors [4-8], is quite difficult to obtain.

J. Barker et al. [1, 2, 9, 10] had proposed that $LiVPO_4F$ crystallized in the same space group as $LiAlPO_4F$ which is a member of Tavorite (refer to the general introduction) type structure. Based on the analogy with $LiAlPO_4F$, J. Barker proposed that the Li atoms were located within 2 crystallographic sites with 50% occupancy in each. However, the position of one of the Li sites is highly hypothetical as we will discuss later.

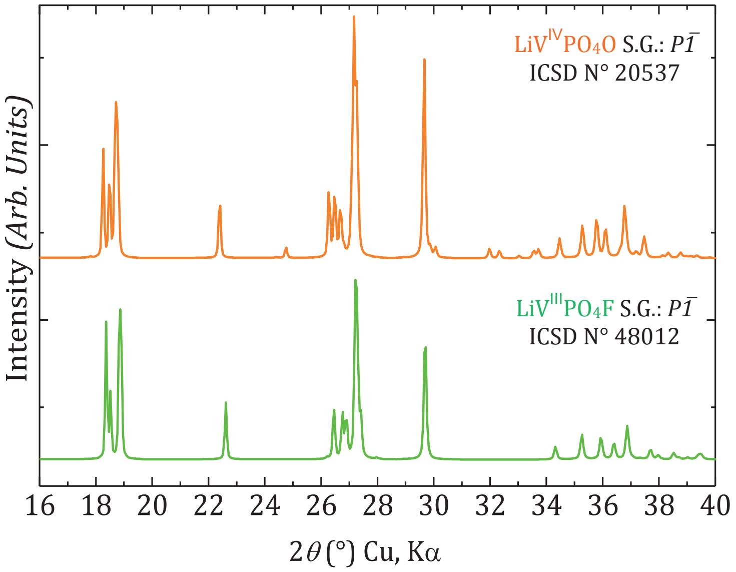

Figure I-1: Simulated XRD patterns of $LiVPO_4O$ (orange) and $LiVPO_4F$ (green) from ICSD N° 20537 and $LiAlPO_4F$ (ICSD N° 48012, where Al was replaced by V) respectively.

In the two following chapters, we will compare $LiVPO_4F$ with the triclinic lithium vanadium oxyphosphate $LiVPO_4O$ which is often obtained by a sol-gel process [8, 11, 12]. The only structural studies of $LiVPO_4O$ were carried out by a Russian group 30 years ago [13] and no other structural determination was done so far!!! The tavorite phases $LiVPO_4O$ and $LiVPO_4F$ are homeotypic, their X-ray Diffraction (XRD) patterns being very similar (Figure I-1) but in fact differ. A closer inspection shows additional diffraction peaks for $LiVPO_4O$ displayed at 25°, 32.2°, and 32.5° in 2θ (d = 3.56 Å, 2.78 Å, and 2.75 Å, respectively) compared to the simulated XRD pattern of $LiVPO_4F$ (simulation obtained from $LiAlPO_4F$ (ICSD N° 48012) where Al was replaced by V).

In this chapter we present our results in defining a reliable procedure for the ceramic synthesis of pure phases of $LiVPO_4F$ and $LiVPO_4O$. Their crystal structure as well as their magnetic structure will be presented, as a result of refinements of both X-Ray and neutron diffraction data.

I-2. CERAMIC SYNTHESIS OF $LiVPO_4F$ AND $LiVPO_4O$

I-2a. One-step Ceramic Synthesis of $LiVPO_4F$

We attempted to synthesize $LiVPO_4F$ through a one-step ceramic route using either V_2O_3 or V_2O_5 as vanadium precursors. Stoichiometric amounts of V_2O_3 vanadium (III) oxide (99.9%, from CERAC), $NH_4H_2PO_4$ ammonium phosphate monobasic, and LiF lithium fluoride (both from Aldrich) were mixed in a planetary ball milling machine and then pressed as a pellet. A first thermal treatment was undertaken at 300 °C during 5 hours under argon flow so as to remove ammonia [14]. After grinding the obtained powder for homogenization, new pellets were heated up to 800 °C for 10 h under argon flow.

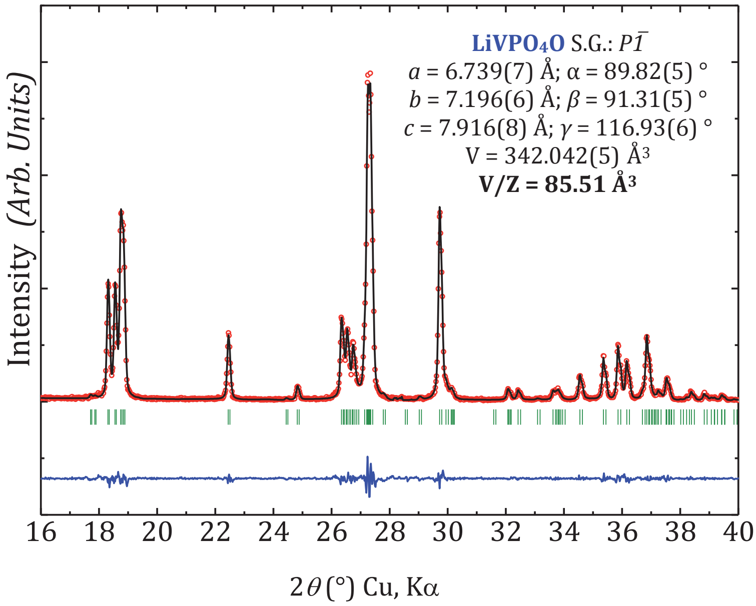

Figure I-2: XRD pattern refinement of $LVPO_4O$ obtained through a one-step reaction using LiF as lithium precursor

The recovered powder was “pale green” in color, and its X-ray diffraction (XRD) pattern was successfully refined using the lattice parameters of $LiVPO_4O$ (Figure I-2) instead of those reported for $LiVPO_4F$. To the best of our knowledge, this triclinic phase of $LiVPO_4O$ had never been synthesized directly by a ceramic route as only a sol–gel procedure had been reported previously [11, 12]. The obtention of $LiVPO_4O$ using LiF as a precursor (so as to obtain $LiVPO_4F$) raised two main observations:

- *The absence of fluorine in the final product whereas LiF was used as lithium precursor.* This was also observed by C. Allen et al. [8] who mixed VPO_4 and LiF in stoichiometric proportions together with $CH_3(CH_2)_4COOH$ and ended up with the monoclinic α-$Li_3V_2(PO_4)_3$ in which the vanadium oxidation state is +3. The absence of fluorine in the final product was due to the formation of HF which reacted together with NH_3 on the quartz tube to form $(NH_4)_2SiF_6$ (NH_3 which is generated from both NH_4VO_3 and $NH_4H_2PO_4$ precursors, can react with SiO_2 and form $H_2NSiOOH$ as established by M. Zhou et al. [15]). We therefore believe that during the synthesis of $LiVPO_4F$, C. Allen obtained a decomposition of the complex $H_2NSiOOH$ and formed $(NH_4)_2SiF_6$ according to the reaction ①:

①
$$6\ HF + 2\ NH_3 + SiO_2 \rightarrow (NH_4)_2SiF_6 + 2\ H_2O$$

As it will be discussed later based on XRD data refinement, we also did not observe the presence of fluorine in the final product as would have been the case in the solid solution $LiVPO_4O_xF_y$.

- *The oxidation of vanadium from V^{3+} to V^{4+} whereas the synthesis was performed in argon.* It appeared that the tubular furnace used was not well hermetic and hence favored this vanadium oxidation, which allowed us, by the way, to discover the direct synthesis of pure $LiVPO_4O$. In order to avoid the oxidation of vanadium which leads to the formation of $LiVPO_4O$ instead of $LiVPO_4F$, we have performed the direct synthesis in a hermetic furnace. We ended up with the monoclinic α-$Li_3V_2(PO_4)_3$ as a main phase together with small amounts of unknown impurities.

The second attempt of the synthesis of $LiVPO_4F$ through a one-step ceramic route was done using V_2O_5 as the vanadium precursor instead of V_2O_3. Just as previously, we mixed stoichiometric proportions of vanadium oxide (V) with ammonium phosphate ($NH_4H_2PO_4$) and lithium fluoride (LiF). In order to reduce the oxidation state of vanadium, we added in a stoichiometric proportion highly divided carbon source (C_{sp}). Carbon favors the formation of carbon monoxide (CO) at high temperature and thus leads to the reduction of the oxidation state of vanadium. This type of reaction is called carbothermal reduction (CTR). Using V_2O_5 as a vanadium source led to the formation of the α-$Li_3V_2(PO_4)_3$ and V_2O_3 as final products. We did not succeed to synthesize $LiVPO_4F$ through a one-step ceramic route and hence developed a different two-step ceramic route.

I-2b. Two-Step Ceramic Route for the Synthesis of $LiVPO_4F$

As presented in the introduction of this chapter, J. Barker et al. reported the synthesis of $LiVPO_4F$ through an intermediate phase VPO_4 which had been obtained by carbothermal reduction (CTR) [1, 16]. CTR is a solid-state synthesis method using a highly divided carbon which reacts with a transition metal oxide in order to reduce the oxidation state of the corresponding metal. The CTR method is widely used in industry in order to reduce a metal oxide to a metal state and relies on two reactions:

② $C + O_2 \Leftrightarrow CO_2$

③ $2\ C + O_2 \Leftrightarrow 2\ CO$

While the formation enthalpy of CO_2 is lower than the one of CO (-394 kJ·mol^{-1} *vs.* -220 kJ·mol^{-1}), the formation entropy of CO_2 is much more lower (2 J·mol^{-1}·K^{-1} for CO_2 *vs.* 177 J·mol^{-1}·K^{-1} for CO). Consequently, according to the Ellingham diagram, the overall free energy of formation for CO_2 by oxidation of carbon is almost constant and independent of the temperature, while the CO free energy formation is a decreasing line (negative slope). Carbon is unique in the sense of having an oxide (CO) whose free energy of formation becomes increasingly negative as the temperature increases. CO is therefore more stable at higher temperatures. This means that providing a higher enough reaction temperature, carbon can reduce any metal oxide so as to form CO and a metal [16].

i- Synthesis of the intermediate phase: C-VPO_4

To synthesize VPO_4, we mixed (according to the reaction ④) stoichiometric proportions of vanadium oxide (V_2O_5, 99.9% from Aldrich), ammonium phosphate ($NH_4H_2PO_4$ from Aldrich) and carbon according to the equation ④.

④ $$V_2O_5 + 2\ NH_4H_2PO_4 + 2\ C_{SP} \rightarrow 2\ VPO_4 + 2\ NH_3 + 3\ H_2O + 2\ CO$$

To enable complete vanadium reduction and to ensure the presence of residual carbon in the final product, 5% mass excess of carbon was used, therefore producing a C-VPO_4 composite. The choice of carbon is important since highly divided carbon yields better reduction of the metal oxide and we therefore choose carbon super P (C_{sp}) which XRD diffraction pattern (Figure I-3) exhibits broad lines at $(002)_{P6_3mc}$ and $(101)_{P6_3mc}$.

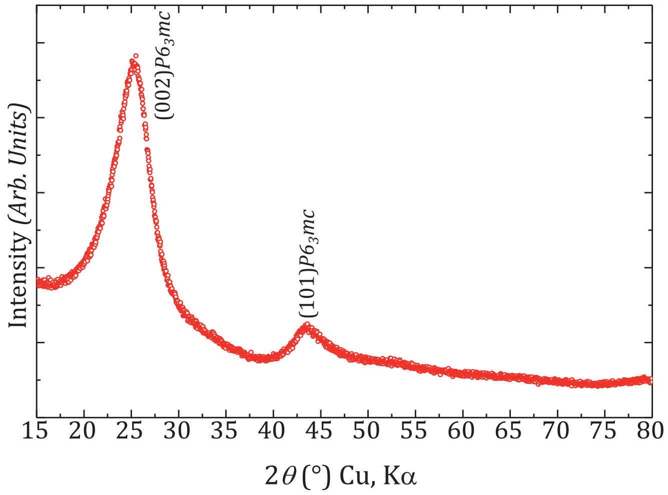

Figure I-3: XRD pattern of C_{SP} used for carbothermal synthesis of VPO_4

The precursors were ball milled in a Spex grinder for 90 min. (or in a planetary grinder for 12 hours). We observed that during milling, the powder color changed from orange for a small milling time, to green for a medium milling time and black for a long milling time (90 min in Spex or 12 hours in planetary grinder). The milled powder was pressed into a pellet and then heated up to 300 °C during 8 hours under argon flow (pretreatment) prior to a grinding and a final treatment at 800 °C during 10 hours under argon flow. Figure I-4 shows the result obtained from a full-pattern matching refinement of VPO_4 XRD data based on a structural model described in a monoclinic unit cell in the space group *Cmcm* (N° 63). The lattice parameters obtained (insert in Figure I-4) are close to those reported in ICSD N° 36521.

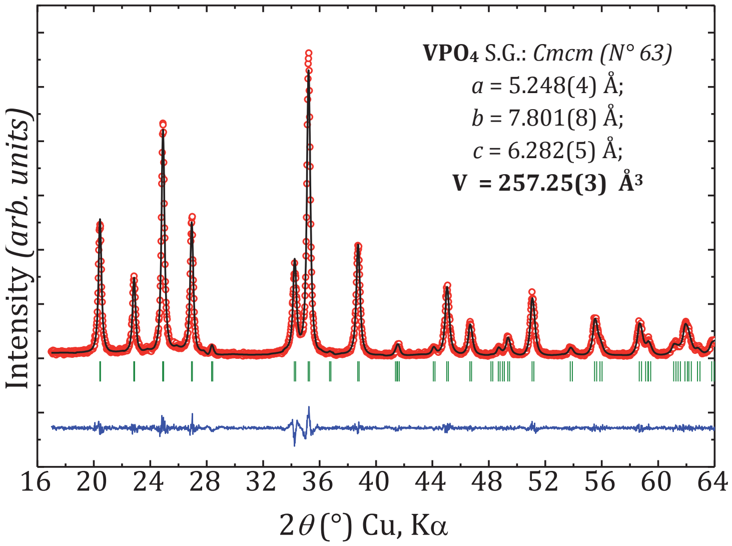

Figure I-4: XRD pattern refinement of C–VPO_4 obtained through a CTR process

ii- Synthesis of $LiVPO_4F$

VPO_4 was mixed with lithium fluoride in stoichiometric proportions (according to the reaction ⑤) and the obtained powder was pressed into a pellet, subsequently heated up to 750°C under argon flow in a crucible during one hour.

$$⑤ \qquad VPO_4 + LiF \rightarrow LiVPO_4F$$

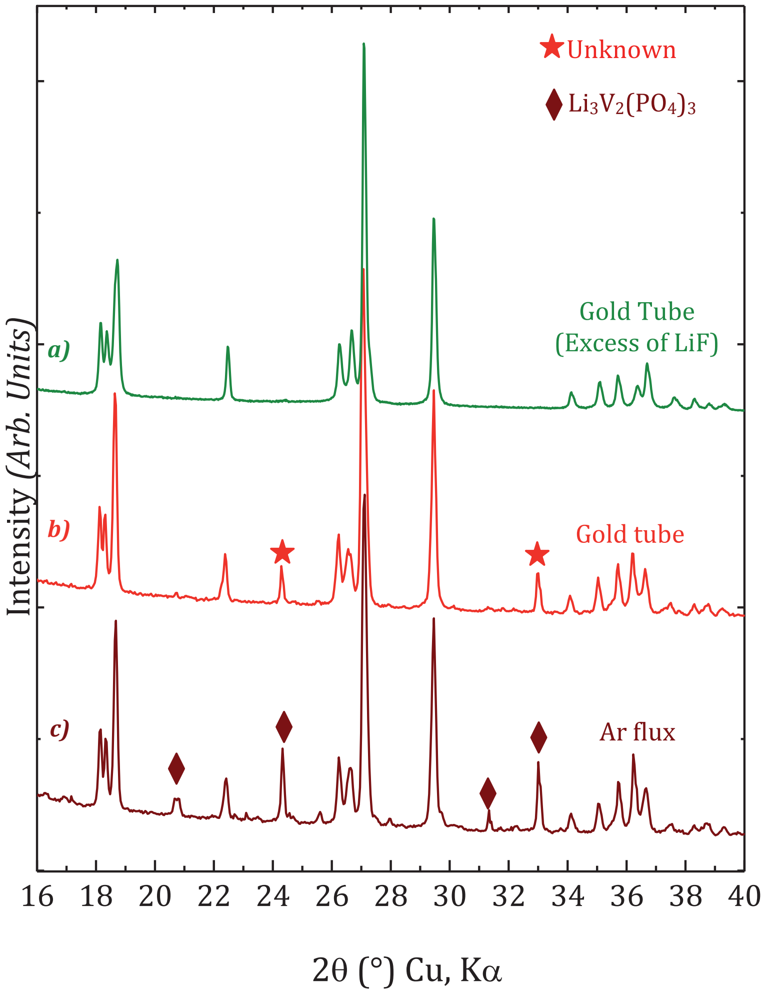

Figure I-5: X-ray diffraction patterns of different powders prepared in this work a) pellet under Ar flux in crucible, b) pellet in a gold sealed tube, c) stoichiometric proportions of VPO_4/LiF in a gold sealed tube.

The XRD data of the "dark grey" product obtained (Figure I-5a) is comparable to the simulated XRD pattern of $LiVPO_4F$. Nevertheless, careful analysis showed the presence of α-$Li_3V_2(PO_4)_3$ as an impurity. This impurity, containing a V/P ratio of 2/3, was produced by the sublimation of VF_3 from the reaction mixture, as mentioned also by F. Zhou et al. [7], according to the reaction scheme:

$$⑥ \qquad 3\ LiVPO_4F \rightarrow Li_3V_2(PO_4)_3 + VF_{3(gaz)}$$

To bypass the sublimation of VF_3, we decided to perform the synthesis by placing the VPO_4/LiF mixture in a gold tube sealed in an argon-filled glove box, so as to avoid the argon flow. The tube was then heated up to 750°C during 1 h and quenched in liquid nitrogen. The XRD pattern (Figure I-5b) shows that the two first peaks of the impurity obtained are similar to the previous α-$Li_3V_2(PO_4)_3$. However, the full-pattern matching refinement revealed that the lattice parameters of that impurity did not converge to those of α-$Li_3V_2(PO_4)_3$. Moreover, we observed that this unknown impurity is soluble in water, the solution becoming green after 12 hours of stirring. After filtration and drying, pure $LiVPO_4F$ was obtained. Q. Zhang et al. [4] reported the synthesis of $LiVPO_4F$ and claimed to observe Li_3PO_4 as an impurity. This impurity was not encountered during our many attempts of synthesis of $LiVPO_4F$.

In order to obtain Li/V/P/F proportions as close as possible to the ideal stoichiometry, thermal gravimetric analysis experiments (TGA) of C-VPO_4 have been performed so as to determine the exact amount of remaining carbon in the synthesized C-VPO_4 composite. Figure I-6a displays the TGA and DSC data of C-VPO_4 heated under O_2 flow, the final product being VPO_4O (XRD pattern displayed in Figure I-6b) according to the reaction ⑦:

⑦ $$\text{C-VPO}_4 + 3/2\ \text{O}_2 \rightarrow \text{VPO}_4\text{O} + \text{CO}_2$$

The percentage of carbon found in C-VPO_4 (7.68 %) has then been taken into account for the subsequent synthesis of $LiVPO_4F$ so as to ensure the best stoichiometric proportions between VPO_4 and LiF. A highly pure $LiVPO_4F$ powder was obtained by this procedure (Figure I-5c) which was used successfully several times with excellent reproducibility.

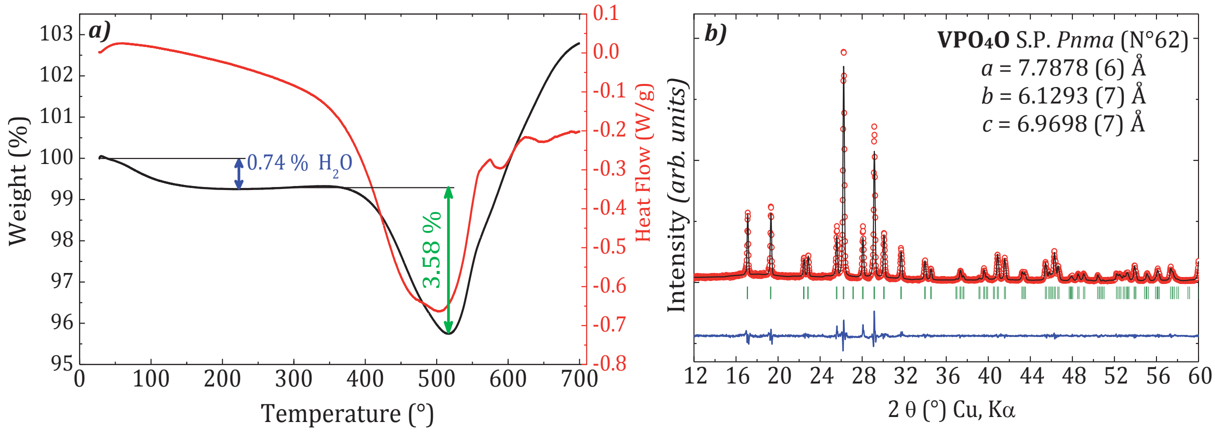

Figure I-6: a) TGA (black line) and DSC (red line) of VPO_4 performed under O_2 flow b) Full-pattern refinement of the XRD data of VPO_4O obtained after TGA in air.

I-2c. Synthesis of $LiVPO_4O$

As described previously (I-1a) we succeeded in the synthesis of $LiVPO_4O$ via a one-step ceramic route, using V_2O_3 as a vanadium precursor together with $NH_4H_2PO_4$ and LiF. The presence (or not) of LiF raised some questions which we attempted to answer. We tried to synthesize $LiVPO_4O$ using Li_3PO_4 instead of LiF according to the reaction ⑧.

⑧ $$1/2\ V_2O_3 + 1/3\ Li_3PO_4 + 2/3\ NH_4H_2PO_4 + 1/2\ O_2 \rightarrow LiVPO_4O + 2/3\ NH_3 + H_2O$$

The exact same procedure as described above (one-step ceramic synthesis of $LiVPO_4O$ using LiF) was used. In Table I-1 we gathered the lattice parameters of $LiVPO_4O$ from literature (ICSD N° 20537) which are compared with $LiVPO_4O$ obtained from LiF and from Li_3PO_4. As one can notice there is almost no difference of lattice parameters between the three materials.

Table I-1 Comparison of the published $LiVPO_4O$ lattice parameters (ICSD N°20537) with those obtained in this study

Space Group $P\bar{1}$ (N° 2); Z = 4								
$LiVPO_4O$ from	***a* (Å)**	***b* (Å)**	***c* (Å)**	**α (°)**	**β (°)**	**γ (°)**	**Volume (Å³)**	**V/Z (Å³)**
ICSD N° 20537	6.748	7.206	7.922	89.84	91.32	116.99	343.16	85.79
"LiF"	6.747(2)	7.195(7)	7.918(9)	89.84(3)	91.33(2)	116.93(6)	343.18(6)	85.79
"Li_3PO_4"	6.748(6)	7.199(8)	7.923(3)	89.86(8)	91.34(8)	116.98(8)	343.20(6)	85.80

It is worth to notice at this stage that the above mentioned $LiVPO_4O$ which crystallizes in the triclinic system differs from the well known α-$LiVPO_4O$ and β-$LiVPO_4O$ polymorphs reported in literature:

- **α–$LiVPO_4O$** crystallizes in tetragonal symmetry (*P4/nmm* (N° 129)) and can be obtained by dehydration of $LiVPO_4O{\cdot}2H_2O$ [17] or by electrochemical lithiation of α_I- and α_{II}-VPO_4O [18, 19]. The structure of α–$LiVPO_4O$ (Figure I-7a) is built up by vanadate (VO_5) and phosphate (PO_4) layers of $[VPO_4O]_\infty$ as proposed by A.S. Hameed et al. [17]. The long V–O bond length (1.93 Å) led A.S. Hameed to consider a penta-coordinated vanadium. The layers of $[VPO_4O]_\infty$ are stacked along the ***c*** direction and are symmetrically bridged by lithium ions in octahedra.

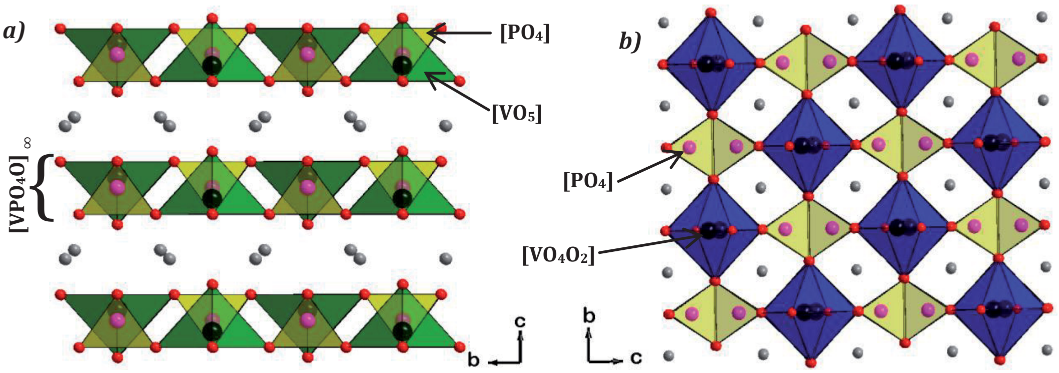

Figure I-7: Skeleton representation of a) α–LiVPO₄O and b) β–LiVPO₄O along the a direction

- **β–LiVPO₄O** crystallizes in orthorhombic symmetry (*Pnma (N° 62)*) and can be obtained by a ceramic CTR route using VPO_4O and Li_2CO_3 (mixed with carbon and heated at 450 °C) [20] or by electrochemical lithiation of β-VPO_4O [21]. The β-$LiVPO_4O$ framework structure is closely related to that found in β-VPO_4O and comprises infinite chains of corner-shared VO_6 octahedra, cross-linked by corner-sharing PO_4 tetrahedra. Just as for α–$LiVPO_4O$, alternative short (1.63 Å) and long (2.43 Å) V–O bonds are observed.

One should note that the notation for the different polymorphs of $LiVPO_4O$ in the literature is confusing. For instance T.A. Kerr et al. [22] and C. Allen et al. [8] referred to the triclinic phase when designated α-$LiVPO_4O$, but Y. Yang et al. [12] and B.M. Azmi et al. [11] did not put any symbol in front of $LiVPO_4O$ to designate the same triclinic phase. For homogenization with $LiVPO_4F$ notation, we decided to put no symbol in front of $LiVPO_4O$.

I-2d. Morphology and Magnetic Behavior of LiVPO₄X (X = O/F)

As gathered in Figure I-8, we succeeded in preparing phase-pure $LiVPO_4F$ and $LiVPO_4O$ for which the XRD patterns can be fully indexed in the $P\bar{1}$ triclinic space group. The unit-cell used to describe $LiVPO_4O$ (343.2 Å^3) is nearly twice bigger than that used to describe $LiVPO_4F$ (174.4 Å^3), as will be detailed further in the next section. An interesting and useful observation is that the V/Z ratio is significantly smaller in $LiV^{IV}PO_4O$ (85.8 Å^3) than in $LiV^{III}PO_4F$ (87.2 Å^3) as a result of different oxidation states of vanadium (with ionic radii of 0.063 nm for V^{4+} and of 0.074 nm for V^{3+}).

High resolution scanning electron microscopy (SEM) analysis of metalized samples (*i.e.* Pd plating on particles) was performed using a Hitachi S-4500 microscope. The SEM micrographs (inset of Figure I-8) of $LiVPO_4F$ indicate a particle size of about 1–2 μm surrounded by particles of carbon (80–60 nm), whereas the primary particles size of $LiVPO_4O$ is about 1 μm with agglomerates of about 5–6 μm.

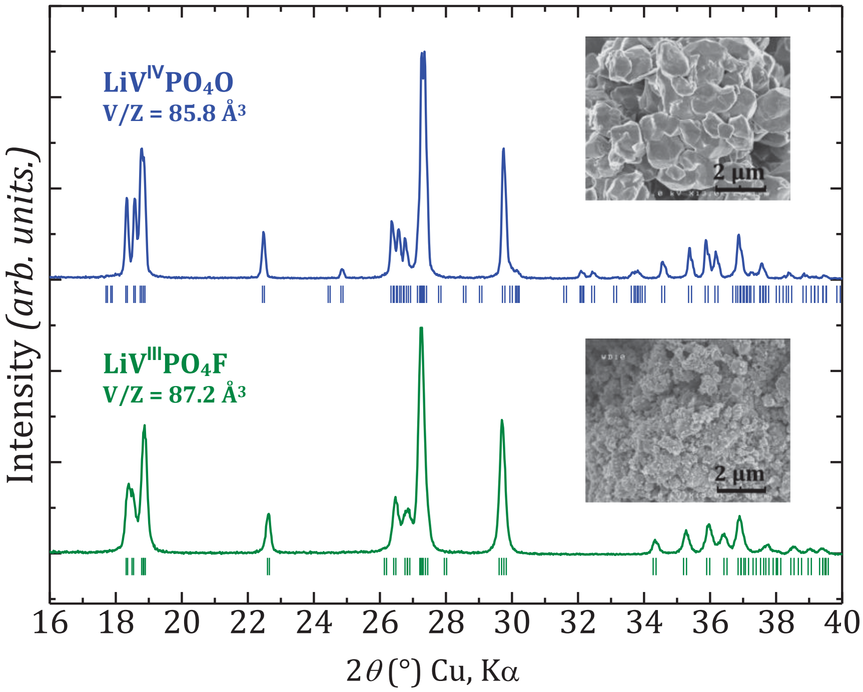

Figure I-8: XRD patterns of phase-pure $LiVPO_4F$ and $LiVPO_4O$ with calculated Bragg positions. SEM images are included in the insets

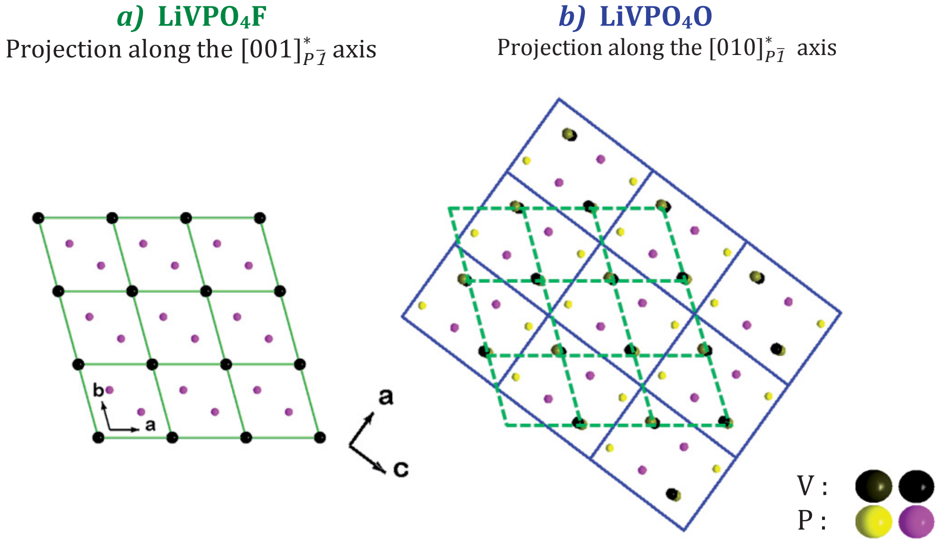
***a)* $LiVPO_4F$**
Projection along the $[001]^*_{P\bar{1}}$ axis

***b)* $LiVPO_4O$**
Projection along the $[010]^*_{P\bar{1}}$ axis

$$\begin{pmatrix} a \\ b \\ c \end{pmatrix}_{LiVPO_4O} = \begin{bmatrix} 1 & 1 & 0 \\ 0 & 0 & 1 \\ 1 & -1 & 0 \end{bmatrix} \begin{pmatrix} a \\ b \\ c \end{pmatrix}_{LiVPO_4F}$$

Figure I-9: Illustration of the transformation matrix from $LiVPO_4O$ to $LiVPO_4F$ unit cells.

The unit cell of $LiVPO_4O$ is almost two times bigger than that of $LiVPO_4F$ through a transformation matrix from $LiVPO_4F$ to $LiVPO_4O$, illustrated in

Figure *I-9*. The transformation matrix M is $\begin{bmatrix} 1 & 1 & 0 \\ 0 & 0 & 1 \\ 1 & -1 & 0 \end{bmatrix}$.

In order to confirm the chemical compositions of the samples, the Li, V, and P contents were determined using an ICP-OES spectrometer (Varian 720-ES Optical Emission Spectrometer) after complete dissolution of the powders into a hydrochloric acid solution. Stoichiometries of $Li_{1.13}/V_{1.04}/P_{1.00}$ and $Li_{1.05}/V_{0.97}/P_{1.00}$ were found for $LiVPO_4F$ and $LiVPO_4O$, respectively, which agree reasonably well with the formulas expected.

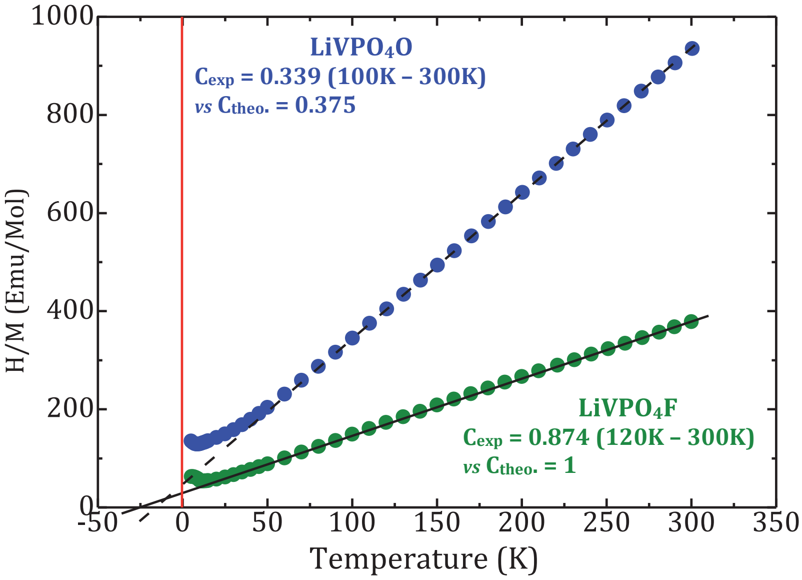

Figure I-10: Temperature dependence of the H/M ratio for $LiVPO_4F$ and $LiVPO_4O$. Comparison of experimental and theoretical Curie constants is given for the two phases with, for information, the temperature range used for their calculation.

The static molar magnetic susceptibilities of the two materials ($\chi(T) = M(T)/H$ (H = 1 T) with H as the magnetic field and M as the magnetization) were measured between 5 and 300 K using a SQUID magnetometer (Quantum Design) for the two materials. The zero field cooled χ values were obtained by cooling the sample in zero field down to 5 K and then heating them under the measuring field. The diamagnetic contributions were corrected using the atomic values from G.A. Bain and J.F. Berry [23] yielding the χ_M paramagnetic susceptibility contribution. The temperature dependence of the H/M ratio for both $LiVPO_4F$ and $LiVPO_4O$ is shown in Figure I-10. Both compounds show curvatures indicative of onsets of antiferromagnetic ordering, with Néel temperatures of 13 and 9 K for $LiVPO_4F$ and $LiVPO_4O$, respectively. Curie–Weiss type paramagnetism appears for temperatures higher than 50 K for $LiVPO_4F$ and 100 K for $LiVPO_4O$. The obtained Curie constants of 0.874 and 0.339 are close to the theoretical values for octahedral V^{3+} and V^{4+} ($C_{theo}(LiV^{III}PO_4F) = 1$ and $C_{theo}(LiV^{IV}PO_4O) = 0.375$). Further confirmation of the different oxidations states of vanadium in these two samples is given through bond valence calculations within the crystal structures. The magnetic structure will be described in a next paragraph based on the neutron diffraction data recorded at low temperature (below Néel temperature).

I-2e. Summary and Conclusion

In this section, we reported on the reproducible synthesis of pure $LiVPO_4F$ and $LiVPO_4O$, summarized as follows:

- $LiVPO_4O$ can be synthesized by a direct ceramic route using V_2O_3 as the vanadium precursor and LiF. In presence of O_2, we ended up with $LiVPO_4O$ for which the oxidation state of vanadium is +4 instead of +3. This lithium vanadium oxyphosphate was also successfully synthesized using Li_3PO_4 instead of LiF.

- $LiVPO_4F$ was obtained through a two-step ceramic route using a carbon coated VPO_4 (C-VPO_4) and LiF. In a gold-sealed tube, C-VPO_4 was mixed in a stoichiometric proportion with LiF. All our (many) attempts to prepare $LiVPO_4F$ through a single-step reaction using V_2O_3 (or V_2O_5) as the vanadium precursors generated mixtures of powders containing variable amounts of $Li_3V_2(PO_4)_3$ and others unknown impurities.

- The oxidation state of vanadium in both compounds was confirmed through a Curie constant determined based on magnetic susceptibility measurement *vs.* temperature. The unit cell of $LiVPO_4O$ is almost two times bigger than the one of $LiVPO_4F$.

I-3.CRYSTAL AND MAGNETIC STRUCTURES OF $LiVPO_4F$

As presented in the introduction, $LiVPO_4F$ and the triclinic $LiVPO_4O$ crystallize in the Tavorite structure. Simonov et al. [24] had published the crystal structure of $LiAlPO_4F$ where two sites of lithium were proposed, each site being occupied at 50% and separated from the other by a distance of 0.5 Å. To the best of our knowledge, no neutron diffraction study had been performed to localize the Li sites so that the two positions of Li in $LiAlPO_4F$ were questionable.

During the submission of our paper reporting the structural determination of $LiVPO_4F$ [25], we became aware of a structure determination just published by B.L. Ellis et al. [26] which had been determined using synchrotron XRD. The differences between the model proposed by B.L. Ellis et al. and ours will be presented in this section.

X-Ray diffraction data were collected from a Panalytical diffractometer (X'Pert PRO MPD) with a Cu $K\alpha_1$ radiation (Germanium monochromator), by using counting steps of 700 sec. per 0.008 ° between 2θ = 10 ° and 2θ = 130 °. Neutron diffraction was performed at the Institute Laue Langevin (Grenoble, France) in collaboration with E. Suard on the high-resolution diffractometer D2B. The sample was contained in an 8 mm diameter vanadium tube and the diffraction pattern was collected in transmission mode at room temperature with a wavelength of 1.59355(3) Å (refined by fixing the cell parameters to the values determined from the X-ray diffraction data) between [0–140 °] angular ranges using a 0.05 ° (2θ) step with an accumulation time of 9 hours. Correction of the absorption was necessary in order to take into account a decrease of the experimental diffracted intensity compared to the expected one. The calculated absorption correction coefficient (μR factor in the FullProf program with μ being the absorption of the sample and R the radius of the vanadium tube [27]) was found to be equal to 0.290 for $LiVPO_4F$ and 0.295 for $LiVPO_4O$.

I-3a. The Crystal structure of $LiVPO_4F$

The combined Rietveld refinements of neutron and XRD data for $LiVPO_4F$ were carried out using the structural model of Tavorite-type $LiAlPO_4F$ reported by Simonov et al. [24] [ICSD N° 48012]. The different steps used for the refinement were as follows:

1. We first refined the positions of the heaviest atoms (since Li is almost "transparent" to X-rays) with the structural model $[V(1)_{1a}V(2)_{1b}]P_{2i}(O_{2i})_4F_{2i}$: in this model vanadium atoms occupy special *1a* (0, 0, 0) and *1b* (0, 0, 1/2) positions, contrary to the *1a* (0, 0, 0) and *1h* (1/2, 1/2, 1/2) positions mentioned by Barker through analogy with the crystal structure of $LiAlPO_4F$ [1, 2, 9, 10]. B.L. Ellis et al. [26] mentioned positions of *1a* (0, 0, 0) and *1b* (0, 1/2, 1/2) but the Wyckoff position of *1b* is actually (0, 0, 1/2) for $P\overline{1}$ space group.

2. The Rietveld refinements were then conducted by using the structural model $[Li(1)_{2i}Li(2)_{2i}][V(1)_{1a}V(2)_{1b}]P_{2i}(O_{2i})_4F_{2i}$ of $LiAlPO_4F$ where the two atomic positions for Li are *2i*(0.98, 0.64, 0.26) and *2i*(0.18, 0.56, 0.50) *i.e.* distant of 1.94 Å and partially occupied at 50% each.

3. The structural model obtained at this stage showed large standard deviations of atomic coordinates for Li(2) when compared to all other atomic positions of the structure (10 times higher). Additionally, a very short Li(2)-O(2) distance of 1.23 Å was spotted with occupancies of 0.9 and 0.2 for Li(1) and Li(2), respectively.

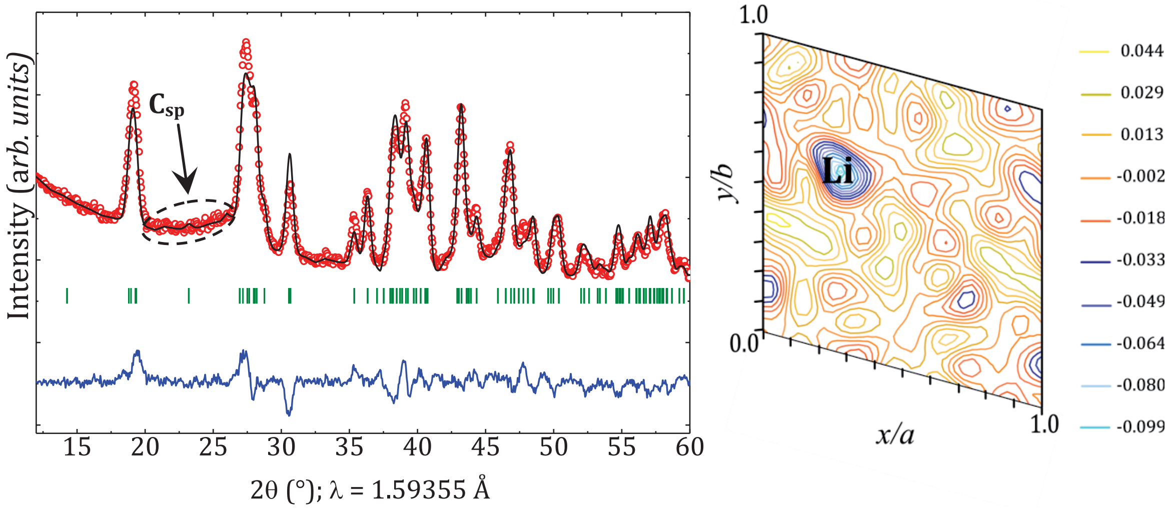

Figure I-11: a) Rietveld refinement of neutron diffraction data (only heaviest atoms are considered) b) 2D section of 3D difference Fourier maps at y = 0.68 with the maxima corresponding to the Li(1) site for the crystal structure of $LiVPO_4F$

4. As this questioned the existence of two independent crystallographic sites for Li, we then calculated Fourier difference maps using the GFourier software within the FullProf_suite program considering only the host structure $[V(1)_{1a}V(2)_{1b}]P_{2i}(O_{2i})_4F_{2i}$ determined previously from XRD data and thus without the two Li ions. As illustrated in Figure I-11a, the refinement of the neutron diffraction data showed very bad minimization of the intensity difference (the blue line representing the difference between the data recorded and the calculated pattern) with very poor reliability factors. Since Li is the only atom in $LiVPO_4F$ composition with a negative coherent diffusion wavelength ($-0.19 \cdot 10^{-4}$ Å [28] in natural $^6Li/^7Li$ abundance) it was therefore possible to localize lithium in the $LiVPO_4F$ unit cell. The calculated Fourier (Figure I-11b) differential map showed a maximum negative residual nuclear density located in *2i* position at (~0.29, ~0.62, ~0.28). The presence of carbon in $LiVPO_4F$ (resulting from the reaction between C-VPO_4 and LiF) is visible in the neutron diffraction pattern where the background is high.

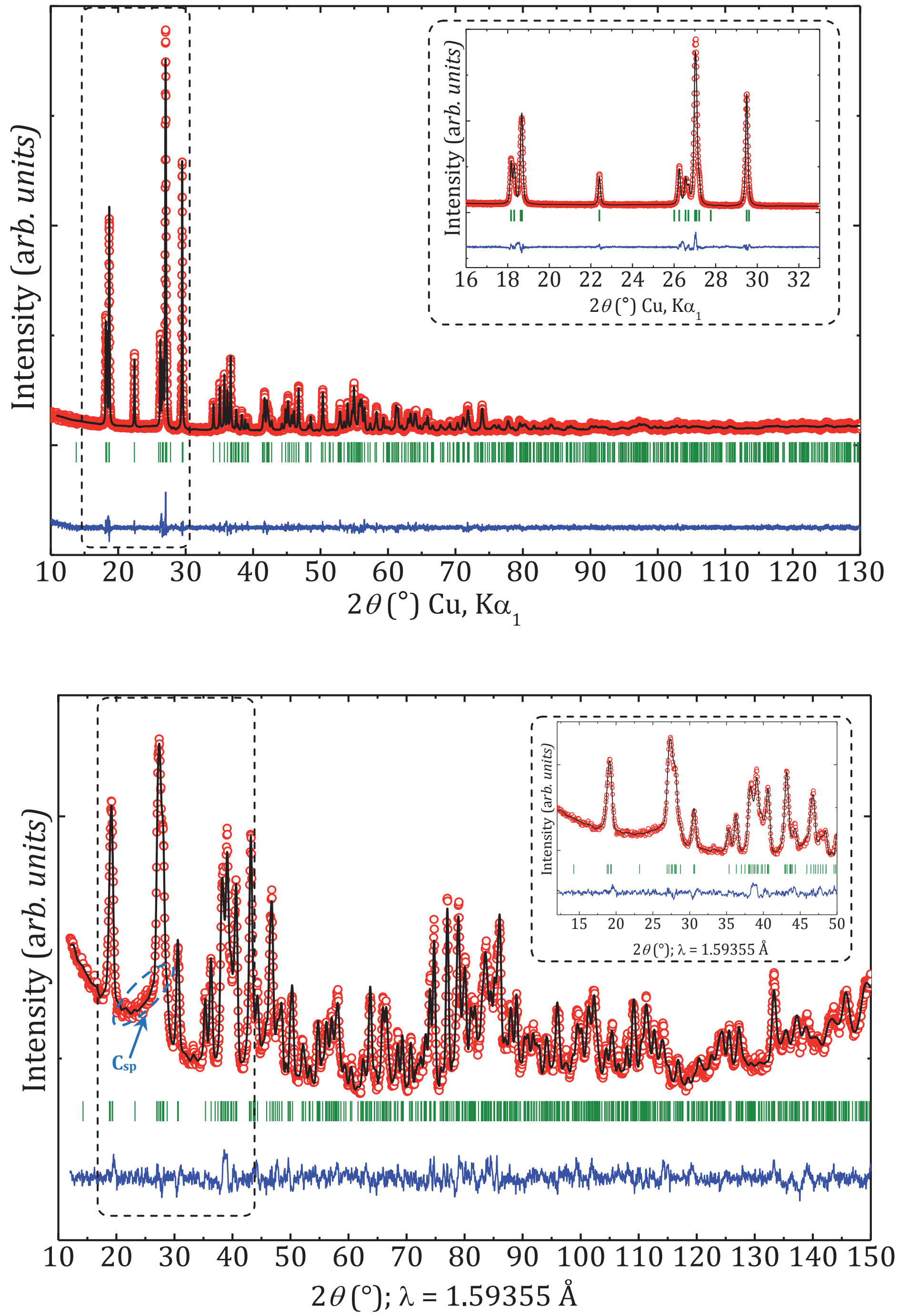

Figure I-12: Observed (red dots), calculated (black line), and difference (blue line) plots obtained for the Rietveld refinement of (a) X-ray diffraction data and (b) neutron diffraction data for $LiVPO_4F$

5. This position was hence included in the atomic coordinates list so as to refine properly the neutron diffraction data. Subsequent Fourier difference maps showed non residual nuclear densities and we thus adopted a structural model with only one Li(1) crystallographic site at *2i*(0.371(1), 0.703(1), 0.233(1)). Separate refinements of thermal motion factors and occupancies led to satisfactory reliability factors (ANNEX I, Table I-1) and good minimization of the intensity difference (I_{obs} - I_{calc}), for X-rays and neutron data refinements, as shown in Figure

I-12. The lattice parameters as well as the atomic positions are gathered in table I-1 of the ANNEX I. The resulting inter-atomic distances are recorded in Table I-2 of ANNEX I.

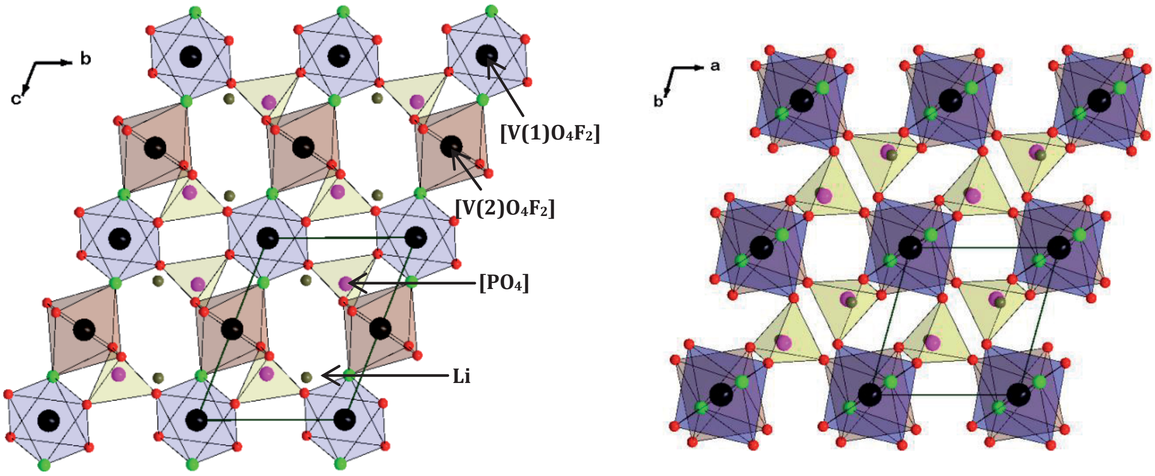

Figure I-13: Representations of the crystal structure of $LiVPO_4F$

As mentioned earlier, $LiVPO_4F$ crystallizes in the Tavorite structure, built up by $[VO_4F_2]$ octahedra which share common fluorine atoms so as to form ···V···F···V···F···V··· infinite chains running along the $[001]_{P\bar{1}}$ direction (Figure I-13 and Figure I-14). The chains are connected to each other via isolated (with respect to each other) $[PO_4]$ tetrahedra through ···V···O···P···O···V··· sequences. Vanadium lies in two octahedral sites with a very narrow range of V–O distances, 1.96–1.99 Å (ANNEX I table I-2).

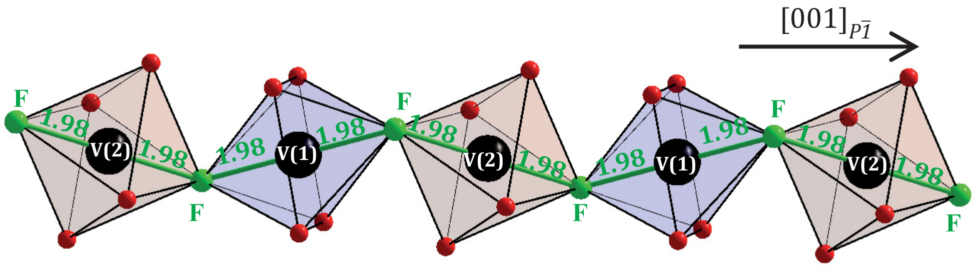

Figure I-14: Representation of chains along the c axis in the structure of $LiVPO_4F$

The V–F distances along the chain of [–F–VO_4–F–VO_4–F–] are very homogeneous with a value of 1.98 Å (Figure I-14). This value is quite small compared to those encountered in $VPO_4 \cdot H_2O$ [29, 30] another Tavorite-like structure (which crystallizes in *C2/c* space group) containing V^{III} where the distances V–(OH_2) (running along the chain) are 2.17 Å. The $[V(1)O_4F_2]$ octahedron is slightly more distorted than the $[V(2)O_4F_2]$ octahedron ($\Delta = 3.98 \times 10^{-5}$ and $\Delta = 2.28 \times 10^{-5}$, respectively). The phosphorus atom lies within a regular tetrahedron ($\Delta = 2.22 \times 10^{-4}$) with P–O distances in the range of 1.50–1.55 Å (Figure I-15a).

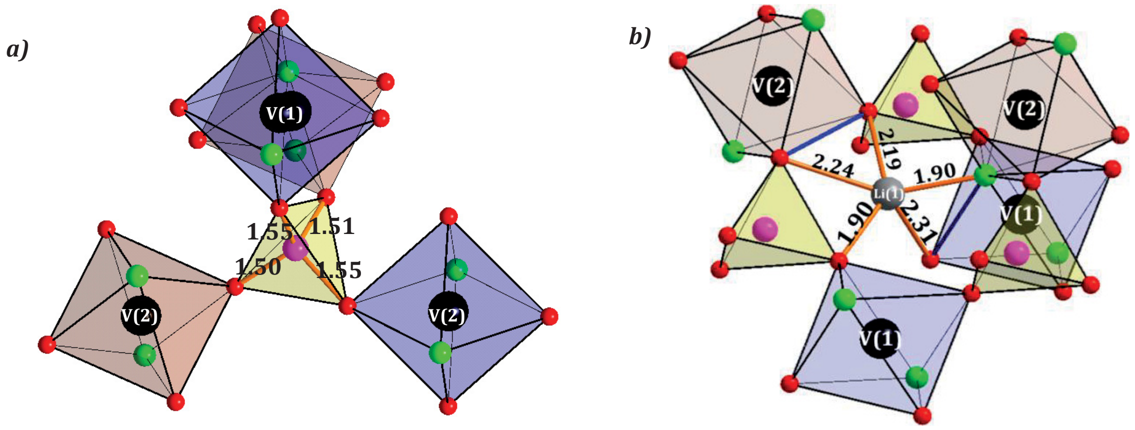

Figure I-15: Schematic representation of tetrahedra PO_4 (a) and pentahedra LiO_4F (b) local environment in the structure of $LiVPO_4F$

The unique Li(1) site (Figure I-15b) is surrounded by four oxygen atoms and one fluorine, forming a very distorted five-vertex polyhedron (d = 1.90–2.24 Å; $\Delta = 6.83\times10^{-3}$; see table I-2 of ANNEX I). This pentahedron shares one edge with one [$V(2)O_4F_2$] and one edge with one [$V(1)O_4F_2$] octahedron. The corner-sharing polyhedra of $LiVPO_4F$ generate a three-dimensional framework with tunnels running along $[100]_{P\bar{1}}$, $[010]_{P\bar{1}}$, and $[101]_{P\bar{1}}$. The calculated valence bond sums (BVS) for the cations using “Bond_Str” software in FullProf_suite matched remarkably well with expected values and gave respectively $BVS_{V(1)} = 3.02$, $BVS_{V(2)} = 3.01$, $BVS_P = 4.99$, and $BVS_{Li} = 0.90$ in reasonably good agreement with expectations.

Two observations had been previously reported concerning the lithium site in $LiVPO_4F$:

- In analogy with $LiAlPO_4F$ [24], J. Barker proposed the existence of two crystallographic sites for lithium for the structure of $LiVPO_4F$, each site being occupied at 50%. Let us recall that in $LiAlPO_4F$, the two Li sites are separated by 0.5 Å. The fractional coordinates for the single lithium site observed in our study is at the barycenter of the two Li sites proposed for $LiAlPO_4F$ (Figure I-16a).

- B.L. Ellis et al. [26] reported on the crystal structure of $LiVPO_4F$ using 2 sites for Li occupied at 18 % for Li(1) and 82 % for Li(2). The structural determination was performed from the analysis of synchrotron X-ray diffraction data. In order to check for the adequacy of their structural description with our data, we decided to refine our neutron diffraction data using B.L. Ellis structural model. The obtained refinement converged to only one lithium site: the first site Li(1) was refined as empty and the coordinates of the second Li(2) converged to a position very close to the unique Li site we had found [25]. The schematic representation of both Li sites in

B.L. Ellis structure ($Li(1)_{Ellis}$ and $Li(2)_{Ellis}$) and Li site (Li_{Ateba}) in our structure (Figure I-16b) revealed that $Li(2)_{Ellis} = Li_{Ateba}$.

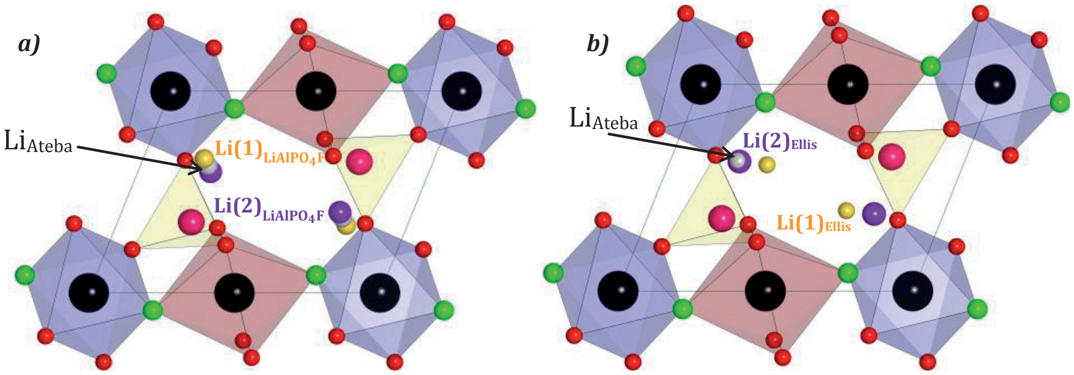

Figure I-16: Skeleton representation of $LiVPO_4F$ structure along the c direction presenting: a) 2 sites of Li as suggested by J. Barker et al. [25] based on the analogy with $LiAlPO_4F$, represented as $Li(1)_{LiAlPO_4F}$ and $Li(2)_{LiAlPO_4F}$ b) 2 sites of Li as observed by B.L. Ellis et al. [26], represented by $Li(1)_{Ellis}$ and $Li(2)_{Ellis}$ In both cases the Li's position found in this work is presented as Li_{Ateba}

I-3b. NMR Study of $LiVPO_4F$

In order to confirm (or infirm) the presence of only one lithium site in the structure of $LiVPO_4F$, we have performed in collaboration with M. Ménétrier and M. Duttine (ICMCB-Bordeaux), ^7Li MAS NMR as part of a large NMR study currently performed on Tavorite type systems in our laboratory. In this section (and only in this section) two samples of $LiVPO_4F$ are used and labeled as follows:

- *GEN II* refers to a second generation of $LiVPO_4F$ samples (see Figure I-5b) which contains an unknown impurity.

- *GEN III* refers to a pure sample of $LiVPO_4F$ (see Figure I-5c) obtained by adjusting the stoichiometry (1:1) in LiF/C-VPO_4 mixture

The ^7Li MAS NMR spectra were recorded on a Bruker Advance spectrometer with a 7T magnet (116 MHz resonance frequency for ^7Li), using a standard Bruker 2.5 MAS probe at a 30 kHz typical spinning speed. A Hahn echo sequence was applied with a 90° pulse of 1.4 microsecond. A recycle delay was typically 2s. The 0 ppm external reference was a 1M LiCl aqueous solution.

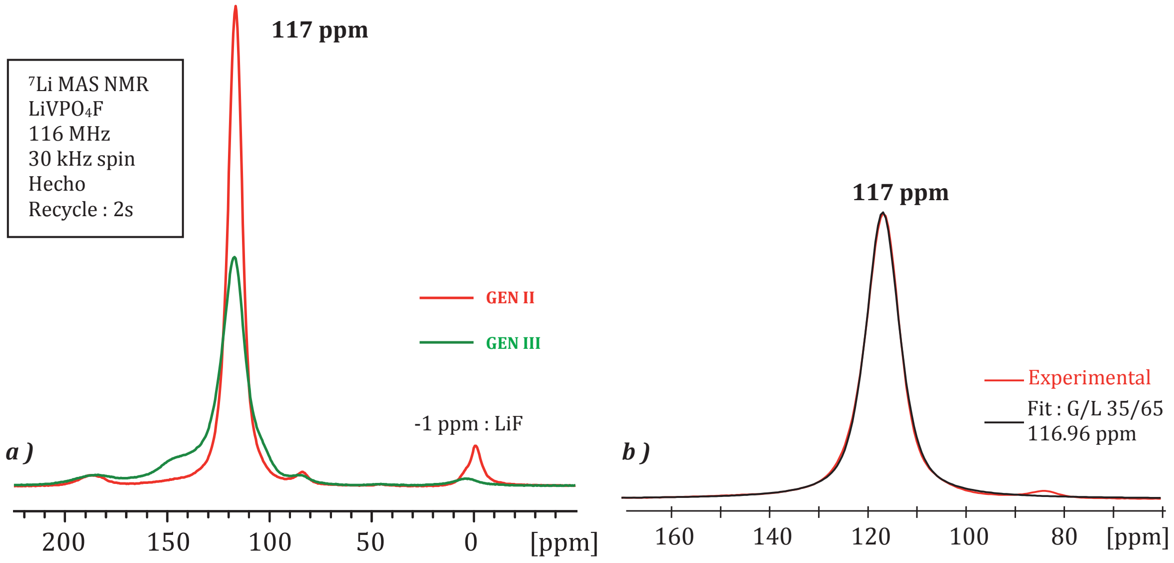

Figure I-17: ⁷Li MAS NMR spectra a) of GEN II (red line) and GEN III (green line). The magnitude is scaled to the mass of active material in the NMR rotor. b) An example of the fit is given for the signal at 117 ppm.

Figure I-17a shows the isotropic signals (*i.e.* without spinning site band) of the ^{7}Li NMR spectra recorded for two samples of $LiVPO_4F$ corresponding (see Figure I-5) respectively to GEN II (red trace) and to GEN III (green trace). A rather sharp peak centered at 117 ppm is observed in both cases, which agrees well with the unique Li site determined by diffraction. A fit of this line with a single Gaussian/Lorentzian contribution is given for the sample GEN II in Figure I-17b, showing indeed no hint of several components in this signal. The observed NMR shift (117 ppm) is close to the one published by B.L. Ellis et al. [26] (112 ppm). Note that B.L. Ellis et al. proposed a decomposition of their Li NMR signal into two components, but specified that this was not the unique decomposition possible. The spectrum for the GEN II sample also exhibits a weak signal at -1 ppm assigned to the presence of residual LiF which is absent for the GEN III sample prepared with exact stoichiometry of LiF and C-VPO_4.

Both spectra also exhibit additional signals at 4, 84 and 186 ppm and the spectrum for the pure sample exhibits two additional components seen as shoulders of the main peak at 102 and 147 ppm. Since no other compound was detected by diffraction, these may correspond either to Li in undetected impurities or to Li in the material with different environments (about 5% in GEN II and 25% in GEN III). Indeed, recent 2D dipolar homonuclear correlation NMR experiments have been performed on the GEN II by the NMR platform of the RS2E network[1] (Rob Messinger and Michael Deschamps at CEMHTI Orléans) which show that all these additional signals are correlated to the main one. It therefore appears that these signals correspond to Li in the same material, but in environments modified by defects in the structure (this is supported by the presence of Gaussian contribution in the fit of the signal as shown in Figure I-17b). It is important to note that these NMR shifts are governed by the influence of the electron spins from the V ions on the Li nuclei, mostly from the Fermi contact interaction. The electron spin transfer mechanisms at the origin of this interaction are under investigation in the group at ICMCB by D. Carlier, in a similar strategy as applied to other Li-transition metal phosphates [31, 32]. A consequence of the magnitude of this Fermi contact interaction is that subtle changes in the electronic configuration of the vanadium ions can give rise to very different Li NMR shifts even with relatively minor structural distortions, which can therefore remain unnoticed by diffraction.

---

[1] RS2E: Réseau sur le Stockage Electrochimique de l'Energie – French network for electrochemical energy storage. Web site: http://www.energie-rs2e.com/fr

^{31}P MAS NMR spectra (Figure I-18) were recorded on a Bruker Advance III spectrometer with a 2.35T magnet (40.6 MHz resonance frequency for ^{31}P), a standard Bruker 2.5 MAS probe at a 30 kHz typical spinning speed. A Hahn echo sequence was used with a 90° pulse of 1.1 microsecond. A recycle delay was 1s. A secondary external reference was $Al(PO_3)_{3(solid)}$ (-50.8 ppm *vs.* H_3PO_4 85%).

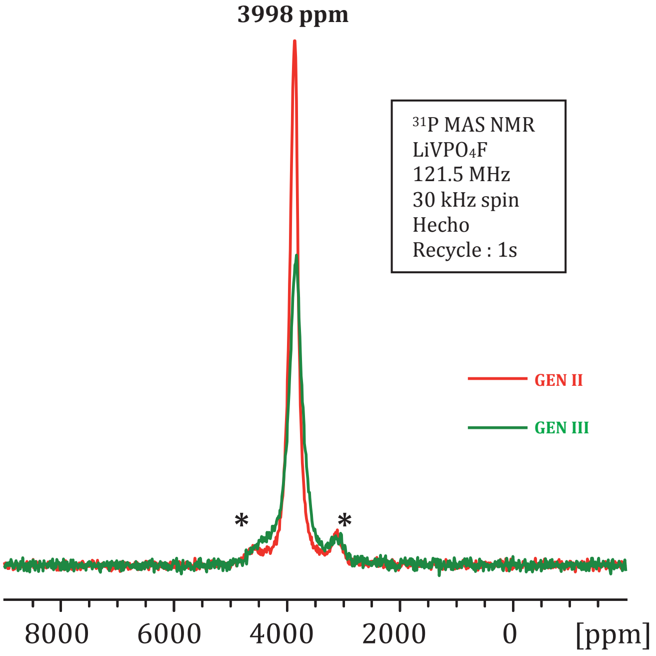

Figure I-18: ^{31}P MAS NMR spectra of GEN II (red line) and GEN III (green line). The magnitude is scaled to the mass of active material in the NMR rotor and the spinning sidebands are marked with asterisks.

Both samples of $LiVPO_4F$ exhibit (Figure I-18) a single relatively sharp ^{31}P MAS NMR signal at 3998 ppm with its spinning sidebands marked by asterisks in agreement with the unique phosphorous site present in the structure determined by Rietveld refinement. The shoulder at around 4500 ppm most probably corresponds to the presence of defects with different magnitude/nature for the two samples as observed previously for Li. The shift in $LiVPO_4F$ is less pronounced than in $VPO_4{\cdot}H_2O$ for which A. Castets et al. [29, 32] observed a shift of 5535 ppm for ^{31}P. Since the two structures lead to relatively similar V–O–P configurations and contain the same V^{3+} paramagnetic cation, it is tempting to elaborate a discussion about this difference in shift. However, there is a strong difference between the two compounds in the elongation of their respective octahedra (bond length V–(OH_2) is 2.17 Å for [VO_6] octahedron and bond length V–F is 1.98 Å for [VO_4F_2] octahedron). In $VPO_4 \cdot H_2O$ a strong elongation exists along the bridging O direction, which lifts the degeneracy of the t_{2g} orbitals, and leads to occupation of the d_{xz} and d_{yz} orbitals by the two electron spins [32]. In $LiVPO_4F$ however, there is no clear elongation, and the change in the nature of the bridging anion (F for O) obviously changes the nature of the bonds. It would therefore be hazardous to comment further on the NMR shift difference in the two compounds. An analysis of the DOS from DFT calculations is currently in progress in the group at ICMCB to this aim.

^{19}F MAS NMR spectra were recorded on a Bruker Advance III spectrometer with a 2.35T magnet (94.3 MHz resonance frequency for ^{19}F), using a standard Bruker 2.5 MAS probe at a 30 kHz typical spinning speed. A Hahn echo sequence was used with a 90° pulse of 1 microsecond. A recycle delay of 1s was applied. The 0 ppm external reference was $CFCl_3$.

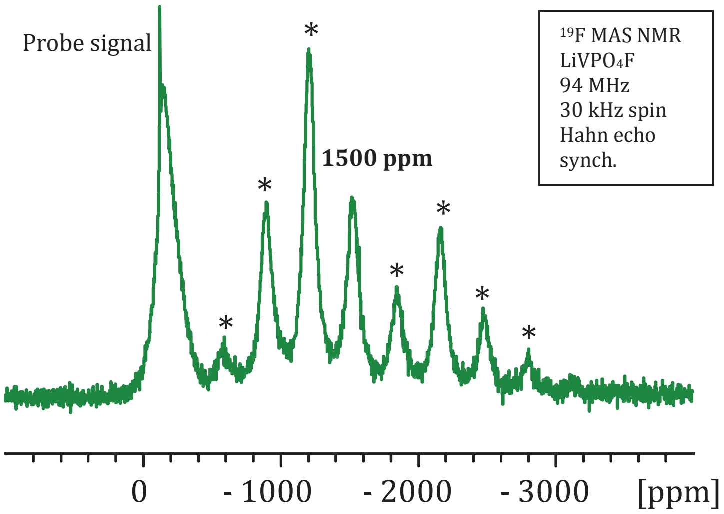

Figure I-19: ^{19}F MAS NMR spectrum for GEN III sample. The spinning sidebands are marked with asterisks.

The complete ^{19}F MAS NMR spectrum for the *GEN III* sample (Figure I-19) exhibits a strong parasitic contribution from the probe around -150 ppm, and a broad spinning sidebands manifold corresponding to fluorine in the material, again strongly shifted by Fermi contact type interactions with the electron spins from the V ions. Determining the isotropic contribution is not trivial, since the temperature change induced by changes of the spinning speed leads to strong changes in these shifts. Using DFT calculations D. Carlier succeeded in determining that the isotropic signal was the -1500 ppm one [33]. This is to our knowledge the first report and analysis of the ^{19}F NMR signal in such a paramagnetic sample.

Although pure LiVPO$_4$F was obtained based on the X-ray/neutron diffraction (*GEN III*; Figure I-5c), this NMR study has enlightened the existence of defects in the LiVPO$_4$F structure. Therefore, other techniques (such as EPR), sensitive to the local and to the electronic configuration of the transition metal ion, have to be used to characterize each generation of LiVPO$_4$F sample (GEN II and GEN III) to check for the possible presence of V^{IV} in these materials as the existence of LiVPO$_4$F$_x$O$_y$ cannot be totally ruled out.

I-3c. Magnetic structure of LiVPO$_4$F

In collaboration with E. Suard (ILL–Grenoble) and G. Rousse (UPMC–Paris), we performed neutron powder diffraction at low temperature, on LiVPO$_4$F, in order to determine a possible magnetic ordering below T_N = 13 K. This has been done on the diffractometer D20 of ILL with a wavelength of λ = 2.40 Å. The neutron diffraction pattern indeed presents extra peaks below 13 K in accordance with the temperature obtained from magnetic susceptibility data recorded vs. temperature (Figure I-10). Although vanadium is transparent to neutrons, we can see its presence through the ordering of its magnetic moment at low temperature. Indeed, some tiny peaks are seen in the diffraction pattern at 2K, that were absent at 50K, as pictured in Figure I-20a. Those peaks increase significantly from 13 K down to 2K (Figure I-20b) and are however very small because of the small number of electrons on the vanadium (V^{3+}, 3d^2) and of the small resulting magnetic moment.

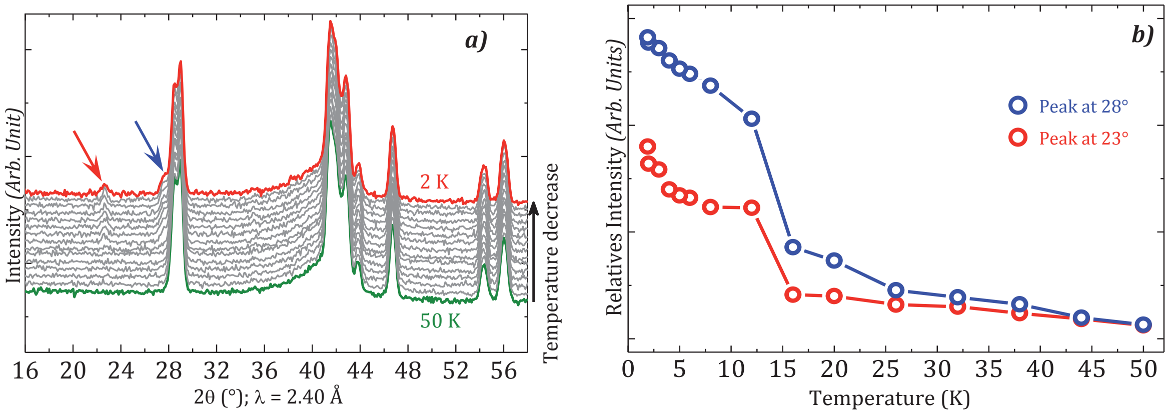

Figure I-20: a) Low temperature neutron diffraction experiment (on D20) carried out on LiVPO$_4$F; b) The change in intensities versus time of the magnetic superstructure peaks

The magnetic peaks can be indexed using a **k** = (½ ½ 0) propagation vector, so that the magnetic cell is 4 times larger than the nuclear cell. The latter being of triclinic ($P\bar{1}$) symmetry, there is no constraint to be added between the magnetic moments due to the symmetry analysis: indeed the

2 metal atoms of the nuclear cell are distributed on the 1*a* and 1*b* Wyckoff positions. We had therefore considered two possible cases: the moment on metal sitting in the two Wyckoff sites are parallel or antiparallel, so that the resulting magnetic structure would be collinear.

The preliminary refinements of the 2K structure using these two different models, and allowing the magnetic moment to orient in any direction, led to a much better refinement when the two moments were antiparallel. It appeared that it was rather difficult to fully solve the magnetic structure since vanadium was transparent to neutrons, and V^{3+} presents a d^2, $t_{2g}^2\ e_g^0$, **S**=1, **L**=3 configuration, so that the magnetic moment is expected to be weak (lower than theoretical 2 μ_B expected). We therefore ended up with a model that could properly fit the data, and for which the magnetic moment of V^{3+} is refined to 1.22(5)μ_B.

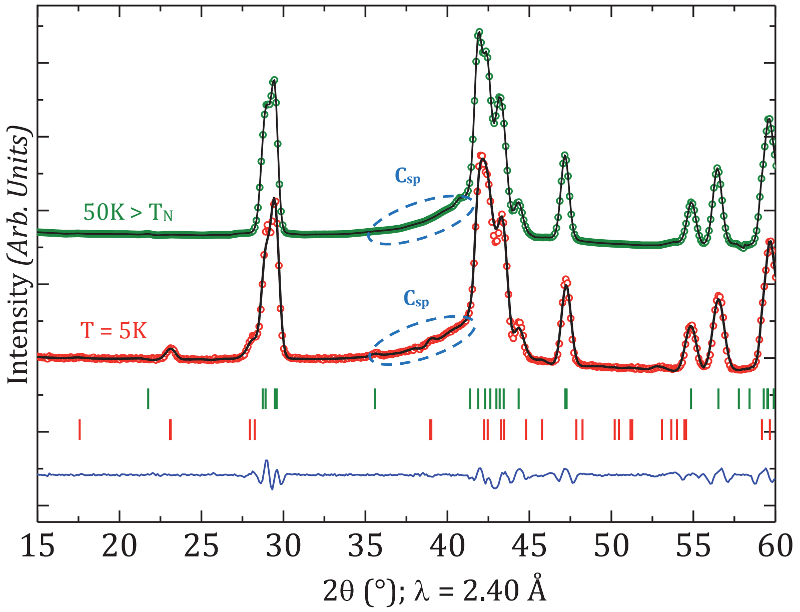

Figure I-21: Magnetic Rietveld Refinements of LiVPO₄F: Observed versus calculated (black line) powder neutron diffraction patterns of LiVPO₄F collected on D20 with λ = 2.40 Å, at 2K (red dots) and 50K (green dots). The difference pattern (blue line) of the 2K pattern is displayed at the panel bottom. The positions of the Bragg reflections are shown as vertical bars below.

The result of the Rietveld refinement is given in Figure I-21 and compared to that of the pattern recorded above T_N to highlight the presence of the magnetic peaks. The resulting magnetic structure is presented in Table I-2, and shown in Figure I-22a where the magnetic moments that are along the chains are oriented antiparallel, and the chains are also antiparallel through the propagation vector **k** confirming the antiferromagnetic behavior observed with magnetic measurements. Figure I-22b exhibits the orientation of the magnetic moment in both [$V(1)O_4F_2$] and [$V(2)O_4F_2$] octahedra which are oriented so that the equatorial plane of oxygen atoms is perpendicular to fluorine vertices. The magnetic moment of V(1) is almost perpendicular to the equatorial plane of oxygen and almost oriented toward fluorine atoms. In the case of V(2) the magnetic moment is slightly tilted out of the oxygen equatorial plane and oriented through the O(1)–O(2) edge.

Table I-2: Magnetic moments (in μ_B) at 2 K, the components are given along the a, b and c axes. Propagation vector k = (½, ½, 0), Magnetic R-factor=19.5%

LiVPO$_4$F				
Atom	m_a	m_b	m_c	M_{Total} (μ_B)
V (0 0 0)	0.9(2)	-0.2(1)	-0.5(2)	1.22(5)
V (0 0 ½)	-0.9(2)	0.2(1)	0.5(2)	1.22(5)

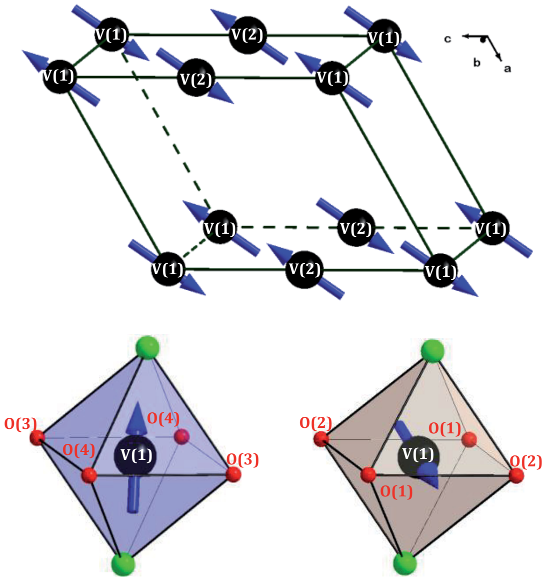

Figure I-22: Illustration of the proposed magnetic structure of LiVPO$_4$F: a) 3D view of the magnetic moments bore by vanadium atoms b) 3D view of isolated octahedra.

A comparative analysis and discussion of magnetic structures in Tavorite-type materials will be given in chapter III through the study of the magnetic structure of LiFePO$_4$F.

I-3d. Conclusion and Summary

Based on simultaneous Rietveld refinements carried out from XRD and neutron diffraction data, we demonstrated that there is only one lithium site in the structure of LiVPO$_4$F. This atomic position for Li happens to be the barycenter of the two Li sites proposed by J. Barker and fits well with one of the two positions of lithium published (the one occupied at 82%) by B.L. Ellis. An unique ^{7}Li NMR signal shifted at 117 ppm was observed in agreement with the unique lithium site obtained after Rietveld refinement of both XRD and neutron diffraction data. Although not detected in XRD and neutron diffraction data, ^{7}Li NMR revealed the existence of some defects. These defects were also present in ^{31}P NMR which exhibited a unique signal (in good agreement with the unique phosphorous site present in the structure of $LiVPO_4F$) strongly shifted at 3998 ppm. Interestingly, we observed a ^{19}F NMR signal for the $LiVPO_4F$, shifted at -1500 ppm and this is the first time that such an observation could be done on a paramagnetic sample.

Neutron diffraction data performed at low temperature (at 2 K) revealed the existence of magnetic moment ordering and confirmed the antiferromagnetic behavior observed by magnetic measurements. The magnetic moments that lie along the chain are oriented antiparallel and the chains are antiparallel. The magnetic moment found was 1.22(5) μ_B.

I-4.CRYSTAL STRUCTURE AND NMR STUDY OF $LiVPO_4O$

I-4a. Crystal structure of $LiVPO_4O$

As mentioned previously, the only known structural determination for the triclinic $LiVPO_4O$ was carried out by A.V. Lavrov et al. [13]. For a better comparison with $LiVPO_4F$, we have decided to re-investigate the structure of $LiVPO_4O$ using both X-ray and neutron diffraction. The full-pattern matching refinement of $LiVPO_4O$ was done starting from the published lattice parameters of $LiVPO_4O$ (ICSD N° 20537). Simultaneous Rietveld refinements of both neutron and X-ray diffraction data were done using the same sequence of refinements than that used for $LiVPO_4F$.

1. The positions of the heaviest atoms were refined using the published structure of $LiVPO_4O$. Contrary to $LiVPO_4F$, each vanadium atom is not occupying a special position but is in *2i* general Wyckoff position for $P\bar{1}$ space group. The structural model we used is therefore $[V(1)_{2i}V(2)_{2i}][P(1)_{2i}P(2)_{2i}][O_{2i}]_{10}$.

2. As presented in Figure I-24, the refinement of neutron diffraction data showed very bad minimization of the intensity difference and reliability factors, and high Chi (χ) value. The calculated Fourier differential map shows two maximum negative residual nuclear density located in *2i* position at (~0.22, ~0.160, ~0.087) for Li(1) and (~0.703, ~0.156, ~0.576) for Li(2). It is worth noticing a flat background in the neutron diffraction pattern of $LiVPO_4O$ contrary to $LiVPO_4F$ were the background was "domed" at around 24-25° as a consequence of the presence of carbon.

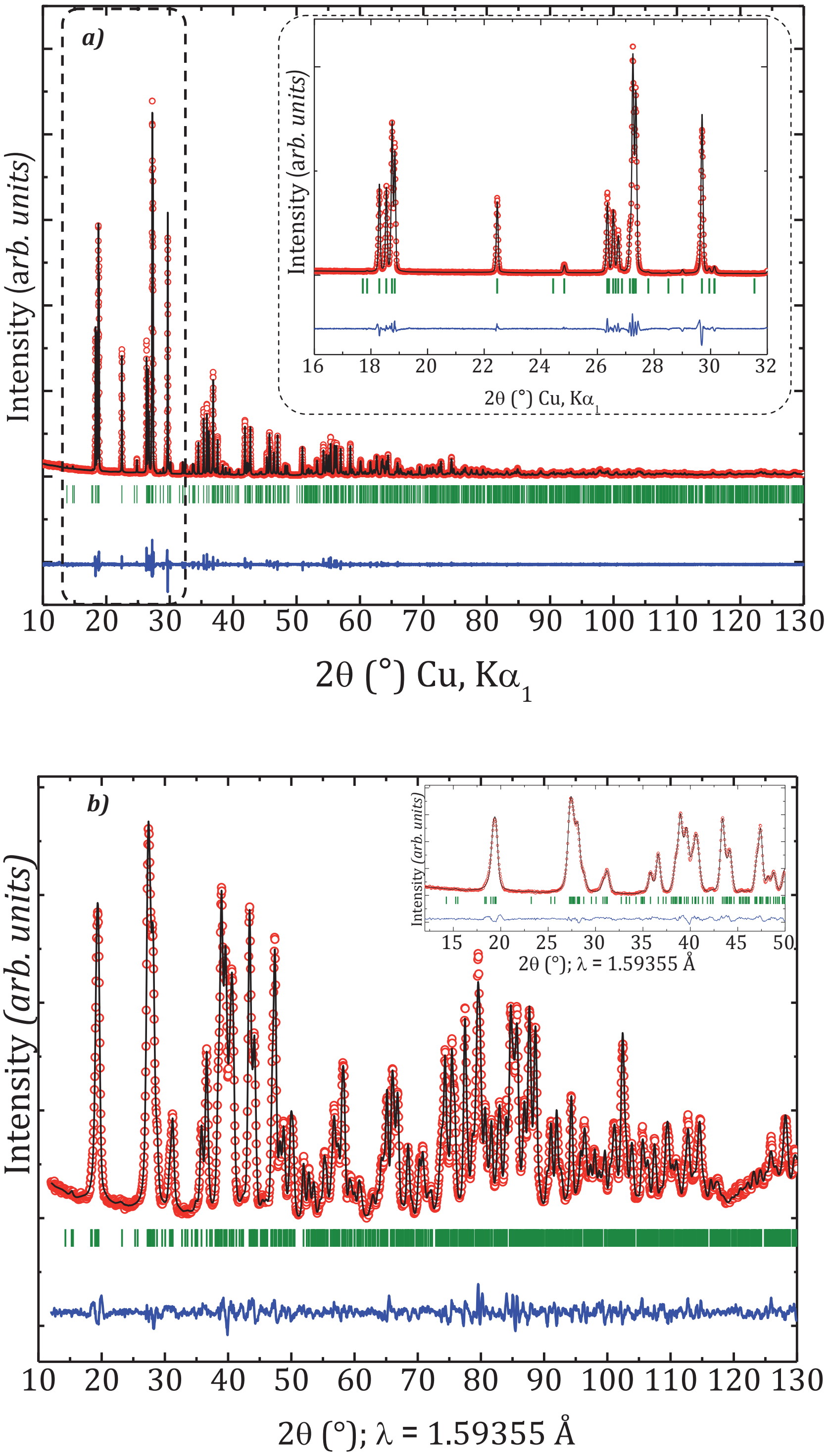

Figure I-23: Observed (red dots), calculated (black line), and difference (blue line) plots obtained for the Rietveld refinement of (a) X-ray diffraction and (b) neutron diffraction data for $LiVPO_4O$

3. Two independent positions for lithium were then included in the Rietveld refinements of both neutron and X-ray diffraction data. The refinement of neutron and X-ray diffraction data showed good minimization of the difference between the experiment and calculated patterns as can be seen in Figure I-23. The subsequent Fourier Difference maps showed no residual nuclear densities and we therefore adopted a structural model with two crystallographic sites for

lithium at (0.204(5), −0.688(5), 0.075(4)) and (0.273(5), −0.207(5), 0.409(4)) for Li(1) and Li(2) respectively. Separate refinements of thermal motion factors and occupancies led to satisfactory reliability factors (Table I-3 in ANNEX I). The lattice parameters as well as the atomic positions are gathered in Table I-3 of ANNEX I. The resulting inter-atomic distances and angles are recorded in Table I-4 of ANNEX I.

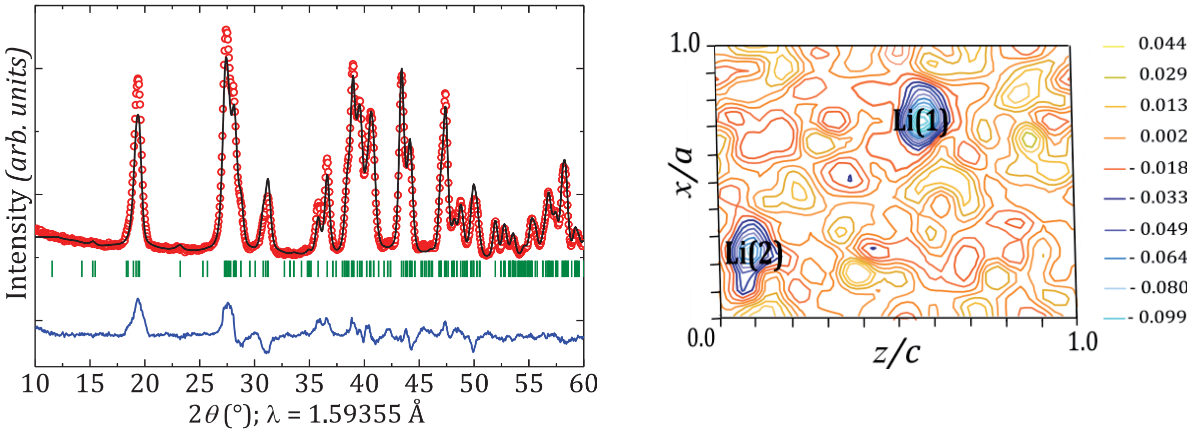

Figure I-24: (Left) Rietveld refinement of neutron diffraction data (only heaviest atoms are considered); (Right) 2D section of 3D Fourier difference map at y = 0.156 with the maxima corresponding to the Li(1) and Li(2) sites for the crystal structure of $LiVPO_4O$

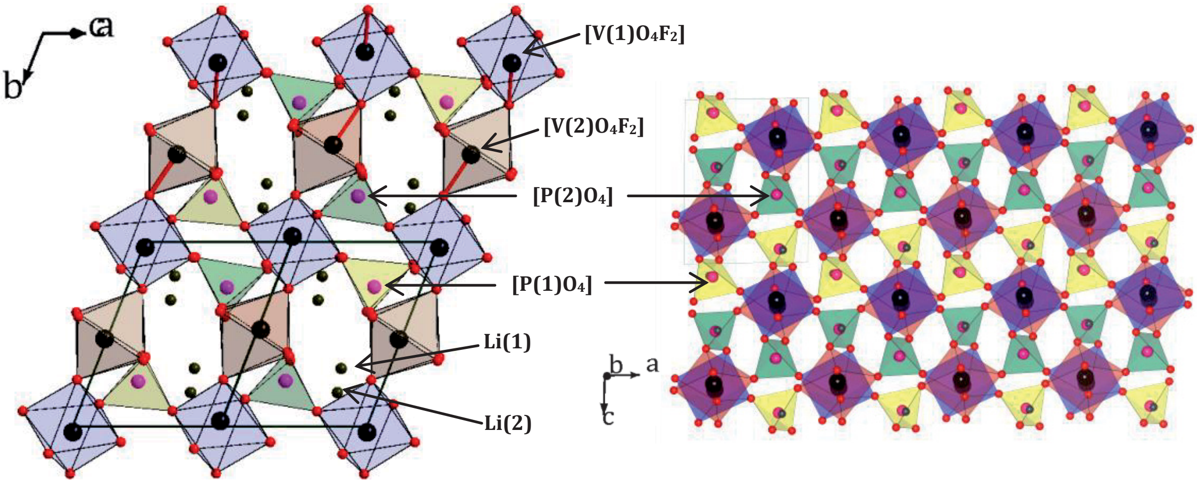

Figure I-25: (Left) Representation of the crystal structure of $LiVPO_4O$ (Right) Octahedra chains connected alternatively by different tetrahedra along the c direction

The 3D structure of $LiVPO_4O$ (Figure I-25) is basically similar to that of $LiVPO_4F$ and is built up by chains of [V(1)O_6] and [V(2)O_6] octahedra connected alternatively through their corners by the O(6) and O(5) oxygen sites. These chains run along $[010]_{P\bar{1}}$ and are connected to each other by [P(1)O_4] and [P(2)O_4] tetrahedra characterized by P–O distances in between 1.50 and 1.58 Å (Figure I-26). The two different tetrahedra connect the vanadium chains alternatively along the $[001]_{P\bar{1}}$ as presented in Figure I-25b. The vanadium cations lie within two octahedral sites with a wide range of V–O distances: 1.62–2.17 Å for V(1) and of 1.71–2.21 Å for V(2), as a typical example of alternate short and long distances in vanadyl-containing compounds (Table I-3) . The short and long V–O distances in [VO$_4$O$_2$] octahedra chains are alternated along the $[101]_{P\bar{1}}$ direction. One notes that the [V(2)O$_4$O$_2$] octahedron is slightly more symmetrical than the [V(1)O$_4$O$_2$] octahedron ($\Delta = 5.51\times10^{-3}$ and $\Delta = 7.63\times10^{-3}$ respectively). The tunnels generated by these polyhedra run along the $[1\bar{1}0]_{P\bar{1},}$ $[101]_{P\bar{1}}$, and $[10\bar{1}]_{P\bar{1}}$ directions.

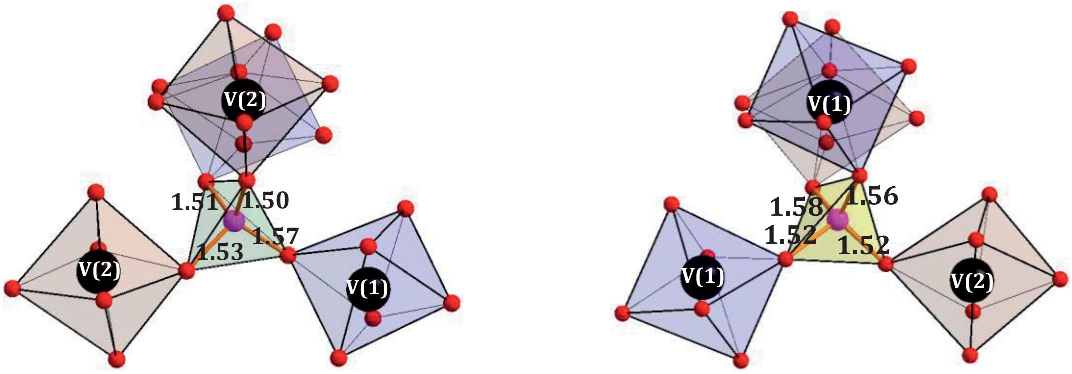

Figure I-26: Schematic representation of [P(1)O$_4$] (left) and [P(2)O$_4$] (right) local environments in LiVPO$_4$O

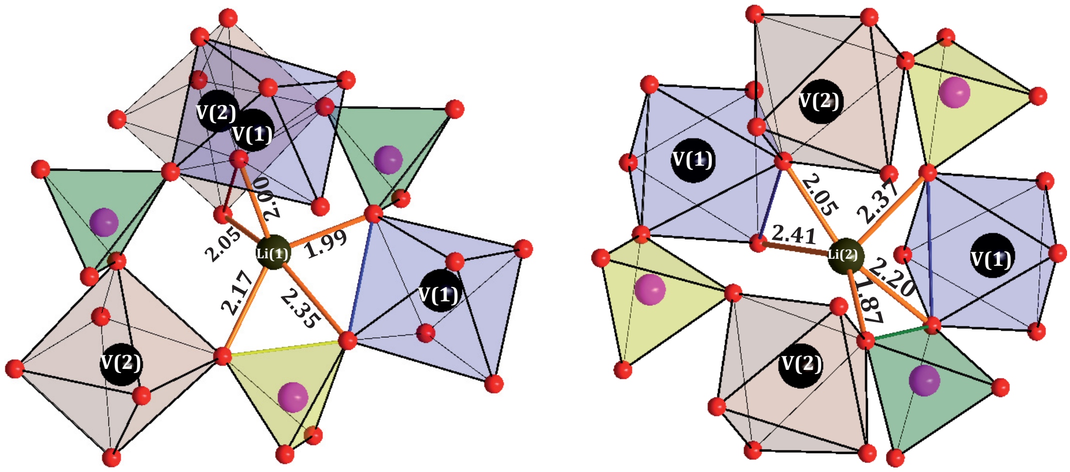

Figure I-27: Schematic representation of Li(1)O$_5$ (left) and Li(2)O$_5$ (right) local environments in LiVPO$_4$O

The lithium ions are distributed over two fully occupied distinct crystallographic sites, Li(1) and Li(2), due to the doubling of the unit-cell, at a distance from each other of 3.44 Å. They lie in two very distorted pentahedral sites ($\Delta = 3.96\times10^{-3}$ and $\Delta= 8.52\times10^{-3}$; Figure I-27). The shortest Li–P distances are along the $[100]_{P\bar{1}}$ direction, so that each type of Li sites lies perpendicular to one type of phosphorous site. This can be seen in Figure I-25b where Li(1) is above (seen in figure) or under (hidden in the figure) P(2) and Li(2) is above or under P(1) with the distances of 2.77 Å for Li(1)–P(2) and 2.61 Å for Li(2)–P(1).

The cations BVS values calculated for V(1), V(2), P(1), P(2), Li(1), and Li(2) are respectively $BVS_{V(1)}$ = 4.02, $BVS_{V(2)}$ = 3.98, $BVS_{P(1)}$ = 5.01, $BVS_{P(2)}$ = 5.03, $BVS_{Li(1)}$ = 0.94, and $BVS_{Li(2)}$ = 1.03, in very good agreement with expectations.

Table I-3: long (V-O) and short (V=O) distances (in Å) in $LiVPO_4O$ and VPO_4O polymorphs.

	V=O (Å)	V-O (Å)	S.G	Symmetry
δ-VPO_4O (ICSD N° 420073)	1.62	1.84	*$P4_2/mbc$*	Tetragonal
ε-VPO_4O (ICSD N° 415924)	1.57	2.56	*Cc*	Monoclinic
γ-VPO_4O (ICSD N° 415213)	1.50	2.70	*Pnam*	Orthorhombic
	1.62	1.81		
β-VPO_4O (ICSD N° 9413)	1.56	2.59	*Pnma*	Orthorhombic
α_{II}-VPO_4O (ICSD N° 2889)	1.58	2.86	*P4/n*	Tetragonal
α_{I}-VPO_4O (ICSD N° 108983)	1.63	2.48	*P4/n*	Tetragonal
β-$LiVPO_4O$ (ICSD N° 80613)	1.63	2.34	*Pnma*	Orthorhombic
α-$LiVPO_4O$ (ICSD N° 99618)	1.58	1.95	*P4/nmm*	Tetragonal
$LiVPO_4O$ (in this work)	1.71	2.21	$P\bar{1}$	Triclinic
	1.62	2.17		

I-4b. NMR Study of $LiVPO_4O$

To the best of our knowledge, no NMR investigation of $LiVPO_4O$ had been previously reported. ^7Li and ^{31}P MAS NMR measurements for $LiVPO_4O$ were carried out in the same conditions as for $LiVPO_4F$. ^7Li MAS NMR shows a rather sharp peak at 79 ppm (Figure I-28) less shifted than in $LiVPO_4F$ (116 ppm) due to the change in oxidation state of vanadium. Indeed V^{4+} ($t_{2g}^1e_g^0$) should provide less spin transfer toward the Li nuclei than V^{3+} ($t_{2g}^2e_g^0$). In $LiVPO_4O$ two peaks corresponding to each crystallographic site of lithium might be expected to be observed, which is obviously not the case as shown by the fit of the spectrum by a single Gaussian/Lorentzian contribution. Although the two crystallographic sites for Li are different (the pentahedron of Li(1) shares two edges, one with $[V(1)O_4O_2]$ octahedron and another one with $[V(2)O_4O_2]$ whereas the Li(2) shares two edges with two $[V(1)O_4O_2]$ octahedra), one has again to remember that the interaction governing the shift is governed by the electron spin transfer, in other words by the relative arrangement of the *d* orbitals of the V ions carrying the spins and the Li atoms (via the O possibly). In this respect, the two lithiums do not appear to differ strongly, as confirmed by D. Carlier through DFT calculations. Therefore the two contributions might be included in the single signal identified (in agreement with its strong Gaussian character). Another possible explanation of the observation of one single signal can be found in the mobility of the two Li atoms between the two crystallographic sites but the two sites are separated by 3.44 Å so that the mobility between them is unlikely but possible, and no hint of motion was detected by the NMR. Very high field and fast MAS measurement are planned at the Orleans NMR platform in order to discriminate between these effects.

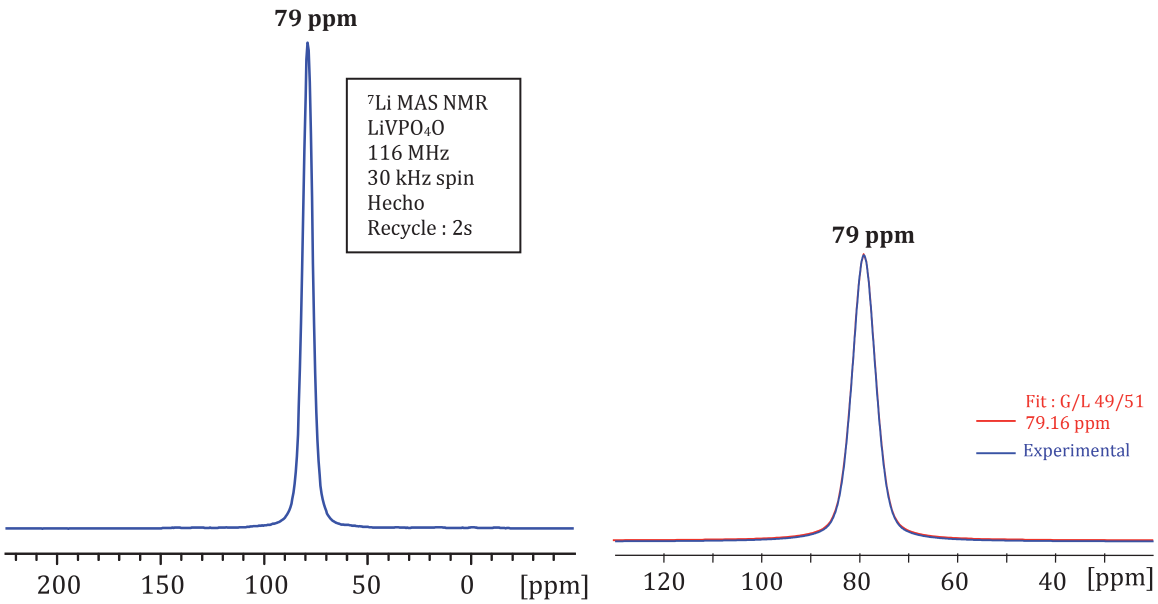

Figure I-28: ^{7}Li MAS NMR spectrum of LiVPO$_4$O (left) and a fit of ^{7}Li MAS NMR spectrum (right). The result is given in the insert

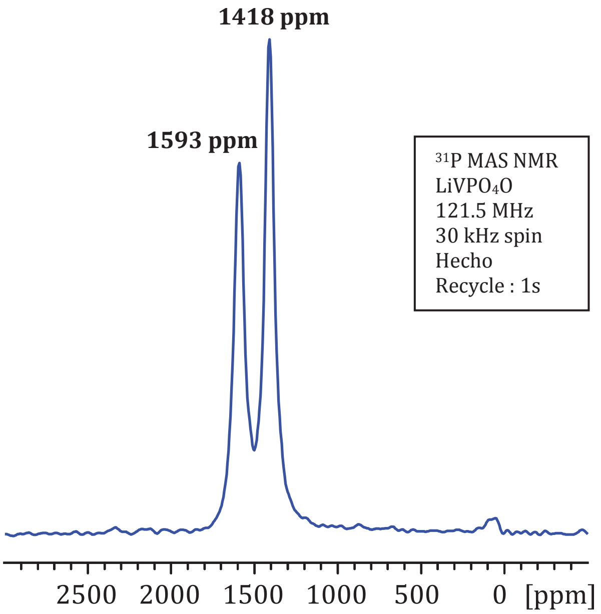

Figure I-29: ^{31}P MAS NMR spectrum (Hahn echo) of LiVPO$_4$O (spinning 30 kHz)..

LiVPO$_4$O was also analyzed by ^{31}P NMR, the spectrum of which is presented in Figure I-29. The two signals at 1593 ppm and 1418 ppm confirm the existence of two different types of P in agreement with the two crystallographic sites (less shifted than in LiVPO$_4$F for the same reason as for ^{7}Li signals). The relative magnitude (*i.e.* area) of the two signals is not strongly different from 1.

Powder neutron diffraction was performed at low temperature on D20 diffractometer in collaboration with E. Suard (ILL–Grenoble). Though the magnetic measurement revealed a magnetic transition at a temperature of 9 K from paramagnetic to antiferromagnetic ordering, no magnetic transition was observed using low temperature neutron diffraction. This is probably due to the transparency of vanadium in neutron diffraction with in addition the electronic configuration of V^{4+} ($t_{2g}^1\ e_g^0$) which displays only one single electron. In the case of $LiVPO_4F$, two tiny peaks were observed at 2 K and the Rietveld refinement led to a small magnetic moment (1.22 μ_B). It was therefore not surprising that no magnetic transition appeared for $LiVPO_4O$.

I-5. Conclusion and summary of this chapter

It was possible to synthesize $LiVPO_4O$ in one-step ceramic route using stoichiometric amounts of V_2O_3, $NH_4H_2PO_4$ and LiF or Li_3PO_4 under O_2 atmosphere. We paid significant efforts in trying to obtain $LiVPO_4F$ through a one step ceramic route using either V_2O_3 or V_2O_5 as vanadium precursors under inert atmosphere and always ended up with the monoclinic α-$Li_3V_2(PO_4)_3$ and V_2O_3 as main impurities. Nevertheless, $LiVPO_4F$ was obtained through a two-step ceramic route which consisted first on the synthesis of carbon coated VPO_4 (C–VPO_4) by CTR process then on the reaction between LiF and the C-VPO_4. SEM images of $LiVPO_4O$ showed particles size of about 1 µm highly agglomerated at 5-6 µm and the particles size of $LiVPO_4F$ as about 1-2 µm. The oxidation state of vanadium in both $LiVPO_4O$ and $LiVPO_4F$ was confirmed by magnetism and Bond Valence Sum (BVS).

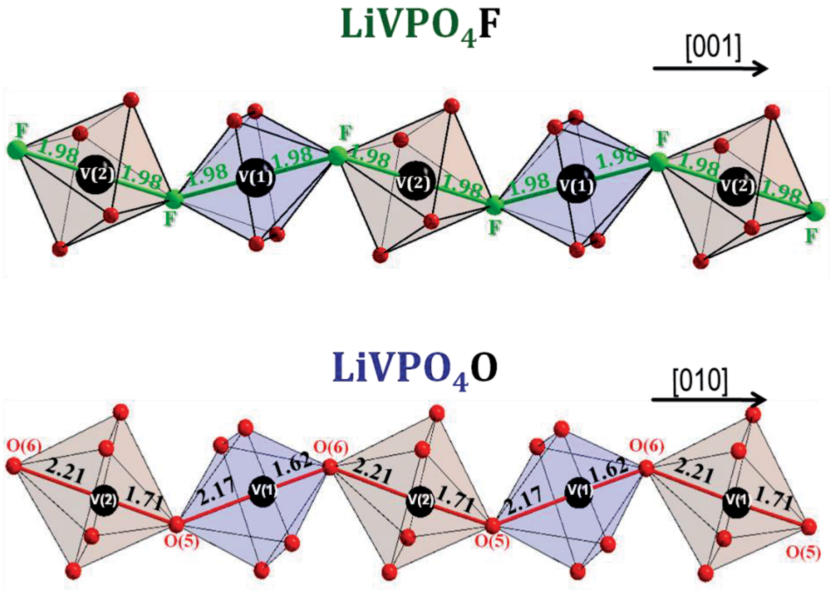

Figure I-30: Comparison of [VO_4X_2] chains in $LiVPO_4X$ (X = F, O).

Both $LiVPO_4O$ and $LiVPO_4F$ crystallize in a Tavorite-like structure with the unit cell volume of $LiVPO_4O$ being two times bigger than the one of $LiVPO_4F$. While one lithium site was found for $LiVPO_4F$ (as shown by Rietveld refinement of neutron diffraction data), two independent sites of lithium fully occupied were observed in the case of $LiVPO_4O$. ^{7}Li NMR exhibited one sharp single signal for $LiVPO_4F$ consistent with the unique site of Li observed. Surprisingly, one single sharp signal was also observed for the ^{7}Li NMR of $LiVPO_4O$ indicating that the two Li sites are similar. ^{31}P NMR confirmed the presence of one site of phosphorous in $LiVPO_4F$ with a signal observed at 3998 pm. In the same way, two signals of ^{31}P NMR were observed (at 1593 ppm and 1418 ppm) for $LiVPO_4O$ corresponding to the two sites of phosphorous present in the structure of $LiVPO_4O$.

One of the main distinctive characteristic between the two structures is found along their respective chains where two independent vanadium sites are encountered with very regular V–F distances in $LiVPO_4F$ (1.98 Å) compared with alternate long and short V–O distances in $LiVPO_4O$ (Figure I-30-30). Noteworthy, the V(1)–F–V(2) angle in $LiVPO_4F$ (132.5°) which is smaller than the corresponding angles V(1)–O(5)–V(2) and V(2)–O(6)–V(1) in $LiVPO_4O$ (138.6° and 137.1°, respectively). We also observed a difference of the dihedral angle in both compounds since $LiVPO_4F$ exhibited a dihedral angle of 25.05° and $LiVPO_4O$ possess a dihedral angle of 24.53°.

References

1. Barker, J.; Saidi, M.Y. and Swoyer, J.; *Lithium Metal Fluorophosphate and Preparation Thereof,* US Patent **2005**, 0142056 A1(US 2005).
2. Barker, J.; Saidi, M.Y. and Swoyer, J.L.; *Electrochemical insertion properties of the novel lithium vanadium fluorophosphate, LiVPO(4)F,* Journal of the Electrochemical Society, **2003**, 150(10): p. A1394-A1398.
3. Li, Y.; Zhou, Z.; Gao, X.P. and Yan, J.; *A Novel Sol–gel Method to Synthesize Nanocrystalline LiVPO(4)F and its Electrochemical Li Intercalation Performances,* **2006**, 160: p. 633-637.
4. Zhang, Q.; Zhong, S.K.; Liu, L.T.; Liu, J.Q.; Jiang, J.Q.; Wang, J. and Li, Y.H.; *A novel method to synthesize LiVPO(4)F/C composite materials and its electrochemical Li-intercalation performances,* Journal of Physics and Chemistry of Solids, **2009**, 70(7): p. 1080-1082.
5. Zheng, J.C.; Zhang, B. and Yang, Z.H.; *Novel synthesis of LiVPO(4)F cathode material by chemical lithiation and postannealing,* Journal of Power Sources, **2012**, 202: p. 380-383.
6. Plashnitsa, L.S.; Kobayashi, E.; Okada, S. and Yamaki, J.; *Symmetric lithium-ion cell based on lithium vanadium fluorophosphate with ionic liquid electrolyte,* Electrochimica Acta, **2011**, 56(3): p. 1344-1351.
7. Zhou, F.; Zhao, X.M. and Dahn, J.R.; *Reactivity of charged LiVPO(4)F with 1 M LiPF(6) EC:DEC electrolyte at high temperature as studied by accelerating rate calorimetry,* Electrochemistry Communications, **2009**, 11(3): p. 589-591.
8. Allen, C.J.; Jia, Q.Y.; Chinnasamy, C.N.; Mukerjee, S. and Abraham, K.M.; *Synthesis, Structure and Electrochemistry of Lithium Vanadium Phosphate Cathode Materials,* Journal of the Electrochemical Society, **2011**, 158(12): p. A1250-A1259.
9. Barker, J.; Gover, R.K.B.; Burns, P.; Bryan, A.; Saidi, M.Y. and Swoyer, J.L.; *Performance evaluation of lithium vanadium fluorophosphate in lithium metal and lithium-ion cells,* Journal of the Electrochemical Society, **2005**, 152(9): p. A1776-A1779.
10. Barker, J.; Gover, R.K.B.; Burns, P.; Bryan, A.; Saidi, M.Y. and Swoyer, J.L.; *Structural and electrochemical properties of lithium vanadium fluorophosphate, LiVPO(4)F,* Journal of Power Sources, **2005**, 146(1-2): p. 516-520.
11. Azmi, B.M.; Ishihara, T.; Nishiguchi, H. and Takita, Y.; *Cathodic performance of LiVOPO(4) prepared by impregnation method for Li ion secondary battery,* Electrochemistry, **2003**, 71(12): p. 1108-1110.
12. Yang, Y.; Fang, H.S.; Zheng, J.; Li, L.P.; Li, G.S. and Yan, G.F.; *Towards the understanding of poor electrochemical activity of triclinic LiVOPO(4): Experimental characterization and theoretical investigations,* Solid State Sciences, **2008**, 10(10): p. 1292-1298.
13. Lavrov, A.V.; Nikolaev, V.P.; Sadikov, G.G. and Poraikoshits, M.A.; *Synthesis and Crystal-Structure of Mixed Vanadyl and Lithium Otho-Phosphate, LiVOPO(4),* Doklady Akademii Nauk Sssr, **1982**, 266(2): p. 343-346.
14. Viswanath, R.S. and Miller, P.J.; *High-Temperature Phase-Transition in NH(4)H(2)PO(4),* Solid State Communications, **1979**, 32(8): p. 703-706.
15. Zhou, M.F. and Chen, M.H.; *Reactions of silicon dioxide with ammonia molecules: formation and characterization of the SiO(2)-NH(3) complex and the H(2)NSiOOH molecule,* Chemical Physics Letters, **2001**, 349(1-2): p. 64-70.
16. Barker, J.; Saidi, M.Y. and Swoyer, J.L.; *A carbothermal reduction method for the preparation of electroactive materials for lithium ion applications,* Journal of the Electrochemical Society, **2003**, 150(6): p. A684-A688.
17. Hameed, A.S.; Nagarathinam, M.; Reddy, M.V.; Chowdari, B.V.R. and Vittal, J.J.; *Synthesis and electrochemical studies of layer-structured metastable alpha(I)-LiVOPO(4),* Journal of Materials Chemistry, **2012**, 22(15): p. 7206-7213.
18. Dupre, N.; Gaubicher, J.; Angenault, J. and Quarton, M.; *Electrochemical study of intercalated vanadyl phosphate,* Journal of Solid State Electrochemistry, **2004**, 8(5): p. 322-329.

19. Dupre, N.; Wallez, G.; Gaubicher, J. and Quarton, M.; *Phase transition induced by lithium insertion in alpha(I)- and alpha(II)-VOPO(4),* Journal of Solid State Chemistry, **2004**, 177(8): p. 2896-2902.
20. Barker, J.; Saidi, M.Y. and Swoyer, J.L.; *Electrochemical properties of beta-LiVOPO(4) prepared by carbothermal reduction,* Journal of the Electrochemical Society, **2004**, 151(6): p. A796-A800.
21. Gaubicher, J.; Le Mercier, T.; Chabre, Y.; Angenault, J. and Quarton, M.; *Li/beta-VOPO4: A new 4 V system for lithium batteries,* Journal of the Electrochemical Society, **1999**, 146(12): p. 4375-4379.
22. Kerr, T.A.; Gaubicher, J. and Nazar, L.F.; *Highly reversible Li insertion at 4 V in epsilon-VOPO(4)/alpha-LiVOPO(4) cathodes,* Electrochemical and Solid State Letters, **2000**, 3(10): p. 460-462.
23. Bain, G.A. and Berry, J.F.; *Diamagnetic corrections and Pascal's constants,* Journal of Chemical Education, **2008**, 85(4): p. 532-536.
24. Simonov, V.I. and Belov, N.V.; *The Crystal Structure of Amblygonite,* Doklady Akademii Nauk Sssr, **1958**, 119(2): p. 354-356.
25. Ateba Mba, J.M.; Masquelier, C.; Suard, E. and Croguennec, L.; *Synthesis and Crystallographic Study of Homeotypic LiVPO(4)F and LiVPO(4)O,* Chemistry of Materials, **2012**, 24(6): p. 1223-1234.
26. Ellis, B.L.; Ramesh, T.N.; Davis, L.J.M.; Goward, G.R. and Nazar, L.F.; *Structure and Electrochemistry of Two-Electron Redox Couples in Lithium Metal Fluorophosphates Based on the Tavorite Structure,* Chemistry of Materials, **2011**, 23(23): p. 5138-5148.
27. Rinard, P.M.; *Neutron Interactions with Matter. ,* Passive Nondestructive Assay of Nuclear Materials, **1991**, NUREG/CR-5550 /LA-UR-90-732(Edited by Reilly, D, N.Ensslin, H. Smith, Jr, and S. Kreiner.): p. Chapter 12.
28. Sears, V.F.; *Neutron scattering lengths and cross section,* Neutron News, **1992**, 3(3): p. 26-37.
29. Castets, A.; *RMN de matériaux paramagnétiques: mesures et modélisation,* Bordeaux 1 University, **2012**.
30. Vaughey, J.T.; Harrison, W.T.A.; Jacobson, A.J.; Goshorn, D.P. and Johnson, J.W.; *Synthesis, Structure, and Properties of 3 New Vanadium (III) Phosphates - VPO(4) Center Dot H2O and V1.23(PO4)(OH)0.69(H2O)0.31 Center Dot 0.33H2O,* Inorganic Chemistry, **1994**, 33(11): p. 2481-2487.
31. Castets, A.; Carlier, D.; Zhang, Y.; Boucher, F.; Marx, N.; Croguennec, L. and Menetrier, M.; *Multinuclear NMR and DFT Calculations on the LiFePO(4)center dot OH and FePO(4)center dot H(2)O Homeotypic Phases,* Journal of Physical Chemistry C, **2011**, 115(32): p. 16234-16241.
32. Castets, A.; Carlier, D.; Zhang, Y.; Boucher, F.; Marx, N.; Gautier, R.; Le Fur, E.; Le Polles, L.; Croguennec, L. and Menetrier, M.; *NMR study of the LiMnPO(4)center dot OH and MPO(4)center dot H(2)O (M=Mn, V) homeotypic phases and DFT calculations,* Solid State Nuclear Magnetic Resonance, **2012**, 42: p. 42-50.
33. Duttine, M.; Carlier, D.; Ateba Mba, J.M.; Croguennec, L.; Masquelier, C. and M., M.; *19F, 7Li and 31P MAS NMR Charaterization and DFT Calculations for the Tavorite-Type LiVPO4F,* Journal of Physical Chemistry C, **2013**, SUBMITTED.

Chapter II

ELECTROCHEMICAL BEHAVIOR OF LiVPO$_4$X (X = O or F)

Contents

II-1. Introduction 61

II-2. ELECTRODE PREPARATION AND BATTERY CONFIGURATION 64

II-3. ELECTROCHEMICAL BEHAVIOR OF LiVPO$_4$F 66

- **II-3a. Reversible Li$^+$ insertion into LiVPO$_4$F (V^{3+}/V^{2+} couple) 66**
- **II-3b. Reversible Li$^+$ extraction from LiVPO$_4$F (V^{4+}/V^{3+} couple) 69**
- **II-3c. Crystal Structures of Li$_x$VPO$_4$F (x = 2, 0.67, 0) 77**
  - ***i- Crystal Structure of VPO$_4$F 78***
  - ***ii- Hypothesis on the structure of Li$_{0.67}$VPO$_4$F 80***
  - ***iii- Structure of Li$_2$VPO$_4$F 81***
  - ***iv- Comparative NMR Study of Li$_x$VPO$_4$F phases (with x = 1, 0.67 and 0) 84***
- **II-3d. Conclusion 86**

II-4. ELECTROCHEMICAL BEHAVIOR OF LiVPO$_4$O 88

- **II-4a. Reversible Li$^+$ insertion into LiVPO$_4$O (V^{3+}/V^{4+} couple) 89**
- **II-4b. Reversible Li$^+$ extraction from LiVPO$_4$O (V^{4+}/V^{5+} couple) 92**

II-5. Conclusions and summary of this chapter 97

II-1. Introduction

$LiVPO_4F$ is an attractive material as a positive electrode in Li-ion battery as it displays one of the highest V^{4+}/V^{3+} redox couple among known polyanionic compositions (Table II-1). As an example, the average redox potential of the V^{4+}/V^{3+} couple in $LiVPO_4F$ is 4.2 V *vs.* Li^+/Li, much higher than for the well-known α-$Li_3V_2(PO_4)_3$ [1-5] (Figure II-1). It is worth noticing that both $LiVP_2O_7$ and $LiVPO_4F$ have the same average potential [6-9] (Figure II-1) but the advantage of $LiVPO_4F$ is that the total energy is higher (655 Wh/Kg) than that of $LiVP_2O_7$ (486 Wh/Kg).

Table II-1: Average potentials, capacities and energy densities of vanadium phosphates reported in the literature.

	Initial/final Active material	**Average Potential (V *vs.* Li)**	**Theoretical Capacity (mAh/g)**	**Energy density (Wh/g)**
Li batteries	$V^{V}PO_4O{\cdot}2H_2O$ / $Li_xV^{IV}PO_4O{\cdot}2H_2O$ [10, 11]	3.7	135	499
	$V^{V}PO_4O{\cdot}H_2O$ / $Li_xV^{IV}PO_4O{\cdot}H_2O$ [10]	3.6	149	536
	$V^{V}PO_4O$ / $LiV^{IV}PO_4O$ [11-16]	3.9	165	643
	$V^{IV}O(H_2PO_4)_2$ / $LiV^{III}O(H_2PO_4)_2$ [17]	4.2	103	433
	$LiV^{III}PO_4F$ / $V^{IV}PO_4F$ [18-28]	4.2	156	655
	$LiV^{IV}PO_4O$ / $V^{V}PO_4$ [11-16, 27, 29-42]	3.9	159	620
	$LiV^{III}P_2O_7$ / $V^{IV}P_2O_7$ [6-8, 43]	4.2	116	487
	$Li_2V^{IV}P_2O_7$ / $V^{V}P_2O_7$ [44]	4.2	105	441
	$Li_2V^{IV}O(HPO_4)_2$ / $LiV^{V}O(HPO_4)_2$ [17]	4.2	98	412
	$Li_3V^{III}_2(PO_4)_3$ / $LiV^{IV}_2(PO_4)_3$ [1-5]	3.7	131	485
	$Li_4V^{IV}O(PO_4)_2$ / $Li_5V^{V}O(PO_4)_2$ [17, 45]	4.1	94	385
	$Li_5V^{III}(PO_4)_2F_2$ / $Li_4V^{IV}(PO_4)_2F_2$ [46]	4.1	171	701
Na batteries	$Li_{1.1}Na_{0.4}V^{3.7}PO_{4.8}F_{0.7}$ / $V^{V}PO_{4.8}F_{0.7}$ [47]	4.0	140	560
	$NaV^{III}PO_4F$ / $V^{III}PO_4F$ [48-50]	4.0	143	572
	$Na_3V^{III}_2(PO_4)_2F_3$ / $NaV^{IV}_2(PO_4)_2F_3$ [51-55]	3.9	192	749

The electrochemical performances of $LiVPO_4F$ had been widely studied by J. Barker et al. [19-21, 49, 56-60]. During the charge of $LiVPO_4F$ (electrochemical extraction of Li^+ from $LiVPO_4F$), two plateaus were observed and located at 4.24 V *vs.* Li^+/Li for the first one and at 4.28 V *vs.* Li^+/Li for the second one. Surprisingly, during the subsequent discharge (electrochemical insertion of Li^+ in VPO_4F) only one plateau was observed at a potential of 4.2 V *vs.* Li^+/Li.

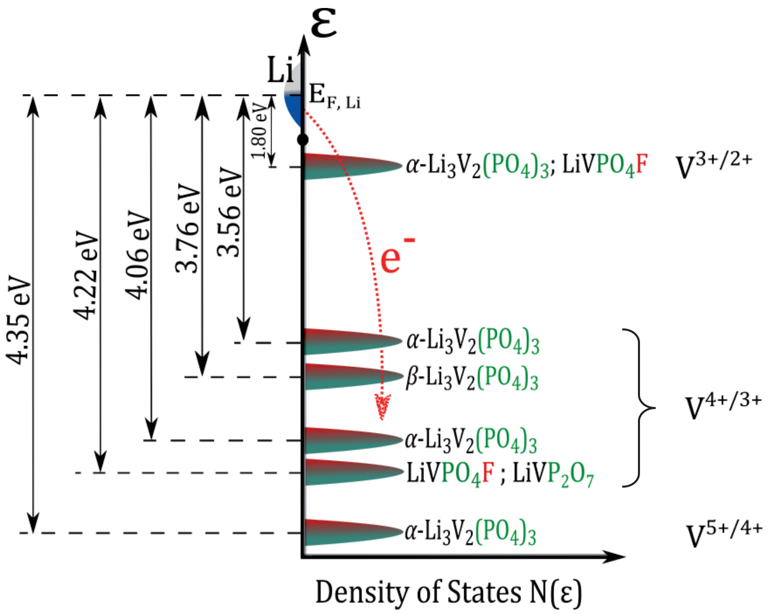
ε
Li
E_F, Li
1.80 eV
3.56 eV
3.76 eV
4.06 eV
4.22 eV
4.35 eV
e⁻
α-Li3V2(PO4)3; LiVPO4F
V3+/2+
α-Li3V2(PO4)3
β-Li3V2(PO4)3
α-Li3V2(PO4)3
LiVPO4F ; LiVP2O7
V4+/3+
α-Li3V2(PO4)3
V5+/4+
Density of States N(ε)

Figure II-1: Respective positions of $V^{n+}/V^{(n-1)+}$ redox couples in phosphate, diphosphate and NASICON-like polyanionic structures. α- and β-$Li_3V_2(PO_4)_3$ refer to Anti-NASICON (monoclinic) and NASICON (rhombohedral) forms respectively.

J. Barker also showed that it was possible to insert lithium into $LiVPO_4F$ electrochemically at a potential of 1.80 V *vs.* Li^+/Li leading to Li_2VPO_4F [60]. Based on the two redox potentials involved during first charge (V^{4+}/V^{3+}) and during first discharge (V^{3+}/V^{2+}), J. Barker envisioned the preliminary performance of a symmetrical Li-ion cell $LiVPO_4F||LiVPO_4F$ (EC/DMC in 2:1, by weight proportion, was used as electrolyte) which can operate with an average voltage of 2.4 V *vs.* Li^+/Li (Figure II-2)

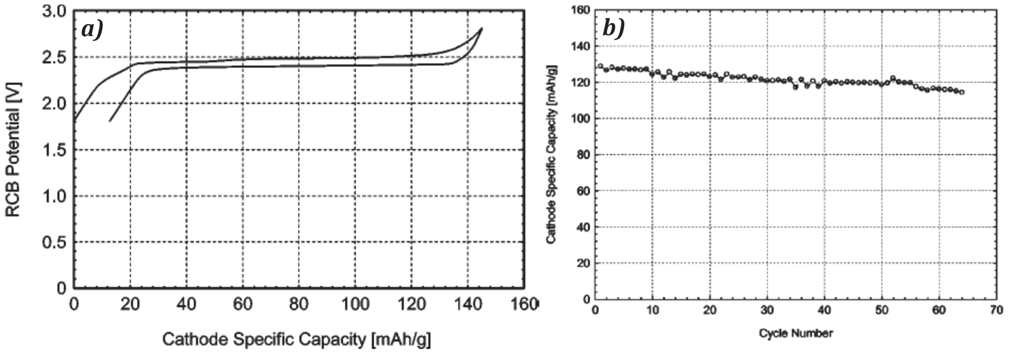

Figure II-2: a) Electrochemical behavior of a typical symmetrical $LiVPO_4F||LiVPO_4F$ cell cycled between 1.80 V and 2.80 V as reported by J. Barker together with b) the corresponding capacity vs. cycles number [60].

The initial active specific capacity reported at a rate of C/5 by J. Barker was 128 mAh/g for both electrodes, which dropped down to 116 mAh/g after 65 cycles (corresponding to 9% of capacity fade). L.S. Plashnitsa et al. [61] studied the performance of $LiVPO_4F||LiVPO_4F$ cells using either $LiPF_6$ in EC-DMC (with proportion of 1:1 by weight) or $LiBF_4$/$EMIBF_4$ in ionic liquid (IL). For the first case, the symmetrical cell operated at 2.4 V *vs.* Li^+/Li with an initial capacity of 120 mAh/g which dramatically decreased (Figure II-3) reaching 20 mAh/g after only 9 cycles. Interestingly, less capacity fade was observed for the symmetrical battery of $LiVPO_4F$ using the IL-based electrolyte, with a capacity retention of 60 mAh/g after 19 cycles (Figure II-3c and 3d).

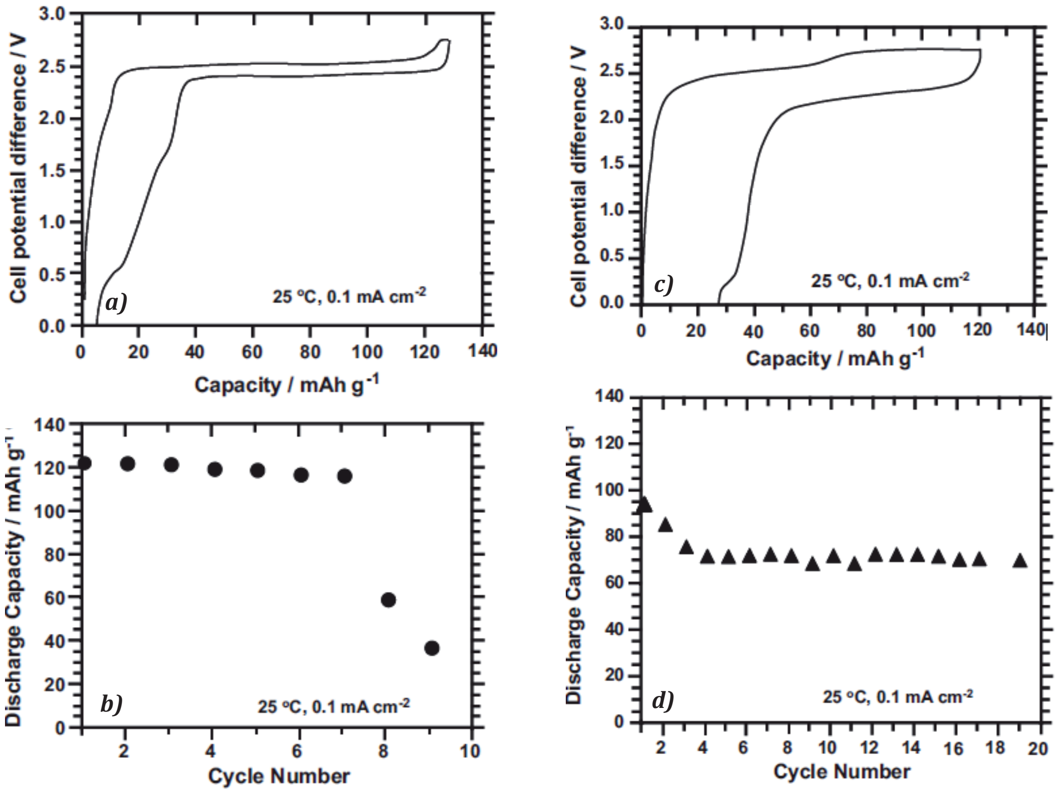

Figure II-3: a) The first charge/discharge galvanostatic data for the $LiVPO_4F$/[1M] $LiPF_6$/EC-DMC (1:1)/$LiVPO_4F$ cell and b) the corresponding capacity vs. cycles number. c) The first charge/discharge galvanostatic data for the $LiVPO_4F$/[1M] $LiBF_4$/$EMIBF_4$/$LiVPO_4F$ cell and d) the corresponding capacity vs. cycles number [61].

T.A. Kerr et al. [13] reported on the first electrochemical signature of the triclinic $LiVPO_4O$ which had been obtained by chemical lithiation of ε-VPO_4O. The obtained $LiVPO_4O$ exhibited a capacity of ~110 mAh/g (theoretical specific capacity of $LiVPO_4O$ is 159 mAh/g) with an operating potential of 3.9 V *vs.* Li^+/Li. T.A. Kerr also showed that ε-VPO_4O can accommodate Li^+ leading to the formation of the triclinic phase $LiVPO_4O$. B.M. Azmi et al. [29] reported for the first time the electrochemical behavior of the "as-prepared" $LiVPO_4O$. The obtained electrochemical signature presented very small capacity retention (~10 mAh/g at C/50). Y. Yang et al. [36] investigated the poor electrochemical performances of the triclinic $LiVPO_4O$ and associated it to the very low intrinsic electronic conductivity. Recently, during this thesis, C. Allen et al. [39] demonstrated that Li^+ can be extracted from $LiVPO_4O$ with a relatively good reversible capacity of 120 mAh/g. Note that C. Allen reported particles size of 2-5 μm for the "as-prepared" $LiVPO_4O$ and found a discharge capacity of the triclinic $LiVPO_4O$ higher than the one of the orthorhombic $LiVPO_4O$ (both described in Chapter I, Figure I-7).

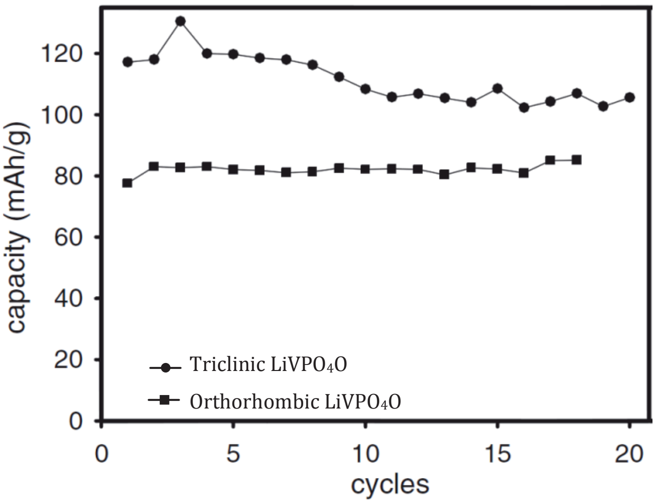

Figure II-4: Discharge capacities vs. cycle number of triclinic $LiVPO_4O$ (dots) and orthorhombic $LiVPO_4O$ (squares) phases. The cycling rate was C/10. [39]

In this chapter, we are reporting on the electrochemical behavior of both $LiVPO_4F$ and $LiVPO_4O$ used as positive electrode materials in Li-ion batteries. Structural changes associated with the reversible insertion/extraction of Li^+ out of/in these structures will be presented, as investigated by both *ex situ* and *in situ* X-Ray diffraction.

II-2. ELECTRODE PREPARATION AND BATTERY CONFIGURATION

We have performed electrochemical tests in coin cells assembled in an argon-filled dry glove box. Prior to be used as positive electrodes, the active materials were ball milled with 12 wt % of C_{SP} when $LiVPO_4F$ was concerned and 15 wt % of C_{SP} when $LiVPO_4O$ was used. In both cases, 12 wt % of PVdF binder was added. In order to ensure porosity and rapid electrolyte uptake within the electrodes, 33 wt % of Dibutylphtalate (DBP) was used. Finally some drops of acetone were added and the slurry was stirred for 1-2 hours prior to be casted (thickness ~150 µm) on a glass plate. After drying, electrodes of 1 cm in diameter were cut and soaked in ether in order to get rid of DBP. The electrodes loading were about 3-4 mg/cm^2.

The cells consisted of the positive electrode (as described above), 1 cm^2 Li disk as negative electrode and 1 M of $LiPF_6$ in a mixture of EC-DMC (1:1) as the electrolyte (LP30). The assembled cells were cycled between 3 V and 4.55 V *vs.* Li^+/Li when attention was given to Li^+ extracted from $LiVPO_4X$ (X = F, O) first and between 3 V and 1.50 V *vs.* Li^+/Li when attention was given to Li^+ inserted into $LiVPO_4X$ (X = F, O) first.

For *in situ* XRD, the synthesized $LiVPO_4F$ powder was mixed with 12 wt % C_{SP} (15 wt % of C_{SP} was used in the case of $LiVPO_4O$) and subsequently mixed/ground under argon using a Spex grinder for 15 minutes. The XRD patterns were recorded, during battery operation, with a Bruker D8 Advance diffractometer operating in Bragg-Brentano geometry with the CuK_α radiation. A special stainless steel *in situ* cell designed by J.B. Leriche et al. [62] (see Figure II-5) was assembled in an argon-filled dry box. Li metal was used as the negative electrode pasted on a Whatman glass fiber sheet separator saturated with a 1M $LiPF_6$ in ethylene carbonate (EC) and dimethyl carbonate (DMC) (1:1 in wt%) electrolyte. The positive electrodes were prepared by directly depositing ~ 15 mg of powder behind a thin aluminum sheet (thickness of 3 μm) used to protect the beryllium window from possible oxidation at high voltage. The cell was connected to a Mac-Pile system operating in galvanostatic cycling mode. Typically, each electrochemical cell was charged (or discharged) at a current equivalent to a C/50 rate during which the XRD patterns were collected, every hour, between 2θ = 13° and 2θ = 45°. After 45°, high-intensity diffraction peaks of Be (51°) tend to "screen" those of the studied phase. At 38.6°in 2θ ($d_{(hkl)}$ = 2.33 Å), the diffraction peak of Aluminum was present and used as a position-reference peak for successive experiments.

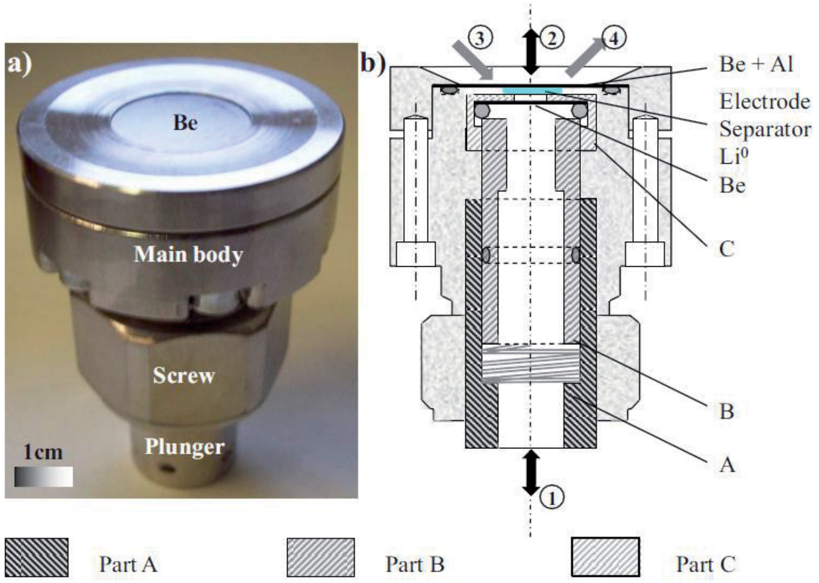

Figure II-5: a) Photography and b) detailed description of the Leriche's in situ cell used for in situ XRD experiments [62]

II-3. ELECTROCHEMICAL BEHAVIOR OF $LiVPO_4F$

The lithium-ion extraction/insertion reaction from $LiVPO_4F$, in the upper voltage range, relies on the reversibility of the V^{4+}/V^{3+} redox couple, and the lithium insertion/extraction reaction in the lower voltage range relies on the reversibility of the V^{3+}/V^{2+} redox couple. The two electrochemical reactions associated can be summarized as:

$LiV^{III}PO_4F \rightarrow V^{IV}PO_4F + Li^+ + e^-$ Theoretical capacity: 156 mAh/g

$LiV^{III}PO_4F + Li^+ + e^- \rightarrow Li_2V^{II}PO_4F$ Theoretical capacity: 156 mAh/g

II-3a. Reversible Li^+ insertion into $LiVPO_4F$ (V^{3+}/V^{2+} couple)

As established by J. Barker et al. [60], $LiVPO_4F$ can accommodate electrochemically one Li that leads to the formation of Li_2VPO_4F at a potential of 1.80 V *vs.* Li^+/Li. We have performed a GITT experiment (Galvanostatic Intermittent Titration Technique) in order to determine the mechanism of Li insertion/extraction between 1.50–3.00 V as well as the exact position of the plateau previously observed by J. Barker. The GITT (Figure II-6a) measurements consisted of a series of current-pulses applied at a rate of C/100 during 1 hour, followed by a long relaxation time for which the condition was set to dV/dt < 4 mV/h *i.e.* the variation of the potential is lower than 4 mV per 1 hour. The relaxation condition was reached within about 4 hours on the plateau as witnessed by the zoom-in (Figure II-6b) of time *vs.* potential. We therefore confirmed that the electrochemical insertion of Li into $LiVPO_4F$ occurred at the exact potential of 1.81 V *vs.* Li^+/Li (Figure II-6b) and the very flat plateau suggested a biphasic mechanism of Li insertion into $LiVPO_4F$.

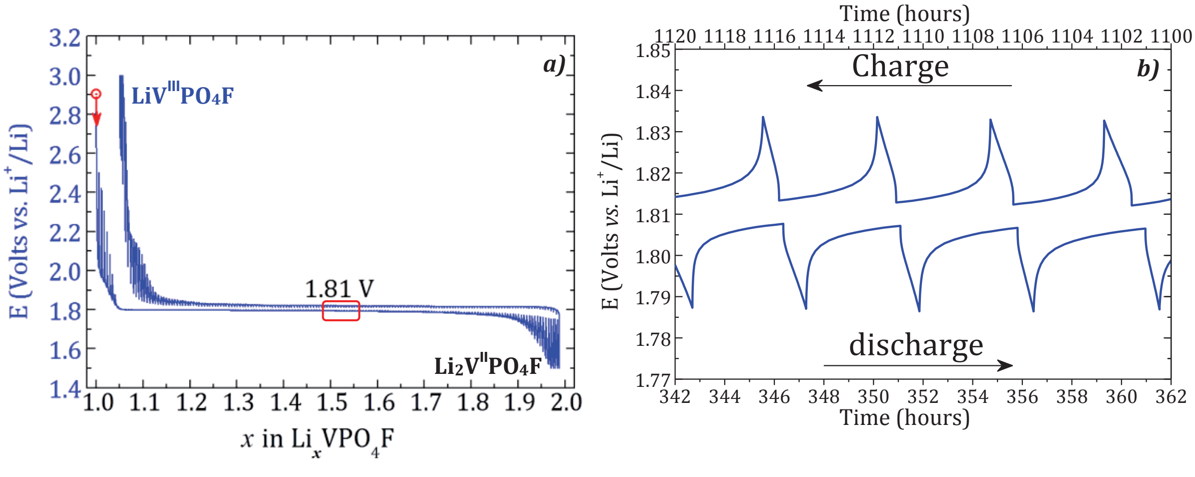

Figure II-6: GITT measurement of $LiVPO_4F$ between 1.5–3 V vs. Li. a) Potential vs. Li_xVPO_4F and b) in the region of $Li_{0.5}VPO_4F$, potential vs. time.

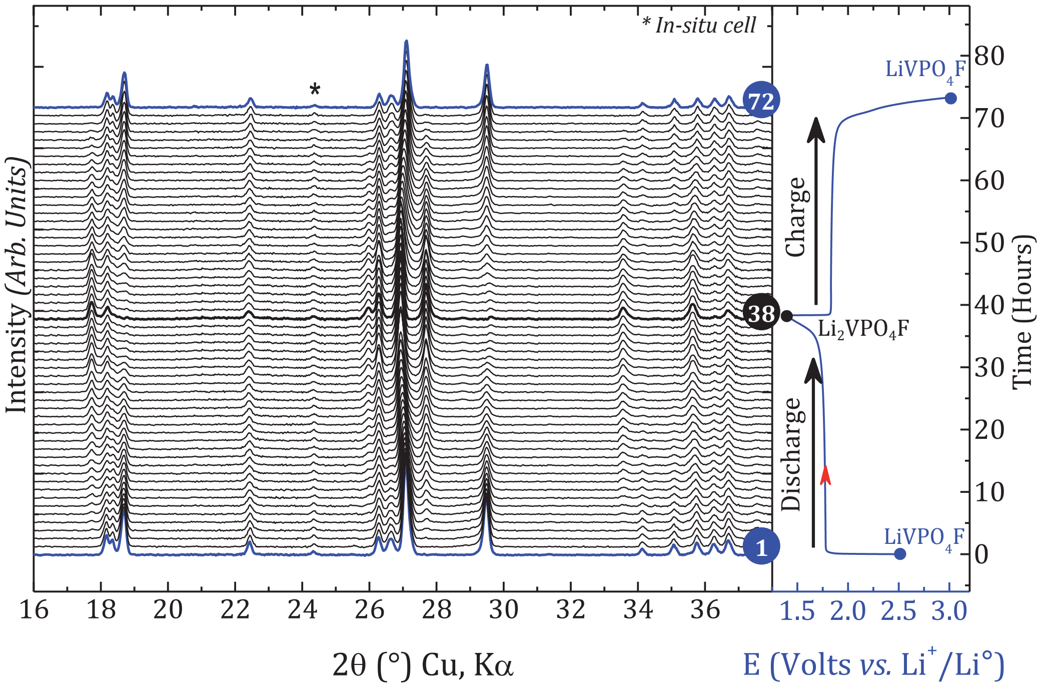

Figure II-7: 2D View of collected in-situ XRD patterns for the global electrochemical reaction $LiVPO_4F \Leftrightarrow Li_2VPO_4F$ (left) and corresponding galvanostatic cycling data (right). The XRD patterns highlighted in blue refer to $LiVPO_4F$ and the dark black one to Li_2VPO_4F

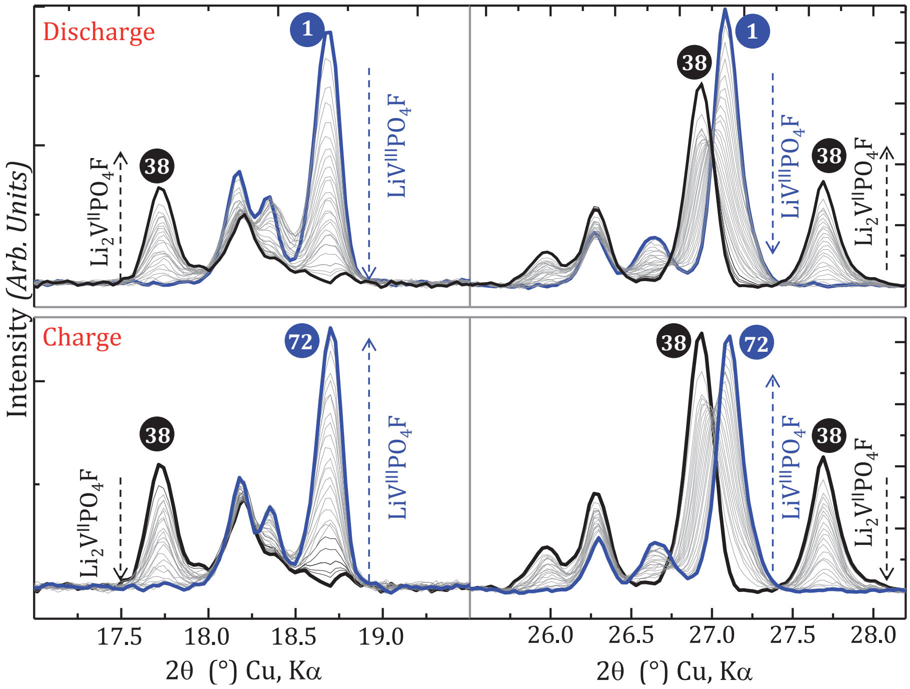

Figure II-8: Selected 2θ regions showing the respective growths and disappearances of the phases involved in the $LiVPO_4F \Leftrightarrow Li_2VPO_4F$ reaction.

A detailed *In situ* XRD experiment was performed in order to follow the mechanism of Li insertion/extraction into $LiVPO_4F$. As presented in Figure II-7 during the discharge of $LiVPO_4F$ from 2.5 V down to 1.5 V, all the diffraction peaks of the starting $LiVPO_4F$ phase, progressively vanish in a continuous manner. The diffraction peaks selected in the $17° \leq 2\theta \leq 19.5°$ and $25.5° \leq$

2θ ≤ 28° regions (Figure II-8) clearly illustrate the two-phase mechanism as none of them are shifted towards higher or lower 2θ diffraction angles.

Figure II-9 illustrates the appearance of the $(200)_{C2/c}$ peak of Li_2VPO_4F as a function of xLi$^+$ overall content. It shows an experimental (black dots line) deviation from the theoretical (dash-red line) increase intensity at midcharge. The decrease in the intensity of the $(110)_{P\bar{1}}$ peak of $LiVPO_4F$ (blue dots lines) fit with the theoretical.

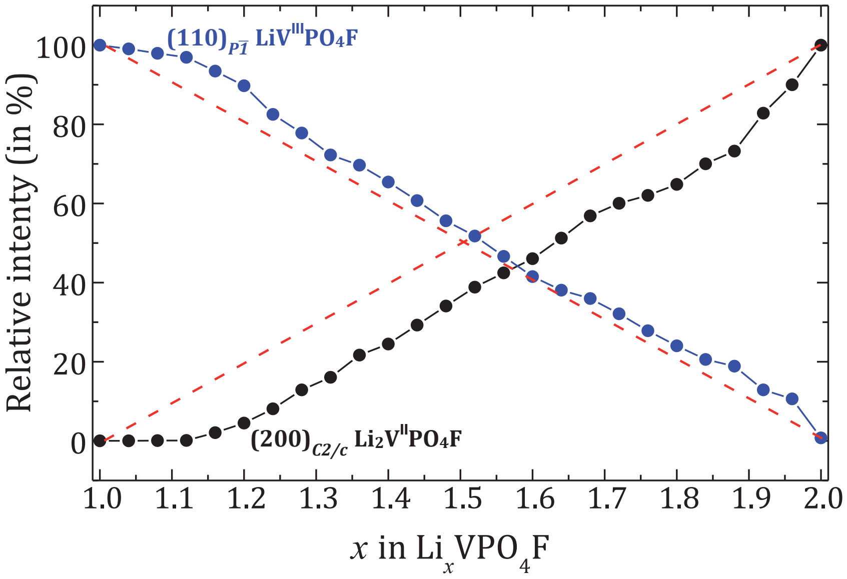

Figure II-9: variations of normalized intensities of the $(110)_{P\bar{1}}$ peak of $LiVPO_4F$ (blue) and the $(200)_{C2/c}$ peak of Li_2VPO_4F (red) as a function of x Li^+.

A possible occurrence of an amorphous phase might explain the apparent delay in the Li_2VPO_4F formation as also observed in the $LiFePO_4$–$FePO_4$ system [62, 63].

The refined lattice parameters of $LiVPO_4F$ before and after a full electrochemical cycle and the refined lattice parameters of Li_2VPO_4F are gathered in Figure II-10. The lattice parameters of the two $LiVPO_4F$ (the initial one and the fully charged one after a complete electrochemical cycling) are very similar and as expected, exhibit a V/Z lower than the one of Li_2VPO_4F (~87.5 Å^3 for $LiVPO_4F$ *vs.* ~93.8 Å^3 for Li_2VPO_4F). This is a consequence of the V^{2+} ionic radii (0.088 nm) which is bigger than the one of V^{3+} (0.074 nm).

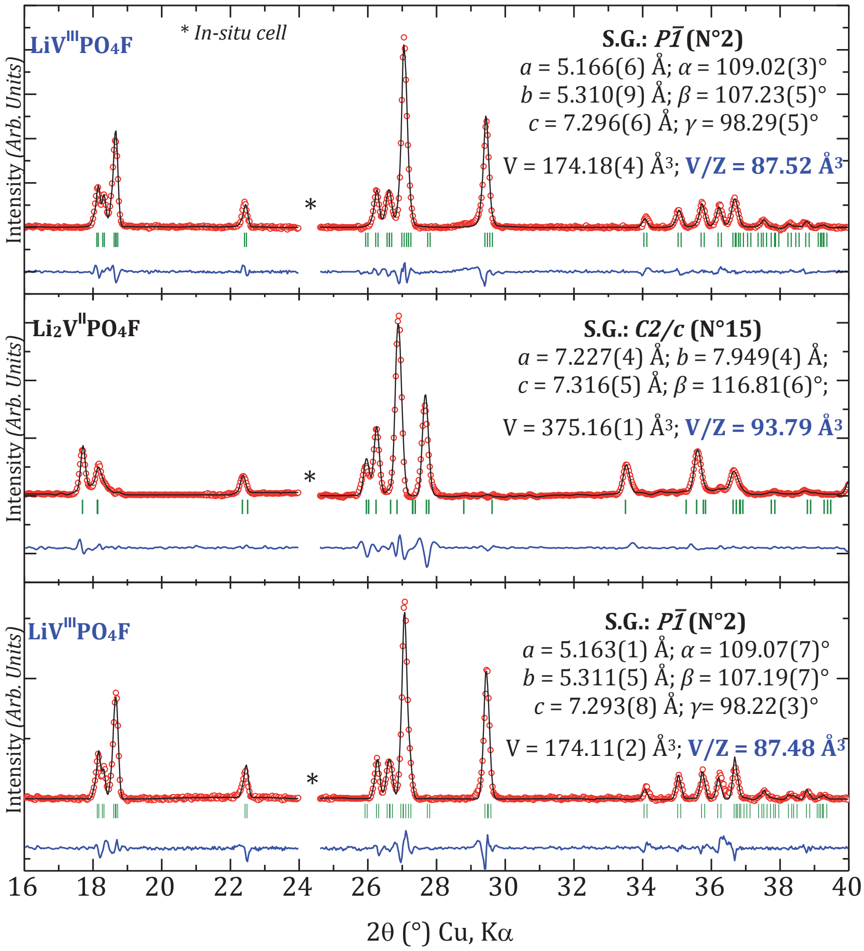

Figure II-10: XRD patterns and full-pattern matching refinements of initial $LiVPO_4F$, reduced Li_2VPO_4F and fully charge $LiVPO_4F$. The space groups, the lattice parameters and the volumes are inserted for each XRD pattern.

II-3b. Reversible Li^+ extraction from $LiVPO_4F$ (V^{4+}/V^{3+} couple)

Galvanostatic data of $LiVPO_4F$ have been recorded between 3 and 4.55 V at a rate of C/50 for 4 different samples (see Figure I-5 in chapter I), and presented in Figure II-11. $LiVPO_4F$ containing small amounts of α-$Li_3V_2(PO_4)_3$ as impurity, exhibited three small plateaus at potentials of 3.57 V, 3.65 V and 4.04 V *vs.* Li^+/Li (Figure II-11a), barely seen in the differential capacity curve. Those plateaus are located at the same potentials as those observed for α-$Li_3V_2(PO_4)_3$ [1, 3-5, 64]. F. Zhou et al. [24] who also obtained the α-$Li_3V_2(PO_4)_3$ as impurity during the synthesis of $LiVPO_4F$ also observed the same plateaus located at the same potentials.

Figure II-11b shows two galvanostatic electrochemical data: the blue one corresponds to $LiVPO_4F$ containing an unknown impurity (see Figure I-5b in chapter I) and the red one is the galvanostatic data of a material that had been washed with water (as described in chapter I). We note the absence of the three small plateaus previously observed, and a similarity between the two electrochemical data. Figure II-11c shows the electrochemical data of a pure $LiVPO_4F$

sample where the capacity at the end of charge (full Li extraction from $LiVPO_4F$) was 154 mAh/g. Note that pure $LiVPO_4F$ exhibited higher capacity on charge, but lower capacity on discharge. However the capacity retention recorded was the highest compared with other non-pure $LiVPO_4F$ powders.

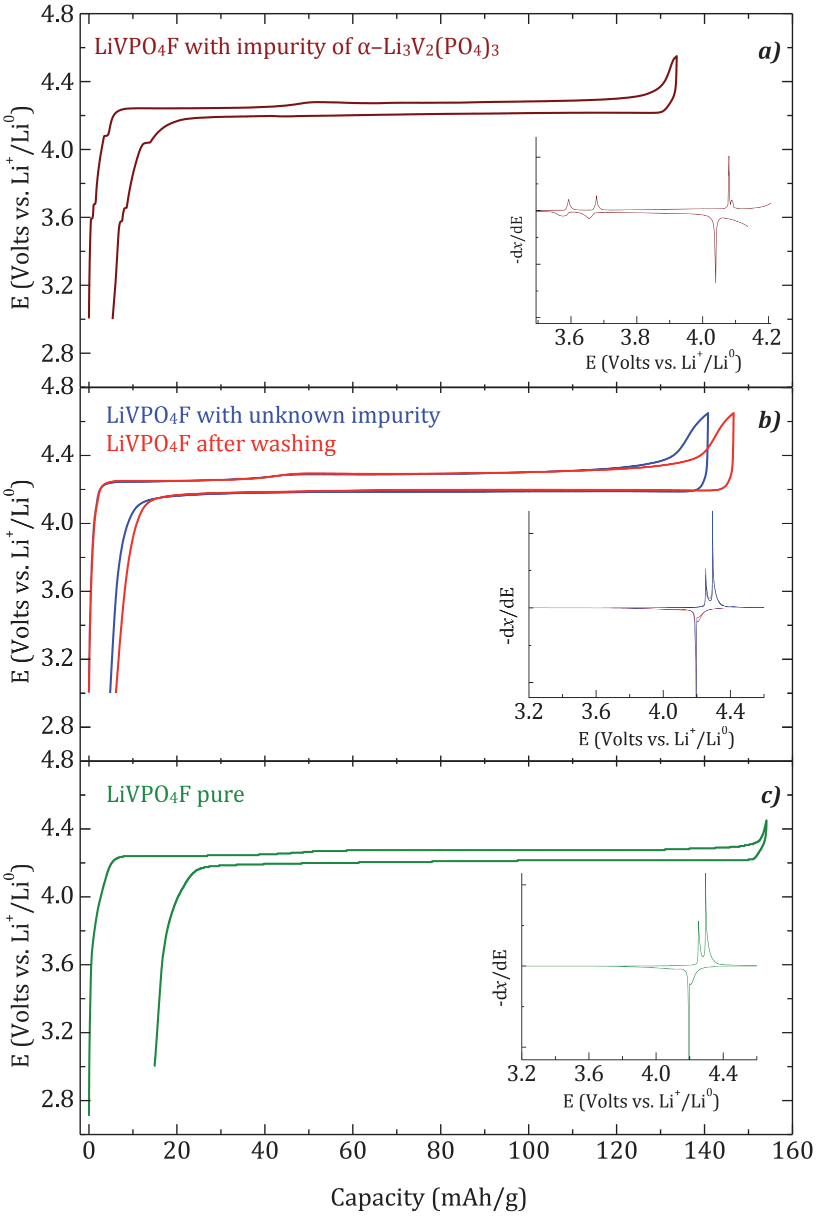

Figure II-11: Electrochemical behavior of different $LiVPO_4F$ samples cycled between 3.00–4.60 V vs. Li^+/Li at C/50: a) $LiVPO_4F$ samples containing α-$Li_3V_2(PO_4)_3$ as impurity, b) $LiVPO_4F$ sample containing an unknown impurity before (red) and after washing (blue), and c) pure $LiVPO_4F$

Figure II-12 exhibits the GITT measurement recorded during Li^+ extraction first from $LiVPO_4F$ performed in the same conditions as previously (for Li^+ insertion first into $LiVPO_4F$). Close inspection of the data indicated the presence of a small inflection at a relaxed potential of 4.25 V *vs.* Li^+/Li between two plateaus: a shorter one (1/3 Li) at 4.24 V and a longer one (2/3 Li) at 4.26 V *vs.* Li. J. Barker et. al. interpreted this inflection in the charge profile as the extraction of Li^+

from two energetically non-equivalent crystallographic sites within the $LiVPO_4F$ framework structure. Indeed, as the inflection point is observed at the composition $Li_{0.67}VPO_4F$, we could have expected the distribution of Lithium in two sites in the pristine material, with 1/3 Li in one site and 2/3 Li in the other site, and thus the preferential deintercalation of the first versus the second. Nevertheless, as discussed in Chapter I our structural study has shown that lithium occupies a single site in $LiVPO_4F$, which thus tends to rule out the interpretation proposed by J. Barker to explain that peculiar composition $Li_{0.67}VPO_4F$.

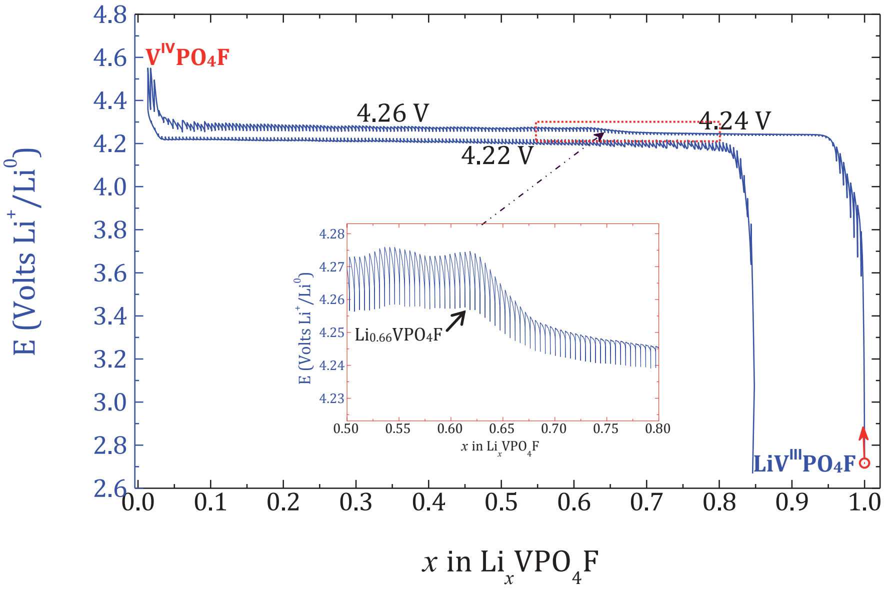

Figure II-12: GITT measurement of $LiVPO_4F$ between 2.7–4.55 V with a current rate of C/100. The relaxation condition was $dV/dt < 4$ mV/h

Several *in situ* XRD experiments were conducted in order to follow carefully the phase formations in the $LiVPO_4F \Leftrightarrow VPO_4F$ system. The *in situ* XRD and electrochemistry data related to a full charge/discharge cycle were gathered in Figure II-13 and Figure II-14. All phenomena are related to two-phase reactions:

- During the first part of the charge, the diffraction peaks of the starting $LiVPO_4F$ phase progressively vanish and new Bragg positions that cannot be indexed with the unit-cell parameters of the fully de-lithiated phase VPO_4F progressively grow. The XRD pattern, recorded at 1/3 of the charge (*i.e.* corresponding to a global composition of $Li_{0.67}VPO_4F$) is highlighted in green in Figure II-13 and Figure II-14 and can be fully indexed as a single phase. At this composition, the pristine phase $LiVPO_4F$ has completely disappeared. From $LiVPO_4F$ to $Li_{0.67}VPO_4F$, a two-phase mechanism is clearly demonstrated here.

① $LiVPO_4F \rightarrow Li_{0.67}VPO_4F + 0.33\ Li^+ + 0.33\ e^-$ $E_{①} = 4.24$ V *vs.* Li^+/Li

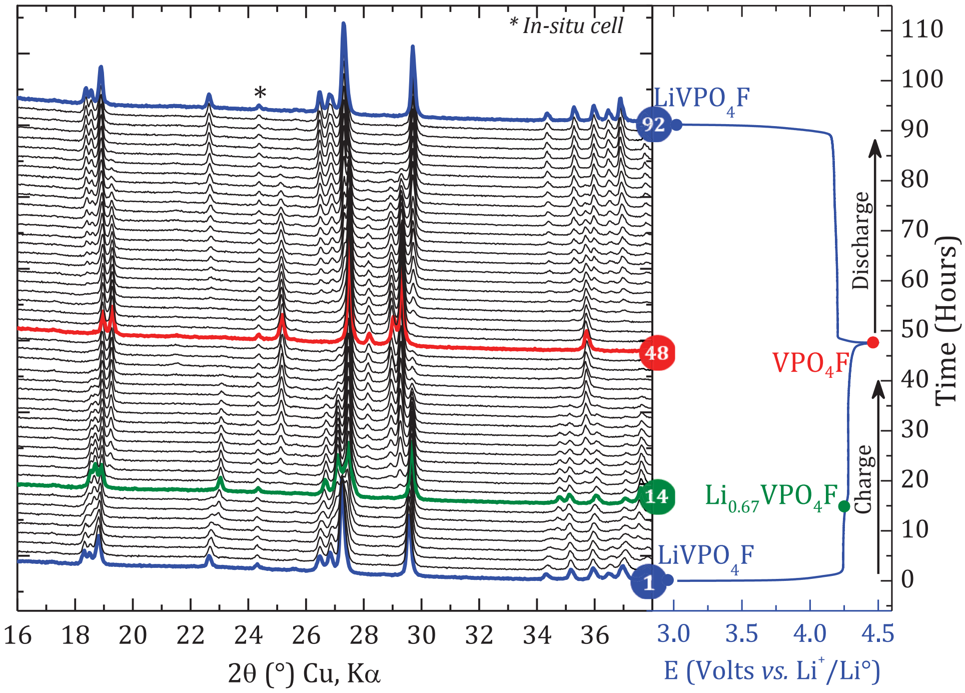

Figure II-13: 2D View of collected in-situ XRD patterns for the global electrochemical reaction $LiVPO_4F \Leftrightarrow VPO_4F$ (left) and corresponding galvanostatic cycling data (right). The XRD patterns highlighted refer to $LiVPO_4F$ (#1 and #92, blue), $Li_{0.67}VPO_4F$ (#14, green) and VPO_4F (#48, red).

- Upon further Li^+ extraction, a similar two-phase process occurs, this time between $Li_{0.67}VPO_4F$ and VPO_4F. The XRD data of the end-member (fully-oxidized VPO_4F phase) were refined in the *C2/c* space group (Figure II-15) and with a unit-cell per formula unit (V/Z) contraction of ~8 % *vs.* $LiVPO_4F$, in good agreement with B.L. Ellis [25]. This V/Z contraction is ~5% for the $LiFeSO_4F/FeSO_4F$ system that belongs to the Tavorite family as well [65, 66].

② $Li_{0.67}VPO_4F \rightarrow VPO_4F + 0.67\ Li^+ + 0.67\ e^-$ $E_{②} = 4.26$ V *vs.* Li^+/Li

- The Li^+ insertion into VPO_4F does not take the same reaction path as the Li^+ extraction from $LiVPO_4F$. Indeed, upon discharge, a single two-phase reaction takes place between VPO_4F and $LiVPO_4F$ with no occurrence (as clearly seen in Figure II-14) of the intermediate phase $Li_{0.67}VPO_4F$.

③ $VPO_4F + Li^+ + e^- \rightarrow LiVPO_4F + Li^+ + e^-$ $E_{③} = 4.22$ V *vs.* Li^+/Li

At the end of the full cycle, the diffraction pattern of the pristine $LiVPO_4F$ is fully re-covered apart from small global intensity changes.

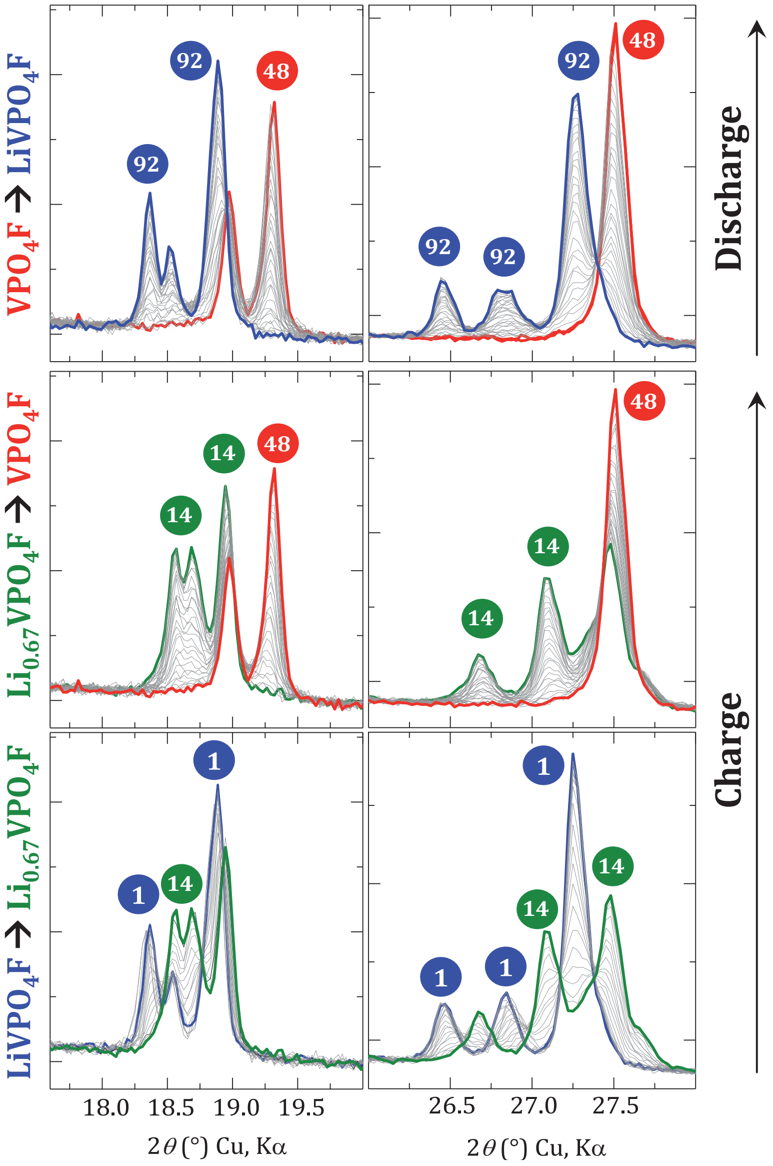

Figure II-14: Selected 2θ regions showing the respective growths and disappearance of the phases involved in the $LiVPO_4F$ ⇔ VPO_4F reaction. The XRD patterns highlighted refer to $LiVPO_4F$ (#1 and #92, blue), $Li_{0.67}VPO_4F$ (#14, green) and VPO_4F (#48, red).

Figure II-15 presents the full-pattern matching refinement of the phases $LiVPO_4F$, $Li_{0.67}VPO_4F$ and VPO_4F together with their space group and lattice parameters.

The overall reaction is pictured in Figure II-15 which includes the unit-cell volumes obtained by refinement of the two-phase XRD patterns. The unit-cell contraction of ~1.5 % between $LiVPO_4F$ and $Li_{0.67}VPO_4F$ is sufficient to trigger a well-defined two-phase reaction upon electrochemical oxidation. As a major result of this study, the peculiar composition "$Li_{0.67}VPO_4F$" pops up as a single phase during charge and as a two-phase mixture $0.33 \times VPO_4F + 0.67 \times LiVPO_4F$ during discharge.

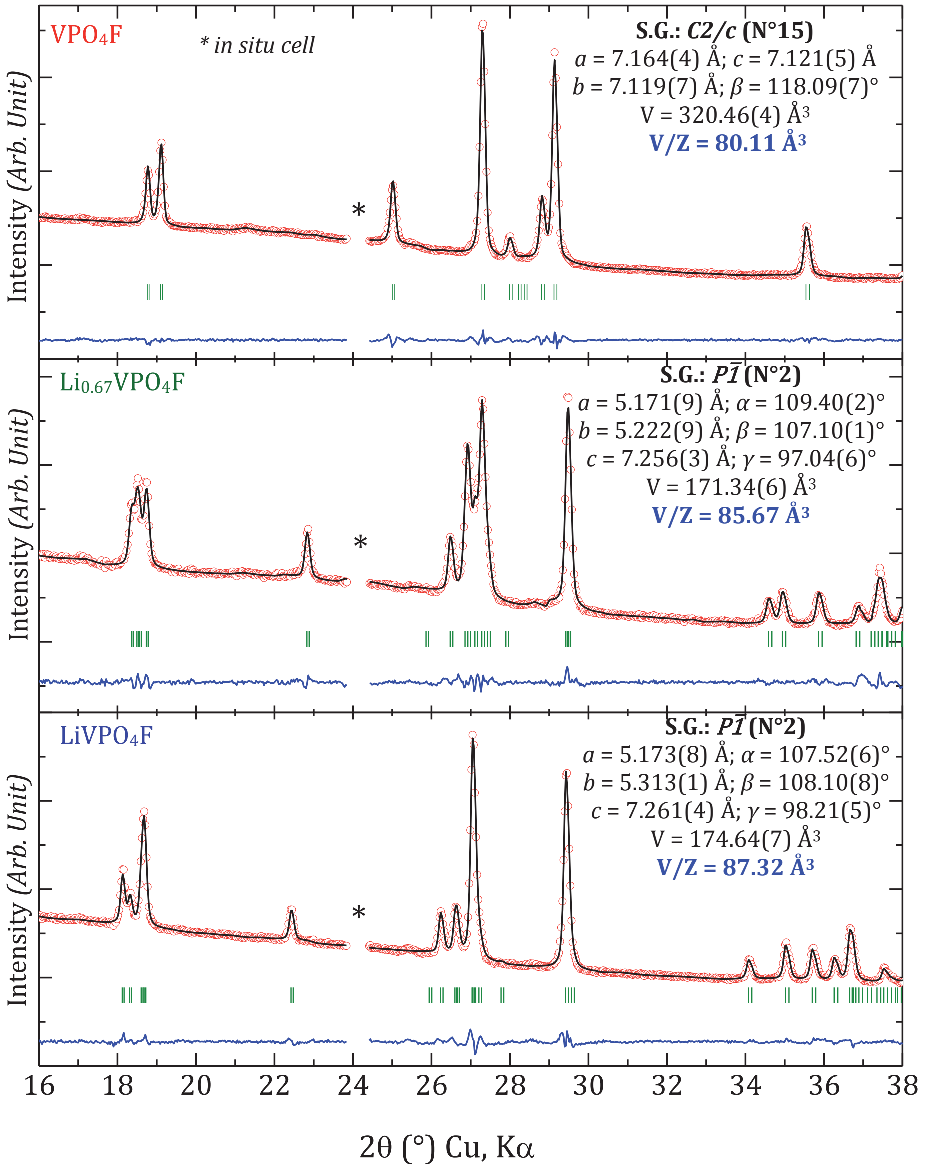

Figure II-15: Full-pattern matching refinements of $LiVPO_4F$, $Li_{0.67}VPO_4F$ and VPO_4F. The lattice parameters as well as the volumes are inserted in each XRD pattern.

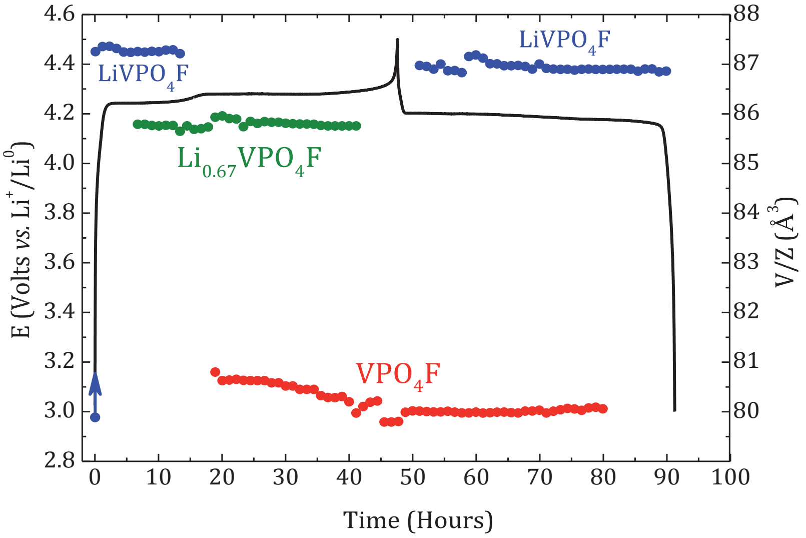

Figure II-16: Unit-cell volume changes during the global electrochemical reaction $LiVPO_4F \Leftrightarrow VPO_4F$ involving successive two-phase reactions.

This phenomenon of 2 plateaus in charge and 1 plateau in discharge was observed for all the further cycles of $LiVPO_4F$, as for the olivine $NaFePO_4$ [67, 68], for which two plateaus were observed in charge at a potential of 2.87 V and 2.97 V *vs.* Na^+/Na (with the formation of the intermediate phase $Na_{0.7}FePO_4$) and only one plateau in discharge. According to M. Casas-Cabanas, the formation of the intermediate phase would allow buffering the internal stresses due to a large cell mismatch between $NaFePO_4$ and $FePO_4$ (~18 % in volume) contrary to $LiFePO_4$ where no intermediate phase is formed as the contraction is only ~7 % between $LiFePO_4$ and $FePO_4$. Note that for the $LiVPO_4F \Leftrightarrow VPO_4F$ system, the contraction is only ~8 % (close to the one of $LiFePO_4 \Leftrightarrow FePO_4$ system), but yet an intermediate phase was observed.

Although a close inspection of the XRD pattern of $Li_{0.67}VPO_4F$ did not reveal visible superstructure reflections, we may suggest the existence of an ordered (charge ordering on vanadium sites and/or Li/vacancy) in this composition that will need further investigation, through e-diffraction at low temperature for instance.

A second series of *in situ* XRD experiments were undertaken to further check on the relative stabilities of the Li_xVPO_4F compositions.

- Upon charge for instance from $LiVPO_4F$ up to $Li_{0.67}VPO_4F$, the insertion of Li^+ into $Li_{0.67}VPO_4F$ led to the formation of $LiVPO_4F$ so that the reaction $Li_{0.67}VPO_4F \Leftrightarrow LiVPO_4F$ is fully reversible (Figure II-17).

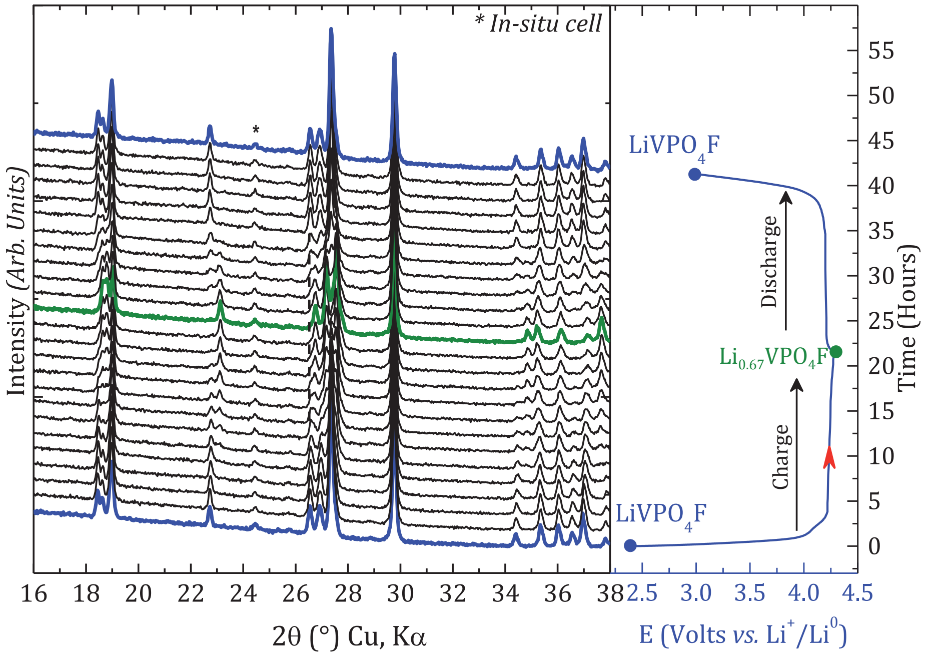

Figure II-17: Galvanostatic cycling of a Li/LP30/$LiVPO_4F$ cell cycled at C/75 (right) and in situ XRD recorded upon oxidation up to the global composition $Li_{0.67}VPO_4F$ and then back to $LiVPO_4F$ (left).

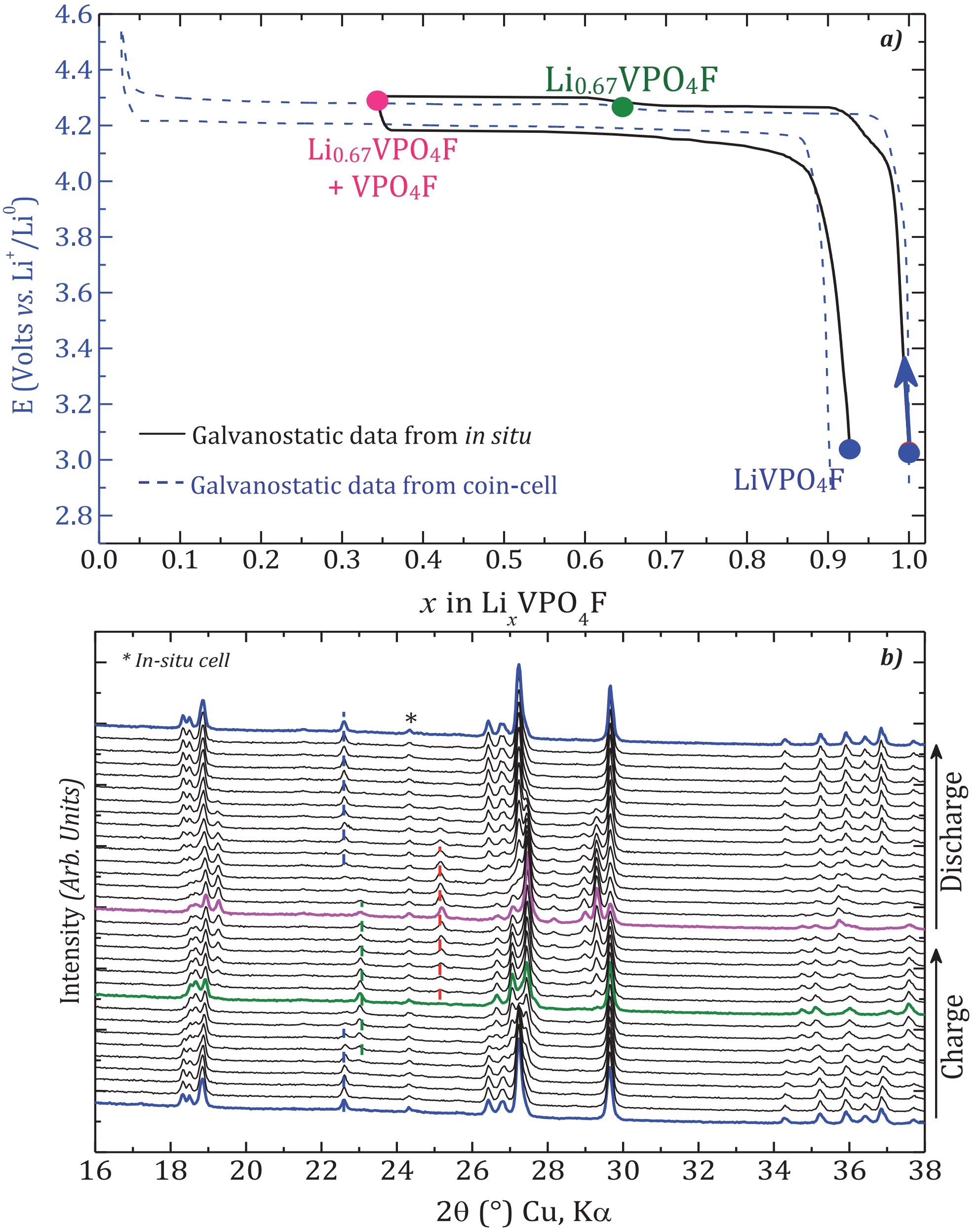

Figure II-18: a) Electrochemical data of a Li/LP30/LiVPO$_4$F cell cycled at C/50 for the present in situ (black line) and galvanostatic data recorded in coin cell (dash blue) b) in situ XRD patterns recorded upon oxidation up to the global composition Li$_{0.33}$VPO$_4$F and then back to LiVPO$_4$F.

- Upon charge from LiVPO$_4$F up to the middle of the second voltage plateau, *i.e.* up to a global composition "Li$_{0.33}$VPO$_4$F", the two phases Li$_{0.67}$VPO$_4$F and VPO$_4$F were present in equal proportions (pink XRD pattern in Figure II-18). Upon subsequent discharge from this two phase mixture, we found a puzzling mechanism that involves the progressive apparition of LiVPO$_4$F and the concomitant disappearance (at different paces) of both Li$_{0.67}$VPO$_4$F and VPO$_4$F. Even under the low discharge rate used for this *in situ* experiment, the consequence is that several XRD patterns actually revealed the presence of the three distinct phases of the system.

II-3c. Crystal Structures of Li_xVPO_4F (x = 2, 0.67, 0)

The Li_xVPO_4F compositions were obtained electrochemically in large battery cells in which ~600 mg of active material were casted on an aluminum foil. All along the charge (*resp.* discharge) process an intermittent galvanostatic experiment was performed with successive 1 hour charge (*resp.* discharge) periods at a rate of C/200 (*resp.* D/200) and 10 hour relaxation periods. Before stopping the batteries a chrono-amperometry was performed during 10 hours at potentials of 4.55 V, 4.25 V and 1.6 V corresponding to the formation of VPO_4F, $Li_{0.67}VPO_4F$ and Li_2VPO_4F respectively. Afterwards, the cycled powder was gently scratched from the aluminum foil current collector, washed with Dimethyl Carbonate (DMC) to get rid of the electrolyte and dried under vacuum. The obtained powder of Li_xVPO_4F was measured by XRD on a Panalytical diffractometer (X'Pert PRO MPD) and on the high resolution powder neutron diffractometer D2B of ILL-Grenoble in collaboration with E. Suard.

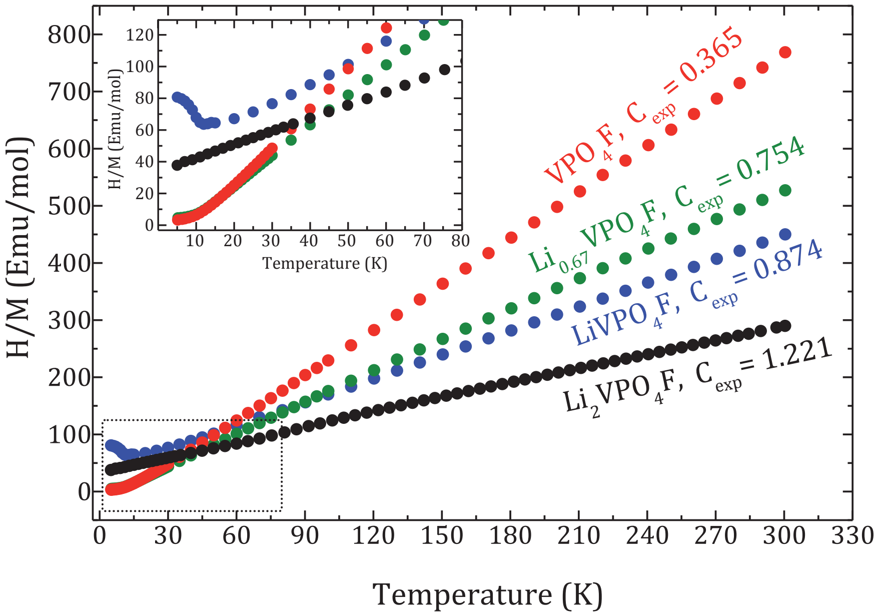

Figure II-19: Temperature dependence of the H/M ratio for Li_xVPO_4F (with x = 2, 1, 0.67 and 0)

The static molar magnetic susceptibilities of Li_xVPO_4F ($\chi(T) = M(T)/H$ (H = 1 T) with H as the magnetic field and M as the magnetization) were measured between 5 and 300 K using a SQUID magnetometer (Quantum Design). The zero field cooled χ values were obtained by cooling the sample in zero field down to 5 K and then heating them under the measuring field. The diamagnetic contributions were corrected using the atomic values from G.A. Bain and J.F. Berry [69] yielding the χ_M paramagnetic susceptibility contribution. The temperature dependence of the H/M ratio is displayed in Figure II-19 for Li_xVPO_4F (with x = 2, 1, 0.67 and 0). Contrary to $LiVPO_4F$ where a significant curvature was observed around 9 K indicating an antiferromagnetic behavior, no indication of the onset of antiferromagnetic ordering was observed for Li_2VPO_4F, $Li_{0.67}VPO_4F$ and VPO_4F so that the phases remained paramagnetic until very low temperature. The calculated Curie constants of $Li_{0.67}VPO_4F$ and VPO_4F were 0.754 and 0.365 respectively. Those values are close to the theoretical Curie values of $V^{3.33+}$ and V^{4+} which are 0.792 and 0.375 respectively. However, the experimental Curie constant of Li_2VPO_4F (C_{exp} = 1.221) was significantly different from the theoretical Curie values of V^{2+} (C_{theo} = 1.875) indicative of an oxidation of Li_2VPO_4F. Note that B.L. Ellis et al. [25] isolated Li_2VPO_4F and VPO_4F by chemical reduction and oxidation respectively. However, B.L. Ellis did not identify the intermediate $Li_{0.67}VPO_4F$.

i- Crystal Structure of VPO$_4$F

The simultaneous refinements of XRD and neutron diffraction data were carried out based on the published structure of $FeSO_4F$ [70] (Figure II-20).

The recorded lattice parameters and atomic positions are gathered in ANNEX I table II-1. Neutron diffraction data were not relevant for the Rietveld refinement of VPO_4F due to the same coherent diffusion wavelength of oxygen ($\lambda_{coh,O}$ = $0.58 \cdot 10^{-4}$ Å [71]) and fluorine ($\lambda_{coh,F}$ = $0.56 \cdot 10^{-4}$ Å [71]) and to the transparency of vanadium towards neutron diffraction. Moreover, the ratio of signal intensity over background for our recorded neutron diffraction data is 1.6, that is much lower than for $LiVPO_4F$ (2.7) and $LiVPO_4O$ (4.5). Nevertheless, the XRD data were suitable for the determination of the structure of VPO_4F which is related to the $LiVPO_4F$ parent. The unique site of vanadium lies within a $[VO_4F_2]$ octahedron which is more distorted than the octahedra in $LiVPO_4F$ ($3.98 \cdot 10^{-5}$ and $2.28 \cdot 10^{-5}$ for $LiVPO_4F$ *vs.* $6.23 \cdot 10^{-4}$ for VPO_4F). The V–F distances along the chain of $[VO_4F_2]$ octahedra are 1.96 Å longer than in the structure of VPO_4F, reported by B.L. Ellis (1.92 Å). The average P–O distances in $[PO_4]$ tetrahedra is shorter in VPO_4F (1.48 Å) than in $LiVPO_4F$ (1.53 Å) and the tetrahedron $[PO_4]$ in VPO_4F is more symmetric than in $LiVPO_4F$ ($\Delta = 1.02 \cdot 10^{-4}$ in VPO_4F *vs.* $\Delta = 2.22 \cdot 10^{-4}$ in $LiVPO_4F$).

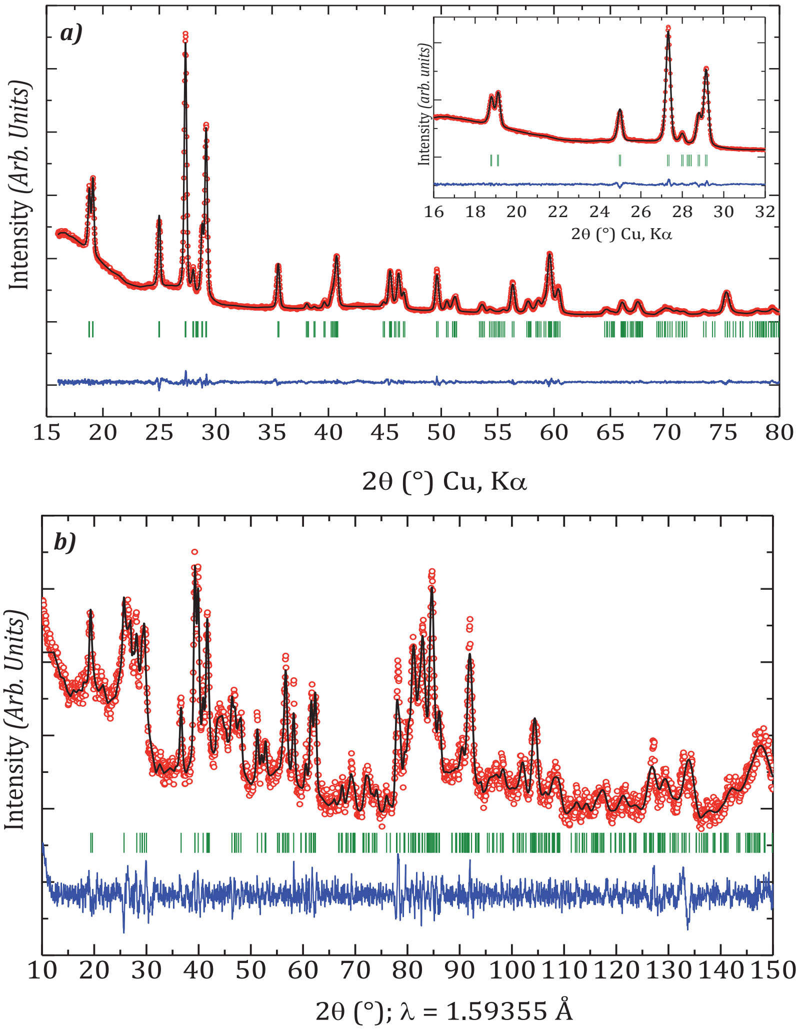

Figure II-20: Observed (red dots), calculated (black line), and difference (blue line) plots obtained for the Rietveld refinement of X-ray diffraction data (a) and neutron diffraction data for VPO_4F (b)

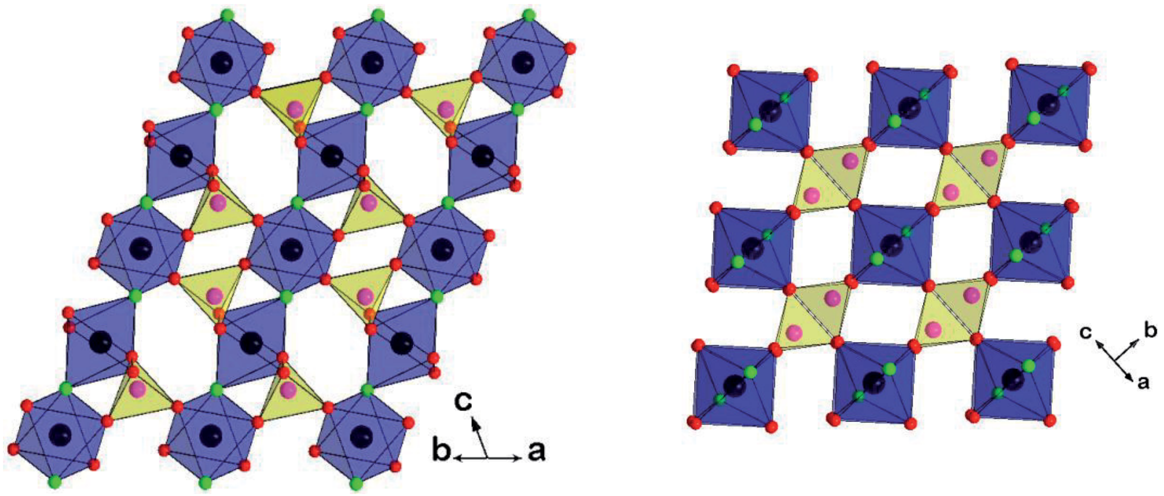

Figure II-21: Representation of VPO_4F skeleton framework structure in the $[001]_{C2/c}$ (left) and $[101]_{C2/c}$ (right) directions

ii- Hypothesis on the structure of $Li_{0.67}VPO_4F$

Both XRD and neutron diffraction data were successfully refined in full-pattern matching (Figure II-) in the $P\bar{1}$ space group. The obtained lattice parameters were: a = 5.240(8) Å; b = 5.192(6) Å; c = 7.273(1) Å; α = 109.156(9)°; β = 107.294(7)° γ = 96.999(2)°, with a volume V = 173.15(1) Å^3. $Li_{0.67}VPO_4F$ had never been reported before in the literature. Electron diffraction experiments were performed (in collaboration with F. Weill from ICMCB) on a JEOL JEM 2100 on a sample prepared by milling the powder sample in ethanol. A drop of the resulting suspension was cast onto a copper grid covered with carbon films. Figure II-22 gives representative electron diffraction patterns of $Li_{0.67}VPO_4F$ which are indexed in $P\bar{1}$. The obtained parameters are consistent with those found with full-pattern matching refinement of XRD and neutron diffraction data. No super-lattice reflections were observed.

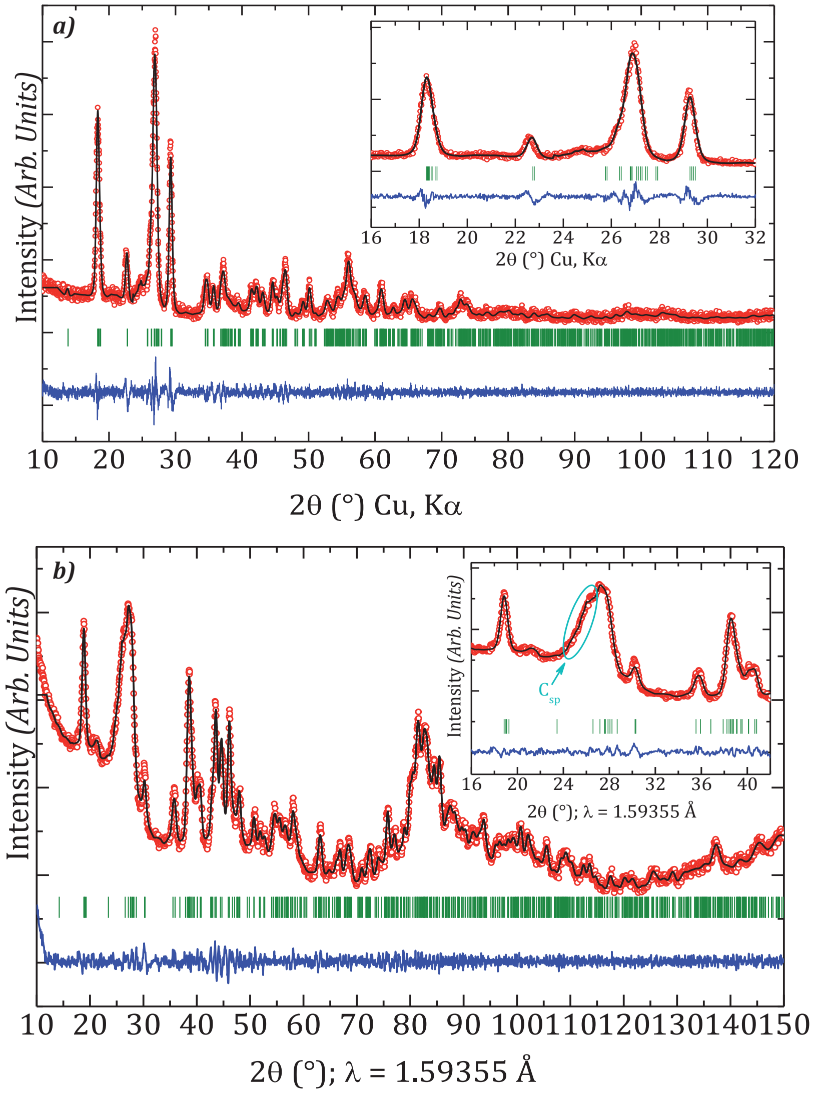

Figure II-22: Observed (red dots), calculated (black line), and difference (blue line) plots obtained for the Rietveld refinement of (a) X-ray diffraction data and (b) neutron diffraction data for $Li_{0.67}VPO_4F$

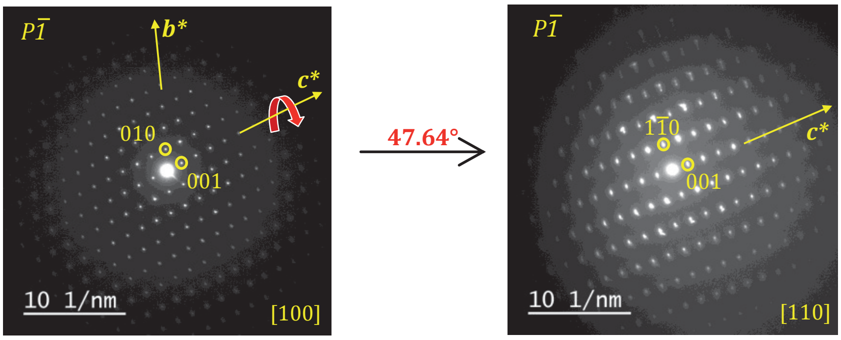

Figure II-22: Electron diffraction patterns of LiVPO$_4$F obtained by rotation around a common direction

iii- Structure of Li$_2$VPO$_4$F

It was difficult to solve the structure of Li$_2$VPO$_4$F due to its high air sensitivity. Indeed, we observed an evolution of the XRD pattern (Figure II-23) even though the material was stored in a dry glove box filled with Ar. The lattice parameters obtained at the end of "oxidation" of Li$_2$VPO$_4$F were very close to those of the pristine LiVPO$_4$F (insert in Figure II-23).

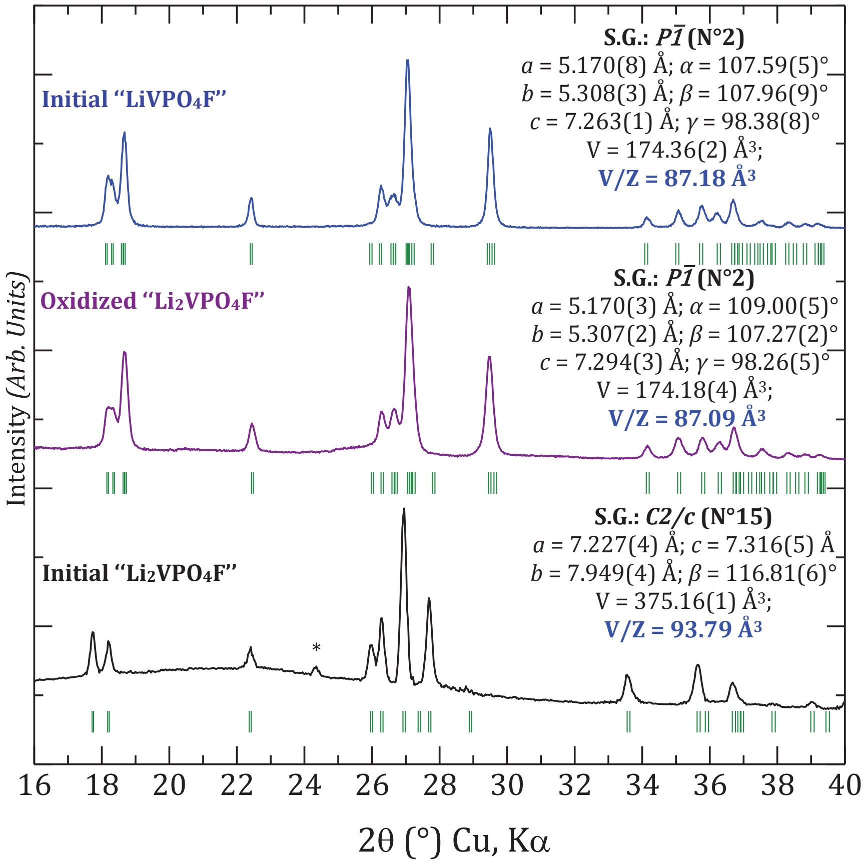

Figure II-23: XRD of Li$_2$VPO$_4$F obtained by chemical lithiation (black) and the product of oxidation of Li$_2$VPO$_4$F (purple) compared with the pristine LiVPO$_4$F (blue). The corresponding Bragg positions are given under each peak.

As the reduction potential of H_2O is higher (~3.45 vs. Li^+/Li) than the one of Li_2VPO_4F (1.81 V *vs.* Li^+/Li), it is thermodynamically favorable to withdraw Li^+ from the host structure when it is exposed to air, leading to LiOH and/or Li_2O which further react with CO_2 to yield Li_2CO_3. The corresponding reaction can be written as:

④ $2\ Li_2VPO_4F + \frac{1}{2}\ O_2 + H_2O \rightarrow 2\ LiVPO_4F + 2\ LiOH$

⑤ $2\ LiOH + CO_2 \rightarrow Li_2CO_3 + H_2O$

To the best of our knowledge, the stability of Li_2VPO_4F had never been reported before. Our second attempt to obtain Li_2VPO_4F was done by chemical lithiation using $LiAlH_4$ as the reducing agent, dissolved in tetrahydrofuran (THF). To this end, stoichiometric proportions of $LiVPO_4F$ and $LiAlH_4$ were mixed in THF. To enable complete $LiVPO_4F$ reduction, a 5 wt % mass excess of $LiAlH_4$ was used. The reaction was stirred during 24 hours, rinsed with THF and dried under vacuum. The XRD pattern of the obtained powder has been successfully indexed in the *C2/c* space group (with the lattice parameters of a = 7.225(4) Å; b = 7.945(2) Å; c = 7.304(5) Å; β = 116.771(1)° and V = 374.381(3) Å^3) contrary to the pristine Tavorite-type $LiVPO_4F$ (which crystallizes in the space group $P\bar{1}$) and in agreement with B.L. Ellis et al. [25] (Figure II-24). Note that no residual peaks of pristine $LiVPO_4F$ were present and therefore, the obtained Li_2VPO_4F was found pure.

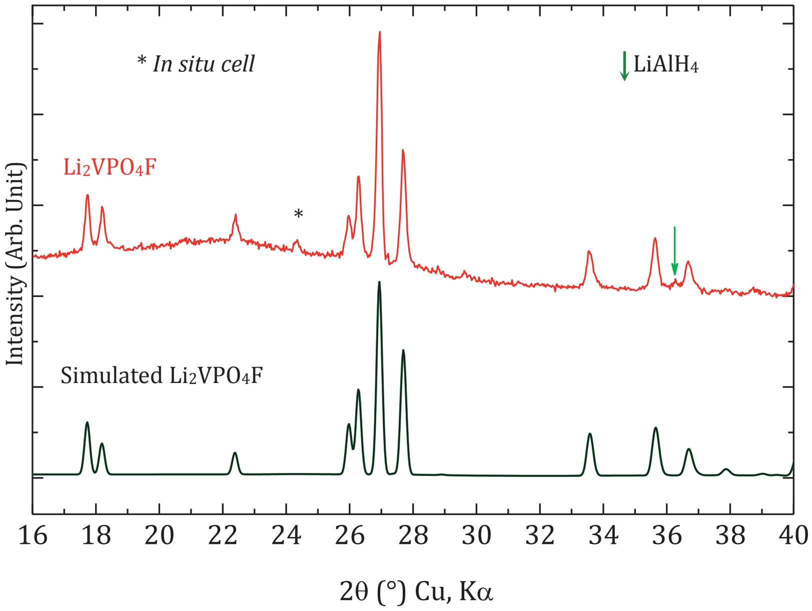

Figure II-24: XRD pattern of Li_2VPO_4F obtained by chemical lithiation in comparison with the simulated pattern of Li_2VPO_4F as published by B.L. Ellis et al. [25] .

The refinement revealed an expansion of 7.58 % for the V/Z value, slightly lower than for the $LiFePO_4F$/Li_2FePO_4F system (8.84 %). Contrary to $LiVPO_4F$, Li_2VPO_4F exhibits only one crystallographic site for vanadium and two distinct crystallographic sites for Li. Similar transitions from triclinic to monoclinic system had been reported for Tavorite-like structure such as $LiFePO_4F$ ($P\bar{1}$) *vs.* Li_2FePO_4F ($C2/c$) [72].

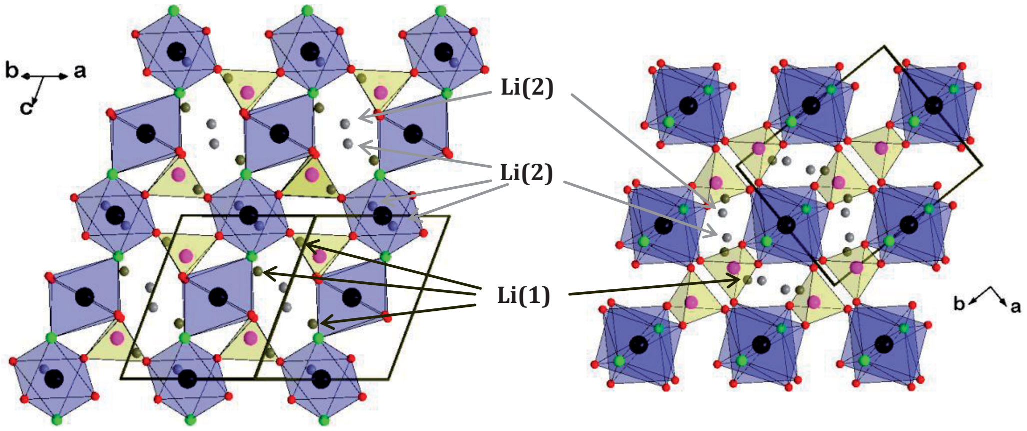

Figure II-25: Skeleton representation of Li_2VPO_4F structure.

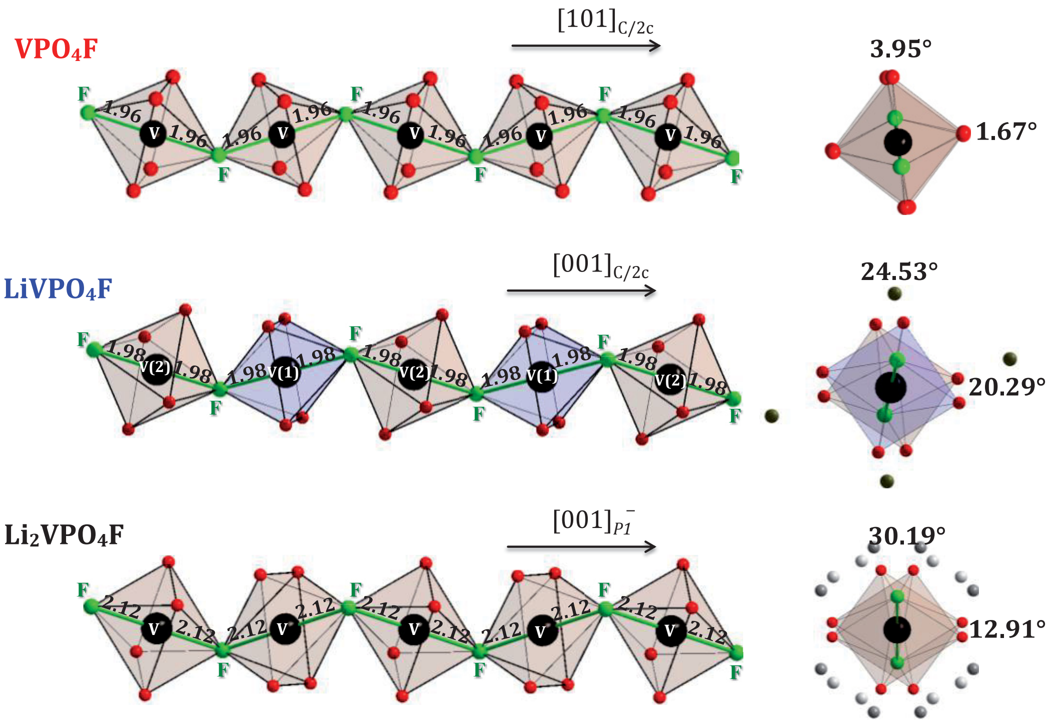

Figure II-26: Comparative distances and dihedral angles in the structure of Li_2VPO_4F, $LiVPO_4F$ and VPO_4F.

As mentioned above, both structures of Li_2VPO_4F and VPO_4F (and in a larger extend $Li_{0.67}VPO_4F$) are related to the Tavorite $LiVPO_4F$ but some differences are spotted such as the V-F distances along their respective chains. Indeed V–F distances in Li_2VPO_4F are 2.12 Å, which move down to 1.98 Å in $LiVPO_4F$ and finally shrink to 1.96 Å for VPO_4F. This evolution is consistent with that of the vanadium ionic radius which decreases from V^{2+} (0.088 nm) in Li_2VPO_4F to V^{3+} (0.074 nm) in $LiVPO_4F$ and being smaller for V^{4+} (0.063 nm) VPO_4F. Interestingly, the dihedral angles along the octahedra $[VO_4F_2]$ chains increase with the presence of Li, so that the presence of Li in the host structure leads to a higher tilt of dihedral angles (Figure II-26). This is not surprising since the presence of lithium induces steric constraints in the host structure and electrostatic repulsions.

iv- Comparative NMR Study of Li_xVPO_4F phases (with x = 1, 0.67 and 0)

^7Li MAS NMR, ^{31}P MAS NMR and ^{19}F MAS NMR experiments were performed in the same conditions as in chapter I. The sample holder (rotor) was filled in an Ar filled glove box in order to avoid a possible air and/or humidity contamination.

Although VPO_4F was supposed to be fully delithiated, the ^7Li MAS NMR spectrum of VPO_4F exhibits 3 tiny signals (red in Figure II-27). The signal at around -2 ppm is assigned to the “SEI” layer and is also present in $Li_{0.67}VPO_4F$ (green in Figure II-27). The small signal at around 116 ppm is similar to that of the pristine $LiVPO_4F$ (blue in Figure II-27) probably due to the presence of some unreacted $LiVPO_4F$. For $Li_{0.67}VPO_4F$, the ^7Li MAS NMR spectrum shows at least 4 signals in addition to a 116 ppm contribution, arising most probably again from unreacted $LiVPO_4F$, and the SEI signal. The 4 signals show the existence of different types of environment for Li. It is very likely that this corresponds to some kind of charge ordering in the material, and further NMR experiments are in progress to investigate this.

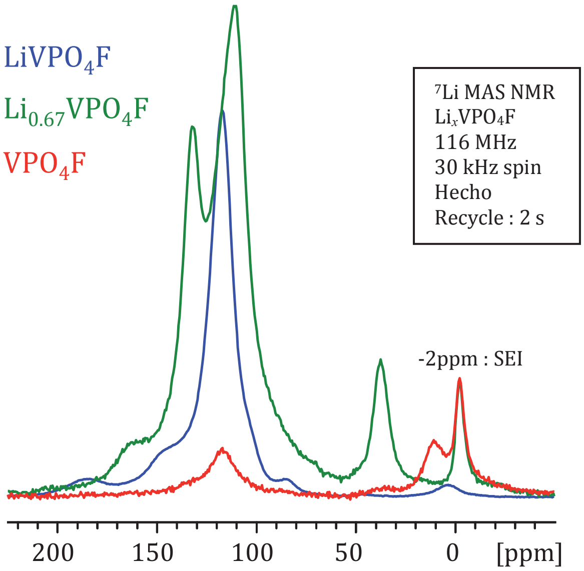

Figure II-27: ^7Li MAS NMR spectra of pristine $LiVPO_4F$ (blue), intermediate $Li_{0.67}VPO_4F$ (green) and fully delithiated VPO_4F (red) The magnitude is scaled to the mass of active material in the NMR rotor.

The ^{31}P MAS NMR spectra of the deintercalated compounds show a narrow contribution close to (-2.6 ppm), due to traces of the $LiPF_6$ salt from the electrolytes and/or decomposition products of the anion in the "SEI". VPO_4F (red Figure II-28) shows a major signal at around 2225 ppm in agreement with the unique site of phosphorous in the VPO_4F structure. This signal is less shifted compared to the one of $LiVPO_4F$ (4000 ppm, blue in Figure II-28) due in first approximation to the higher oxidation state of vanadium which provides less spin transfer to the phosphorous site. In the case of $Li_{0.67}VPO_4F$ (green in Figure II-28), 3 signals are observed, two of which are reminiscent of the extreme $LiVPO_4F$ and VPO_4F compositions. The analysis of these signals indeed requires further investigations, but it seems that the P nuclei feel environments (again, mostly in terms of electronic configuration of the neighboring V ions) similar to those of the extreme compositions plus one kind of intermediate environment. In first approximation, this is also consistent with the picture of a –at least local– charge ordering.

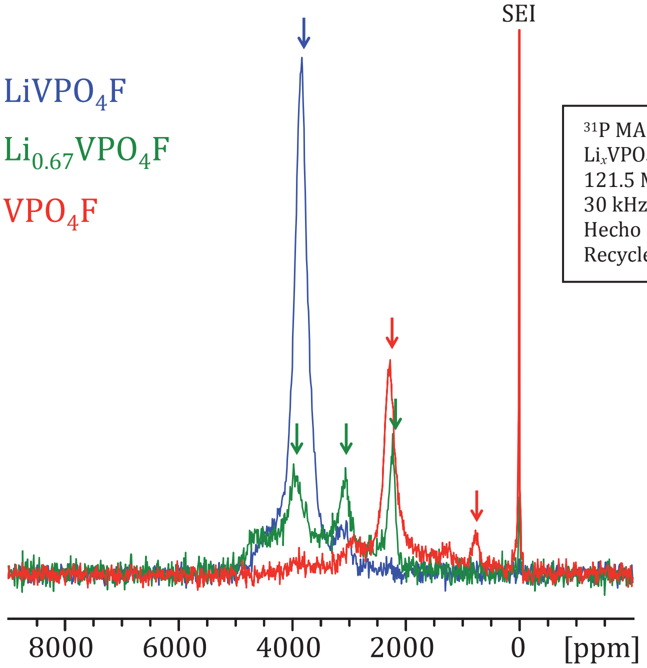

***Figure II-28:** ^{31}P MAS NMR spectra of pure $LiVPO_4F$ (blue), intermediate $Li_{0.67}VPO_4F$ (green) and fully delithiated VPO_4F (red). Due to the existence of spinning side bands for each contribution, the main isotropic contributions are marked by arrows.*

^{1}H MAS NMR spectra were recorded on a Bruker Avance III spectrometer with a 2.35 T magnet (100 MHz resonance frequency for ^{1}H), using a standard Bruker 2.5 MAS probe at a 30 kHz typical spinning speed. A Hahn echo sequence was used with a 90° pulse of 1.1 microsecond. A recycle delay was 1s. The 0 ppm external reference used was tetramethylsilane (TMS).

The ^{1}H MAS NMR spectra of the charged materials are compared to that of the pristine $LiVPO_4F$ in Figure II-29. The signal for the pristine compound is virtually negligible in magnitude, whereas distinct contributions appear for the two deintercalated compounds. It is therefore likely that, during the charge process, some electrolyte decomposition occurs and generates H^+ ions that can exchange with Li^+ in the material. This parasitic electrochemical process also explains why some Li remained in the "fully" charged material.

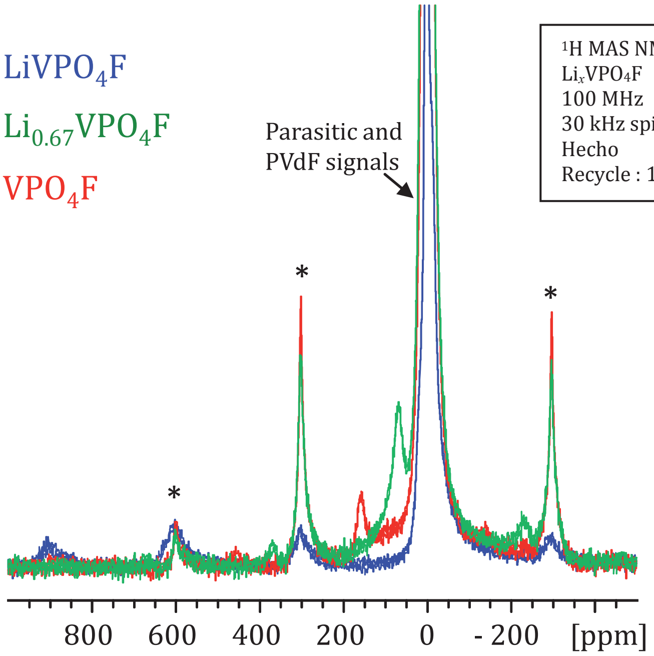

Figure II-29: ^{1}H MAS NMR spectra of pure LiVPO$_4$F (blue), intermediate Li$_{0.67}$VPO$_4$F (green) and fully delithiated VPO$_4$F (red) (spinning sidebands are marked by asterisks)

II-3d. Conclusion

This electrochemical study of LiVPO$_4$F provides a first complete visualization of phases formed during Li^+ electrochemical extraction/insertion at ~4.25 V and 1.8 V *vs.* Li into/from the LiVPO$_4$F structure.

Between 1.5–3.0 V vs. Li^+/Li, LiVPO$_4$F can accommodate Li^+ in its host structure through a biphasic mechanism which leads to the formation of Li$_2$VPO$_4$F. The reduction of V^{3+} to V^{2+} occurs at a potential of 1.81 V *vs.* Li^+/Li with a very small polarization of ~15 mV. The obtained Li$_2$VPO$_4$F crystallizes in the *C2/c* space group and was found to be highly sensitive to moisture.

The extraction of Li^+ from LiVPO$_4$F proceeds through two plateaus and reveals the formation of an intermediate Li$_{0.67}$VPO$_4$F which XRD is completely different from those of LiVPO$_4$F and VPO$_4$F. The two associated electrochemical oxidation plateaus are extremely close to each other, located at 4.24 V and 4.26 V *vs.* Li^+/Li. Surprisingly, subsequent lithium insertion in VPO$_4$F proceeds without any intermediate but at the composition of "Li$_{0.67}$VPO$_4$F" we observed 2 phases instead of one single phase (Figure II-30). This overall mechanism (two phases during charge and one during subsequent discharge) has to be tackled by DFT calculation in order to model the activation energies in both cases. Low temperature e-diffraction for both Li$_{0.67}$VPO$_4$F and "Li$_{0.67}$VPO$_4$F" are planned in our group.

In all the reactions involved, two-phase mechanisms were systematically encountered, without noticeable modifications of the [VPO$_4$F] framework besides significant unit-cell contractions/expansions and overall shifts in symmetry from triclinic $P\bar{1}$ to monoclinic $C2/c$. The overall electrochemical reactions are topotactic and are associated with very small polarization.

LiVPO$_4$F	**Li$_{0.67}$VPO$_4$F**	**VPO$_4$F**
S.G.: $P\bar{1}$ (N°2)	S.G.: $P\bar{1}$ (N°2)	S.G.: $C2/c$ (N°15)
a = 5.173(5) Å; α = 108.98(3)° b = 5.310(1) Å; β = 107.18(7)° c = 7.298(1) Å; γ = 98.30(6)°	a = 5.166(5) Å; α = 109.44(2) ° b = 5.222(4) Å; β = 107.08(2) ° c = 7.253(8) Å; γ = 97.07(3) °	a = 7.172(7) Å; b = 7.348(4) Å c = 7.136(1) Å; b = 121.21(9)°
V = 174.59(8) Å^3 **V/Z = 87.29 Å^3**	V = 171.022(3) Å^3 **V/Z = 85.51 Å^3**	V = 321.67(1) Å^3 **V/Z = 80.42 Å^3**

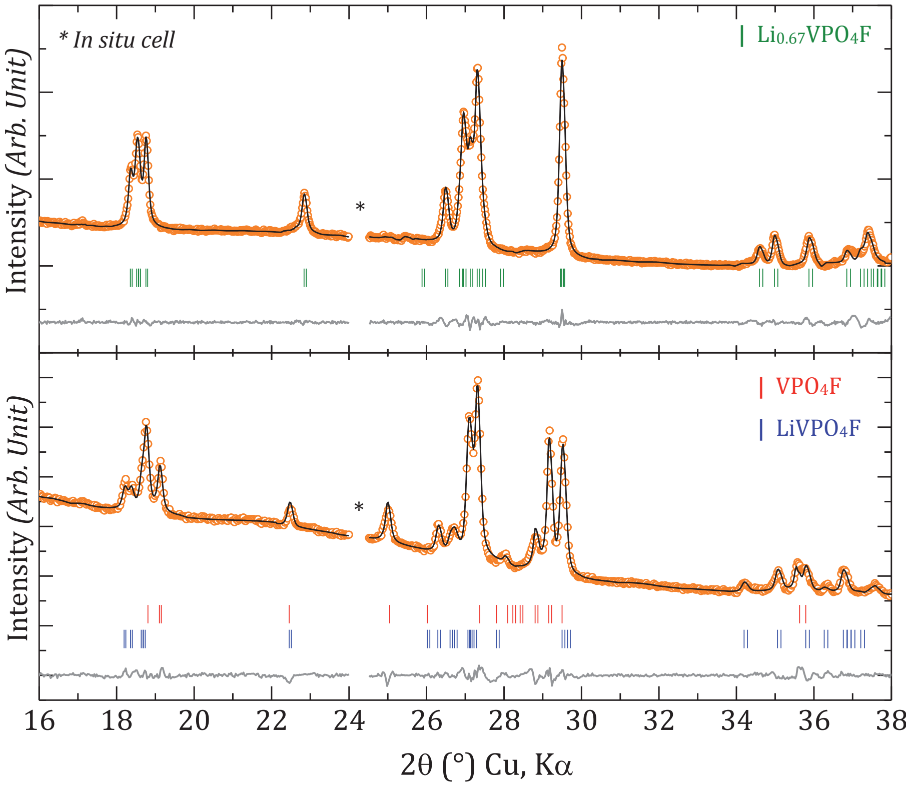

Figure II-30: X-Ray diffraction patterns and full-pattern matching refinements of the global composition "Li$_{0.67}$VPO$_4$F" obtained as a single phase during oxidation (top) and as a two-phase mixture during reduction (bottom)

II-4. ELECTROCHEMICAL BEHAVIOR OF $LiVPO_4O$

The lithium-ion extraction/insertion reaction from $LiVPO_4O$, in the upper voltage range, relies on the reversibility of the V^{5+}/V^{4+} redox couple, and the lithium insertion/extraction reaction in the lower voltage range relies on the reversibility of the V^{4+}/V^{3+} redox couple. The two electrochemical reactions associated can be summarized as:

$LiV^{IV}PO_4O \rightarrow V^{V}PO_4O + Li^+ + e^-$ Theoretical capacity: 159 mAh/g

$LiV^{IV}PO_4O + Li^+ + e^- \rightarrow Li_2V^{III}PO_4O$ Theoretical capacity: 159 mAh/g

$LiVPO_4O$ was cycled between 1.6 V and 4.5 V (Figure II-31) so as to involve the two redox couples of V^{5+}/V^{4+} and V^{4+}/V^{3+}. Although a good reproducibility of each galvanostatic cycling was obtained, one can notice that only 0.5 Li^+ was exchanged between 3.0–4.55 V (Li^+ extraction from $LiVPO_4O$). Nevertheless, between 3.0–1.6 V (Li^+ insertion into $LiVPO_4O$), one Li was inserted in the $LiVPO_4O$ framework leading to a composition close to Li_2VPO_4O.

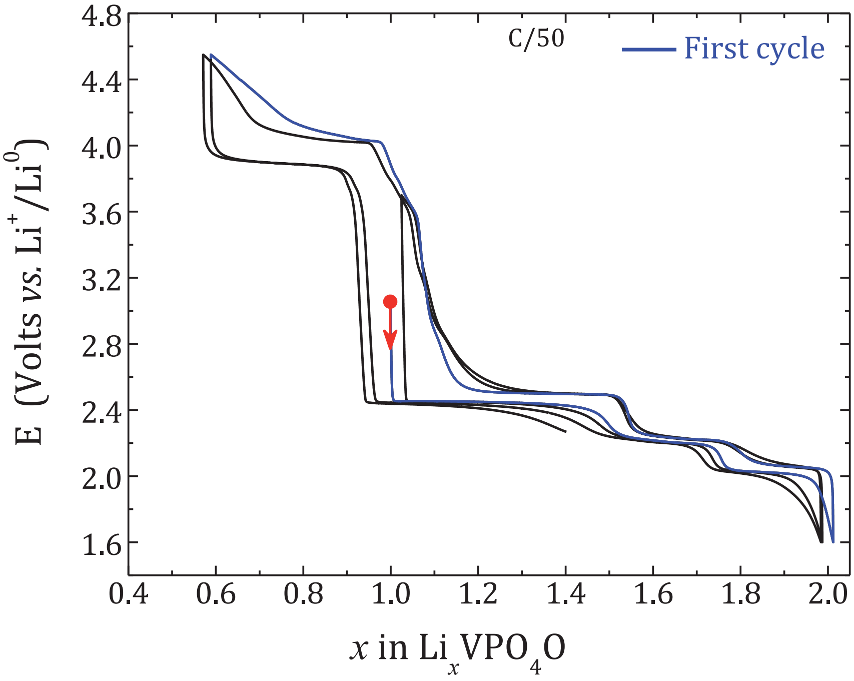

Figure II-31: Galvanostatic cycling from 1.6 V–4.5 V vs. Li^+/Li at C/50 of $LiVPO_4O|LP30|Li$ cell.

The understanding of the mechanisms of Li^+ insertion/extraction (between 3.0–1.6 V) and Li extraction/insertion (between 3.0–4.55 V) in $LiVPO_4O$ will be discussed in this section.

II-4a. Reversible Li^+ insertion into $LiVPO_4O$ (V^{3+}/V^{4+} couple)

We have shown for the first time that the framework structure of $LiVPO_4O$ can accommodate up to one Li with a capacity very close to the theoretical one (158 mAh/g). The electrochemical formation of Li_2VPO_4O from $LiVPO_4O$ was possible through 2 intermediate phases of compositions $Li_{1.5}VPO_4O$ and $Li_{1.75}VPO_4O$ leading to three reversible reactions summarized as:

⑥ $LiV^{IV}PO_4O + 0.5\,Li^+ + 0.5\,e^- \rightarrow Li_{1.5}V^{3.5}PO_4O$

⑦ $Li_{1.5}VPO_4O + 0.25\,Li^+ + 0.25\,e^- \rightarrow Li_{1.75}V^{3.25}PO_4O$

⑧ $Li_{1.75}VPO_4O + 0.25\,Li^+ + 0.25\,e^- \rightarrow LiV^{III}PO_4O$

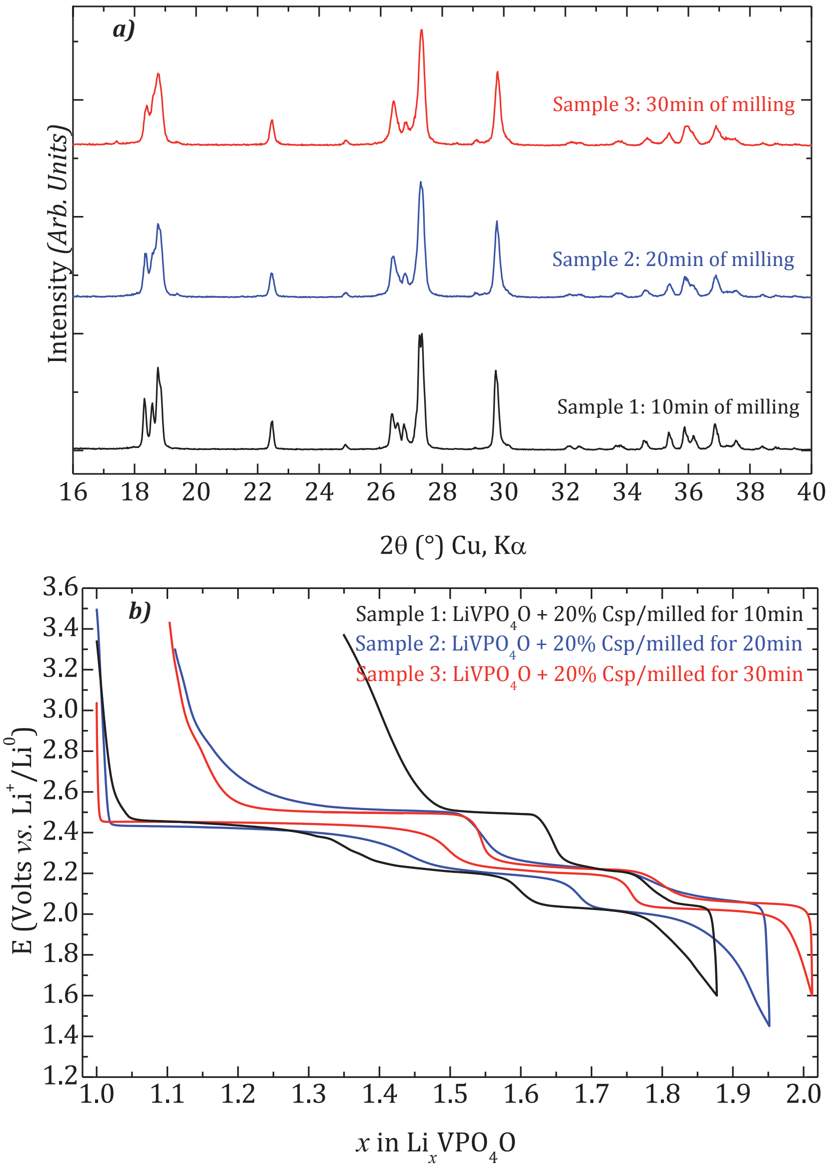

Figure II-32: a) Three different milling durations of a mixture of $LiVPO_4O$ and 20% of C_{sp}.
b) Corresponding electrochemical Li insertion/extraction at C/50

As shown in Chapter I, the synthesis of $LiVPO_4O$ leads to the formation of particles (2-3 μm in size) highly agglomerated (5-6 μm). SPEX grinding has been performed so as to decrease the particle size, as it is well illustrated in Figure II-32 with the observation of a diffraction line broadening with an increasing milling time. Thin electrodes, with 150 μm of thickness, were made by a mixture of $LiVPO_4O$ and 15 wt % of C_{SP} (grinded at different time durations). We added 12 wt % of PVdF as binder. The obtained electrodes were cycled in coin-cells. Figure II-32b displays the galvanostatic data (between 1.4 V and 3 V *vs.* Li) of different samples of $LiVPO_4O$ (Figure II-32a). For a sample milled for a long time (sample 3), the capacity was improved and was very close to the theoretical capacity. The electrochemical data of sample 3 displayed a well defined plateau and a small polarization. One can notice a stronger irreversibility for sample 1, probably due to limited diffusion within these larger particles.

GITT measurements (Figure II-33) show a flat plateau between $LiVPO_4O$ and $Li_{1.5}VPO_4O$ at a potential of 2.45 V *vs.* Li^+/Li, indicating a biphasic mechanism for reaction ⑥. Further Li^+ insertion into $Li_{1.5}VPO_4O$ (reaction ⑦) occurred at a potential close to 2.21 V *vs.* Li^+/Li with a pseudo plateau which indicates that the mechanism might be of second order. Only 0.25 Li^+ can be inserted into $Li_{1.5}VPO_4O$, ending up with a composition of $Li_{1.75}VPO_4O$. Reaction ⑧ is the insertion of Li^+ in $Li_{1.75}VPO_4O$ which occurs at a potential of 2.04 V *vs.* Li^+/Li possibly also through a second order mechanism so as to form Li_2VPO_4O after the insertion of 0.25 Li.

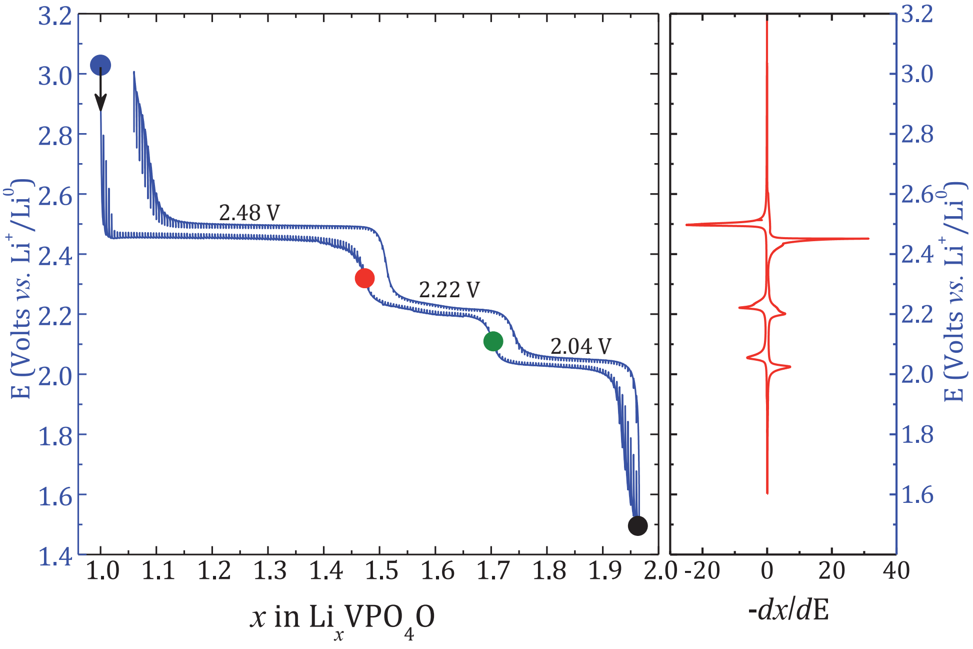

Figure II-33: GITT measurement of $LiVPO_4O$ (left): a current corresponding to a rate of C/200 was applied during one hour with a relaxation time condition of dV/dt< 4mV/h. Derivative curve calculated (right) from GITT.

The very narrow and sharp peak in the derivative curve (Figure II-33) at potential around 2.5 V *vs.* Li^+/Li indicates a biphasic mechanism between $LiVPO_4O$ and $Li_{1.5}VPO_4O$. The peaks at around

2.2 V and 2 V *vs.* Li^+/Li are much broader so that the determination of the mechanism of Li^+ insertion in both $Li_{1.5}VPO_4O$ and $Li_{1.75}VPO_4O$ appears to be not straightforward.

The mechanisms of Li^+ insertion in $LiVPO_4O$ were followed by *in situ* XRD and the recorded XRD data were gathered in Figure II-34 together with the electrochemistry. The *in situ* experiment had been performed on sample 3 (Figure II-32b) with an acquisition time of 2 hours for each different XRD pattern.

- During the first part of the discharge corresponding to the reaction ⑥, the diffraction peaks of the starting $LiVPO_4O$ phase progressively disappeared (Figure II-35) and new Bragg positions located at 28 ° and 28.27 ° in 2θ progressively grew. The XRD pattern, recorded after 15 hours of discharge (red in Figure II-34) corresponds to the pure phase of $Li_{1.5}VPO_4O$, formed at a potential of 2.46 V *vs.* Li^+/Li.

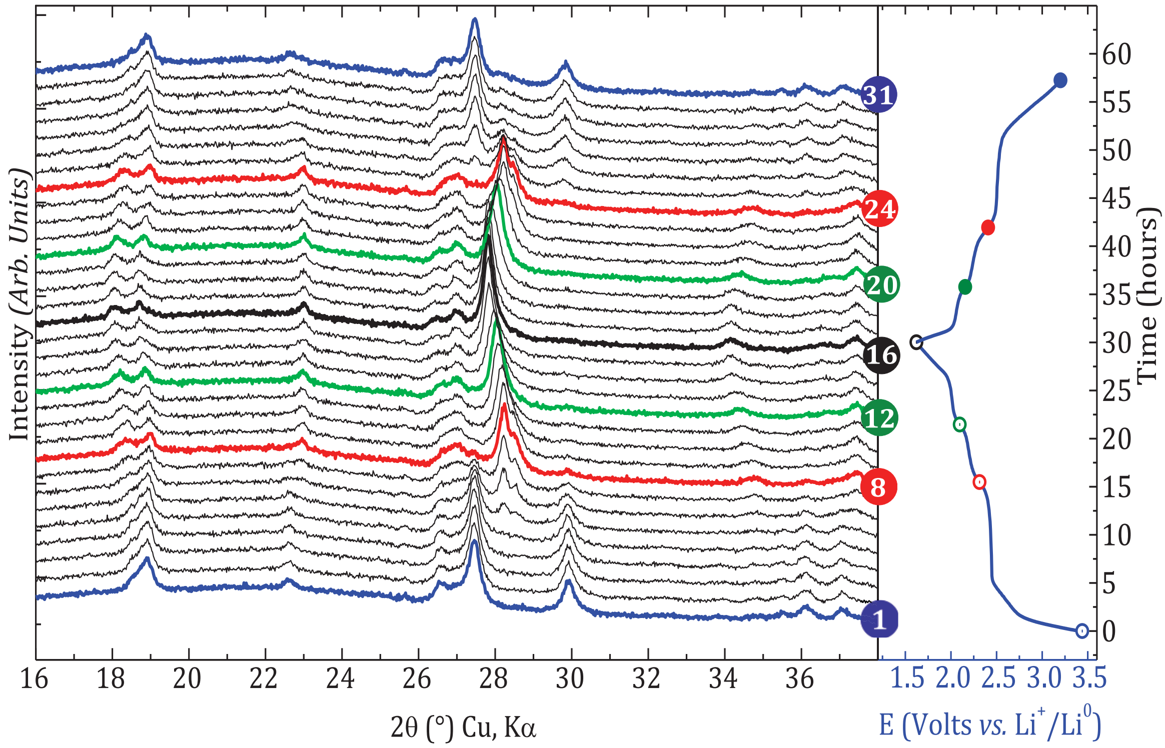

Figure II-34: 2D View of collected in-situ XRD patterns for the global electrochemical reaction $LiVPO_4O$ ⬄ Li_2VPO_4O (left) and corresponding galvanostatic cycling data (right). The XRD patterns highlighted refer to $LiVPO_4O$ (blue), $Li_{1.5}VPO_4O$ (red), $Li_{1.75}VPO_4O$ (green) and Li_2VPO_4O (black).

- Upon further Li^+ insertion into $Li_{1.5}VPO_4O$, the position of the peaks between 17 ° and 18° and the peak at 28 ° in 2θ (Figure II-34 and Figure II-35) seems shifted to lower angles, suggesting a solid solution mechanism. The insertion of Li in $Li_{1.5}VPO_4O$ occurred at the average potential of 2.21 V *vs.* Li^+/Li and leads to $Li_{1.75}VPO_4O$.

- The mechanism of lithium insertion into $Li_{1.75}VPO_4O$ seems also to proceed through a second order mechanism since peaks seems to be shifted to lower 2θ angles (Figure II-35) indicative of a volume increase. The new phase Li_2VPO_4O is formed at the average potential of 2.04 V *vs.* Li^+/Li.

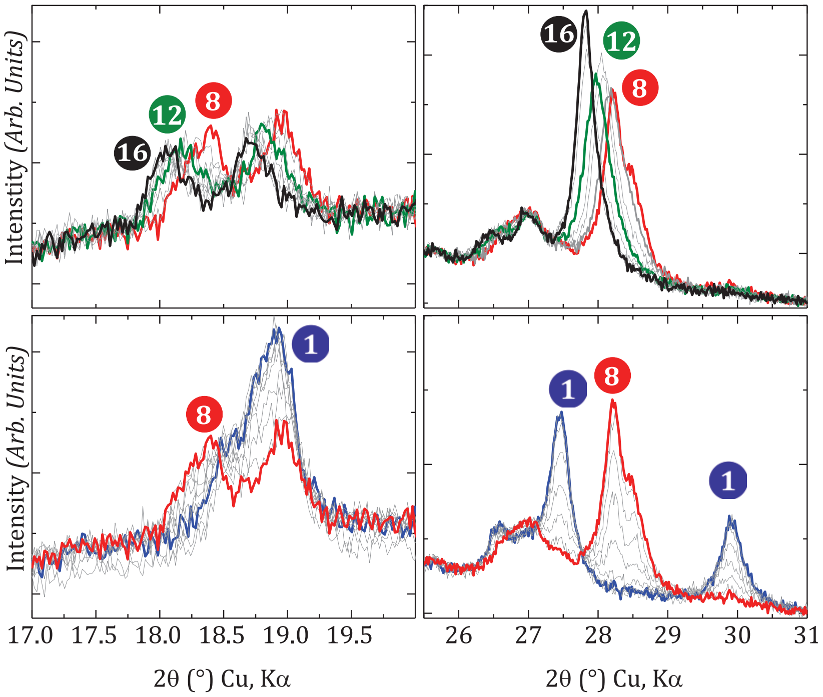

Figure II-35: Selected 2θ regions showing the respective growths and disappearance of the phases involved in the $LiVPO_4O \Rightarrow Li_2VPO_4O$ reaction. The XRD patterns highlighted refer to $Li_{1.5}VPO_4O$ (red), $Li_{1.75}VPO_4O$ (green) and Li_2VPO_4O (black).

These *in situ* XRD experiments fully support the occurrence of a biphasic reaction between $LiVPO_4O$ and $Li_{1.50}VPO_4O$ and also strongly suggest the occurrence of two successive solid solution reactions between $Li_{1.50}VPO_4O$, $Li_{1.75}VPO_4O$ and Li_2VPO_4O. Nevertheless, based on XRD patterns with very limited angular ranges (16-38° (2θ)), it was not possible to determine with a high degree of reliability the unit cells describing the structures of these three phases Li_xVPO_4O (x = 1.50, 1.75 and 2). In the frame of Matteo Bianchini PhD thesis the preparation of these three compositions is in progress *ex situ*, through chemical lithium intercalation. Their XRD patterns are recorded in transmission mode from a capillary sealed under argon in order to get a wide angular range.

II-4b. Reversible Li^+ extraction from $LiVPO_4O$ (V^{4+}/V^{5+} couple)

We have performed electrochemical cycling of $LiVPO_4O$ (from 3 V to 4.6 V at a rate of C/50) in coin cell configuration, as displayed in Figure II-36. The data suggested that only 0.5 Li was extracted at an average potential of 3.95 V *vs.* Li^+/Li. This first, reproducible, result raised two questions:

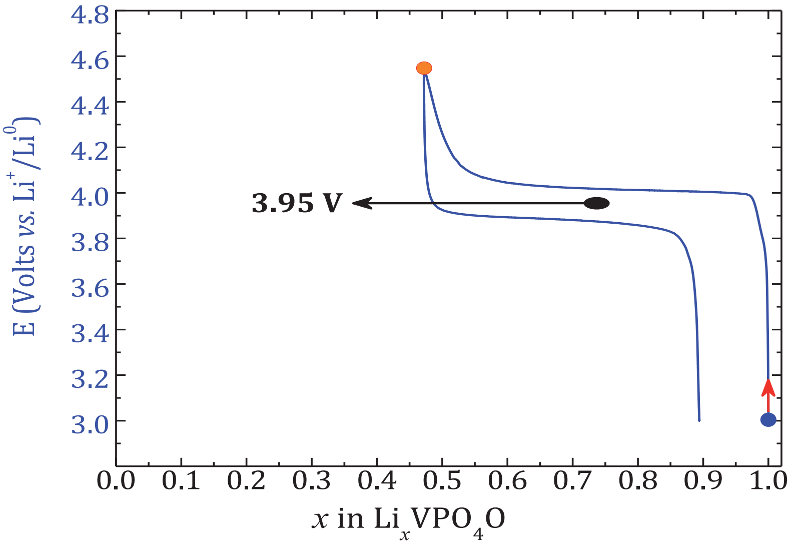

Figure II-36: Galvanostatic cycling of Li/$LiPF_6$ [1M] in EC:DMC (1:1)/$LiVPO_4O$ cell at C/50 from 3 V to 4.6 V

➢ Previous observations about the poor electrochemical activity of $LiVPO_4O$ were confirmed. The electrochemical activity is significantly improved by ball-milling of the electrode with carbon and big particles of $LiVPO_4O$ gave poor rate capability during Li^+ extraction. The data reported in figure II-37 might therefore be related with the reaction:

⑨ $LiVPO_4O \rightarrow ½\, LiVPO_4O + ½\, VPO_4O + ½\, Li^+ + ½\, e^-$

➢ It could also be envisaged that only one (out of two) Li site was emptied from the $LiVPO_4O$ framework structure thus giving rise to the phase of composition $Li_{0.5}VPO_4O$.

⑩ $½\, [Li(1)Li(2)]\, V(1)V(2)[PO_4]_2O_2 \rightarrow ½\, [Li(1)_1Li(2)_0]V(1)V(2)[PO_4]_2O_2 + ½\, Li^+ + ½\, e^-$

^7Li MAS NMR tends to prove that the two sites of Li are equivalent at least in terms of spin transfer from V^{4+} to Li^+. The DFT calculations performed in our group by E. Bogdan and D. Carlier showed that the $Li_{0.5}VPO_4O$ phase is not stable versus $LiVPO_4O$ and VPO_4O, indicating that full extraction of Li^+ from $LiVPO_4O$ is possible.

XRD *in situ* performed between 3 and 4.55 V (Figure II-37) evidenced the two-phase mechanism since no peak was shifted to lower or higher 2θ angles but rather, the appearance of new peaks are visible at 19.5 ° and 29 °. One can notice the presence of the peaks belonging to the initial phase at the end of the charge, showing that the reaction was not complete. The FWHM of initial

XRD patterns of $LiVPO_4O$ is widened as illustrated by the continuous increase of the $(200)_{P\bar{1}}$ peak (Figure II-38) from charge to discharge so that the total increase of FWHM is about 40 %. The shrinkage of the crystallite coherent domain size can be linked to the decrease of the particle size, and therefore enhance the capacity of $LiVPO_4O$.

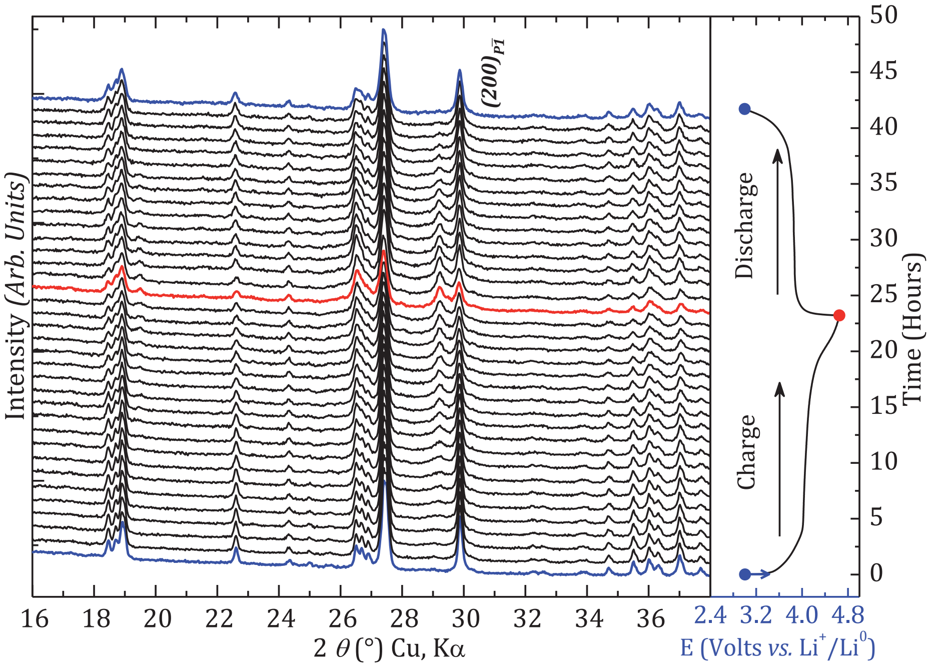

Figure II-37: Galvanostatic cycling of a Li/LP30/LiVPO₄O cell cycled at C/50 up to 4.5 V (right) and in situ XRD patterns (left)

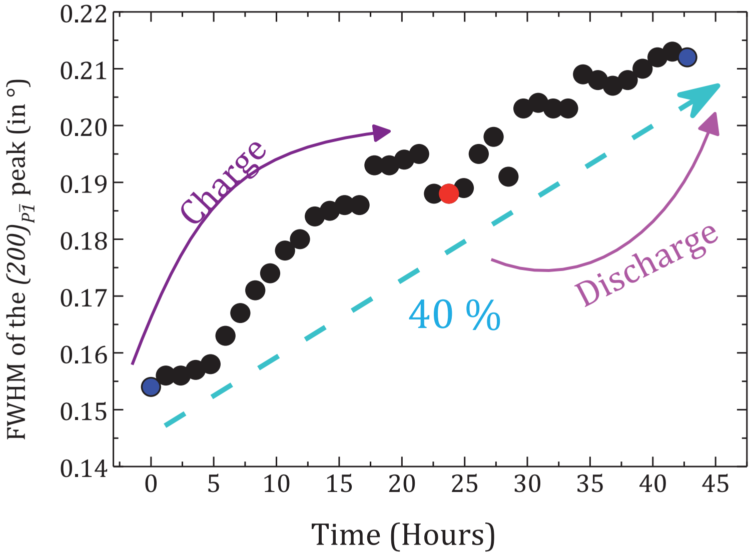

Figure II-38: Evolution (from charge to discharge) of the FWHM for $(200)_{P\bar{1}}$ peaks of LiVPO₄O.

This observation suggested that the large agglomerated particles of $LiVPO_4O$ did not fully contribute to the electrochemical cycling and more interestingly, that the kinetics can be improved. As a consequence of particle size shrinkage, an increase of columbic efficiency was observed, as illustrated in Figure II-39 in which the number of Li^+ exchanged from 3 V to 4.55 V increases with the cycles number. This is also illustrated in Figure II-40a which displays the capacity increase with the numbers of cycling reaching 130 mAh/g after 20 cycles and being then stabilized at a capacity around 134 mAh/g. More interestingly, the polarization decreases with the number of cycles as pictured in Figure II-40b.

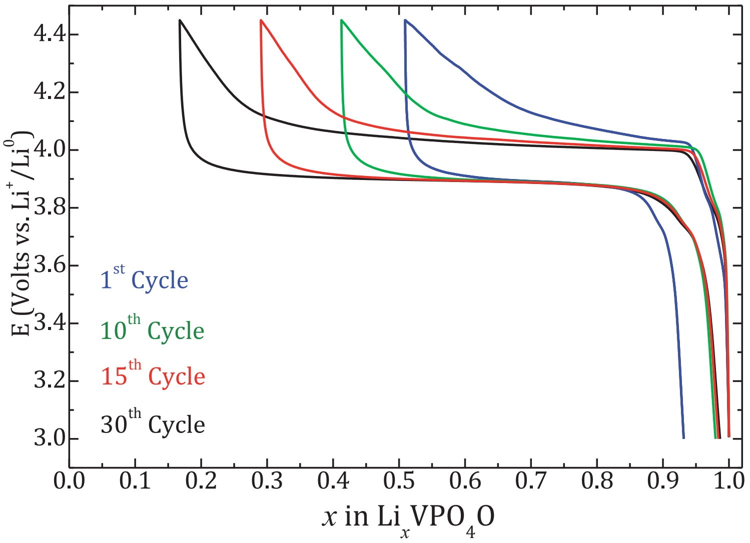

Figure II-39: Different cycles (at a rate of C/20) for Li//LiVPO$_4$O cell

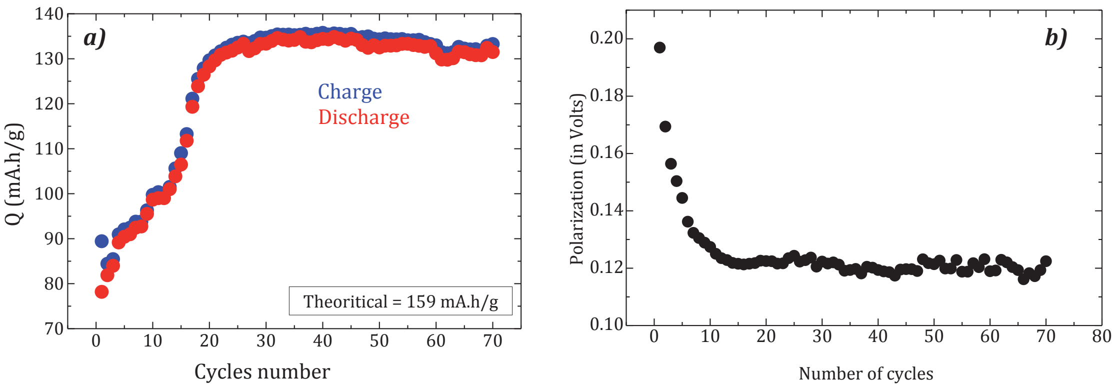

Figure II-40: a) charge and discharge capacity of Li//LiVPO$_4$O cell versus number of cycles b) polarization of each cycle

Since the electrochemical preparation of VPO$_4$O was not straightforward, we succeeded in isolating VPO$_4$O by chemical oxidation using a very powerful oxidant, nitronium tetrafluoroborate (NO$_2$BF$_4$). The redox couple implied from the use of NO$_2$BF$_4$ is NO_2^+/NO_2 which redox potential is ~5.1 V *vs.* Li$^+$/Li in acetonitrile media. The powder of LiVPO$_4$O had been added to a solution of NO$_2$BF$_4$ in acetonitrile, in excess of 5 wt %, to ensure the total oxidation of V^{4+} to V^{5+}. The greenish initial powder of LiVPO$_4$O became yellowish after 12 hours of stirring. The reaction was maintained under stirring during 24 hours and the recovered yellowish powder was separated by centrifugation and washed with acetonitrile. The XRD data were successfully refined in both *Cc* and *C2/c* space groups (but could not be refined within the orthorhombic unit cell of β-VPO_4O). They are displayed in Figure II-41 together with the corresponding lattice parameters. The crystallization of VPO_4O in *C2/c* is unlikely since this will require the presence of vanadium at the center of the VO_6 octahedra with similar V–O distances along the chains as observed in $VPO_4{\cdot}H_2O$ instead of alternate long and short distances as observed in VPO_4O. Another example is VPO_4F which crystallizes in *C2/c* and within which V–F distances are symmetric along the vanadium-centered octahedra. Note however that the oxidation states in $VPO_4{\cdot}H_2O$ and VPO_4F are +3 and +4 respectively, rather than +5 as for VPO_4O [73]. The V/Z obtained after the refinement was 81.9 Å^3 (in *C/c* space group) lower than for the V/Z obtained for $LiVPO_4O$ (85.8 Å^3), in good agreement with an oxidation of V^{4+} to V^{5+}.

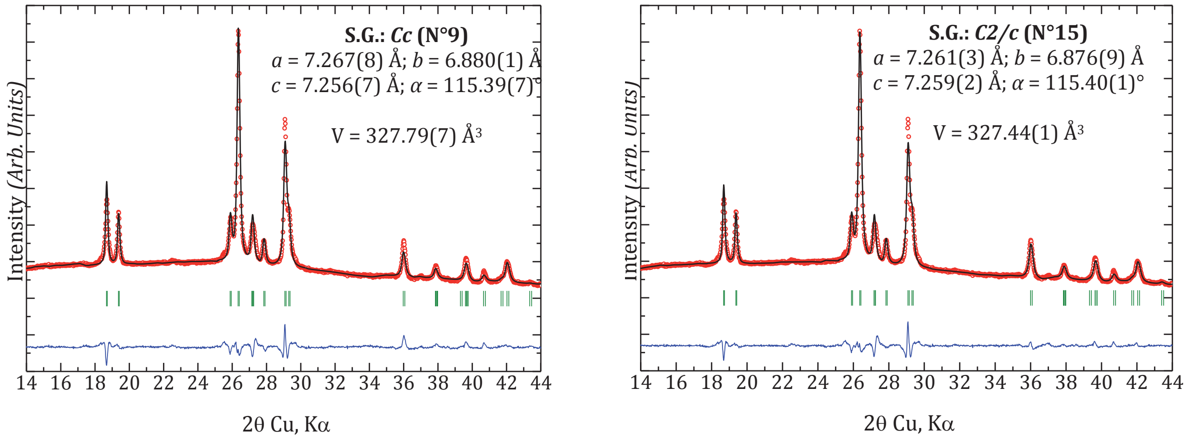

Figure II-41: Full pattern matching refinements of XRD data in Cc (left) and C2/c (right) space groups of VPO_4O obtained by chemical delithiation

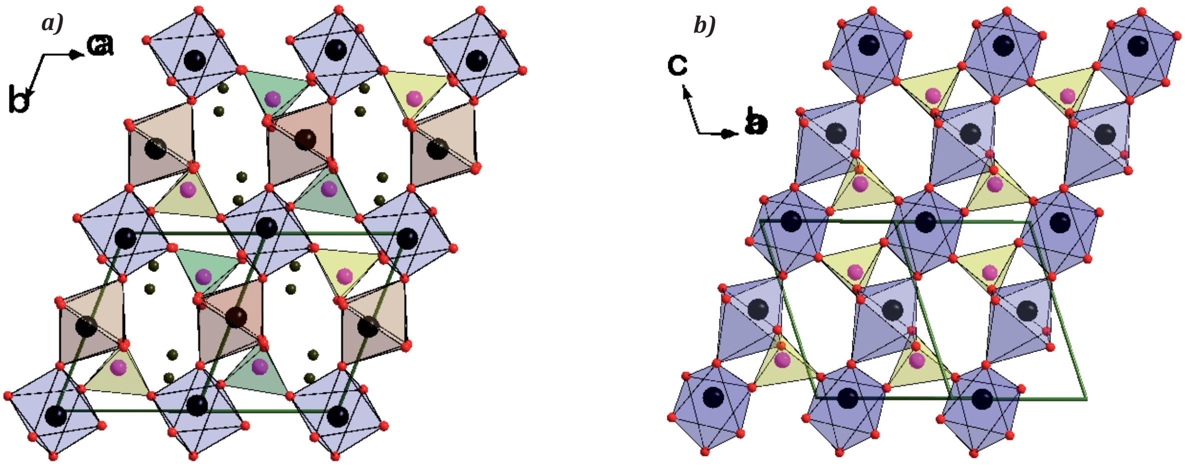

Figure II-42: Representation of the structure of: a) $LiVPO_4O$ and b) ε-VPO_4O along the $(1\bar{1}0)_{C/c}$ and $(10\bar{1})_{P\bar{1}}$ directions.

T.A. Kerr et al. [13] had shown that the insertion of Li^+ in ε-VPO_4O led to the formation of the triclinic $LiVPO_4O$. Figure II-42 illustrates the similitude between the ε-VPO_4O and $LiVPO_4O$ framework structures. Indeed octahedral $[VO_4O_2]$ chains are connected by tetrahedra $[PO_4]$ in the same way for both structures. The extraction of Li^+ from $LiVPO_4O$ is therefore topotactic.

II-5. Conclusions and summary of this chapter

The mechanisms of Li^+ insertion/extraction and extraction/insertion in both $LiVPO_4F$ and $LiVPO_4O$ were studied in order to understand the relationships between crystallographic and electrochemical properties. For $LiVPO_4F$, the insertion of Li^+ leads to the formation of Li_2VPO_4F at a potential of 1.81 V *vs.* Li^+/Li through a biphasic mechanism. Li^+ extraction from $LiVPO_4F$ undergoes a first intermediate phase which composition is $Li_{0.67}VPO_4F$ at a potential of 4.25 V *vs.* Li^+/Li. The fully delithiated phase VPO_4F is obtained by a biphasic mechanism of Li^+ extraction from $Li_{0.67}VPO_4F$ at a potential of 4.26 V *vs.* Li^+/Li. Surprisingly, the subsequent insertion of Li^+ in VPO_4F to $LiVPO_4F$ occurs through a single discharge plateau without occurrence of $Li_{0.67}VPO_4F$. The thermodynamic or kinetic origin of these findings is not fully understood yet and we are tackling it through T-controlled XRD, e^- diffraction, MAS NMR… Besides DFT calculations that could address the relative stabilities of the phases encountered in the VPO_4F–Li_2VPO_4F system, further experiments have to be performed in order to evaluate the stability of the new intermediate phase of $Li_{0.67}VPO_4F$ which has never been reported before.

Despite the unknown structure of the new phase $Li_{0.67}VPO_4F$, the structure of Li_xVPO_4F are related to the parent $LiVPO_4F$ with the same packing of the $[VPO_4F_2]$ unit framework besides significant unit-cell contractions/expansions and overall shifts in symmetry from triclinic $P\bar{1}$ to monoclinic $C2/c$. The overall electrochemical reactions are topotactic and associated with very small polarization. Some features were pointed out just like the increase of V–F distance when one moves from VPO_4F to Li_2VPO_4F and in the same way, the increase of tilted angles along octahedral chains.

The ^7Li MAS NMR signal of VPO_4F displayed a tiny signal at 116 ppm most probably due to unreacted $LiVPO_4F$. The ^7Li MAS NMR signal of $Li_{0.67}VPO_4F$ presented at least 4 signals which show the existence of different types of environment for Li. This result might probably due to charge ordering, which has to be confirmed by further NMR experiments and DFT calculations.

Li^+ insertion into $LiVPO_4O$ undergoes through 3 reversible reactions (the first one being biphasic and the two others most probably solid solutions) and leads to the formation of $Li_{1.5}VPO_4O$, $Li_{1.75}VPO_4O$ and Li_2VPO_4O at potentials of 2.46, 2.2 and 2.02 V vs. Li^+/Li respectively. Li extraction from $LiVPO_4O$ emphasized, with a reaction limited to the exchange of 0.5 Li during the first cycle, the poor electronic conductivity of $LiVPO_4O$ which has to be improved by carbon coating and/or particles size decrease.

It is worth to notice that the V^{4+}/V^{3+} redox couple is located at different potentials in $LiVPO_4X$: around 4.25 V *vs.* Li^+/Li for $LiVPO_4F$ and at around 2.3 V *vs.* Li^+/Li in $LiVPO_4O$. As shown in Figure II-43 the difference between the upper voltage redox couple (V^{4+}/V^{3+}) and lower voltage redox couple (V^{3+}/V^{2+}) in $LiVPO_4F$ is 2.45 V whereas the upper voltage redox couple (V^{5+}/V^{4+}) and lower voltage redox couple (V^{4+}/V^{3+}) in $LiVPO_4O$ is 1.65 V. This difference might come from the presence of vanadyl bonds in $LiVPO_4O$. Indeed the p_y orbitals of oxygen are oriented through d_{yz} vanadium anti-bonding orbitals inducing the increase of V^{4+}/V^{3+} density of state.

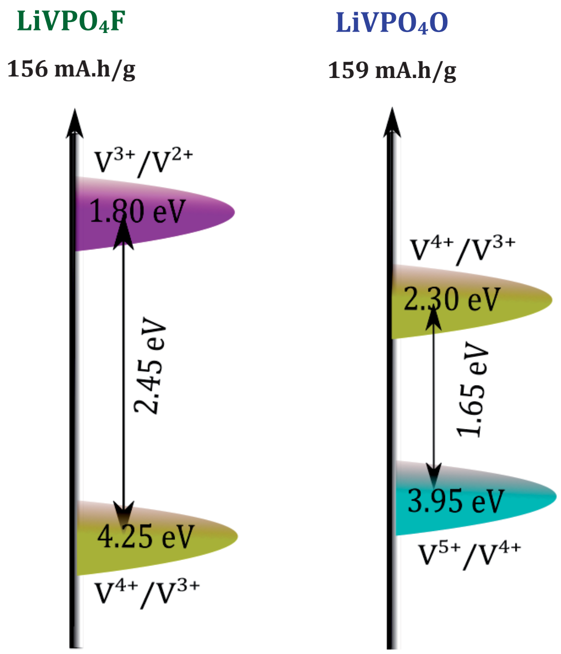
LiVPO₄F
156 mA.h/g
V³⁺/V²⁺
1.80 eV
2.45 eV
4.25 eV
V⁴⁺/V³⁺
LiVPO₄O
159 mA.h/g
V⁴⁺/V³⁺
2.30 eV
1.65 eV
3.95 eV
V⁵⁺/V⁴⁺

Figure II-43: Different schematic densities of state of V^n/V^{n-1} encountered in $LiVPO_4F$ (left) and $LiVPO_4O$ (right)

References

1. Gaubicher, J.; Wurm, C.; Goward, G.; Masquelier, C. and Nazar, L.; *Rhombohedral form of Li(3)V(2)(PO(4))(3) as a cathode in Li-ion batteries,* Chemistry of Materials, **2000**, 12(11): p. 3240-+.
2. Huang, H.; Yin, S.C.; Kerr, T.; Taylor, N. and Nazar, L.F.; *Nanostructured composites: A high capacity, fast rate Li(3)V(2)(PO(4))(3)/carbon cathode for rechargeable lithium batteries,* Advanced Materials, **2002**, 14(21): p. 1525-+.
3. Morgan, D.; Ceder, G.; Saidi, M.Y.; Barker, J.; Swoyer, J.; Huang, H. and Adamson, G.; *Experimental and computational study of the structure and electrochemical properties of Li(x)M(2)(PO(4))(3) compounds with the monoclinic and rhombohedral structure,* Chemistry of Materials, **2002**, 14(11): p. 4684-4693.
4. Morcrette, M.; Leriche, J.B.; Patoux, S.; Wurm, C. and Masquelier, C.; *In situ X-ray diffraction during lithium extraction from rhombohedral and monoclinic Li(3)V(2)(PO(4))(3),* Electrochemical and Solid State Letters, **2003**, 6(5): p. A80-A84.
5. Patoux, S.; Wurm, C.; Morcrette, M.; Rousse, G. and Masquelier, C.; *A comparative structural and electrochemical study of monoclinic Li(3)Fe(2)(PO(4))(3) and Li(3)V(2)(PO(4))(3),* JOURNAL OF POWER SOURCES, **2003**, 119: p. 278-284.
6. Barker, J.; Gover, R.K.B.; Burns, P. and Bryan, A.; *LiVP(2)O(7): A viable lithium-ion cathode material?,* Electrochemical and Solid State Letters, **2005**, 8(9): p. A446-A448.
7. Wurm, C.; Morcrette, M.; Rousse, G.; Dupont, L. and Masquelier, C.; *Lithium insertion/extraction into/from LiMX(2)O(7) compositions (M = Fe, V; X = P, As) prepared via a solution method,* Chemistry of Materials, **2002**, 14(6): p. 2701-2710.
8. Uebou, Y.; Okada, S.; Egashira, M. and Yamaki, J.I.; *Cathode properties of pyrophosphates for rechargeable lithium batteries,* Solid State Ionics, **2002**, 148(3-4): p. 323-328.
9. Rousse, G.; Wurm, C.; Morcrette, M.; Rodriguez-Carvajal, J.; Gaubicher, J. and Masquelier, C.; *Crystal structure of a new vanadium(IV) diphosphate: VP(2)O(7), prepared by lithium extraction from LiVP(2)O(7),* International Journal of Inorganic Materials, **2001**, 3(7): p. 881-887.
10. Dupre, N.; Gaubicher, J.; Angenault, J. and Quarton, M.; *Electrochemical study of intercalated vanadyl phosphate,* Journal of Solid State Electrochemistry, **2004**, 8(5): p. 322-329.
11. Dupre, N.; Gaubicher, J.; Le Mercier, T.; Wallez, G.; Angenault, J. and Quarton, M.; *Positive electrode materials for lithium batteries based on VOPO(4),* Solid State Ionics, **2001**, 140(3-4): p. 209-221.
12. Gaubicher, J.; Le Mercier, T.; Chabre, Y.; Angenault, J. and Quarton, M.; *Li/beta-VOPO4: A new 4 V system for lithium batteries,* Journal of the Electrochemical Society, **1999**, 146(12): p. 4375-4379.
13. Kerr, T.A.; Gaubicher, J. and Nazar, L.F.; *Highly reversible Li insertion at 4 V in epsilon-VOPO(4)/alpha-LiVOPO(4) cathodes,* Electrochemical and Solid State Letters, **2000**, 3(10): p. 460-462.
14. Dupre, N.; Gaubicher, J.; Angenault, J.; Wallez, G. and Quarton, M.; *Electrochemical performance of different Li-VOPO(4) systems,* JOURNAL OF POWER SOURCES, **2001**, 97-8: p. 532-534.
15. Azmi, B.A.; Ishihara, T.; Nishiguchi, H. and Takita, Y.; *Vanadyl phosphates Of VOPO(4) as a cathode of Li-ion rechargeable batteries,* Journal of Power Sources, **2003**, 119: p. 273-277.
16. Dupre, N.; Wallez, G.; Gaubicher, J. and Quarton, M.; *Phase transition induced by lithium insertion in alpha(I)- and alpha(II)-VOPO(4),* Journal of Solid State Chemistry, **2004**, 177(8): p. 2896-2902.
17. Dubarry, M.; Gaubicher, J.; Guyomard, D.; Wallez, G.; Quarton, M. and Baehtz, C.; *Uncommon potential hysteresis in the Li/Li(2x)VO(H(2-x)PO(4))2 (0 <= x <= 2) system,* Electrochimica Acta, **2008**, 53(13): p. 4564-4572.
18. Barker, J.; Saidi, M.Y. and Swoyer, J.L.; *Electrochemical insertion properties of the novel lithium vanadium fluorophosphate, LiVPO(4)F,* Journal of the Electrochemical Society, **2003**, 150(10): p. A1394-A1398.

19. Barker, J.; Gover, R.K.B.; Burns, P.; Bryan, A.; Saidi, M.Y. and Swoyer, J.L.; *Structural and electrochemical properties of lithium vanadium fluorophosphate, LiVPO(4)F,* Journal of Power Sources, **2005**, 146(1-2): p. 516-520.
20. Barker, J.; Gover, R.K.B.; Burns, P.; Bryan, A.; Saidi, M.Y. and Swoyer, J.L.; *Performance evaluation of lithium vanadium fluorophosphate in lithium metal and lithium-ion cells,* Journal of the Electrochemical Society, **2005**, 152(9): p. A1776-A1779.
21. Gover, R.K.B.; Burns, P.; Bryan, A.; Saidi, M.Y.; Swoyer, J.L. and Barker, J.; *LiVPO(4)F: A new active material for safe lithium-ion batteries,* Solid State Ionics, **2006**, 177(26-32): p. 2635-2638.
22. Li, Y.; Zhou, Z.; Gao, X.P. and Yan, J.; *A Novel Sol–gel Method to Synthesize Nanocrystalline LiVPO(4)F and its Electrochemical Li Intercalation Performances,* **2006**, 160: p. 633-637.
23. Zhang, Q.; Zhong, S.K.; Liu, L.T.; Liu, J.Q.; Jiang, J.Q.; Wang, J. and Li, Y.H.; *A novel method to synthesize LiVPO(4)F/C composite materials and its electrochemical Li-intercalation performances,* Journal of Physics and Chemistry of Solids, **2009**, 70(7): p. 1080-1082.
24. Zhou, F.; Zhao, X.M. and Dahn, J.R.; *Reactivity of charged LiVPO(4)F with 1 M LiPF(6) EC:DEC electrolyte at high temperature as studied by accelerating rate calorimetry,* Electrochemistry Communications, **2009**, 11(3): p. 589-591.
25. Ellis, B.L.; Ramesh, T.N.; Davis, L.J.M.; Goward, G.R. and Nazar, L.F.; *Structure and Electrochemistry of Two-Electron Redox Couples in Lithium Metal Fluorophosphates Based on the Tavorite Structure,* Chemistry of Materials, **2011**, 23(23): p. 5138-5148.
26. Ateba Mba, J.M.; Croguennec, L.; Basir, N.I.; Barker, J. and Masquelier, C.; *Lithium Insertion or Extraction from/into Tavorite-Type LiVPO(4)F: An In Situ X-ray Diffraction Study,* Journal of the Electrochemical Society, **2012**, 159(8): p. A1171-A1175.
27. Ateba Mba, J.M.; Masquelier, C.; Suard, E. and Croguennec, L.; *Synthesis and Crystallographic Study of Homeotypic LiVPO(4)F and LiVPO(4)O,* Chemistry of Materials, **2012**, 24(6): p. 1223-1234.
28. Zheng, J.C.; Zhang, B. and Yang, Z.H.; *Novel synthesis of LiVPO(4)F cathode material by chemical lithiation and postannealing,* Journal of Power Sources, **2012**, 202: p. 380-383.
29. Azmi, B.M.; Ishihara, T.; Nishiguchi, H. and Takita, Y.; *Cathodic performance of LiVOPO(4) prepared by impregnation method for Li ion secondary battery,* Electrochemistry, **2003**, 71(12): p. 1108-1110.
30. Barker, J.; Saidi, M.Y. and Swoyer, J.L.; *Electrochemical properties of beta-LiVOPO(4) prepared by carbothermal reduction,* Journal of the Electrochemical Society, **2004**, 151(6): p. A796-A800.
31. Azmi, B.M.; Ishihara, T.; Nishiguchi, H. and Takita, Y.; *LiVOPO(4) as a new cathode materials for Li-ion rechargeable battery,* JOURNAL OF POWER SOURCES, **2005**, 146(1-2): p. 525-528.
32. Song, Y.N.; Zavalij, P.Y. and Whittingham, M.S.; *epsilon-VOPO(4): Electrochemical synthesis and enhanced cathode behavior,* Journal of the Electrochemical Society, **2005**, 152(4): p. A721-A728.
33. Kuo, H.T.; Bagkar, N.C.; Liu, R.S.; Shen, C.H.; Shy, D.S.; Xing, X.K.; Lee, J.F. and Chen, J.M.; *Structural transformation of LiVOPO(4) to Li(3)V(2)(PO(4))(3) with enhanced capacity,* Journal of Physical Chemistry B, **2008**, 112(36): p. 11250-11257.
34. Nagamine, K.; Honma, T. and Komatsu, T.; *Selective Synthesis of Lithium Ion-Conductive beta-LiVOPO(4) Crystals via Glass-Ceramic Processing,* Journal of the American Ceramic Society, **2008**, 91(12): p. 3920-3925.
35. Ren, M.M.; Zhou, Z.; Gao, X.P.; Liu, L. and Peng, W.X.; *LiVOPO(4) hollow microspheres: One-pot hydrothermal synthesis with reactants as self-sacrifice templates and lithium intercalation performances,* Journal of Physical Chemistry C, **2008**, 112(33): p. 13043-13046.
36. Yang, Y.; Fang, H.S.; Zheng, J.; Li, L.P.; Li, G.S. and Yan, G.F.; *Towards the understanding of poor electrochemical activity of triclinic LiVOPO(4): Experimental characterization and theoretical investigations,* Solid State Sciences, **2008**, 10(10): p. 1292-1298.
37. Ren, M.M.; Zhou, Z.; Su, L.W. and Gao, X.P.; *LiVOPO(4): A cathode material for 4 V lithium ion batteries,* JOURNAL OF POWER SOURCES, **2009**, 189(1): p. 786-789.
38. Ren, M.M.; Zhou, Z. and Gao, X.P.; *LiVOPO(4) as an anode material for lithium ion batteries,* Journal of Applied Electrochemistry, **2010**, 40(1): p. 209-213.

39. Allen, C.J.; Jia, Q.Y.; Chinnasamy, C.N.; Mukerjee, S. and Abraham, K.M.; *Synthesis, Structure and Electrochemistry of Lithium Vanadium Phosphate Cathode Materials,* Journal of the Electrochemical Society, **2011**, 158(12): p. A1250-A1259.
40. Saravanan, K.; Lee, H.S.; Kuezma, M.; Vittal, J.J. and Balaya, P.; *Hollow alpha-LiVOPO(4) sphere cathodes for high energy Li-ion battery application,* Journal of Materials Chemistry, **2011**, 21(27): p. 10042-10050.
41. Wang, L.; Yang, L.B.; Gong, L.; Jiang, X.Q.; Yuan, K. and Hu, Z.B.; *Synthesis of LiVOPO(4) for cathode materials by coordination and microwave sintering,* Electrochimica Acta, **2011**, 56(20): p. 6906-6911.
42. Hameed, A.S.; Nagarathinam, M.; Reddy, M.V.; Chowdari, B.V.R. and Vittal, J.J.; *Synthesis and electrochemical studies of layer-structured metastable alpha(I)-LiVOPO(4),* Journal of Materials Chemistry, **2012**, 22(15): p. 7206-7213.
43. Rousse, G.; Rodriguez-Carvajal, J.; Wurm, C. and Masquelier, C.; *Magnetic structure of two lithium iron phosphates: A- and B-Li(3)Fe(2)(PO(4))(3),* Applied Physics a-Materials Science & Processing, **2002**, 74: p. S704-S706.
44. Kishore, A.S.; Pralong, V.; Caignaert, V.; Varadaraju, U.V. and Raveau, B.; *A new lithium vanadyl diphosphate Li(2)VOP(2)O(7): Synthesis and electrochemical study,* Solid State Sciences, **2008**, 10(10): p. 1285-1291.
45. Kishore, M.S.; Pralong, V.; Caignaert, V.; Varadaraju, U.V. and Raveau, B.; *Synthesis and electrochemical properties of a new vanadyl phosphate: Li(4)VO(PO(4))(2),* Electrochemistry Communications, **2006**, 8(10): p. 1558-1562.
46. Makimura, Y.; Cahill, L.S.; Iriyama, Y.; Goward, G.R. and Nazar, L.F.; *Layered lithium vanadium fluorophosphate, Li(5)V(PO(4))(2)F(2): A 4 V class positive electrode material for lithium-ion batteries,* Chemistry of Materials, **2008**, 20(13): p. 4240-4248.
47. Park, Y.-U.; Seo, D.-H.; Kim, B.; Hong, K.-P.; Kim, H.; Lee, S.; Shakoor, R.A.; Miyasaka, K.; Tarascon, J.-M. and Kang, K.; *Tailoring a fluorophosphate as a novel 4 V cathode for lithium-ion batteries,* Sci. Rep., **2012**, 2.
48. Barker, J.; Saidi, M.Y. and Swoyer, J.L.; *A sodium-ion cell based on the fluorophosphate compound NaVPO(4)F,* Electrochemical and Solid State Letters, **2003**, 6(1): p. A1-A4.
49. Barker, J.; Saidi, M.Y. and Swoyer, J.L.; *A comparative investigation of the Li insertion properties of the novel fluorophosphate phases, NaVPO(4)(4)(FandLiVPO)F,* Journal of the Electrochemical Society, **2004**, 151(10): p. A1670-A1677.
50. Zhao, J.Q.; He, J.P.; Ding, X.C.; Zhou, J.H.; Ma, Y.O.; Wu, S.C. and Huang, R.M.; *A novel sol-gel synthesis route to NaVPO(4)F as cathode material for hybrid lithium ion batteries,* JOURNAL OF POWER SOURCES, **2010**, 195(19): p. 6854-6859.
51. Barker, J.; Gover, R.K.B.; Burns, P. and Bryan, A.J.; *Hybrid-ion - A lithium-ion cell based on a sodium insertion material,* Electrochemical and Solid State Letters, **2006**, 9(4): p. A190-A192.
52. Gover, R.K.B.; Bryan, A.; Burns, P. and Barker, J.; *The electrochemical insertion properties of sodium vanadium fluorophosphate, Na(3)V(2)(PO(4))(2)F(3),* Solid State Ionics, **2006**, 177(17-18): p. 1495-1500.
53. Barker, J.; Gover, R.K.B.; Burns, P. and Bryan, A.J.; *Li(4/3)Ti(5/3)O(4) parallel to Na(3)V(2),(PO(4))(2)F(3): An example of a hybrid-ion cell using a non-graphitic anode,* Journal of the Electrochemical Society, **2007**, 154(9): p. A882-A887.
54. Jiang, T.; Chen, G.; Li, A.; Wang, C.Z. and Wei, Y.J.; *Sol-gel preparation and electrochemical properties of Na(3)V(2)(PO(4))(2)F(3)/C composite cathode material for lithium ion batteries,* Journal of Alloys and Compounds, **2009**, 478(1-2): p. 604-607.
55. Shakoor, R.A.; Seo, D.H.; Kim, H.; Park, Y.U.; Kim, J.; Kim, S.W.; Gwon, H.; Lee, S. and Kang, K.; *A combined first principles and experimental study on Na(3)V(2)(PO(4))(2)F(3) for rechargeable Na batteries (vol 22, pg 20535, 2012),* Journal of Materials Chemistry, **2012**, 22(48): p. 25498-25498.
56. Huang, H.; Faulkner, T.; Barker, J. and Saidi, M.Y.; *Lithium metal phosphates, power and automotive applications,* Journal of Power Sources, **2009**, 189(1): p. 748-751.
57. Barker, J.; Saidi, M.Y.; Gover, R.K.B.; Burns, P. and Bryan, A.; *The effect of Al substitution on the lithium insertion properties of lithium vanadium fluorophosphate, LiVPO(4)F,* Journal of Power Sources, **2007**, 174(2): p. 927-931.

58. Barker, J.; Gover, R.K.B.; Burns, P. and Bryan, A.J.; *A lithium-ion cell based on Li(4/3)Ti(5/3)O(4) and LiVPO(4)F,* Electrochemical and Solid State Letters, **2007**, 10(5): p. A130-A133.
59. Barker, J.; Saidi, M.Y. and Swoyer, J.; *Lithium Metal Fluorophosphate and Preparation Thereof,* US Patent **2005**, 0142056 A1(US 2005).
60. Barker, J.; Gover, R.K.B.; Burns, P. and Bryan, A.; *A symmetrical lithium-ion cell based on lithium vanadium fluorophosphate, LiVPO(4)F,* Electrochemical and Solid State Letters, **2005**, 8(6): p. A285-A287.
61. Plashnitsa, L.S.; Kobayashi, E.; Okada, S. and Yamaki, J.; *Symmetric lithium-ion cell based on lithium vanadium fluorophosphate with ionic liquid electrolyte,* Electrochimica Acta, **2011**, 56(3): p. 1344-1351.
62. Leriche, J.B.; Hamelet, S.; Shu, J.; Morcrette, M.; Masquelier, C.; Ouvrard, G.; Zerrouki, M.; Soudan, P.; Belin, S.; Elkaim, E. and Baudelet, F.; *An Electrochemical Cell for Operando Study of Lithium Batteries Using Synchrotron Radiation,* Journal of the Electrochemical Society, **2010**, 157(5): p. A606-A610.
63. Ouvrard, G.; Zerrouki, M.; Soudan, P.; Lestriez, B.; Masquelier, C.; Morcrette, M.; Hamelet, S.; Belin, S.; Flank, A.M. and Baudelet, F.; *Heterogeneous behaviour of the lithium battery composite electrode LiFePO4,* JOURNAL OF POWER SOURCES, **2013**, 229(0): p. 16-21.
64. Morgan, D.; Ceder, G.; Saidi, M.Y.; Barker, J.; Swoyer, J.; Huang, H. and Adamson, G.; *Experimental and computational study of the structure and electrochemical properties of monoclinic Li(x)M(2)(PO(4))(3) compounds,* JOURNAL OF POWER SOURCES, **2003**, 119: p. 755-759.
65. Recham, N.; Chotard, J.N.; Dupont, L.; Delacourt, C.; Walker, W.; Armand, M. and Tarascon, J.M.; *A 3.6 V lithium-based fluorosulphate insertion positive electrode for lithium-ion batteries,* Nature Materials, **2010**, 9(1): p. 68-74.
66. Tripathi, R.; Ramesh, T.N.; Ellis, B.L. and Nazar, L.F.; *Scalable Synthesis of Tavorite LiFeSO(4)F and NaFeSO(4)F Cathode Materials,* Angewandte Chemie-International Edition, **2010**, 49(46): p. 8738-8742.
67. Moreau, P.; Guyomard, D.; Gaubicher, J. and Boucher, F.; *Structure and Stability of Sodium Intercalated Phases in Olivine FePO(4),* Chemistry of Materials, **2010**, 22(14): p. 4126-4128.
68. Casas-Cabanas, M.; Roddatis, V.V.; Saurel, D.; Kubiak, P.; Carretero-Gonzalez, J.; Palomares, V.; Serras, P. and Rojo, T.; *Crystal chemistry of Na insertion/deinsertion in FePO(4)-NaFePO(4),* Journal of Materials Chemistry, **2012**, 22(34): p. 17421-17423.
69. Bain, G.A. and Berry, J.F.; *Diamagnetic corrections and Pascal's constants,* Journal of Chemical Education, **2008**, 85(4): p. 532-536.
70. Melot, B.C.; Rousse, G.; Chotard, J.N.; Ati, M.; Rodriguez-Carvajal, J.; Kemei, M.C. and Tarascon, J.M.; *Magnetic Structure and Properties of the Li-Ion Battery Materials FeSO(4)F and LiFeSO(4)F,* Chemistry of Materials, **2011**, 23(11): p. 2922-2930.
71. Sears, V.F.; *Neutron scattering lengths and cross section,* Neutron News, **1992**, 3(3): p. 26-37.
72. Ramesh, T.N.; Lee, K.T.; Ellis, B.L. and Nazar, L.F.; *Tavorite Lithium Iron Fluorophosphate Cathode Materials: Phase Transition and Electrochemistry of LiFePO(4)F-Li(2)FePO(4)F,* Electrochemical and Solid State Letters, **2010**, 13(4): p. A43-A47.
73. Girgsdies, F.; Dong, W.S.; Bartley, J.K.; Hutchings, G.J.; Schlogl, R. and Ressler, T.; *The crystal structure of epsilon-VOPO(4),* Solid State Sciences, **2006**, 8(7): p. 807-812.

Chapter III

SYNTHESIS, CRYSTAL STRUCTURE AND ELECTROCHEMICAL PROPERTIES OF $LiFePO_4F$

Contents

III-1. Introduction **107**

III-2. SYNTHESIS OF $LiFePO_4F$ **109**

- III-2a. Iono-thermal Synthesis 110
- III-2b. One-step Ceramic Synthesis 112
- III-2c. Mössbauer spectroscopy and Magnetic properties of $LiFePO_4F$ 113
- III-2d. Conclusion 115

III-3. CRYSTAL AND MAGNETIC STRUCTURES OF $LiFePO_4F$ **116**

- III-3a. Crystal structure of $LiFePO_4F$ 116
- III-3b. NMR measurements 121
- III-3c. Magnetic structure of $LiFePO_4F$ 124

III-4. ELECTROCHEMICAL PROPERTIES OF $LiFePO_4F$ **127**

III-5. Conclusion and summary of this chapter **134**

III-1. Introduction

As established by J.B. Goodenough and coworkers [1, 2] for NASICON-type compositions, it is possible to increase the average operating potential of the Fe^{3+}/Fe^{2+} redox couple by shifting from PO_4 to XO_4 groups (with X = W or S). This could be well established for the Tavorite-type structure $AFeXO_4Y$ as well (with A = Li or H, X = P or S, Y = OH or F) in which the average potential of the redox couple Fe^{3+}/Fe^{2+} increases when substituting SO_4 for PO_4 (illustrated in Table III-1 and Figure III-1). As described previously in this manuscript for vanadium-containing compositions, the presence of fluorine increases the average potential vs. Li of the Fe^{3+}/Fe^{2+} redox couple.

Table III-1: recorded potential vs. Li of the Fe^{3+}/Fe^{2} redox couple, theoretical capacity, and energy density for reported Tavorite type compositions $AFeXO_4Y$ (with A= Li or H, X=P or S, Y = OH or F)

		Average potentials (V vs. Li^+/Li)	Theoretical capacities (mAh/g)	Energy densities (Wh/g)
$FePO_4 \cdot H_2O$	[3]	3.0	159	445
$FeSO_4OH_xF_y$	[4]	3.4	158	537
$FeSO_4F$	[4]	3.6	157	565
$LiFePO_4OH$	[5]	2.6	153	413
$LiFePO_4OH_{0.6}F_{0.4}$	[6]	2.7	168	437
$LiFePO_4F$	[7, 8]	2.8	152	426
$LiFeSO_4F_{(Tavorite)}$	[9, 10]	3.6	151	544
$LiFeSO_4F_{(Triplite)}$	[11, 12]	3.9	151	589

The increase of the electronegativity difference between M and Y leads to a higher ionic character of the M–Y bond, which stabilizes the anti-bonding orbital of the metal M and thus increases the energy difference with the negative Li electrode.

Figure III-1 illustrates that lithium iron sulfates exhibit higher potential *vs.* Li^+/Li compared to lithium iron phosphates. For both sulfates and phosphates, the presence of fluorine widens the potential windows. One can therefore notice that the potential of the Tavorite $LiFeSO_4 \cdot OH$ is 0.35 V higher than the potential of the Tavorite $LiFeSO_4F$ [9, 10, 13, 14]. In the same way, the potential of $LiFePO_4F$ is 0.20 V higher than the potential of $LiFePO_4 \cdot OH$ [3, 8, 9, 15]. The best illustrations of the fluorine effect can be seen in the operating potential of the Tavorite $LiFePO_4OH_{0.4}F_{0.6}$ [6] which appeared to be 2.7 V *vs.* Li^+/Li just in between the operating potential of $LiFePO_4F$ (2.8 V) and $LiFePO_4OH$ (2.6 V). It is worth to notice that the operating potential of the Triplite phase $LiFeSO_4F$ is 3.9 V *vs.* Li^+/Li, known as the highest potential recorded for the redox couple Fe^{3+}/Fe^{2+}.

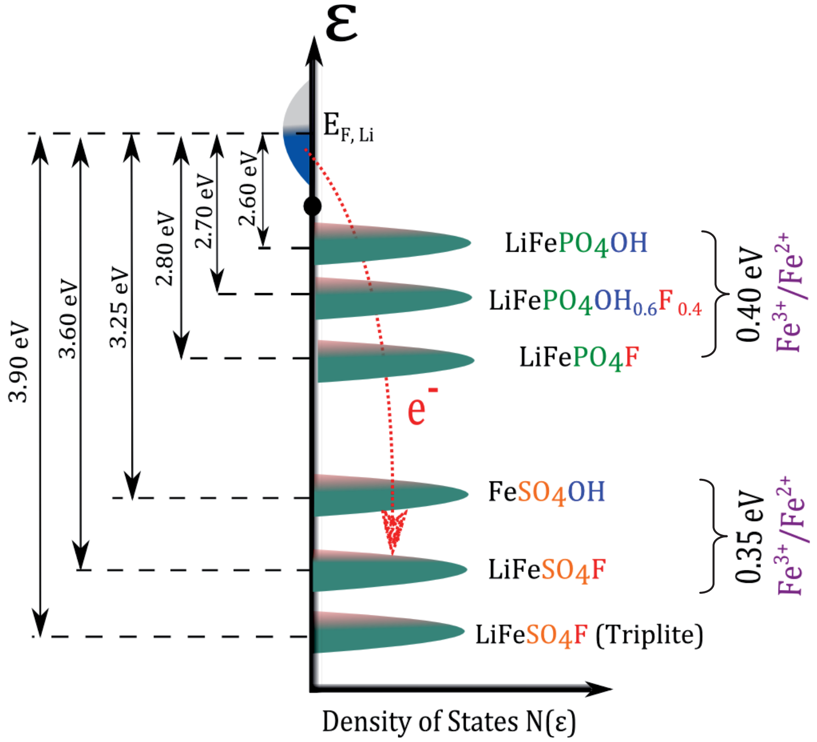

Figure III-1: Respective positions of the Fe^{3+}/Fe^{2+} redox couple in iron phosphates/sulfates

As part of our study on Tavorite-type fluorophosphate materials, we have studied the lithium iron fluorophosphate $LiFePO_4F$ which had been synthesized for the first time by N. Recham et al. [7, 16] using ceramic or iono-thermal synthesis routes. T.N. Ramesh et al. [8] and M. Prabu et al. [15] reported the synthesis of $LiFePO_4F$ through a two-step ceramic synthesis with $FePO_4$ used as an intermediate. In this chapter, we are presenting both iono-thermal and ceramic synthesis routes as well as the advantages and drawbacks of each technique.

N. Recham et al.[7] and T.N. Ramesh et al. [8] published the crystal structure of $LiFePO_4F$ based on laboratory X-Ray diffraction. They both proposed that $LiFePO_4F$ crystallizes in the Tavorite structure with two crystallographic sites for lithium. We will present in this chapter our structural study of $LiFePO_4F$, based on Rietveld refinements of both X-Ray and neutron diffraction data, both being supported by NMR measurements.

Although the two reported electrochemical signatures in literature [7,8] are significantly different, their operating potentials are roughly the same, i.e. ~2.80 V *vs.* Li^+/Li. We are presenting here the electrochemical signature of $LiFePO_4F$ performed at different cycling rates as well as in situ X-Ray diffraction during the charge / discharge processes.

III-2. SYNTHESIS OF $LiFePO_4F$

J. Barker et al. [17] patented the synthesis of $LiFePO_4F$ through a two-step ceramic route using $FePO_4$ as an intermediate. N. Recham et al. [7] reported for the first time the synthesis of $LiFePO_4F$ using iono-thermal or ceramic routes. Iono-thermal synthesis was carried out by using ionic liquid (IL) which is constituted by an association of organic cations and anions. This is the reason why ILs are also sometimes referred to as molten salts. The parallel can be established with inorganic salts (such as NaI), which are used for high temperature syntheses. On contrary, the iono-thermal synthesis generally operates at much lower temperatures. Due to their advantages such as non-flammability, low-vapor pressure, high thermal stability, good electrochemical stability, low toxicity, material compatibility, high ions content…, ILs have been widely studied as agents for extraction and separation processes, organic syntheses and catalysis, as well as potential electrolytes for energy storage devices and electroplating [18-22] and as electrolytes in lithium-ion batteries [23]. However the use of ILs are limited since they are expensive.

For the synthesis of $LiFePO_4F$, N. Recham et al. [7] used 1-butyl-3-methylimidazolium triflate as IL and the synthesis was done at 260 °C for 48 hours using Li_3PO_4 and FeF_3 precursors. The reaction yielded nano-particles of $LiFePO_4F$ as well as the formation of LiF. This is one of the advantages of the iono-thermal synthesis which produces nanometric particles at very low temperatures. Moreover, because of the flexible nature of the cationic/anionic pairs, they present, as solvents, great opportunities to purposely promote nucleation, influencing material properties and allowing the synthesis of materials with specific structure and morphology. The drawback of iono-thermal synthesis is its cost. However, N. Recham et al. [24] mentioned that it was possible to recover and regenerate the IL.

N. Recham et al. [7] also succeeded in the synthesis of $LiFePO_4F$ through a one-step ceramic route by using FeF_3 and Li_3PO_4, which had been ball-milled and placed in a platinum sealed tube. The tube was heated up to 700 °C for 24 hours. As expected, the particles size obtained was bigger compared with those from iono-thermal synthesis (3-6 µm for the ceramic synthesis *vs.* 30-60 nm for the iono-thermal synthesis). The drawback of those syntheses (iono-thermal and ceramic) was the formation of LiF obtained at the end of the reaction which was further removed by washing. This therefore raised the question of $LiFePO_4F$ stability upon moisture.

T.N. Ramesh et al. [8] reported the synthesis of $LiFePO_4F$ through a two-step reaction using $FePO_4$ as an intermediate phase mixed in stoichiometric proportions with LiF. The preparation of $FePO_4$ was carried out by mixing Fe_2O_3 and $NH_4H_2PO_4$ in stoichiometric proportions and heated up to 870 °C during 6-10 hours. The obtained $FePO_4$ was ball-milled with stoichiometric amounts of LiF heated at 575 °C for 1.25 hours under N_2 flow. The SEM indicated that the obtained particle size of $LiFePO_4F$ was 2-5 µm.

M. Prabu et al. [15] published the synthesis of $LiFePO_4F$ through a two-step reaction using $FePO_4$ as an intermediate and further mixed with LiF. The synthesis route of $FePO_4$ differs from the one of T.N. Ramesh since $FePO_4$ was obtained via a co-precipitation of both $FeCl_3 \cdot 6H_2O$ and $Na_3PO_4 \cdot 12H_2O$ which led to $FePO_4$. The obtained $FePO_4$ was dried and further mixed with LiF in stoichiometric proportion prior to be heated up to 575 °C during one hour.

We are describing here the iono-thermal synthesis, which had been done using two different ILs, and the ceramic synthesis. For both synthesis techniques, the lattice parameters of the obtained phases were compared with those from Tavorite hydroxyl/fluoro-phosphate.

III-2a. Iono-thermal Synthesis

The iono-thermal synthesis of $LiFePO_4F$ was carried out using a protocol similar to the patented route described by Recham et al. [16] in which stoichiometric proportions of Li_3PO_4 and FeF_3 (typically 57.9 mg of Li_3PO_4 and 56.4 mg of FeF_3) were ball-milled under inert Ar gas. The powder was recovered in a glove box filled with Ar prior to be introduced in the Teflon beaker of a Bomb Parr® together with 10 ml of IL. The reaction mixture was stirred for 1 hour in order to solubilize faster both Li_3PO_4 and FeF_3. For this experiment, two different ILs were used: i) 1-ethyl-3-methylimadozolium bis-(trifluoromethanesulfonyl imide) commercially well known as EMI-TFSI and ii) trifluoromethanesulfonate which will be named as Triflate for commodity. The Teflon beaker was capped and tightened in a stainless steel Bomb PARR® under Ar atmosphere, prior to be heated for 10 hours up to 260 °C when EMI-TFSI was used and 280 °C when Triflate was used. The synthesis temperatures were lower than the decomposition temperatures of each IL since EMI-TFSI decomposed at around 300 °C whereas Triflate decomposed at 310 °C.

The recovered powders were rinsed with acetone to get rid of IL, washed with a large excess of cold water (Temperature below 10 °C) during ~1 hour in order to remove LiF which was formed during the synthesis. Finally, the powder was dried in the oven at 60 °C overnight. Figure III-2a and Figure III-2b present the full-pattern matching refinement of the XRD data of the grey powder recovered after the synthesis in EMI-TFSI and of the obtained dark green powder obtained when Triflate was used as IL. The use of Triflate yields the formation of "LiFePO$_4$F" accompanied with the triphylite LiFePO$_4$ as an impurity.

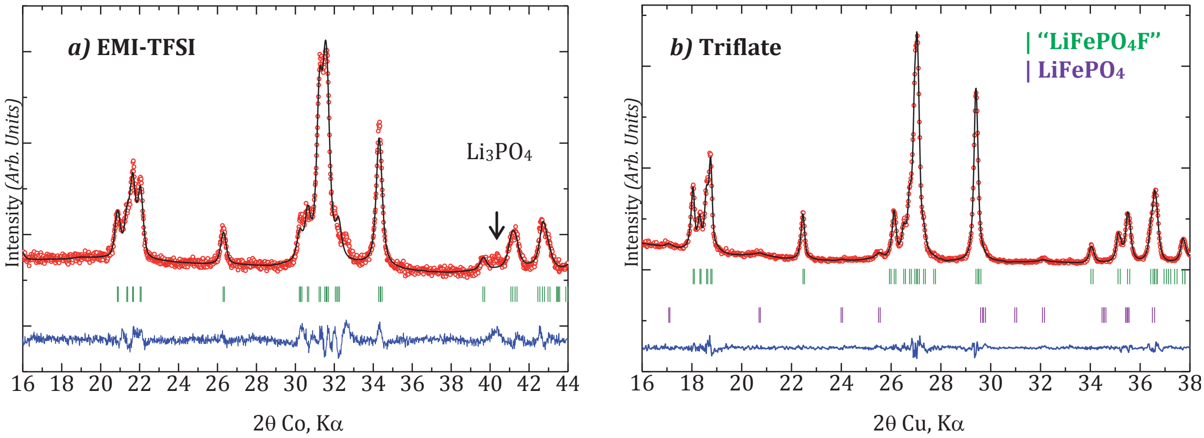

Figure III-2: Full-pattern matching refinements of LiFePO$_4$F synthesized using a) EMI-TFSI and b) Triflate

Table III-2: Lattice parameters and angles of different LiFePO$_4$X (X = OH, F) obtained by iono-thermal syntheses and compared with those reported in literature

LiFePO$_4$X X = OH, F	***a*** **(Å)**	***b*** **(Å)**	***c*** **(Å)**	***α*** **(Å)**	***β*** **(Å)**	***γ*** **(Å)**	**V (Å^3)**	**V/Z (Å^3)**
	Iono-thermal synthesis							
From: EMI-TFSI	5.124(7)	5.330(8)	7.301(6)	106.58(3)	109.17(1)	97.82(1)	174.66(1)	87.33
From: Triflate	5.159(4)	5.320(6)	7.277(1)	107.17(8)	108.49(3)	98.10(2)	174.80(5)	87.37
	Reported LiFePO$_4$X from literature[1]							
LiFePO$_4$F Recham [7]	5.155	5.304	7.261	107.36	107.86	98.62	173.91	86.96
LiFePO$_4$F Ramesh [8]	5.152	5.300	7.260	107.34	107.88	98.56	173.67	86.84
LiFePO$_4$OH$_{0.4}$F$_{0.6}$ Ellis [6]	5.133	5.323	7.288	106.80	109.00	97.82	174.31	87.15
LiFePO$_4$OH Marx [3]	5.119	5.353	7.290	106.36	109.36	97.73	174.98	87.49
	Ceramic synthesis							
Before washing	5.154(2)	5.305(6)	7.258(5)	107.35(4)	107.95(1)	98.47(5)	173.86(5)	86.93
After washing	5.153(8)	5.304(8)	7.257(6)	107.35(2)	107.95(4)	98.47(3)	173.80(3)	86.90

The obtained lattice parameters are gathered in Table III-2 together with the reported lattice parameters of LiFePO$_4$F [7, 8], LiFePO$_4$(OH)$_{0.4}$F$_{0.6}$ [6] and LiFePO$_4$OH [3]. The table indicates that the OH/F content (ligands which bridge the iron octahedra chains) affects the lattice parameters, particularly the unit cell volume. The ionic radii of OH$^-$ is indeed significantly bigger than the one of F^- (0.152 nm for OH^- *vs.* 0.119 nm for F^-) and the close inspection of the V/Z ratios in the powders we obtained from iono-thermal synthesis suggests $LiFePO_4OH_{1-x}F_x$ compositions. One can observe from the XRD patterns of the sample prepared by EMI-TFSI, a low crystallinity of the particles. Contrary to the ceramic route, we observed poor reproducibility of the iono-thermal synthesis route.

---

[1] The lattice parameters from T.N. Ramesh, B.L. Ellis and N. Marx have been put in the proper unit cell as described in the General Introduction.

III-2b. One-step Ceramic Synthesis

The synthesis of $LiFePO_4F$ through a ceramic route was carried out using the patented protocol of N. Recham et al. [16] in which Li_3PO_4 and FeF_3 were chosen as precursors which led to the formation of LiF and $LiFePO_4F$ according to the equation ①:

① $$Li_3PO_4 + FeF_3 \rightarrow LiFePO_4F + 2\ LiF$$

Stoichiometric amounts of Li_3PO_4 and FeF_3 were ball-milled under inert Ar atmosphere. The recovered powder was pressed into a pellet in a glove box filled with Ar and placed in a gold tube sealed under Ar and heated up to 700 °C for 1 hour prior to be quenched in liquid nitrogen.

The obtained yellowish (recalling the color of $LiFePO_4OH$ [3]) pellet was ground and the XRD was performed using a Panalytical diffractometer (X'Pert PRO MPD) with a Cu $K\alpha_1$ radiation. As presented in Figure III-3a, $LiFePO_4F$ was obtained together with LiF (peak at 38.7°) in the non-washed sample as expected from reaction ①. The peaks of the X-ray diffraction patterns are very sharp compared with those issued from the sample obtained from iono-thermal synthesis (see Figure III-2). The SEM image (insert Figure III-3) indicates highly agglomerated particles with particles size around 5-7 µm.

It is possible, using cold water, to get rid of LiF formed during the synthesis. As shown in Figure III-3b LiF disappeared when the sample had been rinsed in cold water. This raised the question of the stability of $LiFePO_4F$. According to the unit cell parameter obtained by full-pattern matching refinement of the XRD data, both washed and non-washed $LiFePO_4F$ exhibited very similar unit cell parameters (Table III-2) and the volumes per formula group unit are in agreement with the presence of F^- ligand instead of mixed OH/F. Since well-crystallized and large amounts of pure $LiFePO_4F$ (~500 mg) can be obtained through a one step-ceramic process, we therefore adopted that method for further study of Tavorite $LiFePO_4F$. The chemical composition of the samples was confirmed by using an ICP-OES spectrometer. The obtained ratio is $Li_{1.01}/Fe_{1.00}/P_{1.04}$ and no residual H (as one might expect regarding the washed sample) was present which agrees well with the expected formula of $LiFePO_4F$.

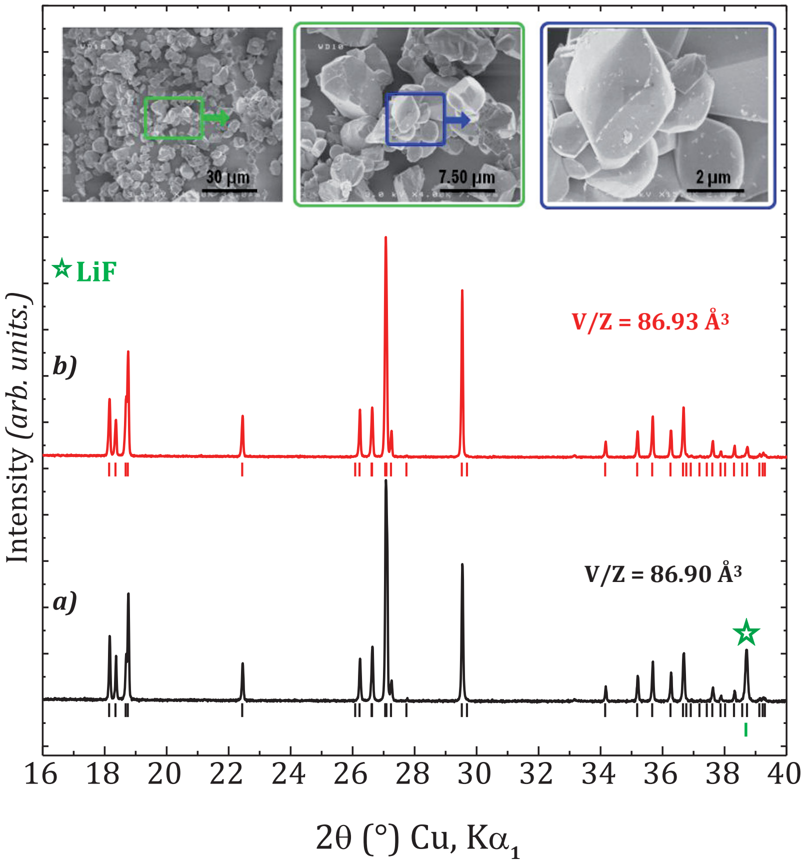

Figure III-3: XRD patterns of $LiFePO_4F$ preparations obtained after ceramic synthesis a) before washing and b) after washing with calculated Bragg positions. SEM images are included in the inserts.

III-2c. Mössbauer spectroscopy and Magnetic properties of $LiFePO_4F$

Both samples (washed and non-washed) have been studied by Mössbauer spectroscopy in collaboration with A. Wattiaux (ICMCB–Bordeaux). The samples were prepared as finely ground powders. The sample holder was formed by a tight stacking of two nylon disks between which the powders were inserted. The samples were analyzed with a constant acceleration Halder–type spectrometer at room temperature using ^{57}Co source (Rh matrix) in transmission geometry. Polycrystalline absorbers containing about 10 mg/cm^2 of iron were used to avoid the experimental widening of the lines. The velocity was calibrated using pure iron metal as the standard material. The calculation of the spectra was performed in two steps using two computer programs. Preliminary calculations adjust the spectra using Lorentzian profile lines, position, amplitude and width of each line are parameters that can be refined. The obtained Mössbauer parameters of isomer shift δ, quadrupole splitting Δ, and half width of peak Γ, are inserted in Figure III-4. For both (washed and non-washed) samples, the value of the isomer shift (δ) and of the quadrupolar splitting (Δ) confirmed the presence of Fe^{3+} lying in octahedral sites, indicating that the washing procedure we used had no impact on the recovered $LiFePO_4F$ phase.

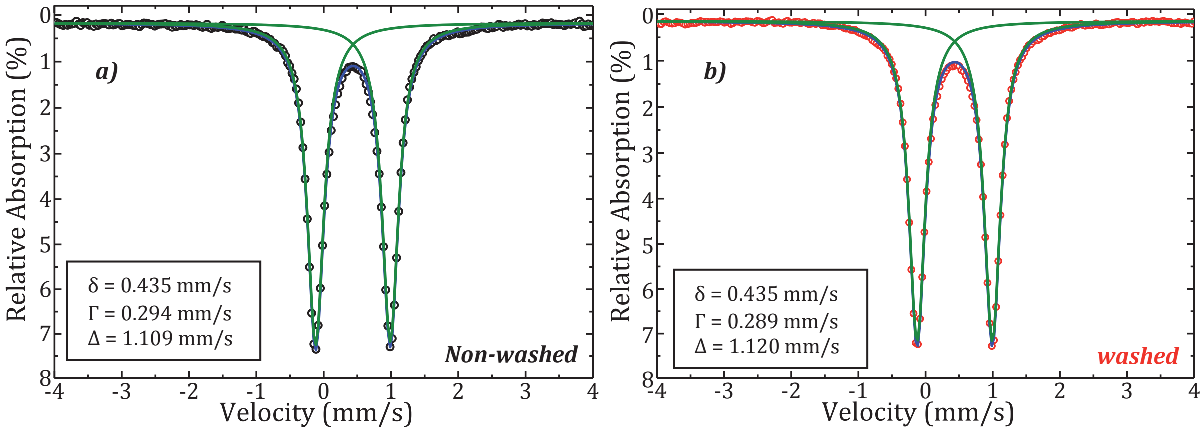

Figure III-4: Calculated spectrum (blue line) and deconvolution (green line) of experimental data obtained a) before washing (black dots) and b) after washing (red dots) for the $LiFePO_4F$ phase obtained by ceramic route

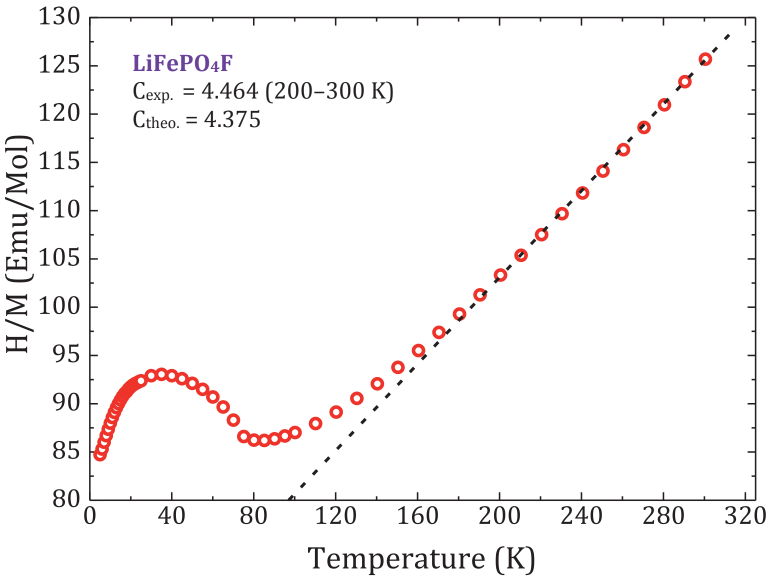

Figure III-5: Temperature dependence of the H/M ratio for the washed $LiFePO_4F$. Comparison of experimental and theoretical Curie constants is given and the temperature range used for its calculation.

The oxidation state of Fe was also confirmed by the measurement of the static molar magnetic susceptibility of a washed sample. The measurement was made between 5 and 300 K using a SQUID magnetometer (Quantum Design). The zero-field cooled χ value was obtained by cooling the sample in zero-field down to 5 K and then heating it under the applied field. The diamagnetic contributions were corrected using the atomic values from Bain and Berry [25] yielding the χ_M paramagnetic susceptibility contribution. The temperature dependence of the H/M ratio for $LiFePO_4F$ is pictured in Figure III-5. A curvature at around 90 K indicates an antiferromagnetic behavior and the Néel temperature was determined as being 80 K. A similar antiferromagnetic behavior was also observed for Tavorite $LiFeSO_4F$ and $FeSO_4F$ [26] within which the oxidation state of Fe is +2 and +3 respectively. Note that the Néel temperature determined for $LiFeSO_4F$ is 25 K and 50 K for the delithiated $FeSO_4F$. In $LiFePO_4F$, Curie–Weiss type paramagnetism appears for temperatures higher than 200 K. The obtained Curie constant of 4.464 is close to the theoretical value expected for HS Fe^{3+} ($C_{theo}(LiFe^{III}PO_4F)$ = 4.375). Further confirmation of the different oxidations states of cations (Fe, P and Li) will be given through bond valence calculations within the crystal structures and the magnetic structure at low temperatures will be determined by Rietveld refinement of neutron diffraction data.

III-2d. Conclusion

The iono-thermal synthesis as well as the ceramic synthesis led to the formation of LiF when Li_3PO_4 and FeF_3 were chosen as precursors, so that $LiFePO_4F$ was obtained indirectly. The use of EMI-TFSI and Triflate as solvent for iono-thermal synthesis, led to the formation of $LiFePO_4OH_xF_{(1-x)}$ within which the ligand (bridging two octahedra) is a mix OH/F instead of F. Particles obtained after using Triflate presented higher crystallinity compared with those from EMI-TFSI. The poor reproducibility and the small amounts of powder obtained led us to use a ceramic route for the syntheses of $LiFePO_4F$.

Ceramic syntheses yielded pure $LiFePO_4F$ powders, free of OH groups and with large and well crystallized particles. ICP analysis confirmed the stoichiometric composition of $LiFePO_4F$. The experimental Curie constant ($C_{exp.}$ = 4.464) of the obtained powder was in good agreement with the theoretical Curie constant ($C_{theo.}$ = 4.375) confirming the oxidation state of iron (Fe^{3+}). LiF was successfully removed from the final product when the sample had been washed with cold water. Mössbauer spectroscopy indicated no changes of the $LiFePO_4F$ phase after washing (iron oxidation state remained +3).

III-3. CRYSTAL AND MAGNETIC STRUCTURES OF $LiFePO_4F$

III-3a. Crystal structure of $LiFePO_4F$

Several proposed crystal structures of $LiFePO_4F$ were published recently, basically with similar descriptions but differing from the occupancies of the Li crystallographic sites. N. Recham et al. [7] described the structure of $LiFePO_4F$ with two crystallographic sites of Li which occupancies had been fixed to 50% for each, separated by a distance of 0.8 Å. T.N. Ramesh et al. [8] described the structure of $LiFePO_4F$ with the occupancies of the two sites of Li being 77% and 23% each and separated by 0.7 Å. In both cases, only lab XRD data were used. We extended this crystallographic study using neutron diffraction data, especially suited for the determination of Li's sites. The structure will be compared with the Tavorite-like analogous $FePO_4{\cdot}H_2O$ and $LiFePO_4OH$ and the Li positions will be compared with the published position of N. Recham and T.N Ramesh.

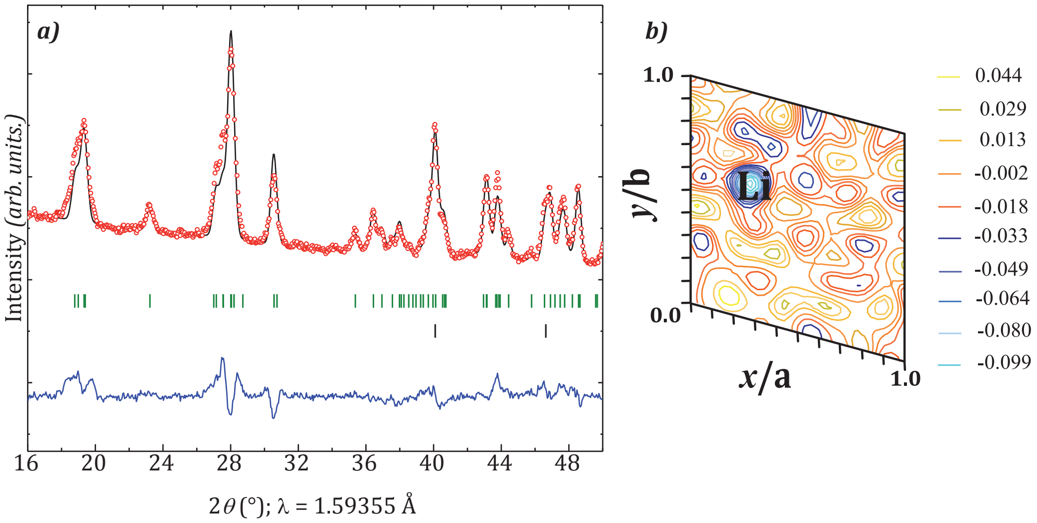

Figure III-6: a) Rietveld refinement of neutron diffraction data (only Fe, P, O and F atoms are considered); b) 2D section of 3D Fourier difference maps at y = 0.278 with the maximum corresponding to the Li site in the crystal structure of $LiFePO_4F$

Just as for $LiVPO_4O$ and $LiVPO_4F$, (chapter I), the XRD data were collected from a Panalytical diffractometer (X'Pert PRO MPD) equipped with a Cu $K\alpha_1$ radiation (thanks to a Ge monochromator), and neutron diffraction was performed at the Institute Laue Langevin (Grenoble, France) on the high-resolution diffractometer D2B. For both XRD and neutron diffraction data, the measurements were carried out on the non-washed sample of $LiFePO_4F$.

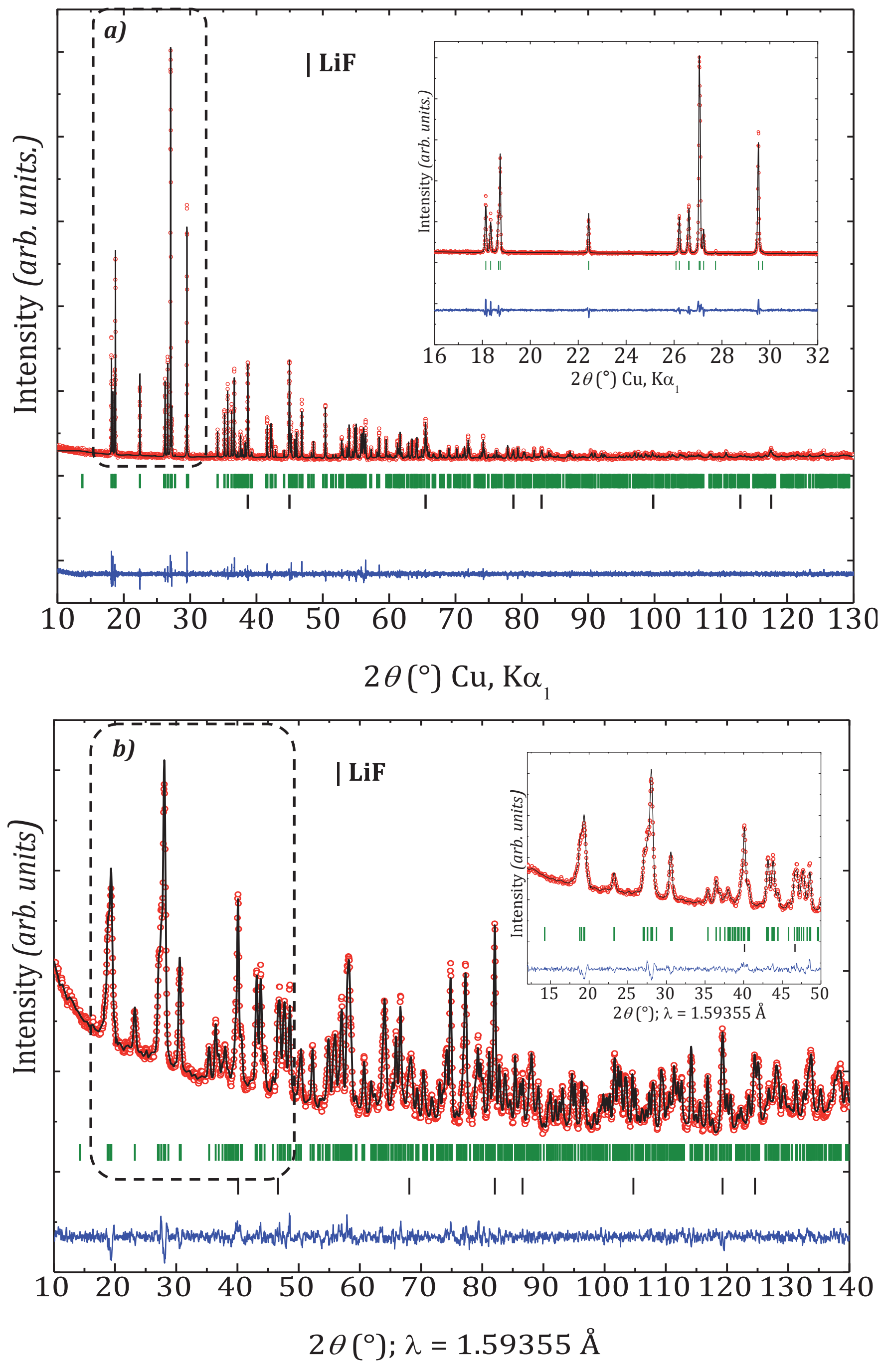

Figure III-7: Observed (red dots), calculated (black line), and difference (blue line) plots obtained for the Rietveld refinement of (a) X-ray diffraction data and (b) neutron diffraction data for $LiFePO_4F$

The absorption coefficient μR is 0.28 [27]. The Rietveld refinements were carried out using the structural model of $LiVPO_4F$ (see Chapter I). The different steps of refinement were as follow:

1. The structural model $Fe(1)_{1a}Fe(2)_{1b}\ P_{2i}[O_{2i}]_4F_{2i}$ free of Li was first refined: in our model, Fe(1) and Fe(2) atoms occupy special *1a* (0, 0, 0) and *1b* (0, 0, 1/2) positions respectively. Figure

III-6a shows, in this case, the poor quality of the refinement with bad minimization of the intensity difference.

2. We then calculated Fourier difference maps considering only the host structure $Fe(1)_{1a}Fe(2)_{1b}P_{2i}[O_{2i}]_4F_{2i}$. The calculated Fourier (Figure III-6b) differential map shows a maximum negative residual nuclear density located in *2i* position at (~0.251, ~0.602, ~0.281).

3. This position was hence included in the atomic coordinates list in order to refine properly the neutron diffraction data. Subsequent Fourier Difference maps showed non residual nuclear densities and we thus adopted a structural model with only one Li(1) crystallographic site at *2i*(0.7198(1), 0.3783(7), 0.233(1)). Separate refinements of thermal motion factors and occupancies led to satisfactory reliability factors (Table III-1 of the ANNEXE I) and good minimization of the difference intensity for X-rays and neutron data refinements, as shown in Figure III-7. The lattice parameters as well as the atomic positions are gathered in Table III-1 of the ANNEX I. The resulting inter-atomic distances are recorded in Table III-2 of the ANNEX I.

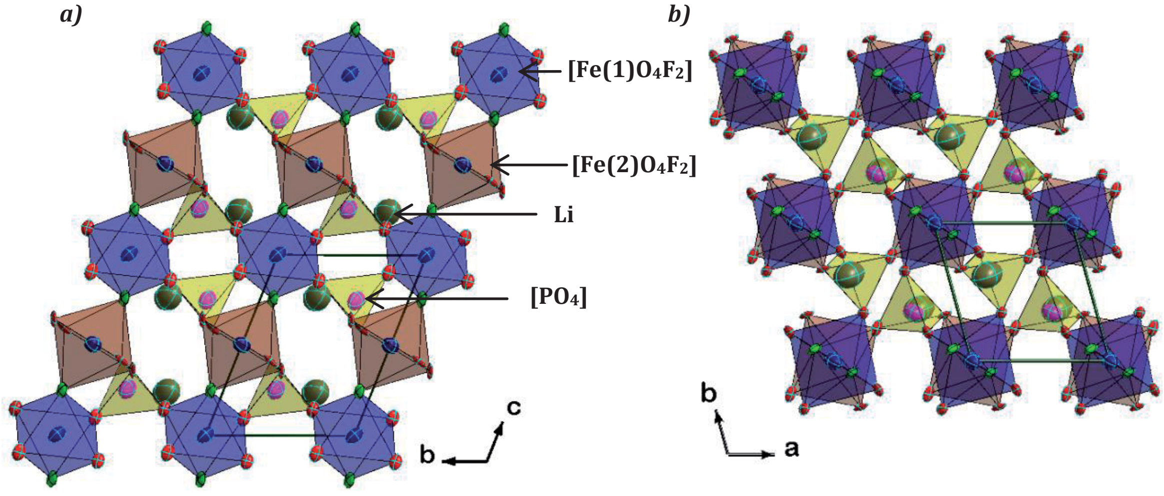

Figure III-8: Skeleton framework structure of Tavorite LiFePO$_4$F with ellipsoid representation of atoms as obtained after thermal motion refinements

It is well-established that lithium iron (III) fluorophosphate belongs to the Tavorite system so that the crystal structure is built up by [FeO$_4$F$_2$] octahedra which share common fluorine atoms. The resulting chains are running along $[001]_{P\bar{1}}$ direction. Fe lies within two octahedral sites with Fe−O distances range of 1.95−2.01 Å (Table III-2 of the ANNEX I). The value of the Fe-F distance (1.98 Å), is the same as the V-F one observed along the chains of [VO$_4$F$_2$] octahedra in the structure of LiVPO$_4$F. Based on the good quality of the XRD and neutron diffraction data, we were able to refine the anisotropic parameters for all atoms (Table III-3). The anisotropic displacement of Fe is oriented in the equatorial plane of oxygen atoms (Figure III-8).

Table III-3: Anisotropic thermal motion parameters U_{ij} (in Å) for $LiFePO_4F$

Atoms	U_{11}	U_{22}	U_{33}	U_{12}	U_{13}	U_{23}
Fe(1)	0.01225	0.01155	0.01373	0.00032	0.00531	0.00029
Fe(2)	0.01465	0.01647	0.01392	0.00234	0.00534	0.00668
P	0.01841	0.01377	0.01825	-0.00085	0.00690	0.00347
O(1)	0.01000	0.01600	0.00900	0.00780	0.00490	0.01040
O(2)	0.01272	0.00393	0.01467	0.00433	0.00373	0.00523
O(3)	0.00821	0.00932	0.01431	0.00358	0.00664	0.00374
O(4)	0.00586	0.01018	0.01689	-0.00032	0.00408	0.00385
F	0.01104	0.00556	0.01220	0.00509	0.00045	0.00291
Li	0.07060	0.04885	0.05152	0.02137	0.01270	0.01366

The Fe–F distance in $LiFe^{III}PO_4F$ is very small compared with the Fe-(OH_2) distance (2.17 Å) observed in the $Fe^{III}PO_4{\cdot}H_2O$ structure [3]. For $LiFe^{III}PO_4OH$, it was established that the Fe-(OH) bond lengths were close to 2.02 Å. The length of the Fe–X bond (X = F, OH, OH_2) increases significantly with the presence of OH and OH_2 (see Figure III-9) due to the high covalency of the O–H bond which further weakens the Fe–X bond through the inductive effect.

$$d_{(Fe\text{-}F)}LiFePO_4F = 1.98\ Å < d_{(Fe\text{-}OH)}LiFePO_4OH = 2.02\ Å < d_{(Fe-OH_2)}HFePO_4OH = 2.17\ Å$$

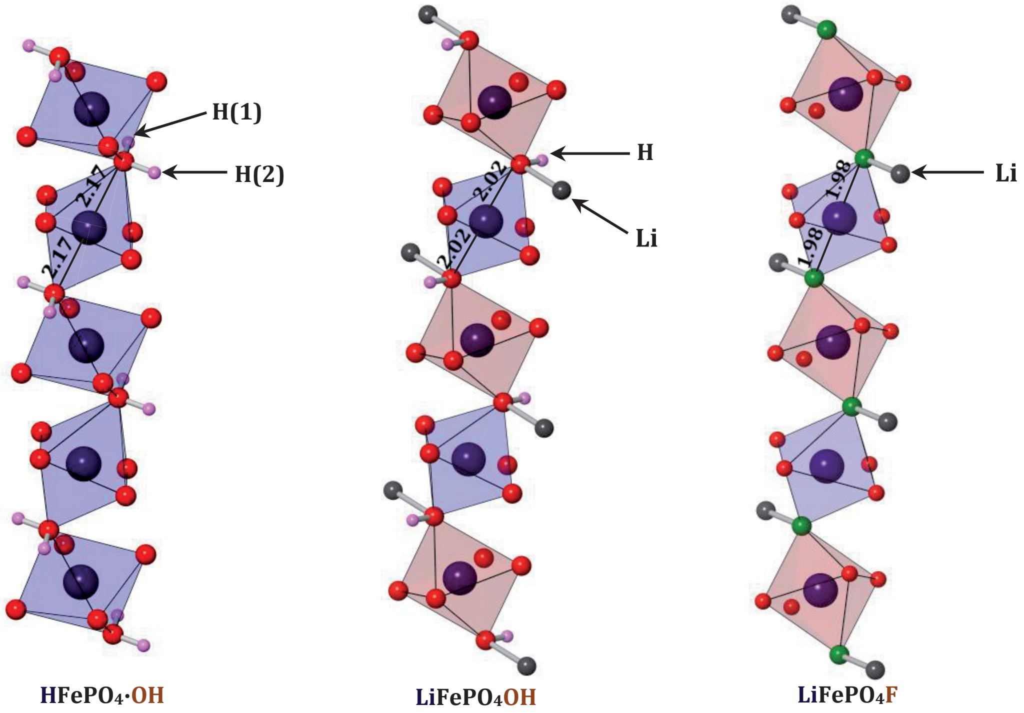

$HFePO_4{\cdot}OH$ **$LiFePO_4OH$** **$LiFePO_4F$**

Figure III-9: Octahedral chains of FeO_4X_2 in $AFePO_4X$ (with A = H or Li and X = OH or F)

In comparison with LiFePO$_4$OH, the distortions of the octahedra in the structure of LiFePO$_4$F are very close to each other ($\Delta_{\mathrm{Fe(1)O_4F_2}}$ = 3.45·10^{-5} and $\Delta_{\mathrm{Fe(2)O_4F_2}}$ = 1.68·10^{-5} in LiFePO$_4$F *vs.* $\Delta_{\mathrm{Fe(1)O_4O_2}}$ = 1.7·10^{-5} and $\Delta_{\mathrm{Fe(2)O_4O_2}}$ = 2.7·10^{-4} in LiFePO$_4$OH). N. Marx et al. [5] had shown that the difference of the distortion of the two iron octahedral sites was visible in Mössbauer spectroscopy data of LiFePO$_4$OH through the asymmetric doublet of the observed line. This asymmetry of the doublet together with the broadness of the lines led N. Marx to consider and to refine the Mössbauer spectrum with two different sites of Fe. We first considered N. Marx's approach (two different crystallographic sites of Fe) for the refinement of the Mössbauer data. The obtained χ^2 value was very poor although we had a very good data resolution. Based on the very similar distortion of the two irons octahedra sites and to the sharpness of the lines, we successfully refined the Mössbauer data considering one distribution site of Fe. The obtained Mössbauer parameters are listed in Table III-4.

Table III-4: Mössbauer parameters, distortions and Fe–X distances of the washed LiFePO$_4$F (LiFePO$_4$F$_w$) and the non-washed LiFePO$_4$F (LiFePO$_4$F$_{nw}$) in this study compared with the reported LiFePO$_4$OH and HFePO$_4$·OH **[3].**

	LiFePO$_4$F$_{nw}$		**LiFePO$_4$F$_w$**		**LiFePO$_4$·OH**		**HFePO$_4$·OH**
Sites	Fe^{3+}(1)	Fe^{3+}(2)	Fe^{3+}(1)	Fe^{3+}(2)	Fe^{3+}(1)	Fe^{3+}(2)	Fe^{3+}
Distortion of [FeO$_4$X$_2$]	3.45·10^{-5}	1.68·10^{-5}	3.45·10^{-5}	1.68·10^{-5}	1.7·10^{-5}	2.7·10^{-4}	2.8·10^{-3}
Fe–X (Å)	1.98	1.98	1.98	1.98	2.02	2.02	2.17
δ (mm/s)	0.435		0.435		0.405	0.415	0.407
Γ (mm/s)	0.294		0.289		0.3	0.3	0.3
Δ (mm/s)	1.109		1.120		0.67	0.57	1.58
%	100		100		49.6	50.4	100

The values of the isomer shifts (δ) are typical for the oxidation state +3 of Fe [28] and the quadrupolar splitting (Δ) fits well with Fe^{3+} in octahedral environment [28]. The isomer shift depends on the oxidation state of Fe and also on the ligand, as illustrated in Table III-4. The FWHM (Γ) were fixed to 0.3 for both LiFePO$_4$OH and FePO$_4$·H$_2$O [29], whereas for LiFePO$_4$F, this value was refined and converged to 0.294 and 0.289 for non-washed and washed samples respectively. N. Marx et al. [29] had linked the quadrupolar splitting with the distortion of [FeO$_4$X$_2$] claiming that the quadrupolar splitting decreases when octahedral site of Fe is more symmetrical. This argument does not apply to LiFePO$_4$F which presents a higher quadrupolar splitting despite less distorted octahedral sites of Fe.

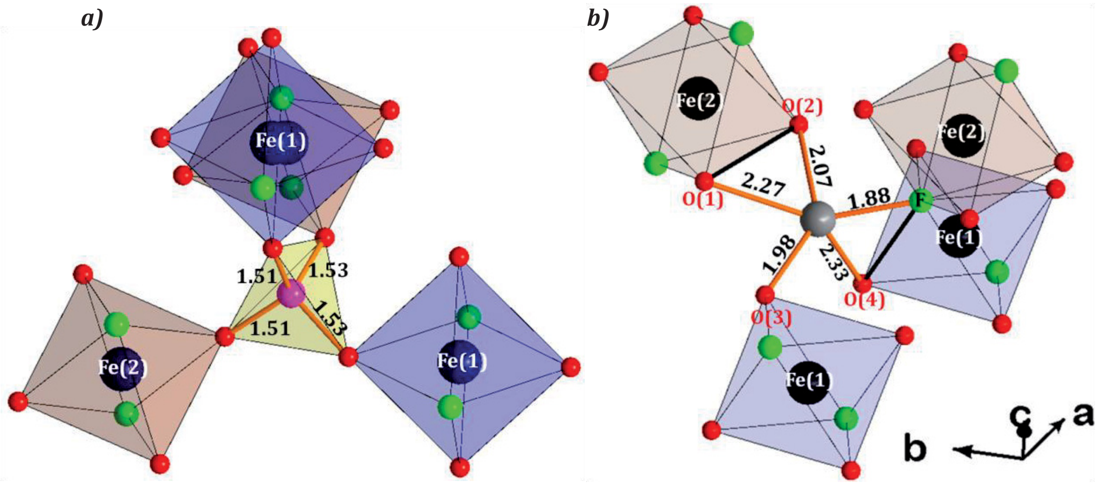

Figure III-10: a) Schematic representation of [PO_4] tetrahedron local environment in $LiFePO_4F$ b) Schematic representation of LiO_4F local environment in $LiFePO_4F$.

The P−O distances in $LiFePO_4F$ are in a very narrow range of 1.50−1.55 Å (Figure III-10a). This unique phosphorus atom lies within a tetrahedron which distortion is $\Delta = 4.14\cdot10^{-5}$, very similar to the distortion of the [PO_4] tetrahedron in $LiFePO_4OH$ ($\Delta = 4.2\cdot10^{-5}$) and different compared with the one from $FePO_4\cdot H_2O$ ($\Delta = 3.8\cdot10^{-4}$).

As seen in Figure III-10b, the unique Li(1) site is surrounded by four oxygen and one fluorine atoms, forming a very distorted five-vertex polyhedron ($\Delta = 6.51\cdot10^{-3}$). Just like in the case of $LiVPO_4F$, the pentahedral site around Li^+ shares one edge with one [$Fe(2)O_4F_2$] and [$Fe(1)O_4F_2$] respectively. As illustrated in Figure III.9 the Li position is in the ligand's neighborhood for both $LiFePO_4OH$ and $LiFePO_4F$. In both structures, Li is oriented in the same direction as H(2) in $FePO_4\cdot H_2O$. The calculated valence bond sums (BVS) for the cations using "Bond_Str" software in Fullprof_suite matched well with expected values and gave respectively $BVS_{Fe(1)}=3.04$, $BVS_{Fe(2)}=3.02$, $BVS_{P(1)}=5.10$, and $BVS_{Li(1)} = 0.95$ in reasonably good agreement with expectations.

III-3b. NMR measurements

The ^7Li, ^{31}P, and ^{19}F MAS NMR spectra were recorded (in collaboration with M. Ménétrier and M. Duttine) at 100MHz in the same conditions as previously reported (Chapter I) using a Bruker Advance III spectrometer equipped with a 2.35 T magnet.

The ^7Li MAS NMR (Figure III-11a) exhibits two sharp isotropic signals located at 203 ppm and -1 ppm corresponding to the unique lithium site in the $LiFePO_4F$ structure and to LiF respectively. This result is in a good agreement with Rietveld refinements of neutron diffraction data which established only one Li site in $LiFePO_4F$ structure. The unique site of lithium in

LiFePO$_4$F is consistent with previous observations in fluorophosphate/sulphate Tavorite compositions where one lithium site has been found [5, 10, 29, 30]. One can notice a tiny shoulder at 150 ppm associated with an impurity which could not be detected by X-ray diffraction. Further NMR studies have to be performed in order to know whether this signal is an impurity or is correlated to the signal at 203 ppm *i.e.* associated to some structural defects in the LiFePO$_4$F structure. The shift in LiFePO$_4$F is stronger than in LiVPO$_4$F, since HS Fe^{3+} contains much more electron spins with a $t_{2g}^{3}\ e_{g}^{2}$ electronic configuration.

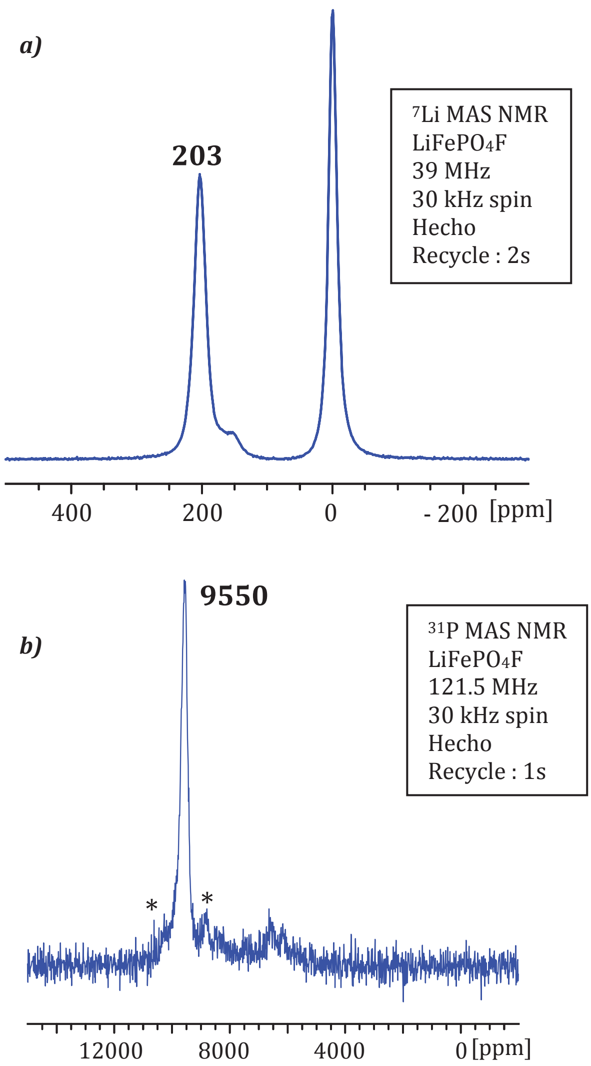

Figure III-11: a) ^{7}Li MAS NMR and b) ^{31}P MAS NMR spectrum of LiFePO$_4$F (spinning sidebands are shown by asterisks).

As expected regarding the above-described structure, ^{31}P MAS NMR exhibits one sharp signal, which is highly shifted at 9550 ppm, a logically higher value again than in the V compound (Figure III-11b). Additional weaker contributions are also present around 6500 ppm, which can be due to impurities and/or defects (like the additional ^{7}Li NMR signal).

No signal was observed by ^{19}F MAS NMR, which is not a surprise since Fe^{3+} with high spin configuration $t_{2g}^3\,e_g^2$ should exert a very strong electron-nucleus dipolar interaction and contribute to a very high electron spin transfer. The ^{19}F NMR signal is therefore expected to be much broader and more shifted (Fermi contact) than the signal in LiVPO$_4$F (-1500 ppm) where the configuration of V^{3+} is $t_{2g}^2\,e_g^0$.

Since LiFePO$_4$OH, FePO$_4$·H$_2$O and LiFePO$_4$F all contain HS Fe^{3+} with all *d* orbitals containing one electron spin, the situation is a priori simpler than in the V case (see chapter I), and it is tempting to discuss the comparison of the Li and P shifts in the three compounds. In FePO$_4$·H$_2$O, the (H2-)O—Fe bond is weakened (and lengthened) by the two antagonistic strongly covalent O—H bonds compared to LiFePO$_4$OH. This leads to shorter and stronger Fe—O—P bonds and consequently to a stronger hyperfine interaction causing a stronger ^{31}P NMR shift in FePO$_4$·H$_2$O than in LiFePO$_4$OH as discussed by Castets et al. [31]. In the LiFePO$_4$F case, one cannot compare the Fe—F distance to that of Fe—O(--H or H$_2$) in order to compare bond strengths or covalency with the oxide compounds, and to discuss the antagonistic (P--)O—Fe bond. However, the latter bond distance in LiFePO4F is somehow intermediate between those in the two oxides, and so is the ^{31}P NMR shift (9550 ppm compared to 7498 ppm for LiFePO$_4$OH and 11 066 ppm for FePO$_4$·H$_2$O). On the contrary, the Li NMR shifts are rather close in LiFePO$_4$F (203 ppm) and LiFePO$_4$OH (214 ppm).

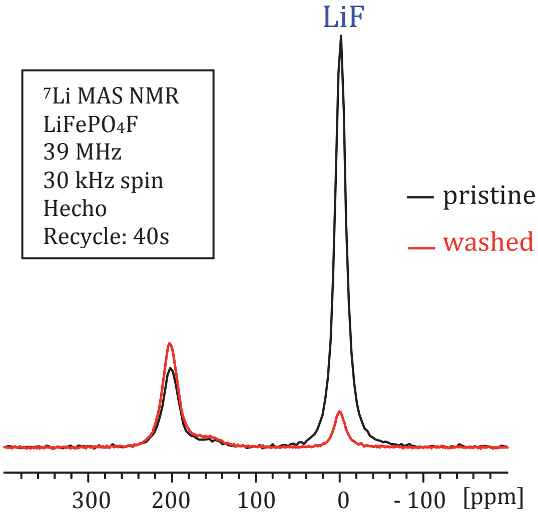

Figure III-12: ^{7}Li MAS NMR spectrum of LiFePO$_4$F before (black) and after (red) washing.

Figure III-12, illustrates the effect of the "washing" procedure we used for LiFePO$_4$F/LiF mixtures: a very small quantity of LiF can be observed in the MAS NMR spectrum of the washed sample indicating that we have not totally removed LiF contrary to what X-ray diffraction data suggested. Note that the relative ratio between the Li in the material and in LiF is different in this figure from above (Figure III-11b). This is due to a longer recycle delay used for the spectra in the present figure, required for a quantitative observation of the Li from LiF due to its longer T1 relaxation time. Besides, the peak at 203 ppm associated to the unique lithium site in $LiFePO_4F$ as well as the peak at 150 ppm has not changed after washing, emphasizing the stability of $LiFePO_4F$.

Further confirmation of the stability of $LiFePO_4F$ has been made using ^1H MAS NMR which shows no significant proton signal in Figure III-13 (the signals present are due to artifacts from the probe and rotor, since they are also observed without a sample), stressing the absence of proton in the washed $LiFePO_4F$, and in particular, the absence of the $LiFePO_4OH$ phase whose spectrum has been added to the figure for comparison [31-33].

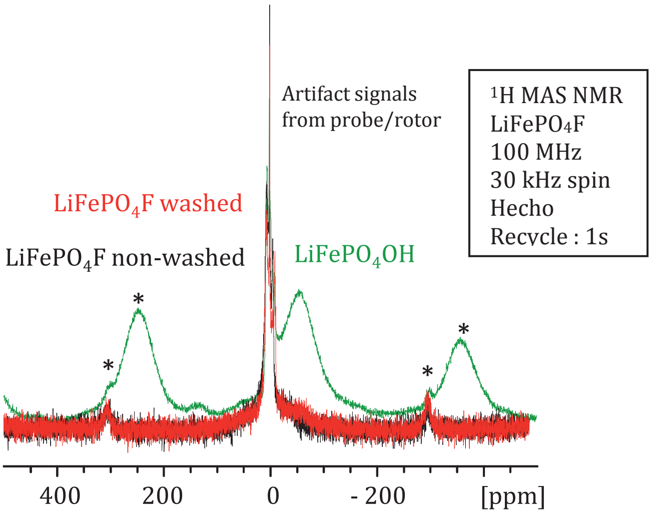

Figure III-13: ^1H MAS NMR spectrum of $LiFePO_4F$ before (black) and after (red) washing compared to the signal for $LiFePO_4OH$ (green). Spinning sidebands are marked by asterisks.

III-3c. Magnetic structure of $LiFePO_4F$

In collaboration with E. Suard (from ILL-Grenoble) and G. Rousse (from UPMC-Paris), we performed neutron powder diffraction at low temperature, on $LiFePO_4F$, in order to determine its possible magnetic structure below T_N = 90 K using the D2B diffractometer. The non-washed $LiFePO_4F$ sample presents extra peak at 2 K that are a consequence of the long range ordering of the magnetic moments. Those peaks are more intense for $LiFePO_4F$ compared to $LiVPO_4F$ where only two tiny extra peaks appeared resulting from the number of electron spins present in both transition metals.

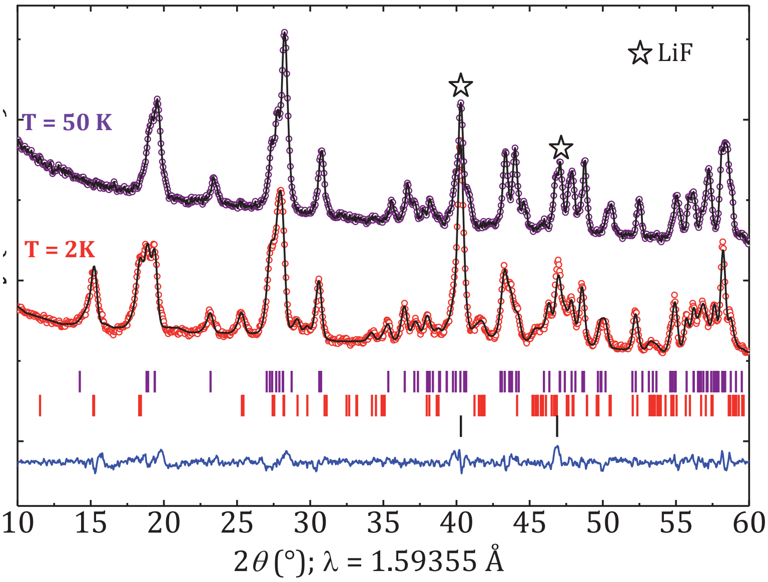

Figure III-14: Rietveld Refinements of neutron diffraction data of the non-washed LiFePO$_4$F: Observed versus calculated (black line) powder neutron diffraction patterns collected at 2K (red dots) and 50 K (purple dots). The difference pattern (blue line) is displayed at the panel bottom. The positions of the Bragg reflections are shown as vertical bars below

The magnetic peaks can be indexed using the **k** = (½ ½ 0) propagation vector, so that the magnetic cell is 4 times larger than the nuclear cell. The latter being of triclinic symmetry ($P\bar{1}$), there is no constraint to be added between the magnetic moments due to the symmetry analysis: indeed the 2 Fe atoms of the nuclear cell are distributed on the 1*a* and 1*b* Wyckoff positions. We have therefore considered (just as for LiVPO$_4$F) two possible cases: either the magnetic moments of metals present on the two Wyckoff sites are parallel or antiparallel, so that the resulting magnetic structure will be collinear. The refinement of the 2K structure using these two different models, and allowing the magnetic moment to orient in any direction, leads to a much better refinement when the two magnetic moments of the metals are antiparallel. The refinement leads to a total magnetic moment of 3.92(4) μ_B. This value is lower than the 5 μ_B expected for Fe^{3+} in high spin configuration: d^5, $t_{2g}^3\ e_g^2$, **S** = 5/2, **L** = 0. B. C. Melot et al. [26] reported a magnetic moment of 4.32 μ_B for Fe^{III}SO$_4$F.

Figure III-14 presents the refinement of neutron data for both temperatures (above and below T$_N$) where better evidence of the magnetic peaks is shown on the pattern recorded below T$_N$. The resulting magnetic structure is presented in Table III-5, and illustrated in Figure III-15. The reliability factor was 4.80% better (lower) than for LiVPO$_4$F (19.5%) probably due to high intensity magnetic peaks observed for LiFePO$_4$F contrary to LiVPO$_4$F in which two tiny peaks were present.

Table III-5: Magnetic moments (μ_B) at 2 K, the components (in μ_B) are given along the a, b and c axes. Propagation vector k = (½, ½, 0), G-type magnetic structure, Magnetic R-factor=4.80%

$LiFePO_4F$					
Atom		m_a	m_b	m_c	M_{Total} (μ_B)
Fe(1)	Fe (0 0 0)	3.4(1)	-1.6(2)	0.7(2)	3.92(4)
Fe(2)	Fe (0 0 ½)	-3.4(1)	1.6(2)	-0.7(2)	3.92(4)

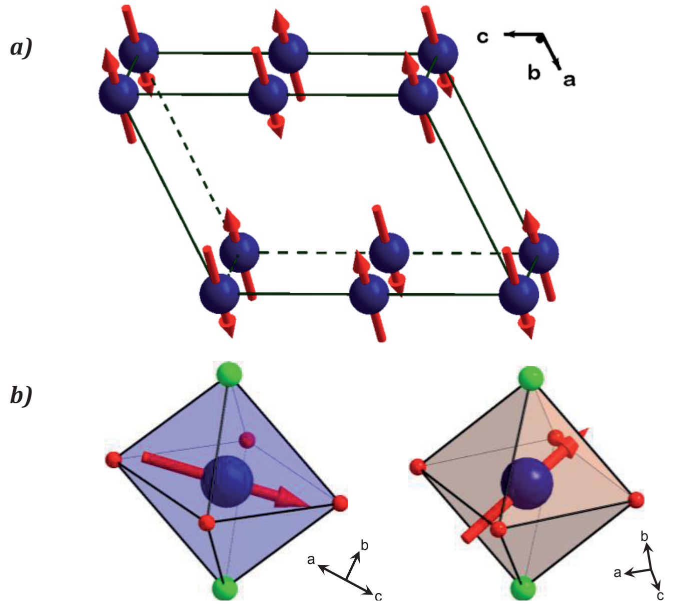

Figure III-15: Illustration of the proposed magnetic structure of $LiFePO_4F$: a) 3D view of the magnetic structure b) 3D view of moment in isolated octahedra: [Fe(1)O_4F_2] octahedra (blue) and [Fe(2)O_4F_2] octahedra (red)

The magnetic moments that are along the chains are oriented antiparallel, and the chains are also antiparallel through the propagation vector **k**. The magnetic structure of $LiFePO_4F$ corresponds to magnetic structures analogous in the G-type antiferromagnetic order of perovskites where all nearest neighbors are antiferromagnetically coupled. The spin sequence is the same as for $LiVPO_4F$ but the orientations of the moments are different. The moments are collinear, and almost lying in the oxygen equatorial plane of the [FeO_4F_2] octahedra similar to the orientation of the magnetic moment supported by V(2) in the case of $LiVPO_4F$. Careful inspection of the moment orientation shows that the moment supported by Fe(1) is oriented throughout oxygen atoms whereas the moment supported by Fe(2) is oriented through opposite octahedral faces. The two moments are perpendicular to the direction of the [FeO_4F_2] octahedra chains.

These different orientations of magnetic moments in both $LiVPO_4F$ and $LiFePO_4F$ may be due to the strong spin-orbit coupling observed for Fe^{3+}, but caution has to be exercised concerning the spin orientation of moments, due to the small number of observed magnetic reflections in $LiVPO_4F$.

When comparing these magnetic structures with the one of the sulfate analog $LiFeSO_4F$ and $FeSO_4F$ [26], we can note the following feature: in terms of spin sequence, the magnetic structure we have here is the same as the one observed for $LiFeSO_4F$ (G-type: all nearest neighbors are antiferromagnetically coupled), although in this latter compound the oxidation state of iron is 2+. In contrary, $FeSO_4F$ (that contains Fe^{3+} like $LiFePO_4F$, but presents a monoclinic *C2/c* space group) presents a magnetic structure that differs since the antiferromagnetic chains are coupled ferromagnetically (A-type: ferromagnetic planes of spins that are coupled antiferromagnetically to each other) in $FeSO_4F$. The magnetic structure of these fluorosulfates and phosphates seems to depend strongly on the geometrical characteristics of the structure, in particular to the Fe-O-O-Fe super-super exchange paths that govern the coupling between adjacent chains. The oxidation state of iron is therefore not the only parameter as $FeSO_4F$ and $LiFePO_4F$ present distinct magnetic structures.

III-4. ELECTROCHEMICAL PROPERTIES OF $LiFePO_4F$

J. Barker et al. [17] reported the synthesis of $LiFePO_4F$ but not, surprisingly, its electrochemical signature. N. Recham et al. [7] reported for the first time the galvanostatic signature of $LiFePO_4F$ (see Figure III-16a) with a capacity of 128 mAh/g for the first cycle (85% of the theoretical) at C/15 in the potential window of 1.2 V–4.2 V. The electrochemical signature presented a pseudo plateau at a potential around 1.5 V *vs.* Li^+/Li which was attributed to a possible conversion reaction. A flat plateau was observed during discharge and charge within the composition range for $Li_{(1+x)}FePO_4F$ (x = 0.05–0.45), and $Li_{(1+x)}FePO_4F$ (x = 0.85–0.45) respectively.

The description of the electrochemical signature of $LiFePO_4F$ as published by N. Recham differs from that of T.N. Ramesh et al. [8] (see Figure III-16b). The latter performed a galvanostatic test at a rate of C/10 leading to a capacity of 145 mAh/g within a potential window of 1.5 V–4.0 V. The composition range of $Li_{(1+x)}FePO_4F$ (x = 0–0.35) exhibited a sloping curve centered around 3.1 V, indicative of a single-phase behavior, followed by a two-phase plateau in the region of $Li_{(1+x)}FePO_4F$ (x = 0.35–0.75). The subsequent charge was similar to the discharge, contrary to the electrochemical curve reported by N. Recham.

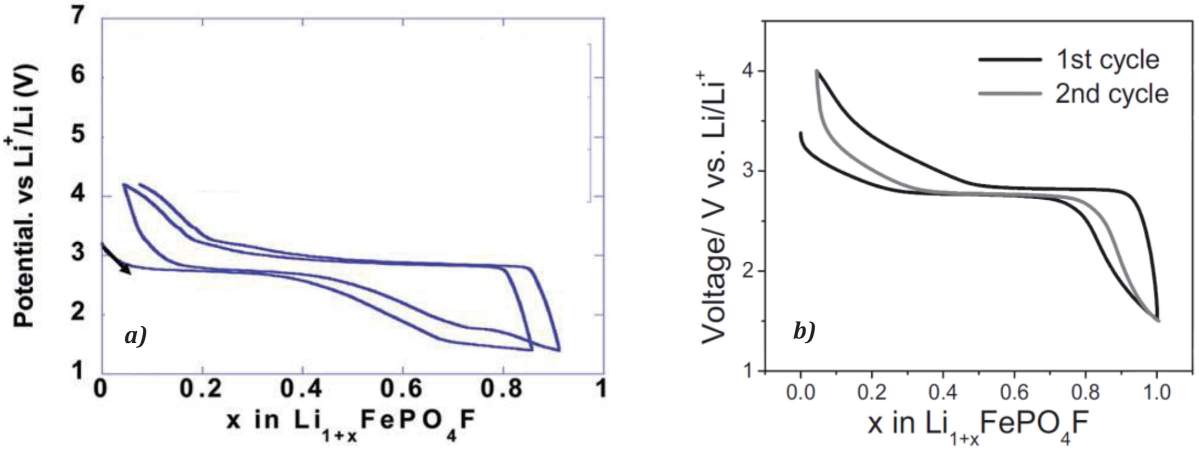

Figure III-16: The electrochemical signature of $LiFePO_4F$ as presented in literature by a) N. Recham et al. [7]; b) T.N. Ramesh et al. [8]

We have performed galvanostatic tests in coin cells assembled in an Ar filled dry glove box. Prior to be used as positive electrodes, the active materials were ball milled with 16 wt% of C_{sp} and 5 wt % of PTFE. The cells consisted of the positive electrode (loading was about 5-7 mg/cm^2), 1 cm^2 Li disks as negative electrode, and $LiPF_6$ (1 M) in a mixture of EC-DMC (1:1) as electrolyte. The lithium insertion/extraction relies on the reversibility of the Fe^{3+}/Fe^{2+} redox couple, so that the electrochemical reaction associated can be summarized as:

$$LiFe^{III}PO_4F + Li^+ + e^- \rightarrow Li_2Fe^{II}PO_4F \qquad \text{Theoretical capacity: 151 mAh/g}$$

The galvanostatic cycling was performed at different current rates and our data are gathered in Figure III-17a-b. Figure III-17a presents the electrochemical performances of $LiFePO_4F$ at a rate of C/10 similar to the one reported in literature. Surprisingly, the reversible capacity was of 83 mAh/g, lower than those reported, but at C/100 the capacity increased up to 143 mAh/g with significantly lower polarization as well. Those results are a consequence of the low kinetics of the obtained phase due to the large particles size of the powders we prepared. The electrochemical signature at C/100 is similar to the one reported by T.N. Ramesh et al [8]. However, at a potential around 3.2 V *vs.* Li^+/Li (and a composition close to $LiFePO_4F$), one can notice a small inflection point, also presents within the data recorded at C/10.

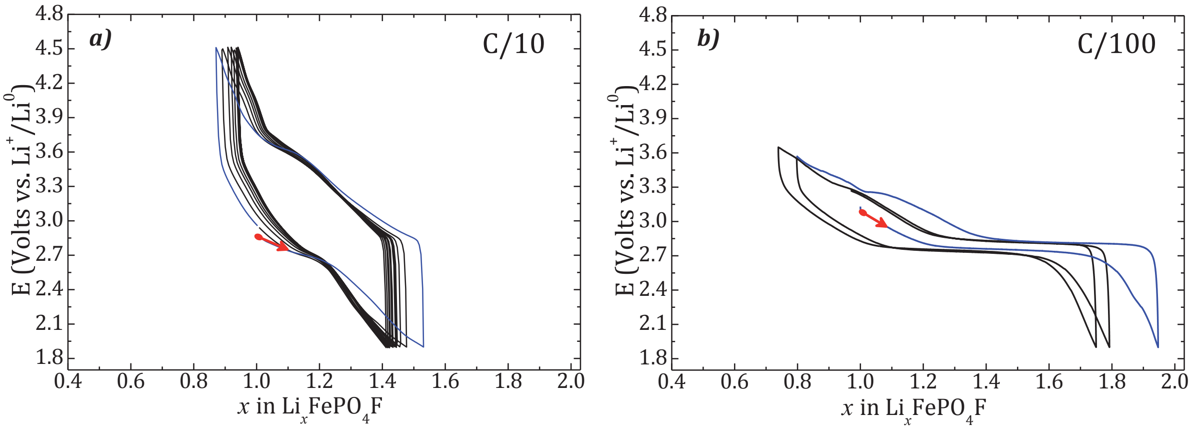

Figure III-17: Electrochemical behavior of $LiFePO_4F$ performed at different C rates a) C/10; b) C/100. The blue line is the first cycle.

More interestingly is that during charge, the electrochemical data presented a sloping outgrowth curve beyond the composition of $LiFePO_4F$, so that the end of the charge process would represent the formation of the $Li_{0.7}FePO_4F$ composition at C/100. This result would suggest an oxidation of $LiFePO_4F$, i.e. implying the rarely encountered oxidation of Fe^{3+} into Fe^{4+}. However the Fe^{4+}/Fe^{3+} couple cannot be present at such low potential. This particular electrochemical signature can be due to the degradation of the $LiFePO_4F$ sample. The XRD pattern of a mixture of $LiFePO_4F$ and C_{sp} (in the weight proportion of 85:15) presented broad peaks (Figure III-18b) after 15 min of Spex milling. After 3 months, the XRD pattern of the previous sample presented extremely broad diffraction peaks probably induced either by an amorphization or a degradation of the sample. The corresponding Mössbauer data tends to suggest that $LiFePO_4F$ get degraded after air exposure of the milled sample: additional lines suggest the presence of iron oxide.

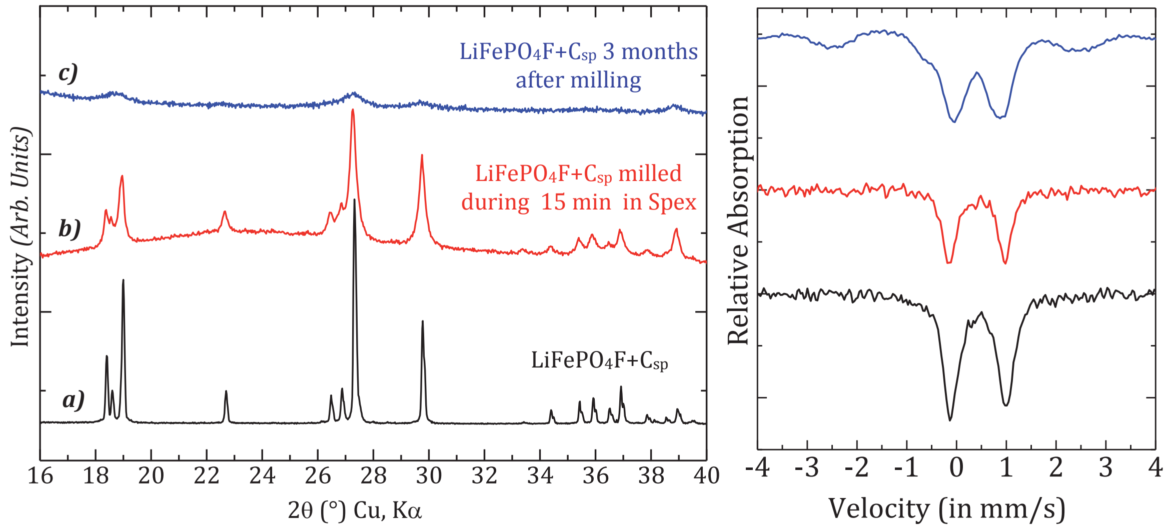

Figure III-18: XRD patterns (left) and the corresponding Mössbauer spectra (right) showing the degradation of a mixture of $LiFePO_4F$ and C_{sp} (85:15 wt %) after Spex milling and air exposure: a) initial $LiFePO_4F$ and C_{sp}, b) 15 min of Spex milling, c) air exposure during 3 months.

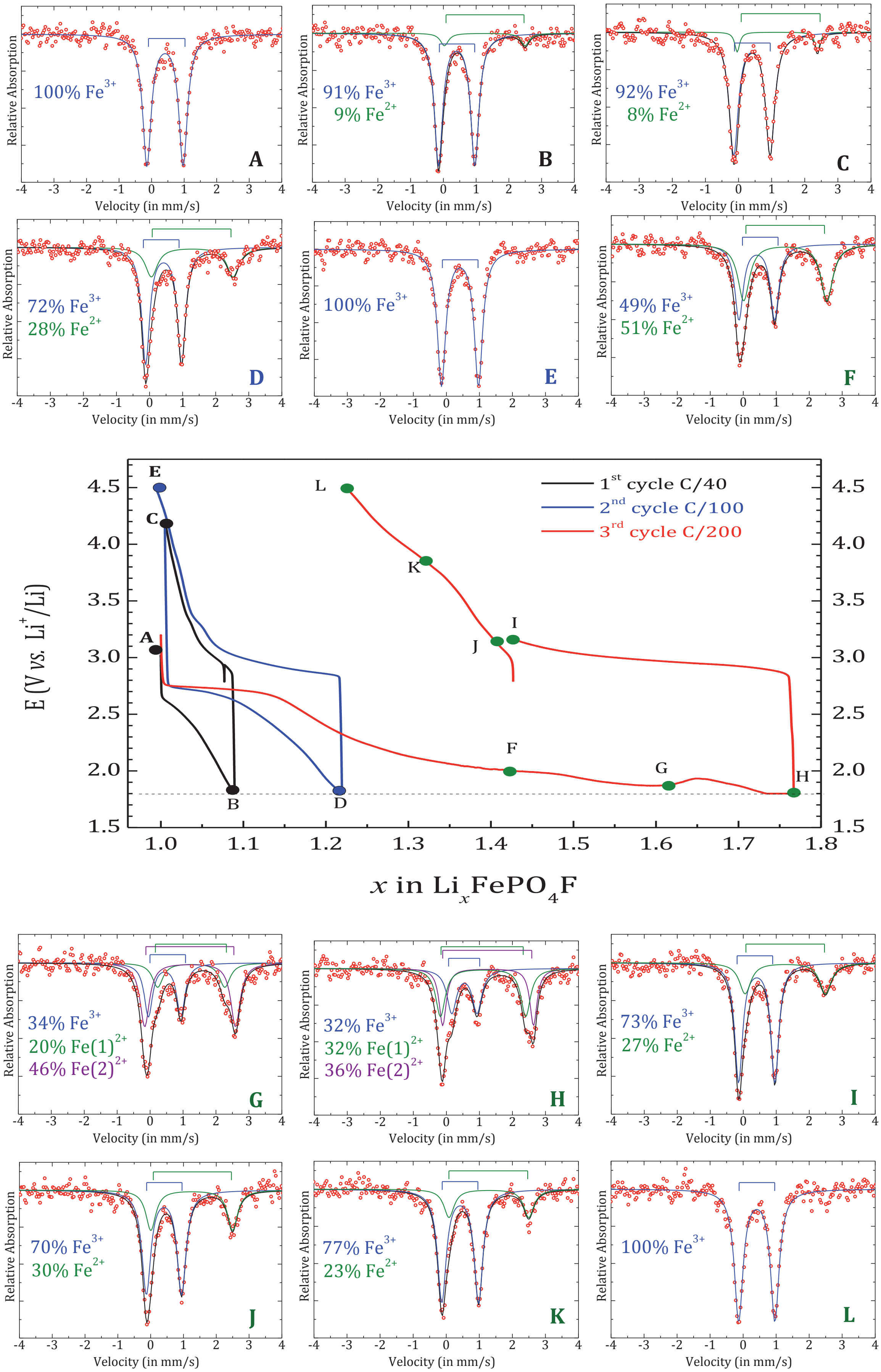

Figure III-19: Mössbauer in situ study of LiFePO₄F: the galvanostatic data are surrounded by the spectra (from A to M)

We have performed, in collaboration with M. Sougrati (ICG Montpellier), an *in situ* Mössbauer spectroscopy experiment upon discharge and charge using a stainless steel Swagelok-type cell similar to the one described in Chapter II, with a special plunger which enabled the γ rays to pass throughout the electrode and the Swagelok cell. The powder was prepared from a hand milled (in mortar instead of Spex milled in order to avoid possible degradation) mixture of $LiFePO_4F$ and C_{sp} (85:15 wt %). All the spectra have been recorded at room temperature in transmission geometry using a 0.55 Gbq source of $^{57}CoRh$ in constant acceleration mode. The velocity range was reduced to ±2.5 mm/s for a better resolution data. For the electrochemical tests, the galvanostatic data were recorded between 1.8 V and 4.5 V *vs.* Li^+/Li. Three successive rates were performed: at C/40 for the first cycle then at C/100 for the second cycle and finally at C/200 for the third cycle. The capacity retention was very poor probably due to the milling conditions.

The first Mössbauer spectroscopy data (recorded at point A, before discharge) confirmed the presence of Fe^{3+} only in the pristine sample. At the end of the first discharge (for C/40), the capacity delivered was about 15 mAh/g and the Mössbauer spectroscopy (at the point B) exhibited 91% of Fe^{3+} indicating a presence of unreacted initial $LiFePO_4F$. At the end of the second discharge (point D), the presence of Fe^{3+} decreased down to 72 % for C/100 and to 32 % for C/200.

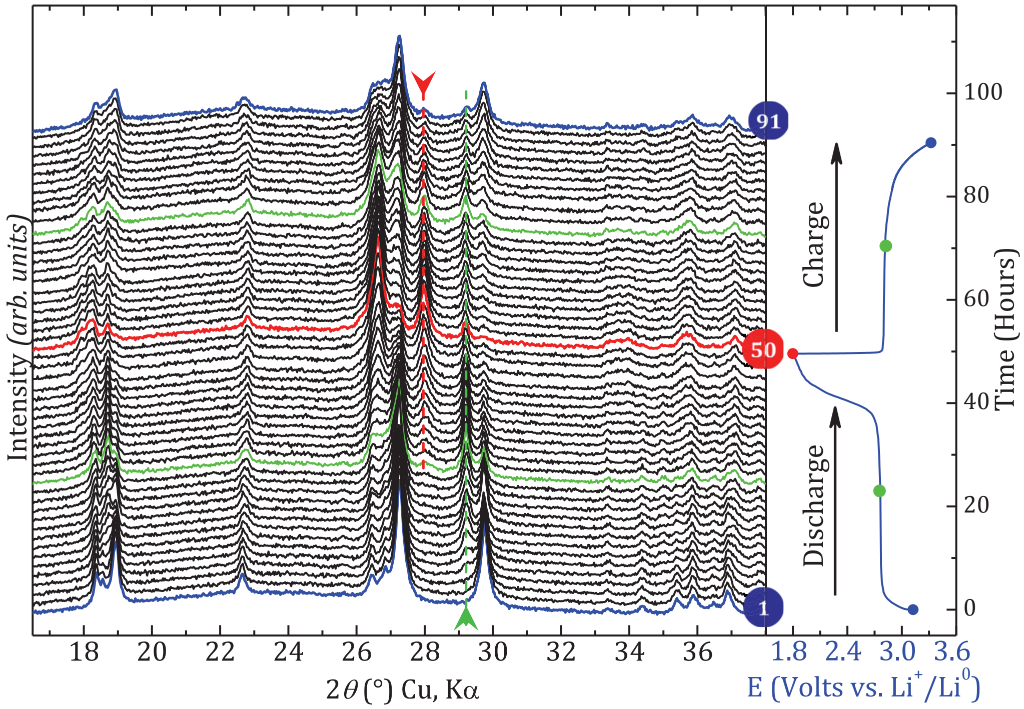

Figure III-20: 2D View of collected in situ XRD patterns for the global electrochemical reaction $LiFePO_4F$ ⇔ Li_2FePO_4F (left) and corresponding galvanostatic cycling (right). The XRD patterns highlighted in blue refer to $LiFePO_4F$ and the red one to Li_2FePO_4F. The XRD pattern of the intermediate phase is presented in green.

In order to investigate the phase transformation mechanism upon discharge from $LiFePO_4F$ to Li_2FePO_4F, an *in situ* XRD experiment was performed using the same conditions as in Chapter II. The recorded XRD patterns and the associated galvanostatic data are gathered in Figure III-20 and Figure III-21. No solid solution was observed, as suggested by Ramesh, since no XRD peaks were shifted to higher or lower 2θ angles (Figure III-21). The XRD data showed the appearance of a new phase at a composition of $Li_{1.5}FePO_4F$ as witnessed by the appearance of the peak at around 29.5° in 2θ. At first sight, one might have thought that this new phase corresponded to Li_2FePO_4F but surprisingly, at the middle of the plateau, the fraction of that new phase is maximum (Figure III-22). However, no intermediate phase ($Li_{1.5}FePO_4F$) was observed by Mössbauer. The peak at 29.5° (corresponding to the intermediate phase) did not completely disappear at the end of the discharge (Figure III-22).

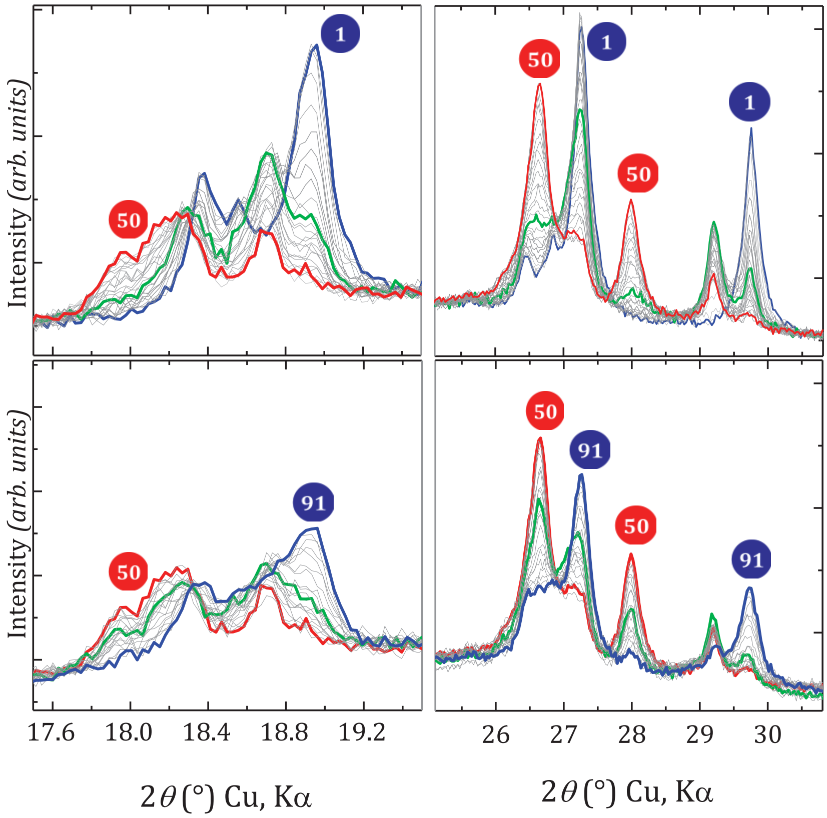

Figure III-21: Selected 2θ regions showing the respective growth and disappearance of the phases involved in the $LiFePO_4F$ (blue) ⇔ Li_2FePO_4F (red) reaction. The XRD pattern of the intermediate phase is presented in green.

Additionally, from the composition of $Li_{1.5}FePO_4F$, a new diffraction peak at 28 ° appeared which reached a maximum intensity at the end of discharge. This new peak can be ascribed to Li_2FePO_4F, as shown in Figure III-23 which presents the XRD patterns at the end of discharge together with the simulated Li_2FePO_4F XRD patterns (simulated from the published Li_2FePO_4F [8]). The diffraction peaks at 29.5 ° and 18.7 ° do not belong to the Li_2FePO_4F phase.

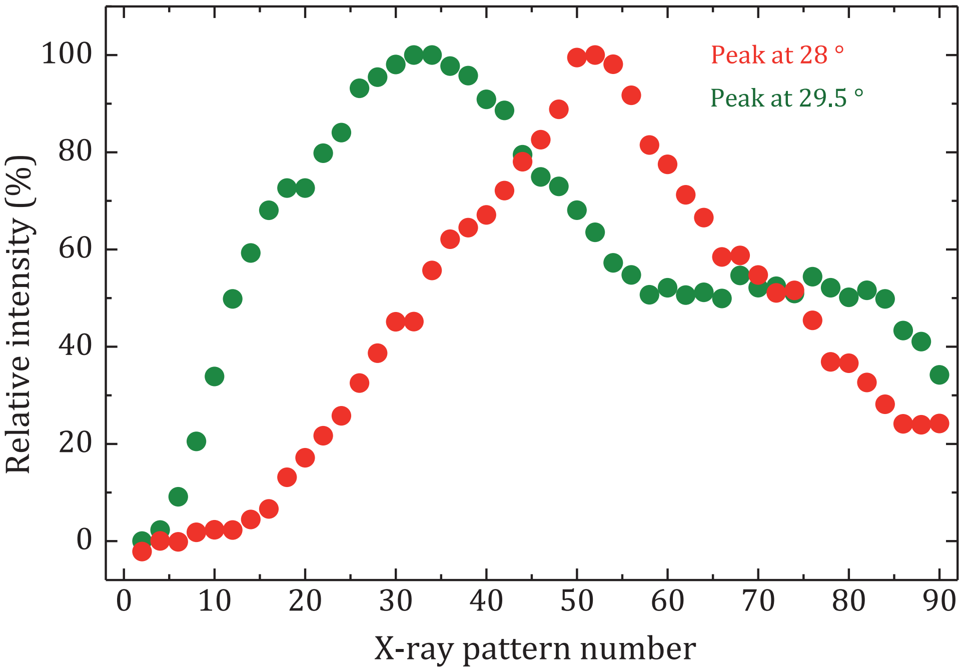

Figure III-22: Relative peak intensities for the peak corresponding to an intermediate phase (green) and a fully lithiated phase Li_2FePO_4F (red)

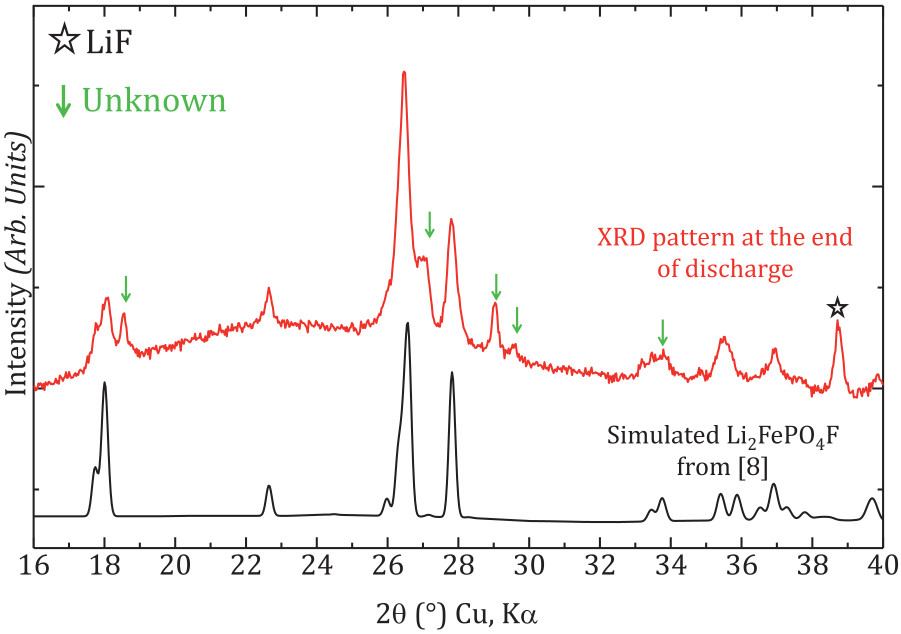

Figure III-23: Fullpattern refinement of the XRD data n° 50 corresponding to a fully lithiated phase. Bragg positions are those taken from Ramesh et al. [8]

III-5. Conclusion and summary of this chapter

Two synthesis routes have been performed for the synthesis of $LiFePO_4F$: the iono-thermal synthesis yielded the formation of a mixed OH/F $LiFePO_4X$ powder, as shown by the lattice parameters. Moreover we observed low crystallinity and bad reproducibility of the obtained phase so that the synthesis of $LiFePO_4F$ by iono-thermal synthesis was not straightforward. During the ceramic synthesis routes, we ended up with high crystallinity of $LiFePO_4F$. The particles size obtained through ceramic route were about 5-7 μm. Both ceramic and iono-thermal routes can be considered as indirect synthesis of $LiFePO_4F$ since LiF was formed as the main phase. Nevertheless, LiF can be removed using a cold-water washing. Based on Mössbauer spectroscopy and NMR, we have shown that $LiFePO_4F$ is stable upon moisture. The Curie constant obtained (based on the susceptibility measurement vs. temperature) confirmed the oxidation state of 3+ for Fe. Moreover, the magnetic data indicated an antiferromagnetic behavior with a Néel temperature of 80 K.

The Tavorite structure of $LiFePO_4F$ was determined by simultaneous Rietveld refinements of both X-ray and neutron diffraction data. The resolved structure of $LiFePO_4F$ was compared with those of $FePO_4 \cdot H_2O$ and $LiFePO_4OH$ in which the Fe–X distance along the octahedra chain is 2.17 Å and 2.02 Å, longer than the Fe–F distance (1.98 Å) in $LiFePO_4F$. The two sites of Fe are very close to each other, so that we could not distinguish them while refining the Mössbauer data. Contrary to previous publications from Ramesh et al. [8] and Recham et al. [7], we observed only one Li site in the structure of $LiFePO_4F$. This result was supported by ^7Li MAS NMR which exhibited a sharp signal shifted at 203 ppm, stronger than in $LiVPO_4F$ (117 ppm) compound since Fe^{3+} contains much more electron spins with a $t_{2g}^3\, e_g^2$ electronic configuration. In similar way the ^{31}P MAS NMR exhibited a stronger Fermi shift in $LiFePO_4F$ than in $LiVPO_4F$ (9550 ppm vs. 3998 ppm).

The magnetic structure of $LiFePO_4F$ was determined by Rietveld refinement of neutron diffraction data performed at low temperature. All nearest neighbors magnetic moments present in the Fe atoms are antiferromagnetically coupled (G-type) and the magnetic moment was 3.92 μ_B.

$LiFePO_4F$ exhibited an operating potential around 2.8 V *vs.* Li^+/Li. The electrochemical data presented a sloping outgrowth curve beyond the composition of $LiFePO_4F$ so that the end of the charge suggested an oxidation of Fe^{3+} to Fe^{4+}, which is clearly not possible at such low potential.

This particular and surprising signature can be ascribed to a possible air degradation of a Spex milled mixture of $LiFePO_4F$ and C_{sp}. The *in situ* XRD displayed no solid solution during Li insertion into $LiFePO_4F$ but revealed two biphasic mechanisms with an intermediate which formation is still unknown. Note worthy that this intermediate phase was neither detected in Mössbauer nor noticed in galvanostatic data.

References

1. Goodenough, J.B.; *Mapping of Redox Energies,* Molecular Crystals and Liquid Crystals Science and Technology Section a-Molecular Crystals and Liquid Crystals, **1998**, 311: p. 1-14.
2. Padhi, A.K.; Manivannan, V. and Goodenough, J.B.; *Tuning the position of the redox couples in materials with NASICON structure by anionic substitution,* Journal of the Electrochemical Society, **1998**, 145(5): p. 1518-1520.
3. Marx, N.; Croguennec, L.; Carlier, D.; Bourgeois, L.; Kubiak, P.; Le Cras, F. and Delmas, C.; *Structural and Electrochemical Study of a New Crystalline Hydrated Iron(III) Phosphate FePO(4)center dot H(2)O Obtained from LiFePO(4)(OH) by Ion Exchange,* Chemistry of Materials, **2010**, 22(5): p. 1854-1861.
4. Ati, M.; Sougrati, M.T.; Rousse, G.; Recham, N.; Doublet, M.L.; Jumas, J.C. and Tarascon, J.M.; *Single-Step Synthesis of FeSO(4)F(1-y)OH(y) (0 <= y <= 1) Positive Electrodes for Li-Based Batteries,* Chemistry of Materials, **2012**, 24(8): p. 1472-1485.
5. Marx, N.; Croguennec, L.; Carlier, D.; Wattiaux, A.; Le Cras, F.; Suard, E. and Delmas, C.; *The structure of tavorite LiFePO(4)(OH) from diffraction and GGA plus U studies and its preliminary electrochemical characterization,* Dalton Transactions, **2010**, 39(21): p. 5108-5116.
6. Ellis, B.L. and Nazar, L.F.; *Anion-Induced Solid Solution Electrochemical Behavior in Iron Tavorite Phosphates,* Chemistry of Materials, **2012**, 24(6): p. 966-968.
7. Recham, N.; Chotard, J.N.; Jumas, J.C.; Laffont, L.; Armand, M. and Tarascon, J.M.; *Ionothermal Synthesis of Li-Based Fluorophosphates Electrodes,* Chemistry of Materials, **2010**, 22(3): p. 1142-1148.
8. Ramesh, T.N.; Lee, K.T.; Ellis, B.L. and Nazar, L.F.; *Tavorite Lithium Iron Fluorophosphate Cathode Materials: Phase Transition and Electrochemistry of LiFePO(4)F-Li(2)FePO(4)F,* Electrochemical and Solid State Letters, **2010**, 13(4): p. A43-A47.
9. Recham, N.; Chotard, J.N.; Dupont, L.; Delacourt, C.; Walker, W.; Armand, M. and Tarascon, J.M.; *A 3.6 V lithium-based fluorosulphate insertion positive electrode for lithium-ion batteries,* Nature Materials, **2010**, 9(1): p. 68-74.
10. Tripathi, R.; Ramesh, T.N.; Ellis, B.L. and Nazar, L.F.; *Scalable Synthesis of Tavorite LiFeSO(4)F and NaFeSO(4)F Cathode Materials,* Angewandte Chemie-International Edition, **2010**, 49(46): p. 8738-8742.
11. Barpanda, P.; Ati, M.; Melot, B.C.; Rousse, G.; Chotard, J.N.; Doublet, M.L.; Sougrati, M.T.; Corr, S.A.; Jumas, J.C. and Tarascon, J.M.; *A 3.90 V iron-based fluorosulphate material for lithium-ion batteries crystallizing in the triplite structure,* Nature Materials, **2011**, 10(10): p. 772-779.
12. Ben Yahia, M.; Lemoigno, F.; Rousse, G.; Boucher, F.; Tarascon, J.M. and Doublet, M.L.; *Origin of the 3.6 V to 3.9 V voltage increase in the LiFeSO(4)F cathodes for Li-ion batteries,* Energy & Environmental Science, **2012**, 5(11): p. 9584-9594.
13. Reddy, M.A.; Pralong, V.; Caignaert, V.; Varadaraju, U.V. and Raveau, B.; *Monoclinic iron hydroxy sulphate: A new route to electrode materials,* Electrochemistry Communications, **2009**, 11(9): p. 1807-1810.
14. Delacourt, C.; Ati, M. and Tarascon, J.M.; *Measurement of Lithium Diffusion Coefficient in Li(y)FeSO(4)F,* Journal of the Electrochemical Society, **2011**, 158(6): p. A741-A749.
15. Prabu, M.; Reddy, M.V.; Selvasekarapandian, S.; Rao, G.V.S. and Chowdari, B.V.R.; *Synthesis, impedance and electrochemical studies of lithium iron fluorophosphate, LiFePO4F cathode,* Electrochimica Acta, **2012**, 85(0): p. 572-578.
16. Tarascon, J.M.; Recham, N. and Armand, M.; *Method for Producing Inorganic Compounds,* FR20090055233, **2009**.
17. Barker, J.; Saidi, M.Y. and Swoyer, J.; *Lithium Metal Fluorophosphate and Preparation Thereof,* US Patent **2005**, 0142056 A1(US 2005).

18. Seddon, K.R.; *Ionic liquids for clean technology,* Journal of Chemical Technology and Biotechnology, **1997**, 68(4): p. 351-356.
19. Welton, T.; *Room-temperature ionic liquids. Solvents for synthesis and catalysis,* Chemical Reviews, **1999**, 99(8): p. 2071-2083.
20. Wasserscheid, P. and Keim, W.; *Ionic liquids - New "solutions" for transition metal catalysis,* Angewandte Chemie-International Edition, **2000**, 39(21): p. 3772-3789.
21. Hagiwara, R.; *Electrochemistry using ionic liquid 2. Room temperature alkylimizadolium molten salts containing fluoroanions,* Electrochemistry, **2002**, 70(2): p. 130-136.
22. Ohno, H.; *Electrochemical Aspects of Ionic Liquids,* John Wiley & Sons, **2005**.
23. Devynck, J.; Messina, R.; Pingarron, J.; Tremillon, B. and Trichet, L.; *Electrochemical Intercalation of Lithium into Transition-Metal Compounds in Low-Temperature Chloroaluminate Melts,* Journal of the Electrochemical Society, **1984**, 131(10): p. 2274-2279.
24. Recham, N.; Dupont, L.; Courty, M.; Djellab, K.; Larcher, D.; Armand, M. and Tarascon, J.M.; *Ionothermal Synthesis of Tailor-Made LiFePO(4) Powders for Li-Ion Battery Applications,* Chemistry of Materials, **2009**, 21(6): p. 1096-1107.
25. Bain, G.A. and Berry, J.F.; *Diamagnetic corrections and Pascal's constants,* Journal of Chemical Education, **2008**, 85(4): p. 532-536.
26. Melot, B.C.; Rousse, G.; Chotard, J.N.; Ati, M.; Rodriguez-Carvajal, J.; Kemei, M.C. and Tarascon, J.M.; *Magnetic Structure and Properties of the Li-Ion Battery Materials FeSO(4)F and LiFeSO(4)F,* Chemistry of Materials, **2011**, 23(11): p. 2922-2930.
27. Rinard, P.M.; *Neutron Interactions with Matter. ,* Passive Nondestructive Assay of Nuclear Materials, **1991**, NUREG/CR-5550 /LA-UR-90-732(Edited by Reilly, D, N.Ensslin, H. Smith, Jr, and S. Kreiner.): p. Chapter 12.
28. Menil, F.; *Systematic Trends of the Fe-57 Mössbauer Isomer-Shifts in (FEON) and (FEFN) Polyhedra - Evidence of a New Correlation Between the Isomer-Shift and the Inductive Effect of the Competing Bond T-X(-Fe) (Where X is O or F and T any Element with a Formal Positive Charge),* Journal of Physics and Chemistry of Solids, **1985**, 46(7): p. 763-789.
29. Marx, N.; *Synthèse et Caractérisation de Nouveaux Phosphates Utilisés Comme Matériaux d'Electrode Positive pour Batteries au Lithium,* Univestité de Bordeaux 1, **2010**.
30. Ateba Mba, J.M.; Masquelier, C.; Suard, E. and Croguennec, L.; *Synthesis and Crystallographic Study of Homeotypic LiVPO(4)F and LiVPO(4)O,* Chemistry of Materials, **2012**, 24(6): p. 1223-1234.
31. Castets, A.; Carlier, D.; Zhang, Y.; Boucher, F.; Marx, N.; Croguennec, L. and Menetrier, M.; *Multinuclear NMR and DFT Calculations on the LiFePO(4)center dot OH and FePO(4)center dot H(2)O Homeotypic Phases,* Journal of Physical Chemistry C, **2011**, 115(32): p. 16234-16241.
32. Castets, A.; *RMN de matériaux paramagnétiques: mesures et modélisation,* Bordeaux 1 University, **2012**.
33. Castets, A.; Carlier, D.; Zhang, Y.; Boucher, F.; Marx, N.; Gautier, R.; Le Fur, E.; Le Polles, L.; Croguennec, L. and Menetrier, M.; *NMR study of the LiMnPO(4)center dot OH and MPO(4)center dot H(2)O (M=Mn, V) homeotypic phases and DFT calculations,* Solid State Nuclear Magnetic Resonance, **2012**, 42: p. 42-50.

Chapter IV

SYNTHESIS, CRYSTAL STRUCTURE AND ELECTROCHEMICAL PROPERTIES OF LiTiPO$_4$F

Contents

IV-1. Introduction 143

IV-2. STUDY OF THE PHASE $LiTiPO_4F$ 144

IV-2a. Synthesis of $LiTiPO_4F$ 144

IV-2b. Chemical composition and magnetic behavior of $LiTiPO_4F$..........................145

IV-2c. Crystal Structure of $LiTiPO_4F$ 146

IV-3. WASHING AND AGING EFFECT ON $LiTiPO_4F$ 150

IV-3a. Effect of aging in air on $LiTiPO_4F$ 150

IV-3b. Effect of washing on $LiTiPO_4F$ 154

IV-3c. Conclusion and summary 157

IV-4. ELECTROCHEMICAL BEHAVIOR OF $LiTiPO_4F$ 157

IV-5. Conclusion and summary of this chapter 160

IV-1. Introduction

In the field of Li and Na-ion batteries there is a large panel of Tavorite-like structures reported in literature. The transition metals mainly encountered are: vanadium as in Li_xVPO_4X (x = 1 or 0; X = O, F or H_2O), iron as in Li_xFeYO_4X (x = 0 or 1; Y = P or S; X = F, OH or H_2O) and manganese as in $AMnPO_4OH$ (A = Li or H). Yet, there are only two reported Tavorite-like structures within which titanium is used as transition metal: $LiTiPO_4O$ [1] and $NaTiPO_4O$ [2-5], none of them had been used in Li-ion batteries so far. On the contrary titanium-rich NASICON-like structures were widely explored in Li and Na-ion batteries as positive and negative electrode materials: $LiTi_2(PO_4)_3$ and $NaTi_2(PO_4)_3$ [6-11], $A_{x<1}TiPO_4O$ (with A = Ni [12, 13] or Co [14]), $Mg_{0.5}Ti_2(PO_4)_3$ [15]…

It is worth to notice that $LiTiPO_4O$ and $NaTiPO_4O$ are isostructural to $LiVPO_4O$ (which structure has been described in details in chapter I and is doubled versus that of $LiVPO_4F$) and possess titanium ions at the tetravalent state. The Tavorite-like $LiTiPO_4F$ (with titanium ions at the trivalent state) was first reported by N. Recham et al [16]. N. Recham had noticed that two voltage domains were involved upon cycling of Li//$LiTiPO_4F$ cells, one at lower voltages (2–1.3 V *vs.* Li) and the other at higher voltages (2–4.2 *vs.* Li), with for both of them the exchange of only 0.5 Li^+. Instead of forming $Li_2Ti^{II}PO_4F$ in discharge and $Ti^{IV}PO_4F$ in charge, the phases of compositions $Li_{1.5}Ti^{III/II}PO_4F$ and $Li_{0.5}Ti^{IV/III}PO_4F$ were obtained.

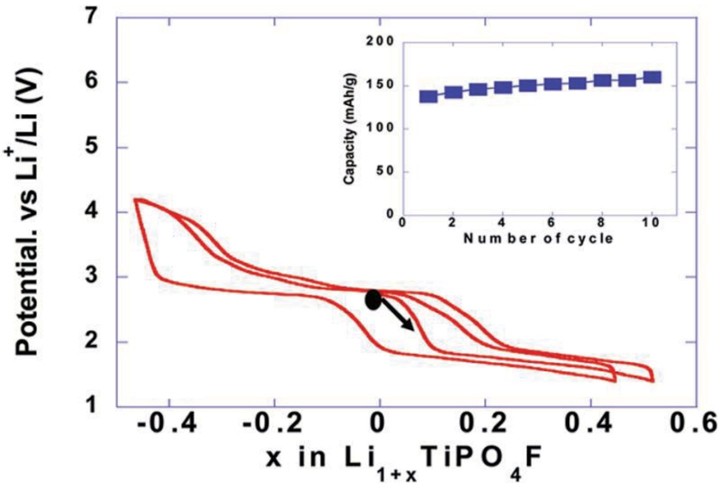

Figure IV-1: Electrochemical cycling of $LiTiPO_4F$ as reported by N. Recham et al. [16]. The inset shows the evolution of the capacity with the cycle numbers.

Those electrochemical limitations can be related to poor electronic conductivity of $LiTiPO_4F$, but cannot be ascribed to a limited diffusion due to the particles size (as discussed in the second part of chapter II for $LiVPO_4O$) since N. Recham prepared nano-particles of $LiTiPO_4F$ (50-70 nm). As it will be discussed in details in the following, we did the hypothesis considering that instead of forming $LiTi^{III}PO_4F$ N. Recham obtained $LiTi^{+4/+3}PO_4F_{1-x}O_x$ ($x \sim 0.5$) or $Li_{1-x}Ti^{+4/+3}PO_4F$ ($x \sim 0.5$). For such compositions, the intercalation of ~0.5 Li^+ at low voltage would be associated to the reduction of all Ti^{4+} ions to the trivalent state. Likewise, at high potential the deintercalation of ~0.5 Li would be associated to the oxidation of all Ti^{+3} ions to the tetravalent state.

This phase $LiTiPO_4F$ was thus included in our extended study of Tavorite-like fluorophosphates as positive electrode materials for Li-ion batteries. We are reporting in this chapter the synthesis of $LiTiPO_4F$, its crystal structure and its electrochemical behavior. We will also discuss about the aging of $LiTiPO_4F$ at room temperature in air or after its washing in water.

IV-2. STUDY OF THE PHASE $LiTiPO_4F$

IV-2a. Synthesis of $LiTiPO_4F$

$LiTiPO_4F$ was synthesized by N. Recham et al. [17, 18] following the same protocol as for the synthesis of $LiFePO_4F$. Li_3PO_4 was used as both lithium and phosphate precursor whereas TiF_3 was used as titanium and fluoride precursor. The reaction scheme is described as follow:

① $Li_3PO_4 + TiF_3 \rightarrow LiTiPO_4F + 2\ LiF$

The reaction was performed by Iono-thermal synthesis as well as by ceramic synthesis. For the iono-thermal syntheses, 1,2-dimethyl-3-(3-hydroxypropyl)imidazolium bis(trifluoromethane sulfonyl)imide was used as ionic liquid and the reaction yielded to the formation of $LiTiPO_4F$ as nanoparticles (30-70 nm in diameter). Despite the same precursors and duration time were used as for iono-thermal syntheses, ceramic synthesis led as expected to the formation of bigger particles (3-4 µm) because it was performed at higher temperature. For both reaction routes LiF was removed by washing the sample with water.

In our case, $LiTiPO_4F$ was obtained through ceramic route. Li_3PO_4 (from Aldrich) and TiF_3 (from Alfa Aesar) were ground/mixed in stoichiometric proportions in an Ar-filled glove box. The mixed powder was then pressed into a pellet, placed in a gold tube which was sealed in the glove box, and heated up to 750 °C for 1 hour prior to be quenched in liquid nitrogen.

The obtained violet powder was recovered in an Ar-filled glove box and placed in a tight sample-holder to prevent its exposure to air during the measure of its XRD pattern on a Siemens D5000 powder diffractometer with the Cu Kα radiation. As depicted in Figure IV-2, the XRD pattern of that (non-washed) sample was successfully refined considering a Tavorite-type structure described in the space group $P\bar{1}$ with lattice parameters larger than those reported by N. Recham for $LiTiPO_4F$. N. Recham et al. [16] reported a unit cell volume of 176.10 $Å^3$ whereas we observed 178.31 $Å^3$. The higher V/Z value obtained in our case, for a non-washed sample, would be consistent with the formation of a mixed valence titanium fluorophosphate by N. Recham as the ionic radii of Ti^{3+} (0.076 nm) is larger than that of Ti^{4+} (0.068 nm). The sample of N. Recham would have been oxidized during the washing process used to remove LiF.

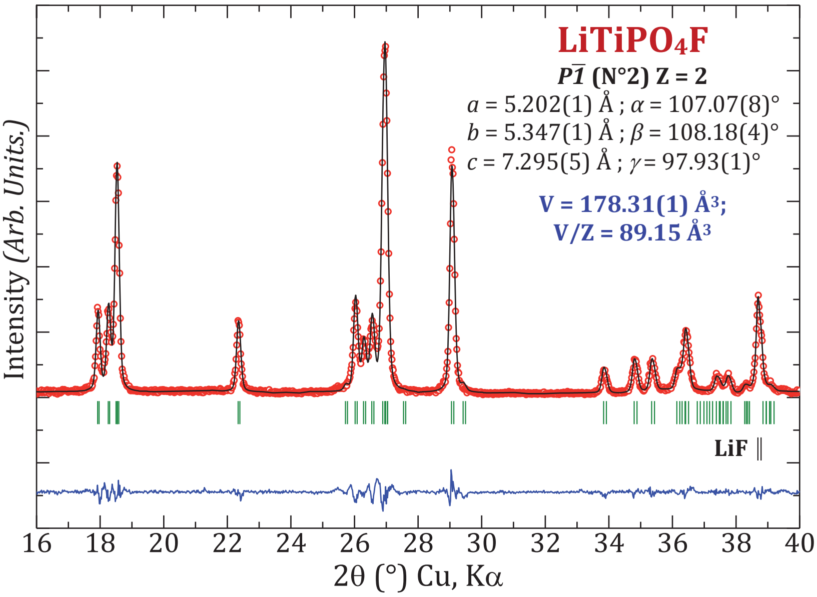

Figure IV-2: Full-pattern matching refinement of the XRD pattern recorded for the pristine (non-washed) $LiTiPO_4F$.

IV-2b. Chemical composition and magnetic behavior of $LiTiPO_4F$

The Li, Ti and P contents were determined using an ICP-OES spectrometer (Varian 720-ES Optical Emission Spectrometer) after complete dissolution of the powder (which contains in fact a mixture of $LiTiPO_4F$ and LiF) into a solution of HCl/H_2O. We observed that this dissolution was more difficult than for $LiVPO_4F$, $LiVPO_4O$ and $LiFePO_4F$. A stoichiometry of $Li_{2.95}/Ti_{1.00}/P_{0.96}$ was determined in rather good agreement with the presence of 2 moles of LiF and 1 mole of $LiTiPO_4F$. More interestingly is the absence of protons which has been checked using CHNS elemental analyzer based on combustion and gas chromatography analysis.

The static molar magnetic susceptibility of the LiTiPO$_4$F/LiF mixture was measured between 5 and 300 K using a SQUID magnetometer (Quantum Design). The zero-field cooled susceptibility (χ) values were obtained by cooling the sample in zero-field down to 5 K and then heating it under the measuring field of 10 000 Oe. The values reported here are given per mol of titanium, which was determined by chemical analyses. The diamagnetic contributions were corrected using the atomic values from G.A. Bain and J.F. Berry [19] yielding the χ_M paramagnetic susceptibility contribution. Contrary to LiVPO$_4$F, LiVPO$_4$O and LiFePO$_4$F no curvature indicative of the antiferromagnetic behavior was present for LiTiPO$_4$F so that the paramagnetic behavior remained all over the temperature range (Figure IV-3). The obtained Curie constant was 0.365 (in the temperature range 3–290 K) very close to the theoretical value of 0.375 for Ti^{3+} which electronic configuration is $t_{2g}^1e_g^0$.

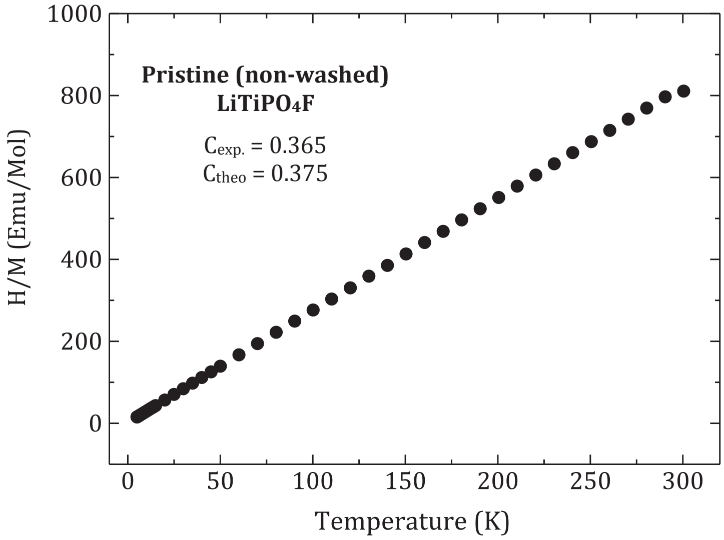

Figure IV-3: Temperature dependence of the H/M ratio for the pristine LiTiPO$_4$F/LiF mixture. The calculated Curie constant is given in insert in comparison with the theoretical one considering a Ti^{3+}-only material.

From these analyses we can thus consider that the material LiTiPO$_4$F containing only Ti^{3+} was effectively formed in the mixture obtained with LiF.

IV-2c. Crystal Structure of LiTiPO$_4$F

Based only on laboratory XRD data, N. Recham et al. [1] determined the structure of LiTiPO$_4$F and did the hypothesis that Lithium ions were distributed equally on two sites, only half occupied and separated by 1.13 Å. Our structural determination however, was based on both laboratory XRD and neutron diffraction. For the determination of the structure of LiTiPO$_4$F, the same methodology as described in chapters I and III was used. We choose to perform this in-depth structural characterization for the pristine (non-washed) material despite it is a mixture of $LiTiPO_4F$ and LiF. Indeed, we wanted to prevent any evolution of the original Tavorite-like phase formed and to study actually $LiTi^{III}PO_4F$. The presence of LiF was taken into account considering a second phase for the refinement. Its unit cell was described in the space group *Fm-3m* (N° 225); its cell parameter was refined whereas the atomic positions were fixed to those reported in the ICSD N° 18012.

1. Only Ti, P, O and F atoms were first considered according to the structural model $[Ti(1)_{1a}Ti(2)_{1b}](P_{2i})\ (O_{2i})_4F_{2i}$: in this model Ti(1) and Ti(2) atoms occupy special *1a* (0, 0, 0) and *1b* (0, 0, 1/2) positions respectively, as also defined by N. Recham. Surprisingly, already at this stage (*i.e.* without considering the Lithium atoms), the refinement of neutron diffraction data (Figure IV-4) seemed to converge with reasonably good reliability factors (R_{wp} = 2.63 %; R_{Bragg} = 0.60 %; χ^2 = 1.66 %) compared to the results obtained previously for the homeotypic phases $LiVPO_4F$ (R_{wp} = 5.40 %; R_{Bragg} = 6.95 %; χ^2 = 4.54 %), $LiVPO_4O$ (R_{wp} = 3.38 %; R_{Bragg} = 4.52 %; χ^2 = 3.63 %) and $LiFePO_4F$ (R_{wp} = 3.81 %; R_{Bragg} = 5.28 %; χ^2 = 3.68 %).

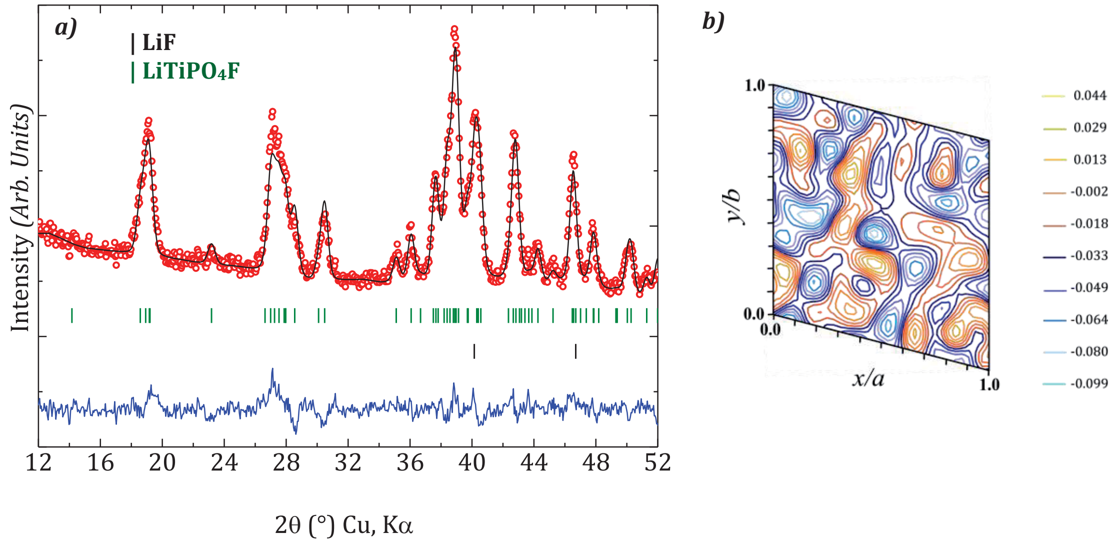

Figure IV-4: a) Neutron diffraction data refinement considering only heaviest atoms (i.e. without Li) and b) Corresponding Fourier difference map.

2. The localization of Li was much more difficult as depicted in Figure IV-4b in which several negative nuclear densities (blue lines) were observed very close to positive nuclear densities (red lines). The difficulty to localize Lithium atoms in this structure is probably due to the coherent scattering length of Ti (which is $-0.34 \cdot 10^{-4}$ Å [20]) higher compared with the Li coherent scattering length ($-0.19 \cdot 10^{-4}$ Å [20]) but with similar sign and magnitude. In addition, the neutron diffraction data were obtained on small amounts of powders and were thus not of optimized quality (signal over noise ratio for instance). The Li positions and the number of Li sites were therefore not determined and the structure of $LiTiPO_4F$ is going to be described in the

following without considering the position of Li and based on the analysis of the X-ray diffraction data (which is not affected by the light element Li). Figure IV-5 presents the Rietveld refinement of XRD data performed with two phases: $LiTiPO_4F$ and LiF. The obtained lattice parameters as well as the atomic positions are gathered in Table IV-1 in ANNEX I and the resulting inter-atomic distances are recorded in Table IV-2 of the same annex.

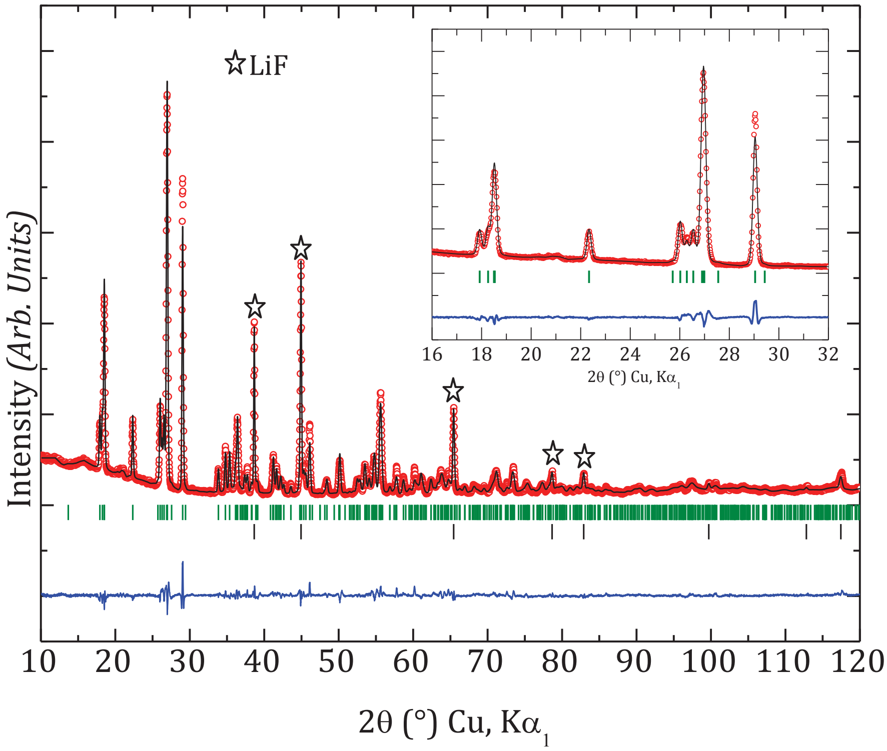

Figure IV-5: Observed (red dots), calculated (black line), and difference (blue line) plots obtained for the Rietveld refinement of X-ray diffraction data for $LiTiPO_4F$. The presence of LiF is indicated by stars.

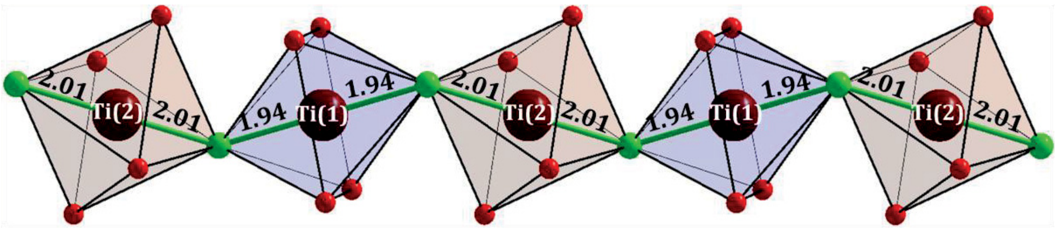

Figure IV-6: Representation of chains along the c axis in $LiTiPO_4F$ structure

We observed that the Ti–F distances along the chains in $[Ti(1)O_4F_2]$ and $[Ti(2)O_4F_2]$ octahedra are 2.01 Å and 1.94 Å respectively (Figure IV-6). Note that N. Recham et al. reported smaller Ti-F distances of 1.91 Å and 2.00 Å for Ti(1)–F and Ti(2)–F respectively, suggesting a larger average oxidation for titanium in their sample. Successive short and long Ti-F distances are observed along the chains for $LiTiPO_4F$ whereas regular M-F distances (of 1.98 Å) were obtained along the chains in the other fluorophosphates $LiVPO_4F$ and $LiFePO_4F$. We also observed that the octahedra in $LiTiPO_4F$ are more distorted than in $LiVPO_4F$ and $LiFePO_4F$. Similarly, the unique phosphorous site encountered in the structure of $LiTiPO_4F$ lies in a more distorted tetrahedral site than those of $LiVPO_4F$ and $LiFePO_4F$ (see ANNEX I).

Although the localization of Li in the $LiTiPO_4F$ structure was not straightforward from diffraction data, the study performed by ^7Li MAS NMR revealed the presence of at least 4 signals at -1, 8, 32 and 63 ppm as shown in Figure IV-7. As previously demonstrated (see Chapter III), the peak at -1 ppm corresponds to the presence of LiF. The three others could be ascribed to 3 different environments for Li in the structure of $LiTiPO_4F$.

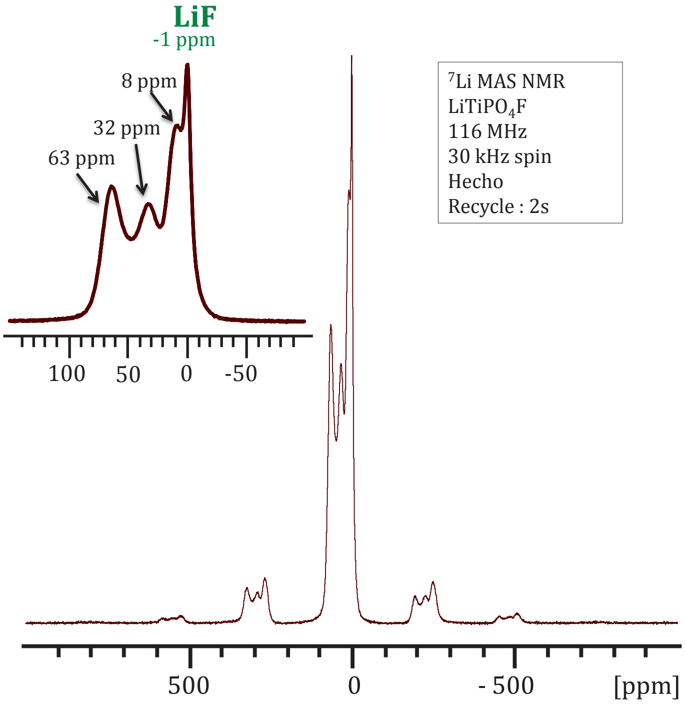

Figure IV-7: ^7Li MAS NMR spectrum of $LiTiPO_4F$

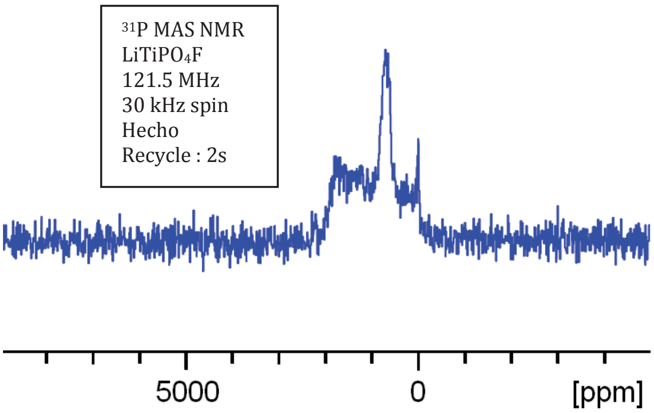

Figure IV-8: ^{31}P MAS NMR spectrum of $LiTiPO_4F$

The ^{31}P MAS NMR shift (see Figure IV-8) is less strong for $LiTiPO_4F$ (800 ppm) compared with $LiVPO_4F$ (4000 ppm) and $LiFePO_4F$ (9550 ppm). One can notice that the intensity of the ^{31}P NMR signal is smaller than those previously observed for $LiVPO_4F$, $LiVPO_4O$ and $LiFePO_4F$. Just as for $LiFePO_4F$, we did not observed any ^{19}F NMR signal, in contradiction with our expectation. Indeed, with only one electron spin for Ti^{3+} ($t_{2g}^1e_g^0$), we were expecting to observe a ^{19}F NMR signal for $LiTiPO_4F$ less shifted than for V^{3+} in $LiVPO_4F$ which possesses two electron spins ($t_{2g}^2e_g^0$) and a ^{19}F NMR signal shifted at 1500 ppm. In the general conclusion, we will present a detailed comparison of all $LiMPO_4F$ structures.

IV-3. WASHING AND AGING EFFECT ON LiTiPO$_4$F

IV-3a. Effect of aging in air on LiTiPO$_4$F

The obtained $LiTi^{III}PO_4F/LiF$ mixture has been exposed to air during 15 hours, 9 months and 1 year in order to check for the stability of $LiTi^{III}PO_4F$ in air. We observed that the color of the powder changed from violet to whitish with aging which could be consistent with an oxidation of Ti^{3+} to Ti^{4+} which electronic configuration is $t_{2g}^0e_g^0$. That oxidation can be associated to a partial substitution of oxygen for fluorine (the Tavorite-like phase $LiTi^{IV}PO_4O$ is white whereas $LiTi^{III}PO_4F$ is obviously violet) and/or to a partial lithium deintercalation according to reactions ② and ③ respectively, but also to the combination of both according to the reaction ④:

② $$LiTiPO_4F + x/2\ H_2O + x/4\ O_2 \rightarrow LiTi^{III}_{(1\text{-}x)}Ti^{IV}_{x}PO_4F_{(1\text{-}x)}O_x + x\ HF$$

③ $$LiTiPO_4F + y/2\ H_2O + y/4\ O_2 \rightarrow Li_{(1-y)}Ti^{III}_{(1\text{-}y)}Ti^{IV}_{y}PO_4F\ + y\ LiOH$$

④ $$LiTiPO_4F + (x{+}y)/2\ H_2O + (x{+}y)/4\ O_2 \rightarrow Li_{(1-y)}Ti^{III}_{(1\text{-}x\text{-}y)}Ti^{IV}_{(x+y)}PO_4F_{(1\text{-}x)}O_x\ +\ y\ LiOH + x\ HF$$

The recorded XRD patterns are gathered in Figure IV-9. An evolution of the XRD patterns is observed between the non-washed sample (initial mixture of $LiTi^{III}PO_4F$ and LiF) and the sample exposed to air for 15 hours, 9 months and one year. Note that the intensity of the peak associated to LiF at about 39° (2θ) progressively decreases with the increasing time of storage in air. Furthermore, all the diffraction peaks of the starting $LiTiPO_4F$ progressively vanish whereas those of a new phase progressively grow. The material obtained after an aging in air during one year contains almost only this new phase, with small residual amounts of a Tavorite-like phase described in the space group *P-1* and of LiF (as revealed especially by the peaks at 22.5° and 38.5° respectively).

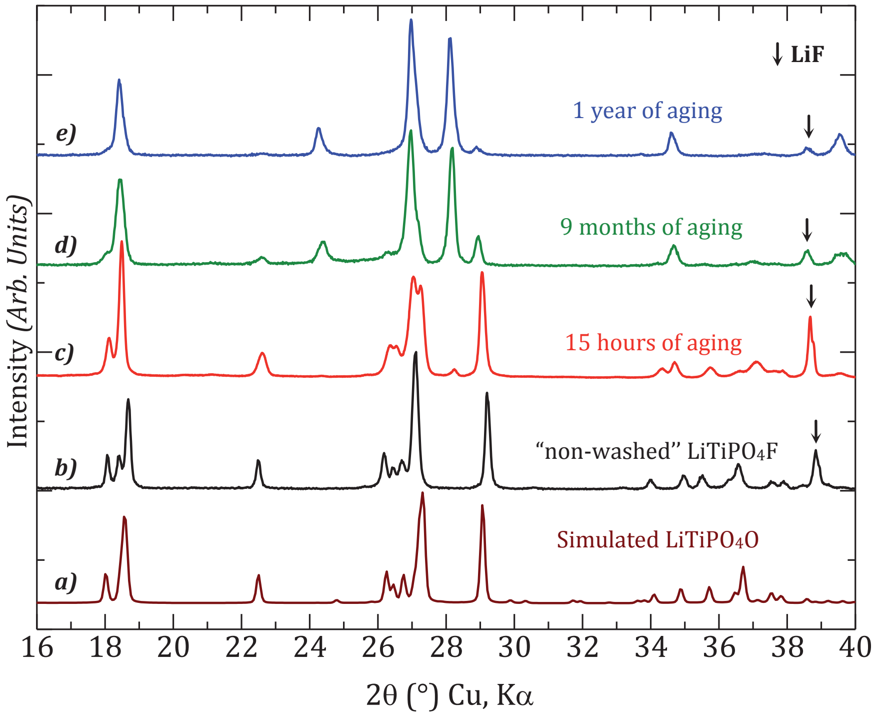

Figure IV-9: The XRD patterns of the "non-washed" sample (a) and the XRD patterns of the samples exposed to air during b) 15 hours, c) 9 months and d) 1 year. The simulated XRD pattern of $LiTiPO_4O$ is also given for comparison.

The XRD pattern of the sample obtained after 1 year of aging in air is completely different from that of $LiTi^{III}PO_4F$ and $LiTi^{IV}PO_4O$ (Figure IV-9), showing immediately that the oxidation process involved upon aging in air is not described (or not only described) by the reaction of oxygen substitution for fluorine (reaction ②). All the diffraction lines associated with the new phase were successfully indexed considering a unit cell described in the space group *Cc* or *C2/c*. Nevertheless, as clearly shown in Figure IV-10 a significantly better refinement was obtained considering the first unit cell and led us to adopt it in the following. The V/Z value obtained for this new phase was found to be around 83.78 Å^3 which is significantly smaller than that determined for $LiTi^{III}PO_4F$ (89.15 Å^3), suggesting again an oxidation of the pristine $LiTi^{III}PO_4F$, but also from that of $LiTi^{IV}PO_4O$. At this step information are not sufficient to propose a chemical formula for this new phase.

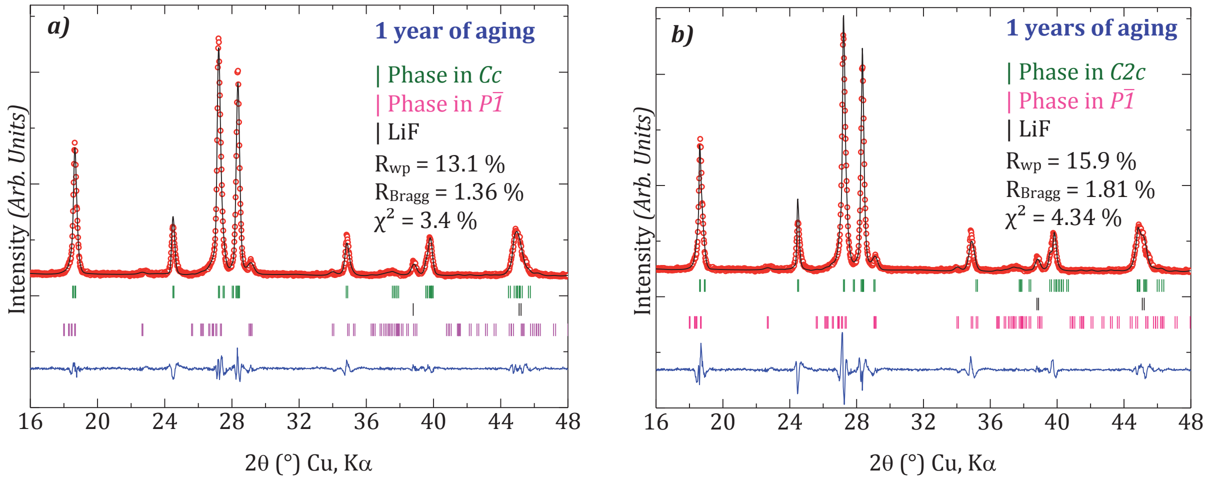

Figure IV-10: Full-pattern matching refinement of the XRD pattern obtained for the sample aged during 1 year in air, considering a) a unit cell described in the Cc space group for the main phase and b) a unit cell described in the C/2c space group for the main phase. The reliability factors are given in inserts.

The XRD patterns obtained for the two other samples aged for 15 hours and during 9 months in air could be refined considering again this new phase, a Tavorite-like phase described in *P-1* and LiF (see Figure IV-11). The lattice parameters, unit cell volumes and V/Z values are compared in Table IV-1 for $LiTi^{III}PO_4F$, $LiTi^{IV}PO_4O$ and the three different samples obtained after their aging in air. Note that already after 15 hours in air the material is modified in depth, with the formation in small amount of the new phase described in *Cc*, but also with a modification of the Tavorite-like phase described in *P-1* whose unit cell volume is significantly decreased, in good agreement also with an oxidation. The refinement of the XRD data is not that satisfactory, particularly in the region of 25-28° in 2θ, for the sample aged during 9 months. Note that it can be explained by the fact that we consider the presence of two phases only whereas a distribution of phases close in compositions is actually present. This is probably due to a gradient in composition for the phases.

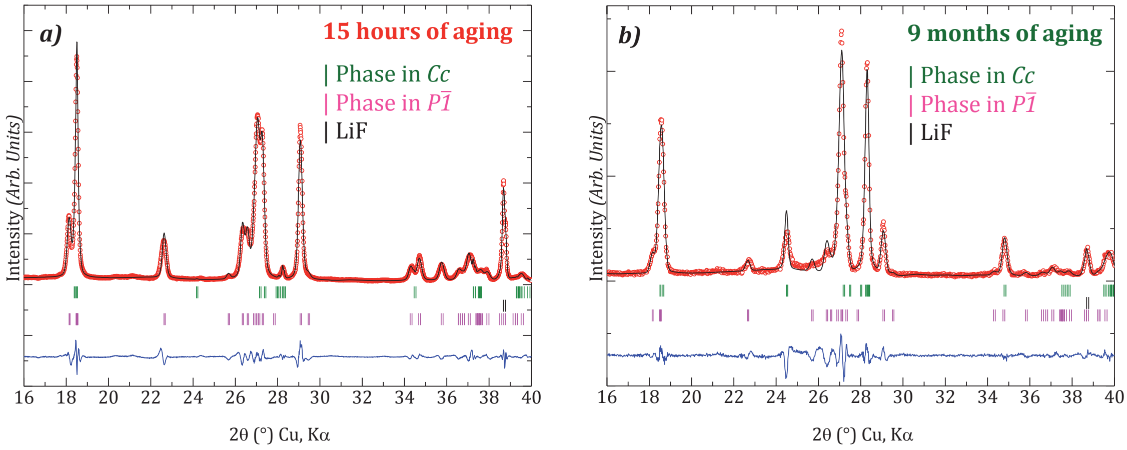

Figure IV-11: Full-pattern matching refinement of the XRD patterns obtained for the samples aged in air during a) 15 hours and b) 9 months.

Table IV-1: Lattice parameters, unit cell volumes and V/Z values obtained after different aging time of LiTiPO$_4$F in air. Comparison with those of LiTiPO$_4$F and LiTiPO$_4$O.

	a (Å)	b (Å)	c (Å)	α (°)	β (°)	γ (°)	V (Å^3)	V/Z (Å^3)
LiTiPO$_4$F ($P\bar{1}$)	5.202(1)	5.347(1)	7.295(5)	107.07(8)	108.18(4)	97.93(1)	178.31(1)	89.15
LiTiPO$_4$O ($P\bar{1}$)	6.904	7.197	7.903	90.45	91.31	117.19	349.13	87.28
15 hours of aging								
Phase $P\bar{1}$	5.210(3)	5.271(8)	7.243(1)	107.19(3)	108.68(2)	97.11(1)	174.71(7)	87.36
New phase Cc	7.353(7)	7.359(9)	7.335(8)	90	120.76(8)	90	341.14(8)	85.29
9 months of aging								
Phase $P\bar{1}$	5.201(9)	5.269(9)	7.231(1)	107.18(8)	108.54(5)	97.09(5)	174.28(9)	87.14
New phase Cc	7.315(2)	7.264(4)	7.350(2)	90	120.70(3)	90	335.84(4)	83.96
1 year of aging								
Phase $P\bar{1}$	5.194(4)	5.278(3)	7.244(1)	107.22(1)	108.65(4)	97.04(4)	174.47(3)	87.23
New phase Cc	7.305(5)	7.264(4)	7.341(3)	90	120.66(3)	90	335.13(3)	83.78

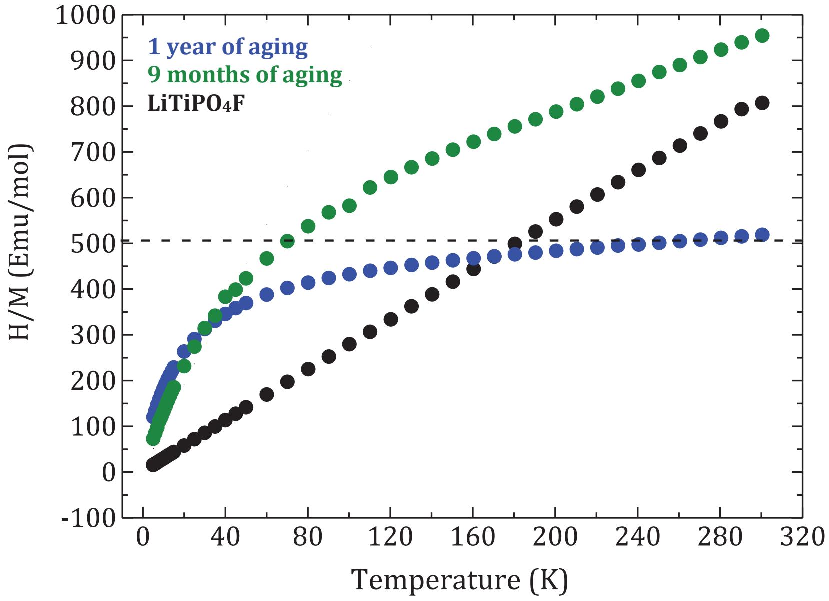

Figure IV-12: Temperature dependence of the H/M ratio for LiTi^{III}PO$_4$F/LiF mixture (black), sample aged for 9 months (green) and the sample aged for 1 year (blue). The molar weight used for the calculation of the H/M ratio for both 9 months and 1 year aged samples was that of TiPO$_4$F

In order to get more insight into the oxidation state of titanium in these aged samples, a magnetic study was performed. The evolution of the curves that give the static molar magnetic susceptibility versus temperature appears rather continuous (based on three samples only), between the pristine sample containing LiTi^{III}PO$_4$F and LiF, the sample aged for 9 months and the sample aged for 1 year. As discussed previously the first shows a paramagnetic behavior in the overall temperature range with titanium ions only at the trivalent state, whereas the third interestingly shows a magnetic susceptibility practically independent from temperature from

160 K up to room temperature (Figure IV-12). This observation indicates a diamagnetic behavior for the sample aged during one year in air and reveals the presence of titanium ions almost all at the tetravalent state in that sample. As expected also from the XRD analysis, the sample aged during 9 months is intermediate between the two.

Considering that the new phase contains only titanium ions at the tetravalent state and is not $LiTi^{IV}PO_4O$, all the compositions $Li_{1-y}Ti^{IV}PO_4F_{1-x}O_x$ such as $(x+y) = 1$ and $y \neq 0$ could be considered. At this step, it is interesting to mention that the description of the Tavorite-like structure was performed in the space group *Cc* for V^VPO_4O that is characterized by successive long and short V-O distances along the chains (see Chapter II). Note that for a mixed oxy-fluorophosphate and especially for the composition $Li_{1/2}Ti^{IV}PO_4F_{1/2}O_{1/2}$, such a sequence of long (Ti-F) and short (Ti-O) distances would be expected with an off-centered position of Ti in the octahedral sites.

IV-3b. Effect of washing on $LiTiPO_4F$

Just as described in Chapter III, it was possible to remove LiF from the mixture of $LiTi^{III}PO_4F$/LiF through its washing with cold water. The corresponding XRD pattern is given in Figure IV-13 in comparison with those obtained for the pristine (non-washed) sample, the sample washed with room temperature water (labeled “RT-washed”) and the sample non-washed but aged in air during 15 hours. The peak at around 38.7° in 2θ, characteristic of LiF, disappeared only when a washing in cold water (labeled “CW-washed”) was performed. More interestingly is that we observed an evolution of the XRD pattern during the washing, the pattern obtained being then very similar to that observed after 15 hours of aging in air.

As well illustrated in Figure IV-14 (through the observation of the intensity difference) the XRD patterns of both “RT-washed” and “CW-washed” samples have been fully explained considering for the first one (in addition to LiF), the presence of a Tavorite-like phase indexed in the space group *P-1* and for the second one, the presence of two Tavorite-like phases, described for the major one in *P-1* and for the minor one in *Cc*. As previously discussed for the samples aged in air (paragraph IV-3a), whatever the washing conditions the phases were oxidized as they show unit cell volumes and V/Z values smaller than that observed for $LiTi^{III}PO_4F$ (see Table IV-2). As already explained for the sample aged during 9 months in air to the quality of the refinements is not that satisfactory for the two samples “RT-washed” and “CW-washed”, considering the only presence of two phases described in *Cc* and $P\overline{1}$. Indeed, each sample is in fact a distribution of phases between the two end members (described in *Cc* and $P\bar{1}$) showing a gradient of compositions.

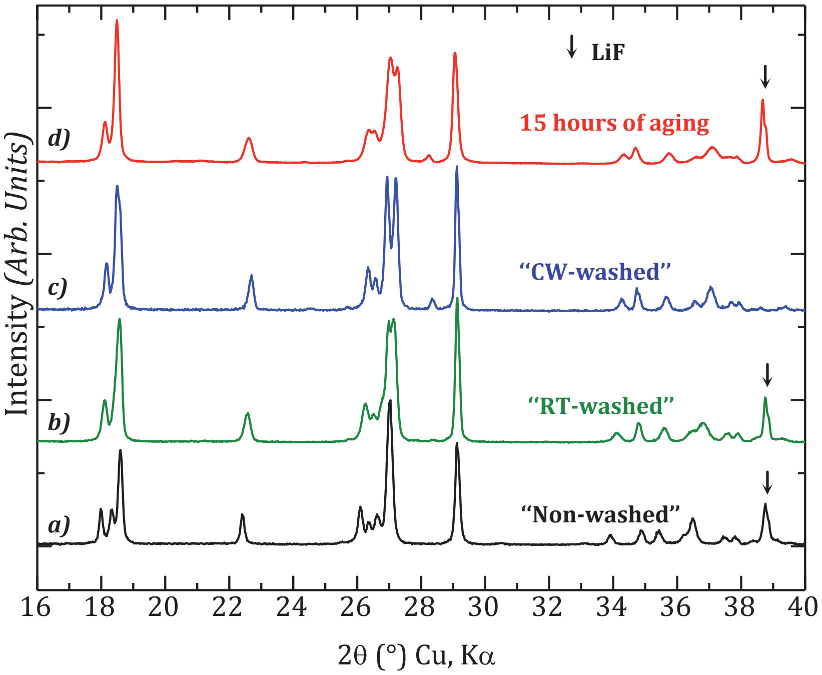

Figure IV-13: XRD patterns of different samples of "LiTiPO₄F":
a) "non-washed", b) "RT-washed" c) "CW-washed" and d) the "non-washed" aged during 15 hours in air

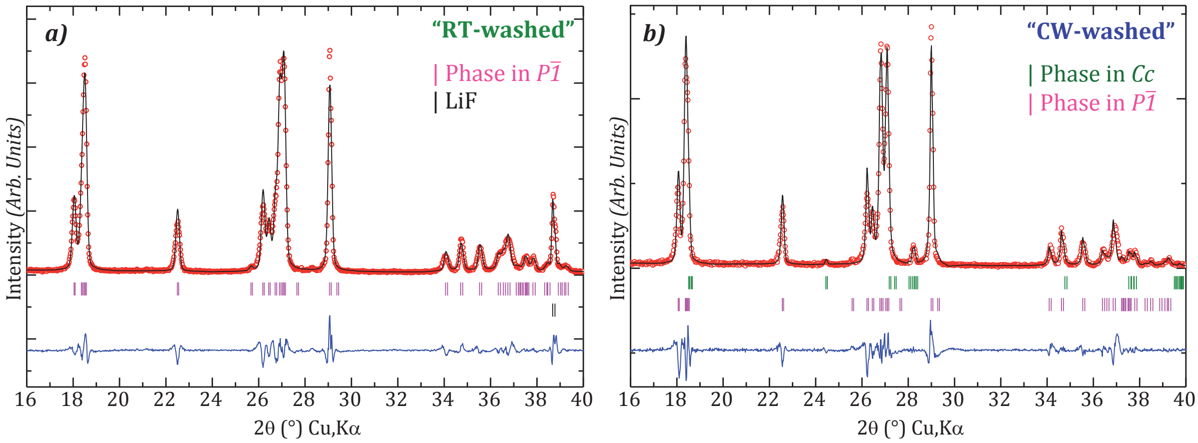

Figure IV-14: Full-pattern matching refinement of the XRD patterns collected for the samples washed with a) room temperature water: the XRD data were refined considering only one phase ($P\bar{1}$) and with b) cold water: the XRD data were refined considering two phases ($P\bar{1}$ and Cc).

Table IV-2: Lattice parameters, unit cell volumes and V/Z values determined for the different phases observed in samples washed with room temperature water and cold water. Comparison with those of $LiTi^{III}PO_4F$.

	a **(Å)**	***b*** **(Å)**	***c*** **(Å)**	***α*** **(°)**	***β*** **(°)**	***γ*** **(°)**	**V (Å³)**	**V/Z (Å³)**
$LiTiPO_4F$ ($P\bar{1}$)	5.202(1)	5.347(1)	7.295(5)	107.07(8)	108.18(4)	97.93(1)	178.31(1)	89.15
"RT-washed"								
Phase $P\bar{1}$	5.210(7)	5. 303(1)	7. 275(6)	107.07(2)	108.64(3)	97.41(3)	176.50(7)	88.25
"CW-washed"								
Phase $P\bar{1}$	5.221(2)	5.298(4)	7.287(2)	107.25(8)	108.79(3)	97.09(4)	176.83(1)	88.41
New phase *Cc*	7.314(6)	7.267(4)	7.345(2)	90	120.54(1)	90	336.29(3)	84.07

The static molar magnetic susceptibilities of "CW-washed" sample was measured between 5 and 300 K, and compared with the "non-washed" sample, and with the samples aged in air during 9 months and 1 year (Figure IV-15). The Curie constant obtained for the "CW-washed" sample was found to be 0.175 (calculated between 120–300 K), *i.e.* smaller than that of the "non-washed" sampled (0.365), confirming a partial oxidation of the "CW-washed" sample. This Curie constant suggests a distribution of 48%: 52% (i.e. close to 1:1) for Ti^{3+}:Ti^{4+}. This result leads us to assume a composition close to $Li_{(1-y)}Ti^{III}_{(1-x-y)}Ti^{IV}_{(x+y)}PO_4F_{(1-x)}O_x$ with (x+y) = 1/2 for "CW-washed" sample.

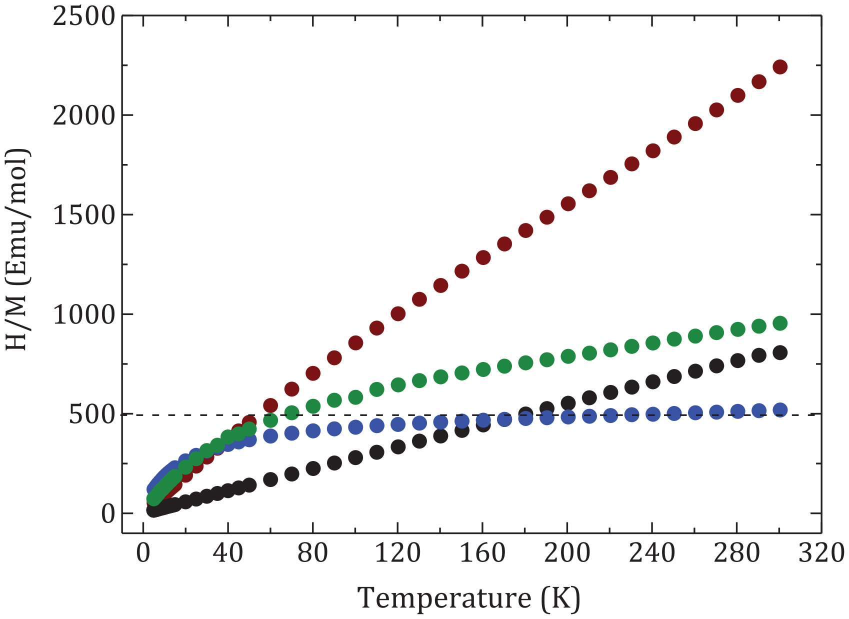

Figure IV-15: Temperature dependence of the H/M ratio for $LiTiPO_4F$/LiF mixture (black), sample aged for 9 months (green), the sample aged for 1 year (blue) and the sample washed with cold water (brown). The molar weight used for the calculation of the H/M ratio for the "CW-washed" sample was that of $TiPO_4F$.

IV-3c. Conclusion and summary

We have succeeded in the synthesis of $LiTiPO_4F$ material obtained together with LiF. The magnetic susceptibility exhibited a paramagnetic behavior all over the temperature range, with a Curie constant of 0.365 consistent with the presence of titanium at the trivalent state only. Due to poor resolution of the neutron diffraction data we were not able to localize the Li^+ ions in the structure of $LiTiPO_4F$. However, ^7Li MAS NMR suggests the presence of three different environments for Li. On the contrary to observations made for $LiVPO_4F$ and $LiFePO_4F$ within which a regular M–F distance of 1.98 Å was observed along the chains, successive short and long distances of 1.94 Å and 2.01 Å were observed for Ti(1)–F and Ti(2)–F respectively.

The $LiTiPO_4F$ phase was shown to be instable in air and during washing in water. Oxidation of titanium was proved from magnetic measurements. The phase formed was shown to be different from $LiTiPO_4O$. Indeed during ageing in air, we have shown the appearance of a new phase which crystallizes in *Cc* space group. We suggest that oxidation of titanium is induced by both oxygen substitution for fluorine and lithium deintercalation with the formation of $Li_{(1-y)}Ti^{III}_{(1-x-y)}Ti^{IV}_{(x+y)}PO_4F_{(1-x)}O_x$.

IV-4. ELECTROCHEMICAL BEHAVIOR OF $LiTiPO_4F$

The two redox couples which can be involved during Li deintercalation and intercalation from/in $LiTiPO_4F$ are Ti^{III}/Ti^{IV} and Ti^{II}/Ti^{II} respectively. The corresponding electrochemical reactions are:

$LiTi^{III}PO_4F \rightarrow Ti^{IV}PO_4F + Li^+ + e^-$ Theoretical capacity: 159 mAh/g

$LiTi^{III}PO_4F + Li^+ + e^- \rightarrow Li_2Ti^{II}PO_4F$ Theoretical capacity: 159 mAh/g

We have performed electrochemical tests of the “non-washed” and “CW-washed” samples in Swagelok cells, assembled in an argon-filled glove box. Prior to be used as positive electrodes, the active materials were ball milled under Ar with 16 wt % of SP carbon and 5 wt % of PTFE. The cells consisted of 1 cm^2 Li disks as negative electrode, $LiPF_6$ (1 M) in a mixture of EC-DMC (1:1) as electrolyte and the positive electrode with a loading in active material of approximately 8 mg/cm^2. The galvanostatic curves were recorded starting either in discharge first (first insertion of Li^+) or in charge first (first extraction of Li^+) with the current rate corresponding to C/50.

0.5 Li^+ were deintercalated from the "non-washed" sample (Figure IV-16a) during the first charge. That reaction is reversible: a capacity of 111 mhA/g is observed after 6 cycles, *i.e.* about 70 % of the theoretical capacity. The average operating potential associated to that reaction and thus to the redox couple Ti^{4+}/Ti^{3+} in this sample was 3 V *vs.* Li^+/Li. It is as expected higher than in other phosphate compounds such as the NASICON $LiTi_2(PO_4)_3$ (2.5 V *vs.* Li^+/Li) [6-8, 10, 21], due to the inductive effect of fluorine. Note that a difference of ~0.7 V is observed between the average potential in charge and that in discharge. It can be most probably mainly ascribed to the presence of a large amount of LiF in the positive electrode (2 mol. LiF *vs.* 1 mol "non-washed" sample).

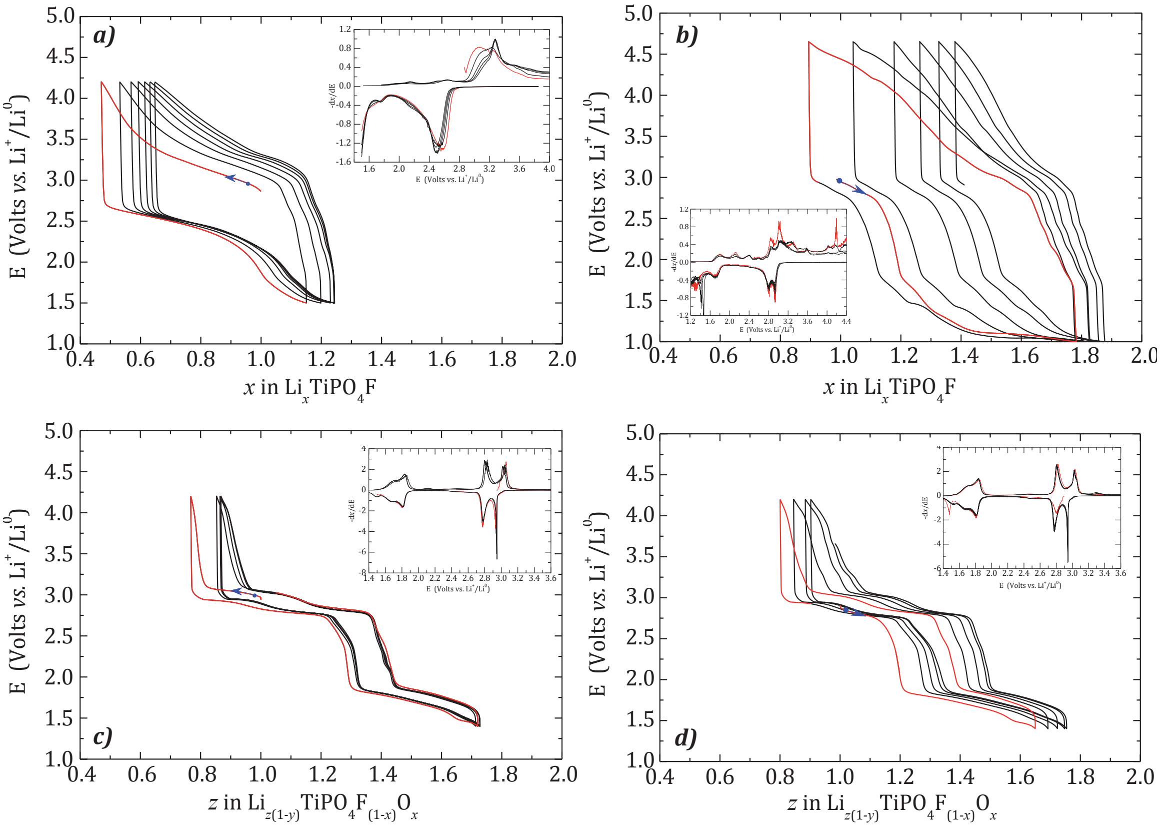

Figure IV-16: Electrochemical behavior of:
a-b) "non-washed" sample starting either by a) the extraction of Li^+ or b) the insertion of Li^+
c-d) "CW-washed" sample starting either by c) the extraction of Li^+ or d) the insertion of Li^+
The derivative curves are given in the inserts.

Using the same sample, we have performed an electrochemical cycling starting this time by the insertion of Li^+ (Figure IV-16b). Note that in that case the redox couple Ti^{2+}/Ti^{3+} is expected to be involved. A very large polarization was observed that led us to increase the potential window down to 1 V *vs.* Li^+/Li. As highlighted by the derivative curve given in insert the reaction

occurring in discharge at low potential around 1.4 V *vs.* Li^+/Li is irreversible, as not observed in charge. No obvious reversible reaction occurs at low voltage, suggesting that Li^+ cannot be intercalated in $LiTi^{III}PO_4F$ and thus that no reduction of Ti^{3+} to Ti^{2+} occurs as it would have been expected with the formation of $Li_2Ti^{II}PO_4F$.
It is interesting to mention that the electrochemical signature obtained for the "non-washed" sample ($LiTiPO_4F/2LiF$) is significantly different from that observed by N. Recham for a sample announced to be $LiTi^{III}PO_4F$ [16] with the absence of a pseudo-plateau at lower potential (below 2 V vs. Li^+/Li).

Both electrochemical signatures (charge first and discharge first) of the "CW-washed" samples (Figure IV-16c-d) were found significantly different from those of the "non-washed" sample just previously described and similar to that reported by N. Recham [16]. That first result reveals thus that the sample reported by N. Recham was in fact not $LiTiPO_4F$. Indeed, as discussed previously, $LiTiPO_4F$ evolved during its washing in water to a mixture of phases with an average composition $Li_{(1-y)}Ti^{III}_{(1-x-y)}Ti^{IV}_{(x+y)}PO_4F_{(1-x)}O_x$. Two voltage domains were observed and located at 3.0 and 1.7 V *vs.* Li^+/Li. Two pseudo-plateaus are in fact observed around 3.0 V, separated by an inflection point corresponding to the composition $Li_{1.1}TiPO_4F_{(1-x)}O_x$. At high voltages (2.3–4.2 V vs. Li^+/Li), the two electrochemical curves exhibited smaller polarizations (~0.2 mV) compared with previous electrochemical cycling curves obtained for the "non-washed" sample (~0.7 V), and only 0.5 Li was reversibly exchanged. At low voltages (2.3–1.4 V vs. Li^+/Li) similar amount of Li was also exchanged. Those galvanostatic behaviors are in good agreement with the presence of both Ti^{3+} and Ti^{4+} in the sample, as revealed by the magnetic measurements. At high voltage all the Ti^{3+} ions are oxidized to Ti^{4+}, whereas at low voltage all the Ti^{4+} ions are reduced to Ti^{3+}.

A very good reversibility of the electrochemical cycles was observed when a charge was performed first for the "CW-washed" sample (Figure IV-16c), on the contrary to the results obtained when a discharge was carried out first (Figure IV-16d): in that latter case all the cycles are shifted to higher x values in good agreement with the observations made by N. Recham. Both electrochemical curves, always started in the middle of the voltage domain located around 3 V *vs.* Li^+/Li, confirming the partial oxidation of the "CW-washed" sample.

We have also performed electrochemical tests on the sample aged for one year (Figure IV-17). During the first charge, almost no Li could be extracted in good agreement with the full oxidation of Titanium to the tetravalent state, as well demonstrated by magnetic measurements. On the contrary, lithium could be intercalated upon discharge. Good reversibility and capacity retention were observed. The larger polarization observed again in that case can be ascribed to the presence of LiF or of Li_2CO_3/LiOH as discussed previously (§ IV-3).

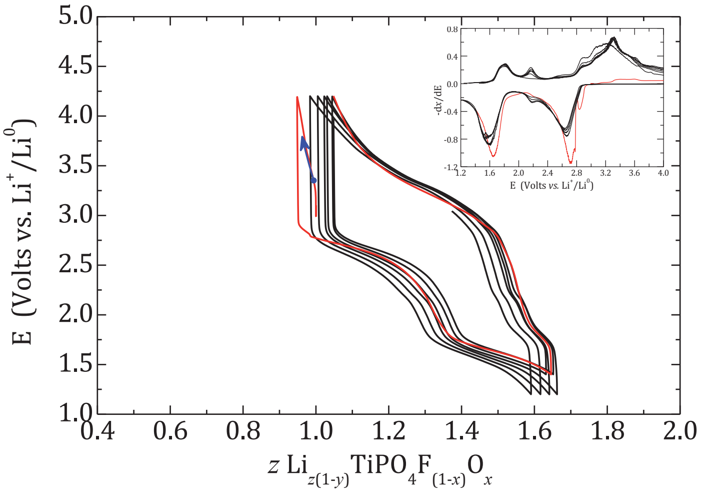

Figure IV-17: Electrochemical signature (starting in charge) of the $LiTiPO_4F$/LiF sample aged during one year

The galvanostatic behavior of "CW-washed" sample was in good agreement with the possible formation of the phase $LiTiPO_4F_{0.5}O_{0.5}$ during washing, whereas the galvanostatic behavior of the sample aged during one year showed no activity during first charge, in a good agreement with the possible formation of the phase $Li_{0.5}TiPO_4F_{0.5}O_{0.5}$.

IV-5. Conclusion and summary of this chapter

We had succeeded in the ceramic synthesis of $LiTiPO_4F$ through a one step ceramic synthesis which involved the use of Li_3PO_4 and TiF_3 as precursors. The chemical composition of $LiTiPO_4F$ was confirmed by ICP and the Curie constant calculated based on the evolution of the magnetic susceptibility with temperature was in good agreement with the oxidation state of Ti^{3+}. The crystal structure was determined based only on XRD data and exhibited a V/Z larger than the one previously reported by N. Recham (89.15 Å vs. 88.05 Å). Interestingly we observed, along the chains of $[TiO_4F_2]$ octahedra, distances of 1.94 Å and 2.01 Å in $[Ti(1)O_4F_2]$ and $[Ti(2)O_4F_2]$ respectively. Although we could not localize Li based on poor resolution of neutron diffraction data, we observed three ^7Li NMR signals suggesting 3 different environments for Li in the $LiTiPO_4F$ host structure.

$LiTiPO_4F$ proved to be highly air sensitive and was easily oxidized according to two reactions: the first reactions led to the formation of a phase which can be described in $P\bar{1}$ space group and the second reaction led to a phase which can be described in *Cc* space group. The magnetic susceptibility recorded versus temperature indicates a paramagnetic behavior for the "CW-washed" phase within which two oxidation states of Ti are present (Ti^{3+}/Ti^{4+}) and a diamagnetic behavior for the sample aged during one year imputable to the only presence of Ti^{4+}.

The average operating potential associated to first Li^+ extraction from $LiTiPO_4F$ (electrochemical oxidation first) and thus to the redox couple Ti^{4+}/Ti^{3+} was 3 V *vs.* Li^+/Li. It is as expected higher than in other phosphate compounds such as the NASICON $LiTi_2(PO_4)_3$ (2.5 V *vs.* Li^+/Li), due to the inductive effect of fluorine. A relatively good capacity retention was obtained contrary to the first Li^+ insertion into $LiTiPO_4F$ (electrochemical reduction first) in which the redox couple Ti^{4+}/Ti^{3+} was involved.

The galvanostatic cycling of the cold-water washed sample of $LiTiPO_4F$ was completely different from that of the pure $LiTiPO_4F$ and exhibited two pseudo-plateaus:

- The upper one located at 3.0 V *vs.* Li^+/Li which can be assigned to Ti^{4+}/Ti^{3+} redox couple. More interestingly is that whether we started by oxidation (Li^+ extraction first) or by reduction (Li^+ insertion first), we were always in the middle of the high voltage domain. The polarization in the upper voltage region was significantly smaller than that observed for the "non-washed" sample ($LiTiPO_4F/2LiF$). This was probably due to the presence of a mixed valence oxidation state for Ti (Ti^{4+}/Ti^{3+}) in the sample. Operating potential of the Ti^{4+}/Ti^{3+} redox couple is higher in that sample than that observed in the NASICON $LiTi_2(PO_4)_3$ which exhibited an average potential of 2.5 V *vs.* Li^+/Li.

- The lower one located at 1.7 V *vs.* Li^+/Li which can be also assigned to the redox couple Ti^{4+}/Ti^{3+}.

In both cases, only 0.5 Li was exchanged clearly indicated the proportion of 50% for each oxidation state of titanium.

References

1. Geifman, I.N.; Furmanova, N.G.; Nagornyi, P.G.; Yun, L.D. and Rotenfeld, M.V.; *Crystalline-Structure and EPR V(+4) in Lithium-Titanium Binary Hydroxyorthophosphate, Alpha-LITIOPO(4),* Kristallografiya, **1993**, 38(6): p. 88-94.
2. Geifman, I.N.; Nagornyi, P.G. and Rotenfeld, M.V.; *V4+ EPR, dielectric characteristics and superionic conductivity in monocrystalline NaTiOPO4,* Fizika Tverdogo Tela, **1994**, 36(12): p. 3550-3555.
3. Stus, N.V.; Slobodyanik, M.S.; Straitiychuk, D.A. and Lisnyak, V.V.; *Pressure induced gamma ->alpha-NaTiOPO4 phase transition,* Journal of Alloys and Compounds, **2005**, 393(1-2): p. 66-69.
4. Bamberger, C.E.; Begun, G.M. and Cavin, O.B.; *SYNTHESIS AND CHARACTERIZATION OF SODIUM TITANIUM PHOSPHATES, NA4(TIO)(PO4)2, NA(TIO)PO4, AND NATI2(PO4)3,* Journal of Solid State Chemistry, **1988**, 73(2): p. 317-324.
5. Dahaoui, S.; Hansen, N.K. and Menaert, B.; *NaTiOPO4 and KTiOPO4 at 110 K,* Acta Crystallographica Section C-Crystal Structure Communications, **1997**, 53: p. 1173-1176.
6. Delmas, C.; Cherkaoui, F.; Nadiri, A. and Hagenmuller, P.; *A nasicon-type phase as intercalation electrode: NaTi2(PO4)3,* Materials Research Bulletin, **1987**, 22(5): p. 631-639.
7. Delmas, C.; Nadiri, A. and Soubeyroux, J.L.; *The NASICON-Type Titanium Phosphates LiTi2(PO4)3, NaTi2(PO4)3 as Electrode Materials,* Solid State Ionics, **1988**, 28: p. 419-423.
8. Aatiq, A.; Menetrier, M.; Croguennec, L.; Suard, E. and Delmas, C.; *On the structure of Li(3)Ti(2)(PO(4))(3),* Journal of Materials Chemistry, **2002**, 12(10): p. 2971-2978.
9. Aravindan, V.; Chuiling, W.; Reddy, M.V.; Rao, G.V.S.; Chowdari, B.V.R. and Madhavi, S.; *Carbon coated nano-LiTi(2)(PO(4))(3) electrodes for non-aqueous hybrid supercapacitors,* Physical Chemistry Chemical Physics, **2012**, 14(16): p. 5808-5814.
10. Delmas, C. and Nadiri, A.; *The Chemical Short-Circuit Method - An Improvement in the Intercalation in the Intercalation-Deintercalation Techniques,* Materials Research Bulletin, **1988**, 23(1): p. 65-72.
11. Eljazouli, A.; Nadiri, A.; Dance, J.M.; Delmas, C. and Leflem, G.; *RELATIONSHIPS BETWEEN STRUCTURE AND MAGNETIC-PROPERTIES OF TITANIUM(III) NASICON-TYPE PHOSPHATES,* Journal of Physics and Chemistry of Solids, **1988**, 49(7): p. 779-783.
12. Belharouak, I. and Amine, K.; *New active titanium oxyphosphate material for lithium batteries,* Electrochemistry Communications, **2005**, 7(7): p. 648-651.
13. Godbole, V.A.; Villevieille, C.; Sommer, H.H.; Colin, J.F. and Novak, P.; *A structural and electrochemical study of Ni(0.5)TiOPO(4) synthesized via modified solution route,* Electrochimica Acta, **2012**, 77: p. 244-249.
14. Essehli, R.; El Bali, B.; Ehrenberg, H.; Svoboda, I.; Bramnik, N. and Fuess, H.; *Co(0.5)TiOPO(4): Crystal structure, magnetic and electrochemical properties,* Materials Research Bulletin, **2009**, 44(4): p. 817-821.
15. Vidal-Abarca, C.; Mba, J.M.A.; Masquelier, C.; Tirado, J.L. and Lavela, P.; *In Situ X-ray Diffraction Study of Electrochemical Insertion in Mg(0.5)Ti(2)(PO(4))(3): An Electrode Material for Lithium or Sodium Batteries,* Journal of the Electrochemical Society, **2012**, 159(10): p. A1716-A1721.
16. Recham, N.; Chotard, J.N.; Jumas, J.C.; Laffont, L.; Armand, M. and Tarascon, J.M.; *Ionothermal Synthesis of Li-Based Fluorophosphates Electrodes,* Chemistry of Materials, **2010**, 22(3): p. 1142-1148.
17. Recham, N.; Chotard, J.N.; Dupont, L.; Djellab, K.; Armand, M. and Tarascon, J.M.; *Ionothermal Synthesis of Sodium-Based Fluorophosphate Cathode Materials,* Journal of the Electrochemical Society, **2009**, 156(12): p. A993-A999.
18. Tarascon, J.M.; Recham, N. and Armand, M.; *Method for Producing Inorganic Compounds,* FR20090055233, **2009**.

19. Bain, G.A. and Berry, J.F.; *Diamagnetic corrections and Pascal's constants,* Journal of Chemical Education, **2008**, 85(4): p. 532-536.
20. Sears, V.F.; *Neutron scattering lengths and cross section,* Neutron News, **1992**, 3(3): p. 26-37.
21. Patoux, S. and Masquelier, C.; *Lithium insertion into titanium phosphates, silicates, and sulfates,* Chemistry of Materials, **2002**, 14(12): p. 5057-5068.

GENERAL CONCLUSION, SUMMARY AND PERSPECTIVES

Syntheses of $LiMPO_4X$

Ceramic route was useful for the synthesis of $LiMPO_4X$ (with M = V, Fe, Ti and X = O or F) whose XRD patterns are displayed in Figure 1. $LiVPO_4O$ was synthesized through a one-step reaction route for the first time. $LiVPO_4F$ was obtained by a two-step ceramic route, the first step being the formation of a carbon coated VPO_4 mixed in rigorous stoichiometric proportions with LiF. The second step of the synthesis of $LiVPO_4F$ was carried out in a sealed gold tube to avoid possible sublimation which leads to the formation of α-$Li_3V_2(PO_4)_3$. Both $LiFePO_4F$ and $LiTiPO_4F$ were obtained together with the formation of LiF which was removed by a washing with cold water.

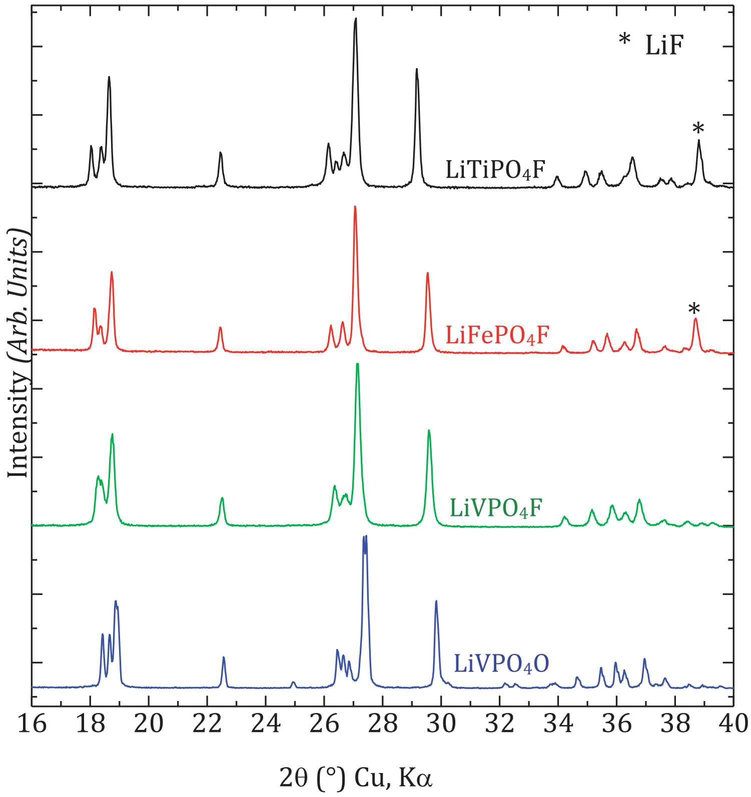

Figure 1: XRD patterns of different $LiMPO_4X$ obtained in this work

We observed a degradation of $LiTiPO_4F$ during aging and/or washing with water. This degradation led to the appearance of two new phases: one crystallizes in $P\bar{1}$ space group and another one crystallizes in *Cc* space group.

We are planning to bypass the effect of washing, by using an additional precursor as $TiCl_3$, we therefore expect to end up with the formation of $LiTiPO_4F$ and LiCl according to the equation ①:

① $Li_3PO_4 + 1/3\ TiF_3 + 2/3\ TiCl_3 \rightarrow LiTiPO_4F + 2\ LiCl$

The choice of those precursors will favor the formation of LiCl which is expected to be removed by a washing with most of the common organic solvents (such as Acetonitrile, Dimethylfurane, acetone...) in Ar-filled glove box.

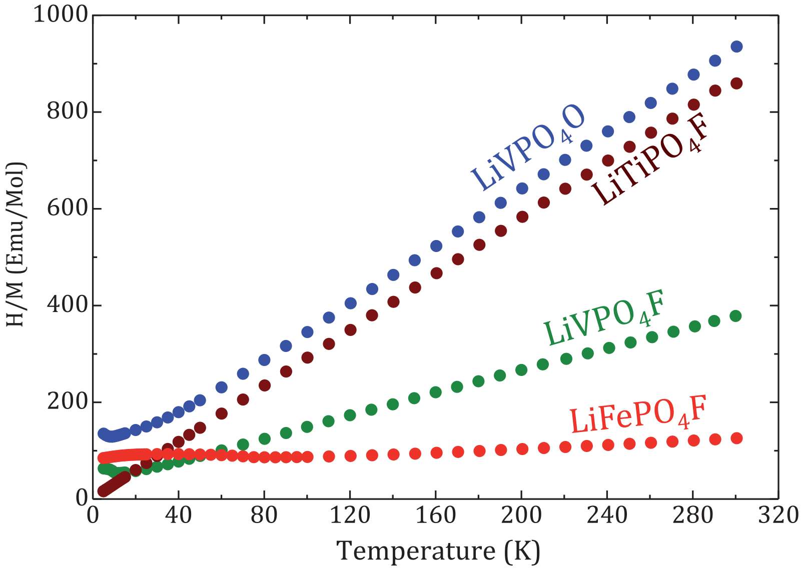

Figure 2: Temperature dependence of the H/M ratio for LiMPO$_4$X

The chemical composition and particularly the Li, M (with M = Ti, V and Fe) and P contents in LiMPO$_4$F were confirmed by ICP titrations. Based on the CHNS analyses, no H was observed in both LiFePO$_4$F and LiTiPO$_4$F. The variation of the susceptibility at low temperature range (Figure 2) indicates an antiferromagnetic behavior with Néel temperature of 9 K, 13 K and 80 K for LiVPO$_4$F, LiVPO$_4$O and LiFePO$_4$F respectively. Moreover, the susceptibility at high temperature range confirmed the oxidation state of each transition metal (Fe^{3+}, V^{3+}, V^{4+}, whose electronic configurations are $t_{2g}^3e_g^2$, $t_{2g}^2e_g^0$ and $t_{2g}^1e_g^0$ respectively). Based on Mössbauer spectroscopy analysis, we could confirm the oxidation state of Fe^{3+} lying in octahedral environment.

Structures of LiMPO$_4$X (with X = O or F)

Complete structural characterization of LiMPO$_4$X was performed using XRD and neutron diffraction data with the support of NMR studies. LiMPO$_4$X crystallizes in Tavorite-type structures and are iso-structural to the mineral LiFePO$_4$OH. Figure 3 displays the bond length along the chains in each structure. The unit cell volume of LiVPO$_4$O is two times bigger than those of LiMPO$_4$F. We observed an alternative long (2.21 Å and 2.17 Å) and short (1.62 Å and 1.71 Å) distances along the LiVPO$_4$O chains (the short distances being vanadyl-type) whereas for LiFePO$_4$F and LiVPO$_4$F, we observed the same and regular M–F distances of 1.98 Å. In the structure of $LiTiPO_4F$, we observed distances of 2.01 Å and 1.94 Å so that the average distance is 1.98 Å.

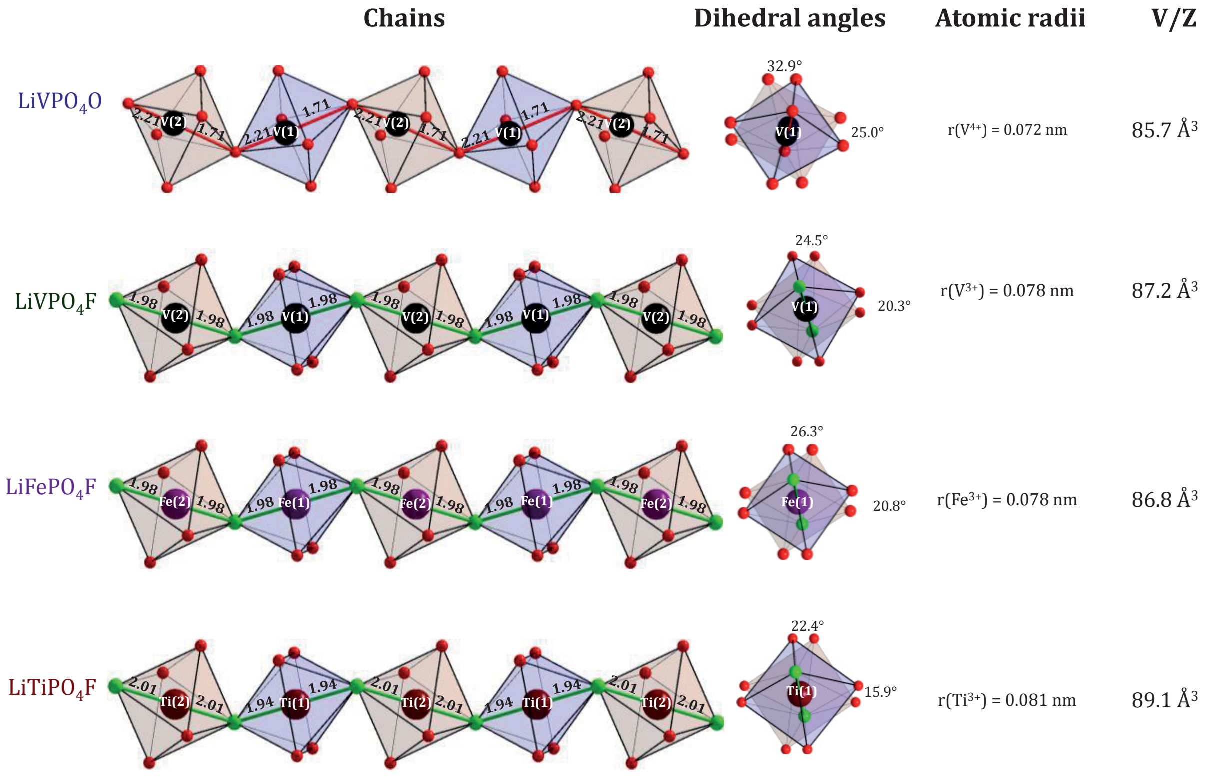
Chains
Dihedral angles
Atomic radii
V/Z
LiVPO4O
2.21 V(2) 1.71
2.21 V(1) 1.71
32.9°
25.0°
V(1)
r(V4+) = 0.072 nm
85.7 Å3
LiVPO4F
1.98 V(2) 1.98
1.98 V(1) 1.98
24.5°
20.3°
r(V3+) = 0.078 nm
87.2 Å3
LiFePO4F
1.98 Fe(2) 1.98
1.98 Fe(1) 1.98
26.3°
20.8°
Fe(1)
r(Fe3+) = 0.078 nm
86.8 Å3
LiTiPO4F
2.01 Ti(2) 2.01
1.94 Ti(1) 1.94
22.4°
15.9°
Ti(1)
r(Ti3+) = 0.081 nm
89.1 Å3

Figure 3: Comparison of [MO_4X_2] chains, dihedral angles, atomic radii of transition metal and V/Z in $LiMPO_4X$ (M = V, Fe, Ti and X = O or F)

The evolution of V/Z is consistent with the atomic radii of the transition metal. Indeed V/Z increases with the increase of atomic radii. The Li steric constrains in each structure is illustrated by larger dihedral angles (as encountered in $LiVPO_4O$). In order to localize precisely the Li site(s) an acquisition of neutron diffraction data with very good resolution has to be performed for $LiTiPO_4F$ (by increasing the acquisition time or the amount of powder).

The unique Li site observed in the structure of $LiVPO_4F$ and $LiFePO_4F$ is coordinated by 4 oxygen atoms and one fluorine, forming a distorted pentahedron which distortion is very similar in both structures with values of $6.00 \cdot 10^{-3}$ in $LiVPO_4F$ and $6.51 \cdot 10^{-3}$ in $LiFePO_4F$. ^7Li MAS NMR performed in both samples exhibited a sharp signal shifted at 117 ppm for $LiVPO_4F$ and 203 ppm for $LiFePO_4F$, those shift being in good agreement with the increasing number of single spins in t_{2g} orbitals (2 for V^{3+} and 3 for Fe^{3+}). The ^7Li MAS NMR of $LiVPO_4F$ presented a shoulder which can be assigned not to the impurity but to structural defects which were not detected by XRD and neutron diffraction.

The two Li sites present in the structure of $LiVPO_4O$ are surrounded by 5 oxygen atoms (forming distorted pentahedra) and are separated by 3.44 Å. Surprisingly, the ^7Li MAS NMR spectrum shows a single signal shifted at 71 ppm. The two Li sites being significantly different (*i.e.* with different V-O distances and O-V-O angles), the observation of a unique signal was not expected. Nevertheless DFT calculations have shown that the two Li sites are in fact not so different, with a rather similar spin transfer from the vanadium paramagnetic ion to the Li nucleus. Therefore, the two contributions might not be separated in the spectrum. Another explanation for this single ^7Li NMR signal could be the mobility between the two Li sites although they are separated by 3.44 Å. Very high field and fast MAS measurements might possibly help discriminate between these two hypotheses. The localization of Li in $LiTiPO_4F$ structure was not successful using both XRD and neutron diffraction data probably due to low resolution data. However ^7Li NMR exhibited 3 signals suggesting at least 3 Lithium sites in the structures.

A highly shifted ^{19}F NMR signal (shifted at -1500 ppm) was observed only for $LiVPO_4F$. No signal was observed for $LiFePO_4F$ probably shifted at a very higher ppm value compared to $LiVPO_4F$ as Fe^{3+} possesses more spins than V^{3+}. Surprisingly no signal was also observed for $LiTiPO_4F$ while Ti^{3+} possesses less spins than V^{3+}.

The magnetic structure of $LiVPO_4F$ and $LiFePO_4F$ was determined by a Rietveld refinement of neutron diffraction data performed at low temperature. The antiferromagnetim of both $LiVPO_4F$ and $LiFePO_4F$ was consistent with the evolution of the static magnetic susceptibility with temperature. The magnetic moment bear by the metal in each compound are antiparallel along the chain and the chains are also antiparallel through the propagation vector. Therefore $LiVPO_4F$ and $LiFePO_4F$ adopt a magnetic structure analogous to a G-type AFM where all nearest neighbors are antiferromagnetically coupled. The resulting magnetic moments were 1.22 μ_B and 3.92 μ_B for $LiVPO_4F$ and $LiFePO_4F$ respectively.

For $LiVPO_4O$, the magnetic measurement revealed a magnetic transition at a temperature of 9 K from paramagnetic to antiferromagnetic ordering. However, no magnetic transition was observed using low temperature neutron diffraction, probably due to the transparency of vanadium in neutron diffraction with in addition the electronic configuration of V^{4+} ($t_{2g}^1\ e_g^0$) which displays only one single electron. Let us recall that in the case of $LiVPO_4F$, two tiny peaks were observed. It was therefore not surprising that no magnetic transition was detected for $LiVPO_4O$.

Electrochemical behavior of $LiMPO_4X$

The electrochemical behavior of $LiMPO_4X$ was followed *vs.* Li^+/Li and compared with other phosphates. We always observed a relatively high potential of the redox couples involved. As an example, $LiVPO_4F$ present an operating potential of 4.22 V, higher than any other vanadium phosphate in which the couple V^{4+}/V^{3+} is present. During the Li^+ extraction from $LiVPO_4F$ (which leads to the formation of VPO_4F) an intermediate phase was spotted at a composition of $Li_{0.67}VPO_4F$. This intermediate was clearly visible by *in situ* XRD and crystallizes in $P\bar{1}$ space group as confirmed by electron diffraction. Further Li^+ extraction from $Li_{0.67}VPO_4F$ results in the formation of VPO_4F which crystallizes in *C2/c* space group. Interestingly, during subsequent Li^+ insertion in VPO_4F the formation of the intermediate $Li_{0.67}VPO_4F$ was not observed as well demonstrated by *in situ* XRD, but only two phases of VPO_4F and $LiVPO_4F$ were present. All those processes rely on biphasic mechanisms as also well demonstrated by *in situ* XRD. We also planned to study the mechanism of Na^+ insertion/extraction into VPO_4F in order to follow the possible formation of $Na_{0.67}VPO_4F$.

$LiVPO_4F$ can also accommodate one Li in its host structure leading to the formation of Li_2VPO_4F through a biphasic mechanism. Li_2VPO_4F crystallizes in *C2/c* space group and proved to be highly air sensitive. Both VPO_4F and Li_2VPO_4F crystallize in *C2/c* space group and are related to the parent phase $LiVPO_4F$. Their oxidation state as well as the one of $Li_{0.67}VPO_4F$ was confirmed by the measurement of the magnetic susceptibility with temperature and contrary to $LiVPO_4F$, the paramagnetism remained all along the temperature range. The structure of $Li_{0.67}VPO_4F$ is still unknown but might probably be related to the parent $LiVPO_4F$. ^7Li MAS NMR of $Li_{0.67}VPO_4F$ shows 4 signals ascribed to different types of environments for Li and corresponding to some kind of charge ordering in the material. Further NMR experiments are in progress to investigate this.

The poor electrochemical performances of $LiVPO_4O$ (small capacity retention, high polarization…) was ascribed to the big sized and highly agglomerated particles. The Li^+ extraction from $LiVPO_4O$ leads to the formation of VPO_4O through a biphasic process, and the V^{5+}/V^{4+} redox couple operates at a potential of 3.95 V *vs.* Li^+/Li. We have demonstrated for the first time that $LiVPO_4O$ can accommodate one Li in his host structure and leads to the formation of Li_2VPO_4O in which vanadium oxidation state is +3. The V^{4+}/V^{3+} redox couple involved in this process is the same as the one involve in the $LiVPO_4F \Leftrightarrow VPO_4F$ system, but with an average potential located at 2.3 V *vs.* Li^+/Li for $LiVPO_4O \Leftrightarrow Li_2VPO_4O$ system and 4.2 V *vs.* Li^+/Li for the $LiVPO_4F \Leftrightarrow VPO_4F$ system. This difference can be the result of the presence of the alternative long

V–O and short V=O distances in the structure of $LiVPO_4O$. A possible reduction of V^{3+} present in Li_2VPO_4O has to be investigated through Li^+ insertion in the structure (chemically or electrochemically).

The insertion/extraction of Li^+ in the structure of $LiVPO_4O$ undergoes reversibly through two intermediate phases of $Li_{1.5}VPO_4O$ and $Li_{1.75}VPO_4O$ never reported before in the literature. Their obtention by chemical lithiation of $LiVPO_4O$ is under process in our laboratory in order to determine their respective structure.

The galvanostatic behavior of $LiFePO_4F$ exhibited an operating potential around 2.8 V *vs.* Li^+/Li. A sloping outgrowth curve was observed beyond the composition of $LiFePO_4F$ so that the end of the charge suggested an improbable oxidation of Fe^{3+}, which is clearly not possible at such low potential. This particular and surprising signature can be ascribed to a possible air degradation of a Spex milled mixture of $LiFePO_4F$ and C_{sp}. The poor electrochemical performances of $LiFePO_4F$ (huge polarization and small amount of Li^+ exchanged) could be by-passed through a sol-gel synthesis of $LiFePO_4F$ expected to end up with the formation of small particles and through a carbon coating of $LiFePO_4F$ particles.

The *in situ* XRD displayed no solid solution during Li insertion into $LiFePO_4F$ but revealed two biphasic mechanisms with an intermediate still unknown. However, we did not observe any intermediate phase using Mössbauer technique and the galvanostatic cycling.

The galvanostatic signature of $LiTiPO_4F$ presented an average redox potential around 3 V *vs.* Li^+/Li for the Ti^{4+}/Ti^{3+} redox couple. The first galvanostatic extraction of Li^+ from the structure of $LiTiPO_4F$ presented a relatively good capacity retention and smaller polarization compared with the first galvanostatic insertion of Li^+ which presented a fast capacity fading and higher polarization.

The galvanostatic cycling of the cold-water washed sample of $LiTiPO_4F$ was completely different from that of the $LiTiPO_4F$ and exhibited two pseudo-plateaus: the upper one located at 3.0 V and 1.7 V vs. Li^+/Li. In each voltage domain, only 0.5 Li was exchanged in good agreement with the average oxidation state of Titanium in that sample which is close to 3.5 (*i.e.* $Ti^{3+}/Ti^{4+} \sim 1/1$). The galvanostatic signature of the sample aged for one year exhibited no capacity during the first Li extraction in good agreement with the presence of tetravalent titanium ions only in the material.

$Na_3V_2(PO_4)_2F_3$: Another vanadium fluorophosphate material

More recently, in the frame of Atif Emre DEMET Master Thesis, we focused our interest on $Na_3V_2(PO_4)_2F_3$ as a positive electrode material for Li and Na-ion batteries as more than one electron per transition metal are expected to be reversibly exchanged and at a high voltage. This composition is with no doubt one of the most attractive candidates for positive electrode for the development of Na-ion batteries. Figure 4 describes the three-dimensional framework of $Na_3V_2(PO_4)_2F_3$ which is built up of $[V_2O_8F_3]$ bi-octahedra and $[PO_4]$ tetrahedra. Each bi-octahedron shares its oxygen atoms with eight $[PO_4]$ tetrahedra, building thus rather large cavities in which Na^+ cations are located. Two types of fluorine exist, the F(1) atoms bridging the two VO_4F_2 octahedra of each $[V_2O_8F_3]$ unit and the two terminal F(2) atoms pointing along the ***c*** direction. We observed a V–F(1) distance (F(1) being the bridging atom between two octahedra) of 1.98 Å, same as for the M–F distances along the chains of the Tavorite-like structure of $LiFePO_4F$ and $LiVPO_4F$. The terminal V–F(2) distance is 1.93 Å.

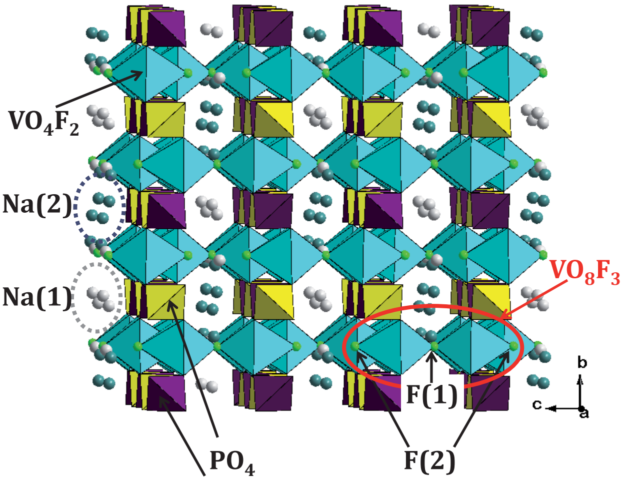

Figure 4: Description of the three-dimensional structure of $Na_3V_2(PO_4)_2F_3$

Figure 5 gives the electrochemical curves obtained for Li||$Na_3V_2(PO_4)_2F_3$ cells cycled in the 2.7–4.5 V potential window. They support the occurrence of several phase transitions upon cycling and reveal the complexity of the phase diagram that is dependent on the potential window used. During the first charge in the 2.7–4.5 V potential window, Na^+ ions are deintercalated from $Na_3V_2^{III}(PO_4)_2F_3$ to form (theoretically) $Na_{3-x}V_2^{III,IV}(PO_4)_2F_3$ ($x \leq 2$) through the oxidation of V^{III} to V^{IV} for charge compensation.

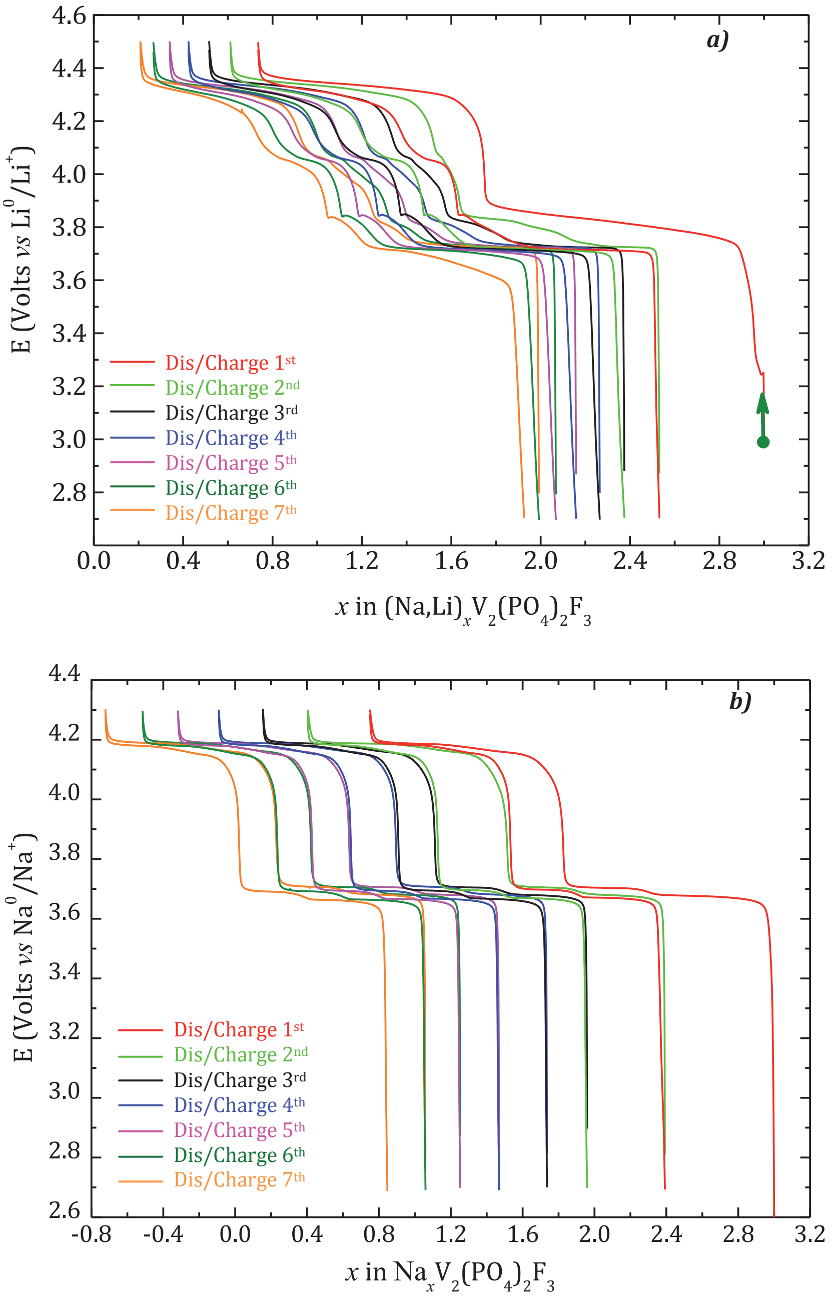

Figure 5 a) Electrochemical curves obtained for Li|LP30|$Na_3V_2(PO_4)_2F_3$ cells cycled between 2.7–4.5 V vs. Li^+/Li at C/50 b) Electrochemical curves obtained for Na|$NaPF_6$ in PC |$Na_3V_2(PO_4)_2F_3$ cells cycled between 2.7–4.3 V vs. Na^+/Na.

In fact, in parallel to Na^+ deintercalation, a Na^+/Li^+ ion exchange occurs and $(Li,Na)_{3-x}V_2^{III,IV}(PO_4)_2F_3$ ($x \leq 2$) is formed. The continuous change during the first two cycles is due to a continuous change in the composition of the material $(Na,Li)_xV_2(PO_4)_2F_3$ ($x \leq 2$) from a Na-rich material to a Li-rich one. Note that depending on the OCV period prior to cycling of the Li||$Na_3V_2(PO_4)_2F_3$ battery and on the cycling rate, the electrochemical signature appears slightly different due to a more or less extended Na^+/Li^+ ion exchange in the pristine or deintercalated material. During the first charge up to 5 V $Na_3V_2^{III}(PO_4)_2F_3$ is fully deintercalated with the exchange of three electrons (*i.e.* the deintercalation of three alkali ions) and the oxidation of vanadium up to the average oxidation state $V^{4.5+}$ (V^{IV}/V^{V}). Interestingly, an irreversible phase transition occurs and then, the cycling takes place between the compositions $V_2(PO_4)_2F_3$ and $Li_{\sim1.5}V_2(PO_4)_2F_3$.

ANNEXE I: CRYSTALLOGRAPHIC DATA

Table I-1: Structural parameters obtained after Rietveld refinement of XRD and neutron diffraction data from phase pure $LiVPO_4F$

$LiVPO_4F$

S.G. : $P\bar{1}$; Z = 2

a = 5.1708(3) Å; α = 107.595(3) °
b = 5.3083(3) Å; β = 107.969(2) °
c = 7.2631(4) Å; γ = 98.388(2) °

V = 174.36(2) Å^3; V/Z = 87.18 Å^3

XRD: R_{wp} = 15.2 %;
R_{bragg} = 1.88 %; χ^2 = 1.73

Neutrons: R_{wp} = 13.0%;
R_{bragg} = 5.11%; χ^2 = 3.93

Atomic parameters

Atoms	Wyckoff position	Atomic position			Occ	B_{iso}
		x/a	y/b	z/c		
V(1)	*1a*	0	0	0	1	0.404(1)
V(2)	*1c*	0	0	1/2	1	0.306(1)
P	*2i*	0.3264(1)	0.6494(1)	0.2533(1)	1	0.557(4)
O(1)	*2i*	0.3737(3)	0.2374(2)	0.5962(2)	1	0.417(3)
O(2)	*2i*	0.1072(2)	-0.3218(2)	0.3508(2)	1	0.425(3)
O(3)	*2i*	0.6906(2)	0.6567(2)	-0.1471(2)	1	0.752(3)
O(4)	*2i*	0.2567(2)	0.7848(2)	0.0885(2)	1	0.299(2)
F	*2i*	-0.1135(2)	0.0873(2)	0.2438(2)	1	0.842(3)
Li(1)	*2i*	0.703(1)	0.371(1)	0.233(1)	1	2.635(2)

Table 0-2: Selected bond lengths (Å) and angles (°) in the structure of LiVPO$_4$F.
Numbers in the diagonals (bold) are V-X distances (X = F or O).
Numbers below the diagonals are X-V-X angles.
Numbers above the diagonals are X-X distances

V(1)O$_4$F$_2$	O(4)a	O(4)b	F(1)a	F(1)b	O(3)a	O(3)b
O(4)a	**1.96(3)**	3.92(2)	2.62(2)	2.94(2)	2.75(3)	2.82(3)
O(4)b	180	**1.96(3)**	2.94(2)	2.62(2)	2.82(3)	2.75(3)
F(1)a	83.40(2)	95.60(2)	**1.98(2)**	3.96(2)	2.79(3)	2.82(2)
F(1)b	95.60(2)	83.40(2)	180	**1.98(2)**	2.82(2)	2.79(3)
O(3)a	88.56(2)	91.43(3)	89.42(2)	90.58(2)	**1.99(2)**	3.97(2)
O(3)b	91.43(3)	88.56(2)	90.58(2)	89.42(2)	180	**1.99(2)**

Distortion: $\Delta = 3.98 \cdot 10^{-5}$

V(2)O$_4$F$_2$	O(1)a	O(1)b	F(1)a	F(1)b	O(2)a	O(2)b
O(1)a	**1.96(3)**	3.86(3)	2.76(2)	2.78(2)	2.71(2)	2.82(3)
O(1)b	180	**1.96(3)**	2.78(2)	2.76(2)	2.82(3)	2.71(2)
F(1)a	89.61(3)	90.38(3)	**1.98(3)**	3.97(3)	2.79(3)	2.82(2)
F(1)b	90.38(3)	89.61(3)	180	**1.98(3)**	2.82(2)	2.79(3)
O(2)a	87.62(2)	92.38(2)	89.58(2)	90.41(3)	**1.98(2)**	3.97(2)
O(2)b	92.38(2)	87.62(2)	90.41(3)	89.58(2)	180	**1.98(2)**

Distortion: $\Delta = 2.28 \cdot 10^{-5}$

PO$_4$	O(1)	O(2)	O(3)	O(4)
O(1)	**1.50(2)**	2.54(3)	2.38(2)	2.54(2)
O(2)	115.11(3)	**1.51(3)**	2.52(2)	2.44(3)
O(3)	102.54(3)	110.69(3)	**1.55(3)**	2.54(3)
O(4)	112.57(2)	105.86(3)	110.13(2)	**1.55(2)**

Distortion: $\Delta = 2.22 \cdot 10^{-4}$

LiO$_4$F	O(1)	O(2)	O(3)	O(4)	F
O(1)	**2.24(3)**	2.71(2)	2.37(3)	4.14(2)	3.98(2)
O(2)	75.39(2)	**2.19(3)**	3.96(2)	3.15(3)	2.94(3)
O(3)	69.58(3)	140.23(3)	**1.90(2)**	3.24(3)	3.42(2)
O(4)	131.00(2)	88.79(2)	100.09(2)	**2.31(3)**	2.62(2)
F	148.37(3)	91.68(2)	128.08(3)	76.18(3)	**1.90(2)**

Distortion: $\Delta = 6.00 \cdot 10^{-3}$

Table 0-3: Structural parameters obtained after Rietveld refinement of XRD and Neutron diffraction data of phase pure $LiVPO_4O$

$LiVPO_4O$

S.G. : $P\bar{1}$; Z = 4

a = 6.7320(1) Å; α = 89.843(1) °
b = 7.1942(1) Å; β = 91.272(1) °
c = 7.9204(1) Å; γ =116.886(4) °

V = 342.92(1) Å^3; V/Z = 85.73 Å^3

XRD: R_{wp} = 13.2 %;
R_{bragg} = 1.73 % χ^2 = 1.92

Neutron R_{wp} = 10.1 %;
R_{bragg} = 3.61 % χ^2 = 2.23

Atomic parameters

Atoms	Wyckoff position	Atomic position			Occ	B_{iso}
		x/a	y/b	z/c		
V(1)	*2i*	0.2534(9)	0.0332(8)	0.7704(6)	1	0.498(6)
V(2)	*2i*	0.2440(9)	-0.4742(8)	0.7350(7)	1	0.974(1)
P (1)	*2i*	0.2317(1)	-0.2507(9)	0.0815(9)	1	0.397(3)
P(2)	*2i*	0.2548(1)	-0.7591(1)	0.4142(1)	1	0.584(2)
O(1)	*2i*	0.5460(5)	0.0936(4)	0.8274(1)	1	0.630(3)
O(2)	*2i*	0.1226(5)	-0.1535(4)	0.9700(3)	1	0.609(7)
O(3)	*2i*	-0.0680(4)	-0.0812(4)	0.6968(1)	1	0.430(8)
O(4)	*2i*	0.3476(5)	0.1237(3)	0.5345(1)	1	0.341(2)
O(5)	*2i*	0.2390(7)	-0.2514(5)	0.6654(4)	1	0.685(9)
O(6)	*2i*	0.2702(6)	0.2524(4)	0.8410(3)	1	0.469(3)
O(7)	*2i*	0.0779(6)	-0.3521(3)	0.2300(1)	1	0.516(1)
O(8)	*2i*	0.2819(4)	-0.3981(5)	-0.0210(2)	1	0.550(1)
O(9)	*2i*	0.4303(8)	-0.6167(14)	0.2921(2)	1	0.837(1)
O(10)	*2i*	0.1796(4)	-0.6160(5)	0.5194(3)	1	0.638(3)
Li(1)	*2i*	0.204(5)	-0.688(5)	0.075(4)	1	2.636(3)
Li(2)	*2i*	0.273(5)	-0.207(5)	0.409(4)	1	2.612(1)

Table 0-4: Selected bond lengths (Å) and angles (°) in the structure of LiVPO$_4$O. Numbers in the diagonals (bold) are V-O distances. Numbers below the diagonals are O-V-O angles. Numbers above the diagonals are O-O distances.

V(1)O$_6$	O(6)	O(1)	O(4)	O(3)	O(2)	O(5)
O(6)	**1.62(8)**	2.58(7)	2.74(3)	2.87(2)	2.82(1)	3.80(3)
O(1)	95.48(2)	**1.86(1)**	2.70(8)	3.85(3)	2.84(7)	2.90(8)
O(4)	97.81(1)	89.10(7)	**1.99(7)**	2.84(3)	3.85(3)	2.66(9)
O(3)	94.53(9)	169.94(5)	90.34(4)	**2.00(8)**	2.66(3)	2.77(2)
O(2)	100.98(5)	94.51(5)	160.41(2)	82.75(7)	**2.01(4)**	2.85(4)
O(5)	177.25(3)	84.02(5)	79.48(7)	86.00(3)	81.75 (3)	**2.17(2)**

Distortion: $\Delta = 7.63 \cdot 10^{-3}$

V(2)O$_6$	O(5)	O(10)	O(7)	O(8)	O(9)	O(6)
O(5)	**1.71(1)**	2.72(5)	2.81(7)	2.75(6)	2.80(1)	3.92(1)
O(10)	96.85(1)	**1.93(5)**	2.60(5)	3.89(1)	2.79(1)	2.86(3)
O(7)	99.44(6)	83.65(1)	**1.98(4)**	2.78(2)	3.93(1)	2.79(6)
O(8)	96.09(5)	166.02(6)	89.06(1)	**1.99(2)**	2.89(3)	2.71(2)
O(9)	97.76(7)	90.48(8)	162.35(5)	92.95(7)	**2.00(2)**	2.71(1)
O(6)	175.40(3)	87.13(3)	83.24(1)	80.16(4)	79.84(8)	**2.21(4)**

Distortion: $\Delta = 5.51 \cdot 10^{-3}$

P(1)O$_4$	O(8)	O(2)	O(7)	O(1)
O(8)	**1.50(2)**	2.44(1)	2.54(6)	2.47(7)
O(2)	109.22(4)	**1.51(1)**	2.44(8)	2.59(1)
O(7)	114.32(3)	107.75(5)	**1.53(4)**	2.42(1)
O(1)	107.76(1)	115.30(1)	102.53(4)	**1.57(1)**

Distortion: $\Delta = 3.08 \cdot 10^{-4}$

P(2)O$_4$	O(3)	O(9)	O(4)	O(10)
O(3)	**1.52(4)**	2.42(8)	2.51(4)	2.59(3)
O(9)	105.43(4)	**1.52(6)**	2.56(3)	2.49(6)
O(4)	108.85(1)	111.91(3)	**1.56(6)**	2.59(1)
O(10)	113.13(4)	106.78(5)	110.64(6)	**1.58(2)**

Distortion: $\Delta = 2.83 \cdot 10^{-4}$

Li(1)$\mathbf{O_4}$O	O(2)	O(6)	O(8)	O(9)	O(3)
O(2)	**1.99(1)**	2.86(5)	3.17(5)	3.87(4)	2.65(9)
O(6)	91.54(3)	**2.00(7)**	2.71(2)	3.70(7)	3.93(1)
O(8)	103.41(3)	83.74(6)	**2.05(5)**	3.30(3)	4.23(4)
O(9)	136.96(9)	124.87(5)	102.71(3)	**2.17(3)**	2.42(8)
O(3)	74.96(1)	128.42(3)	147.54(6)	64.70(6)	**2.35(4)**
		Distortion:	$\Delta = 4.00 \cdot 10^{-3}$		

Li(2)$\mathbf{O_4}$	O(7)	O(5)	O(1)	O(4)a	O(4)b
O(7)	**1.87(3)**	3.56(8)	2.42(1)	3.88(4)	3.88(1)
O(5)	130.36(4)	**2.05(6)**	4.16(6)	2.99(5)	2.66(9)
O(1)	72.39(1)	156.06(8)	**2.20(2)**	2.71(1)	3.50(7)
O(4)a	131.71(4)	84.67(3)	72.401(2)	**2.37(7)**	3.321(9)
O(4)b	129.44(8)	72.90(4)	98.89(2)	87.87(5)	**2.41(1)**
		Distortion:	$\Delta = 8.52 \cdot 10^{-3}$		

Table I0-1: Structural parameters obtained after Rietveld refinement of XRD and neutron diffraction data from phase pure VPO_4F

<table>
<tr><th colspan="7">VPO_4F</th></tr>
<tr><td colspan="7">S.G. : $C2/c$; Z = 4
a = 7.1662(4) Å; b = 7.1267(3) Å
c = 7.1285(4) Å; β = 118.077(2)°
V = 321.22(3) $Å^3$; V/Z = 80.30 $Å^3$
XRD: R_{wp} = 18.9 %;
R_{bragg} = 2.98 % χ^2 = 3.43
Neutrons: R_{wp} = 20.8 %;
R_{bragg} = 0.61 % χ^2 = 1.43</td></tr>
<tr><td colspan="7">Atomic parameters</td></tr>
<tr><td rowspan="2">Atoms</td><td rowspan="2">Wyckoff position</td><td colspan="3">Atomic position</td><td rowspan="2">Occ</td><td rowspan="2">B_{iso}</td></tr>
<tr><td>x/a</td><td>y/b</td><td>z/c</td></tr>
<tr><td>V</td><td>4d</td><td>1/4</td><td>1/4</td><td>1/2</td><td>1</td><td>0.284(8)</td></tr>
<tr><td>P</td><td>4e</td><td>0</td><td>0.6280(5)</td><td>1/4</td><td>1</td><td>0.918(4)</td></tr>
<tr><td>O(1)</td><td>8f</td><td>0.3374(9)</td><td>0.0087(6)</td><td>0.0770(9)</td><td>2</td><td>1.146(1)</td></tr>
<tr><td>O(2)</td><td>8f</td><td>0.3961(5)</td><td>0.2465(7)</td><td>0.3430(1)</td><td>2</td><td>1.007(4)</td></tr>
<tr><td>F</td><td>4e</td><td>0</td><td>0.1530(9)</td><td>1/4</td><td>1</td><td>3.515(4)</td></tr>
</table>

Table I0-2: Selected bond lengths (Å) and angles (°) in the structure of VPO$_4$F.
Numbers in the diagonals (bold) are V-X distances (X = F or O).
Numbers below the diagonals are X-V-X angles.
Numbers above the diagonals are X-X distances

V(1)O$_4$F$_2$	O(2)a	O(2)b	O(1)a	O(1)b	Fa	Fb
O(2)a	**1.85(8)**	3.71(2)	2.74(1)	2.63(3)	2.72(9)	2.67(7)
O(2)b	180	**1.85(8)**	2.63(3)	2.74(1)	2.67(7)	2.72(9)
O(1)a	92.33(3)	87.66(7)	**1.94(1)**	3.88(2)	2.70(2)	2.81(9)
O(1)b	87.66(7)	92.33(3)	180	**1.94(1)**	2.81(9)	2.70(2)
Fa	91.10(7)	88.89(3)	87.55(9)	92.44(1)	**1.96(4)**	3.92(8)
Fb	88.89(3)	91.10(7)	92.44(1)	87.55(9)	180	**1.96(4)**

Distortion: Δ = $6.23\cdot10^{-4}$

PO$_4$	O(2)a	O(2)b	O(1)a	O(1)b
O(2)a	**1.47(3)**	2.41(5)	2.42(7)	2.41(2)
O(2)b	110.07(2)	**1.47(3)**	2.41(2)	2.42(7)
O(1)a	109.47(1)	108.45(1)	**1.50(1)**	2.47(1)
O(1)b	108.45(1)	109.47(1)	110.92(3)	**1.50(1)**

Distortion: Δ = $1.02\cdot10^{-4}$

Table II0-1: Structural parameters obtained after Rietveld refinement of XRD and neutron diffraction data from phase $LiFePO_4F$

$LiFePO_4F$

S.G. : $P\bar{1}$; Z = 2

a = 5.1525(5) Å; α = 107.352(4) ° b = 5.3037(9) Å; β = 107.949(7)° c = 7.2557(9) Å; γ = 98.467(6) °	X-Ray: R_{wp} = 14.3 %; R_{bragg} = 3.97 % χ^2 = 1.71
V = 173.69(3) Å^3; V/Z = 86.84 Å^3	Neutrons: R_{wp} = 12.3 %; R_{bragg} = 6.22 % χ^2 = 2.00

Atomic parameters

Atoms	Wyckoff position	Atomic position			Occ	B_{iso}
		x/a	y/b	z/c		
Fe(1)	*1a*	0	0	0	1	0.907(2)
Fe(2)	*1c*	0	0	1/2	1	0.954(1)
P	*2i*	0.3219(9)	0.6483(1)	0.2519(7)	1	0.969(3)
O(1)	*2i*	0.3774(8)	0.2387(8)	0.5898(8)	1	0.668(3)
O(2)	*2i*	0.1078(7)	-0.3348(3)	0.3595(3)	1	0.669(9)
O(3)	*2i*	0.6906(3)	0.6529(4)	-0.1437(4)	1	0.698(3)
O(4)	*2i*	0.2636(5)	0.7925(2)	0.0975(2)	1	0.910(5)
F	*2i*	-0.1153(9)	0.0855(6)	0.2435(2)	1	0.878(3)
Li	*2i*	0.7198(1)	0.3783(7)	0.2330(1)	1	2.193(2)

Table II0-2: Selected bond lengths (Å) and angles (°) in the structure of $LiFePO_4F$.
Numbers in the diagonals (yellow) are Fe-X distances (X = F or O).
Numbers below the diagonals are X-Fe-X angles.
Numbers above the diagonals are X-X distances

$Fe(1)O_4F_2$	O(3)a	O(3)b	O(4)a	O(4)b	F(1)a	F(1)b
O(3)a	**1.99(6)**	3.99(2)	2.78(1)	2.82(5)	2.81(2)	2.81(4)
O(3)b	180	**1.99(6)**	2.82(5)	2.78(1)	2.81(4)	2.81(2)
O(4)a	89.08(6)	90.91(4)	**1.96(7)**	3.93(5)	2.92(7)	2.65(7)
O(4)b	90.91(4)	89.08(6)	180	**1.96(7)**	2.65(7)	2.92(7)
F(1)a	89.95(3)	90.04(7)	95.44(6)	84.55(4)	**1.98(3)**	3.96(6)
F(1)b	90.04(7)	89.95(3)	84.55(4)	95.44(6)	180	**1.98(3)**

Distortion $\Delta = 3.45\cdot10^{-5}$

$Fe(2)O_4F_2$	O(1)a	O(1)b	O(2)a	O(2)a	F(1)a	F(1)b
O(1)a	**1.95(2)**	3.90(5)	2.87(6)	2.73(5)	2.76(9)	2.79(4)
O(1)b	180	**1.95(2)**	2.73(5)	2.87(6)	2.79(4)	2.76(9)
O(2)a	92.87(4)	87.12(6)	**2.01(5)**	4.03(1)	2.87(8)	2.77(3)
O(2)b	87.12(6)	92.87(4)	180	**2.01(5)**	2.77(3)	2.87(8)
F(1)a	89.47(8)	90.52(2)	92.12(2)	87.87(8)	**1.98(1)**	3.96(2)
F(1)b	90.52(2)	89.47(8)	87.87(8)	92.12(2)	180	**1.98(1)**

Distortion $\Delta = 1.68\cdot10^{-5}$

PO_4	O(1)	O(2)	O(3)	O(4)
O(1)	**1.51(5)**	2.51(3)	2.38(1)	2.51(4)
O(2)	111.05(1)	**1.53(4)**	2.51(4)	2.50(4)
O(3)	102.49(5)	109.87(4)	**1.53(7)**	2.51(8)
O(4)	112.01(1)	110.18(9)	110.99(8)	**1.51(7)**

Distortion $\Delta = 4.14\cdot10^{-5}$

LiO_4F	O(1)	O(2)	O(3)	O(4)	F
O(1)	**2.27(3)**	2.73(5)	2.38(1)	4.23(4)	3.99(9)
O(2)	77.85(2)	**2.07(2)**	3.82(6)	3.23(6)	2.88(1)
O(3)	67.70(6)	141.73(5)	**1.97(7)**	3.24(6)	3.42(6)
O(4)	133.72(9)	94.41(5)	100.09(2)	**2.33(1)**	2.65(7)
F	147.73(2)	93.28(1)	128.08(3)	77.31(5)	**1.88(6)**

Distortion $\Delta = 6.51\cdot10^{-3}$

Table 0V-1: Structural parameters obtained after Rietveld refinement of XRD and neutron diffraction data from phase $LiTiPO_4F$

$LiTiPO_4F$

S.G. : $P\bar{1}$; Z = 2

a = 5.203(9) Å; α = 107.015(4) °
b = 5.345(1) Å; β = 108.183(1) °
c = 7.287(9) Å; γ = 97.93(4) °

V = 178.20(1) $Å^3$; V/Z = 89.1 $Å^3$

XRD: R_{wp} = 15.2 %;
R_{bragg} = 1.88 %; χ^2 = 1.73

Neutrons: R_{wp} = 13.0 %;
R_{bragg} = 5.11 %; χ^2 = 3.93

Atomic parameters

Atoms	Wyckoff position	Atomic position			Occ	B_{iso}
		x/a	y/b	z/c		
Ti(1)	*1a*	0	0	0	1	1.003(1)
Ti(2)	*1b*	0	0	1/2	1	0.079(1)
P	*2i*	0.3230(1)	0.6494(1)	0.2511(6)	1	0.062(4)
O(1)	*2i*	0.3754(1)	0.2529(2)	0.6069(1)	1	0.219(3)
O(2)	*2i*	0.1312(1)	-0.3310(8)	0.3648(1)	1	0.512(3)
O(3)	*2i*	0.6720(9)	0.6559(7)	-0.1524(4)	1	1.086(3)
O(4)	*2i*	0.2561(1)	0.7808(4)	0.0978(1)	1	0.361(2)
F	*2i*	-0.1141(1)	0.0784(1)	0.2711(9)	1	0.226(3)

Table II0-2: Selected bond lengths (Å) and angles (°) in the structure of LiTiPO$_4$F. Numbers in the diagonals (yellow) are Ti-X distances (X = F or O). Numbers below the diagonals are X-Ti-X angles. Numbers above the diagonals are X-X distances

Ti(1)O$_4$F$_2$	O(3)a	O(3)b	O(4)a	O(4)b	Fa	Fb
O(3)a	**2.07(2)**	3.99(2)	2.88(5)	2.87(3)	2.86(2)	2.82(4)
O(3)b	180	**2.07(2)**	2.87(3)	2.88(5)	2.82(4)	2.86(2)
O(4)a	90.60(1)	89.94(1)	**1.99(5)**	4.13(8)	2.67(1)	2.89(2)
O(4)b	89.94(1)	90.60(1)	180	**1.99(5)**	2.89(2)	2.67(1)
F(1)a	90.75(5)	89.24(7)	85.43(2)	94.56(8)	**1.94(1)**	3.88(2)
F(1)b	89.24(7)	90.75(5)	94.56(8)	85.43(2)	180	**1.94(1)**
Distortion	Δ = $7.17\cdot10^{-4}$					

Ti(2)O$_4$F$_2$	O(1)a	O(1)b	O(2)a	O(2)b	Fa	Fb
O(1)a	**1.98(8)**	3.97(7)	2.95(8)	2.78(5)	2.87(1)	2.79(2)
O(1)b	180	**1.98(8)**	2.78(5)	2.95(8)	2.79(2)	2.87(1)
O(2)a	89.54(9)	93.45(1)	**2.07(4)**	4.14(2)	2.86(3)	2.92(1)
O(2)b	93.45(1)	89.54(9)	180	**2.07(4)**	2.92(1)	2.86(3)
Fa	91.58(1)	88.41(9)	88.84(2)	91.15(8)	**2.01(1)**	4.03(2)
Fb	88.41(9)	91.58(1)	91.15(8)	88.84(2)	180	**2.01(1)**
Distortion	Δ = $3.43\cdot10^{-4}$					

PO$_4$	O(1)	O(2)	O(3)	O(4)
O(1)	**1.51(5)**	2.51(3)	2.38(1)	2.51(4)
O(2)	111.05(1)	**1.53(4)**	2.51(4)	2.50(4)
O(3)	102.49(5)	109.87(4)	**1.53(7)**	2.51(8)
O(4)	112.01(1)	110.18(9)	110.99(8)	**1.51(7)**
Distortion	Δ = $4.14\cdot10^{-5}$			

Figures Captions

General Introduction

Figure 1: World total final consumption and world population from 1973 to 2011

Figure 2: Primary Energy reserves by regions (America referred to North and Latin America). The values are given in R/P ratio i.e. amount of known resource/amount used per year

Figure 3: Energy densities of different well-known electrochemical batteries

Figure 4: A schematic representation of a Li-ion battery with graphite as negative insertion electrode material and an insertion compound as positive electrode material.

Figure 5: Schematic representation of the crystal structures of 2D $LiCoO_2$ (left), 3D $LiMn_2O_4$ (center) and polyanionic (here triphylite $LiFePO_4$) (right) [3]

Figure 6: Representation of the Tavorite (left) and Montebrasite (right) crystal structures. The blue and brown polyhedra are MO_4Y_2 octahedra and the yellow are XO_4 tetrahedra.

Figure 7: Illustration of geometrical relationships between the four models used in the literature to describe Tavorite-type structures.

Figure 8: (left) Evolution of the number of articles published based on Tavorite system. (right) Evolution of the citations in each year. (Data recorded for the past 10 years in "web of knowledge")

Figure 9: Overview of redox couple potentials for the transition metal in Tavorite AxMPO4Y [3]

Chapter I : SYNTHESIS AND CRYSTAL STRUCTURE OF $LiVPO_4F$ AND $LiVPO_4O$

Figure I-1: Simulated XRD patterns of $LiVPO_4O$ (orange) and $LiVPO_4F$ (green) from ICSD N° 20537 and $LiAlPO_4F$ (ICSD N° 48012, where Al was replaced by V) respectively.

Figure I-2: XRD pattern refinement of $LVPO_4O$ obtained through a one-step reaction using LiF as lithium precursor

Figure I-3: XRD pattern of C_{SP} used for carbothermal synthesis of VPO_4

Figure I-4: XRD pattern refinement of $C–VPO_4$ obtained through a CTR process

Figure I-5: X-ray diffraction patterns of different powders prepared in this work a) pellet under Ar flux in crucible, b) pellet in a gold sealed tube, c) stoichiometric proportions of VPO_4/LiF in a gold sealed tube.

Figure I-6: a) TGA (black line) and DSC (red line) of VPO_4 performed under O_2 flow b) Full-pattern refinement of the XRD data of VPO_4O obtained after TGA in air.

Figure I-7: Skeleton representation of a) α–LiVPO4O and b) β–LiVPO4O along the a direction

Figure I-8: XRD patterns of phase-pure $LiVPO_4F$ and $LiVPO_4O$ with calculated Bragg positions. SEM images are included in the insets

Figure I-9: Illustration of the transformation matrix from $LiVPO_4O$ to $LiVPO_4F$ unit cells.

Figure I-10: Temperature dependence of the H/M ratio for $LiVPO_4F$ and $LiVPO_4O$. Comparison of experimental and theoretical Curie constants is given for the two phases with, for information, the temperature range used for their calculation.

Figure I-11: a) Rietveld refinement of neutron diffraction data (only heaviest atoms are considered) b) 2D section of 3D difference Fourier maps at y = 0.68 with the maxima corresponding to the Li(1) site for the crystal structure of $LiVPO_4F$

Figure I-12: Observed (red dots), calculated (black line), and difference (blue line) plots obtained for the Rietveld refinement of (a) X-ray diffraction data and (b) neutron diffraction data for $LiVPO_4F$

Figure I-13: Representations of the crystal structure of $LiVPO_4F$

Figure I-14: Representation of chains along the c axis in the structure of $LiVPO_4F$

Figure I-15: Schematic representation of tetrahedra PO_4 (a) and pentahedra LiO_4F (b) local environment in the structure of $LiVPO_4F$

Figure I-16: Skeleton representation of $LiVPO_4F$ structure along the c direction presenting: a) 2 sites of Li as suggested by J. Barker et al. [25] based on the analogy with $LiAlPO_4F$, represented as $Li(1)_{LiAlPO_4F}$ and $Li(2)_{LiAlPO_4F}$ b) 2 sites of Li as observed by B.L. Ellis et al. [26], represented by $Li(1)_{Ellis}$ and $Li(2)_{Ellis}$
In both cases the Li's position found in this work is presented as Li_{Ateba}

Figure I-17: ^7Li MAS NMR spectra a) of GEN II (red line) and GEN III (green line). The magnitude is scaled to the mass of active material in the NMR rotor. b) An example of the fit is given for the signal at 117 ppm.

Figure I-18: ^{31}P MAS NMR spectra of GEN II (red line) and GEN III (green line). The magnitude is scaled to the mass of active material in the NMR rotor and the spinning sidebands are marked with asterisks.

Figure I-19: ^{19}F MAS NMR spectrum for GEN III sample. The spinning sidebands are marked with asterisks.

Figure I-20: a) Low temperature neutron diffraction experiment (on D20) carried out on $LiVPO_4F$; b) The change in intensities versus time of the magnetic superstructure peaks

Figure I-21: Magnetic Rietveld Refinements of $LiVPO_4F$: Observed versus calculated (black line) powder neutron diffraction patterns of $LiVPO_4F$ collected on D20 with $\lambda = 2.40$ Å, at 2K (red dots) and 50K (green dots). The difference pattern (blue line) of the 2K pattern is displayed at the panel bottom. The positions of the Bragg reflections are shown as vertical bars below.

Figure I-22: Illustration of the proposed magnetic structure of $LiVPO_4F$: a) 3D view of the magnetic moments bore by vanadium atoms b) 3D view of isolated octahedra.

Figure I-23: Observed (red dots), calculated (black line), and difference (blue line) plots obtained for the Rietveld refinement of (a) X-ray diffraction and (b) neutron diffraction data for $LiVPO_4O$

Figure I-24: (Left) Rietveld refinement of neutron diffraction data (only heaviest atoms are considered); (Right) 2D section of 3D Fourier difference map at $y = 0.156$ with the maxima corresponding to the Li(1) and Li(2) sites for the crystal structure of $LiVPO_4O$

Figure I-25: (Left) Representation of the crystal structure of $LiVPO_4O$ (Right) Octahedra chains connected alternatively by different tetrahedra along the c direction

Figure I-26: Schematic representation of $[P(1)O_4]$ (left) and $[P(2)O_4]$ (right) local environments in $LiVPO_4O$

Figure I-27: Schematic representation of $Li(1)O_5$ (left) and $Li(2)O_5$ (right) local environments in $LiVPO_4O$

Figure I-28: ^{7}Li MAS NMR spectrum of LiVPO$_4$O (left) and a fit of ^{7}Li MAS NMR spectrum (right).The result is given in the insert

Figure I-29: ^{31}P MAS NMR spectrum (Hahn echo) of LiVPO$_4$O (spinning 30 kHz)..

Figure I-30: Comparison of [VO$_4$X$_2$] chains in LiVPO$_4$X (X = F, O).

Chapter II ELECTROCHEMICAL BEHAVIOR OF LiVPO$_4$X (X = O or F)

Figure II-1: Respective positions of V^{n+}/V$^{(n-1)+}$ redox couples in phosphate, diphosphate and NASICON-like polyanionic structures. α- and β-Li$_3$V$_2$(PO$_4$)$_3$ refer to Anti-NASICON (monoclinic) and NASICON (rhombohedral) forms respectively.

Figure II-2: a) Electrochemical behavior of a typical symmetrical LiVPO$_4$F||LiVPO$_4$F cell cycled between 1.80 V and 2.80 V as reported by J. Barker together with b) the corresponding capacity vs. cycles number [60].

Figure II-3: a) The first charge/discharge galvanostatic data for the LiVPO$_4$F/[1M] LiPF$_6$/EC-DMC (1:1)/LiVPO$_4$F cell and b) the corresponding capacity vs. cycles number. c) The first charge/discharge galvanostatic data for the LiVPO$_4$F/[1M] LiBF$_4$/EMIBF$_4$/LiVPO$_4$F cell and d) the corresponding capacity vs. cycles number [61].

Figure II-4: Discharge capacities vs. cycle number of triclinic LiVPO$_4$O (dots) and orthorhombic LiVPO$_4$O (squares) phases. The cycling rate was C/10. [39]

Figure II-5: a) Photography and b) detailed description of the Leriche's in situ cell used for in situ XRD experiments [62]

Figure II-6: GITT measurement of LiVPO$_4$F between 1.5–3 V vs. Li. a) Potential vs. Li$_x$VPO$_4$F and b) in the region of Li$_{0.5}$VPO$_4$F, potential vs. time.

Figure II-7: 2D View of collected in-situ XRD patterns for the global electrochemical reaction LiVPO$_4$F ⇔ Li$_2$VPO$_4$F (left) and corresponding galvanostatic cycling data (right). The XRD patterns highlighted in blue refer to LiVPO$_4$F and the dark black one to Li$_2$VPO$_4$F

Figure II-8: Selected 2θ regions showing the respective growths and disappearances of the phases involved in the LiVPO$_4$F ⇔ Li$_2$VPO$_4$F reaction.

Figure II-9: variations of normalized intensities of the $(110)_{P\bar{1}}$ peak of LiVPO$_4$F (blue) and the $(200)_{C2/c}$ peak of Li$_2$VPO$_4$F (red) as a function of x Li$^+$.

Figure II-10: XRD patterns and full-pattern matching refinements of initial LiVPO$_4$F, reduced Li$_2$VPO$_4$F and fully charge LiVPO$_4$F. The space groups, the lattice parameters and the volumes are inserted for each XRD pattern.

Figure II-11: Electrochemical behavior of different LiVPO$_4$F samples cycled between 3.00–4.60 V vs. Li$^+$/Li at C/50: a) LiVPO$_4$F samples containing α-Li$_3$V$_2$(PO$_4$)$_3$ as impurity, b) LiVPO$_4$F sample containing an unknown impurity before (red) and after washing (blue), and c) pure LiVPO$_4$F

Figure II-12: GITT measurement of LiVPO$_4$F between 2.7–4.55 V with a current rate of C/100. The relaxation condition was dV/dt < 4 mV/h

Figure II-13: 2D View of collected in-situ XRD patterns for the global electrochemical reaction $LiVPO_4F$ ⇔ VPO_4F (left) and corresponding galvanostatic cycling data (right). The XRD patterns highlighted refer to $LiVPO_4F$ (#1 and #92, blue), $Li_{0.67}VPO_4F$ (#14, green) and VPO_4F (#48, red).

Figure II-14: Selected 2θ regions showing the respective growths and disappearance of the phases involved in the $LiVPO_4F$ ⇔ VPO_4F reaction. The XRD patterns highlighted refer to $LiVPO_4F$ (#1 and #92, blue), $Li_{0.67}VPO_4F$ (#14, green) and VPO_4F (#48, red).

Figure II-15: Full-pattern matching refinements of $LiVPO_4F$, $Li_{0.67}VPO_4F$ and VPO_4F. The lattice parameters as well as the volumes are inserted in each XRD pattern.

Figure II-16: Unit-cell volume changes during the global electrochemical reaction $LiVPO_4F$ ⇔ VPO_4F involving successive two-phase reactions.

Figure II-17: Galvanostatic cycling of a Li/LP30/$LiVPO_4F$ cell cycled at C/75 (right) and in situ XRD recorded upon oxidation up to the global composition $Li_{0.67}VPO_4F$ and then back to $LiVPO_4F$ (left).

Figure II-18: a) Electrochemical data of a Li/LP30/$LiVPO_4F$ cell cycled at C/50 for the present in situ (black line) and galvanostatic data recorded in coin cell (dash blue) b) in situ XRD patterns recorded upon oxidation up to the global composition $Li_{0.33}VPO_4F$ and then back to $LiVPO_4F$.

Figure II-19: Temperature dependence of the H/M ratio for Li_xVPO_4F (with x = 2, 1, 0.67 and 0)

Figure II-20: Observed (red dots), calculated (black line), and difference (blue line) plots obtained for the Rietveld refinement of X-ray diffraction data (a) and neutron diffraction data for VPO_4F (b)

Figure II-21: Representation of VPO_4F skeleton framework structure in the $[001]_{C2/c}$ (left) and $[101]_{C2/c}$ (right) directions

Figure II-22: Observed (red dots), calculated (black line), and difference (blue line) plots obtained for the Rietveld refinement of (a) X-ray diffraction data and (b) neutron diffraction data for $Li_{0.67}VPO_4F$

Figure II-23: Electron diffraction patterns of $LiVPO_4F$ obtained by rotation around a common direction

Figure II-24: XRD of Li_2VPO_4F obtained by chemical lithiation (black) and the product of oxidation of Li_2VPO_4F (purple) compared with the pristine $LiVPO_4F$ (blue). The corresponding Bragg positions are given under each peak.

Figure II-25: XRD pattern of Li_2VPO_4F obtained by chemical lithiation in comparison with the simulated pattern of Li_2VPO_4F as published by B.L. Ellis et al. **[25].**

Figure II-26: Skeleton representation of Li_2VPO_4F structure.

Figure II-27: Comparative distances and dihedral angles in the structure of Li_2VPO_4F, $LiVPO_4F$ and VPO_4F.

Figure II-28: ^7Li MAS NMR spectra of pristine $LiVPO_4F$ (blue), intermediate $Li_{0.67}VPO_4F$ (green) and fully delithiated VPO_4F (red) The magnitude is scaled to the mass of active material in the NMR rotor.

Figure II-29: ^{31}P MAS NMR spectra of pure $LiVPO_4F$ (blue), intermediate $Li_{0.67}VPO_4F$ (green) and fully delithiated VPO_4F (red). Due to the existence of spinning side bands for each contribution, the main isotropic contributions are marked by arrows.

Figure II-30: ^1H MAS NMR spectra of pure $LiVPO_4F$ (blue), intermediate $Li_{0.67}VPO_4F$ (green) and fully delithiated VPO_4F (red) (spinning sidebands are marked by asterisks)

Figure II-31: X-Ray diffraction patterns and full-pattern matching refinements of the global composition "$Li_{0.67}VPO_4F$" obtained as a single phase during oxidation (top) and as a two-phase mixture during reduction (bottom)

Figure II-32: Galvanostatic cycling from 1.6 V–4.5 V vs. Li^+/Li at C/50 of $LiVPO_4O|LP30|Li$ cell.

Figure II-33: a) Three different milling durations of a mixture of $LiVPO_4O$ and 20% of C_{sp}. b) Corresponding electrochemical Li insertion/extraction at C/50

Figure II-34: GITT measurement of $LiVPO_4O$ (left): a current corresponding to a rate of C/200 was applied during one hour with a relaxation time condition of $dV/dt< 4mV/h$. Derivative curve calculated (right) from GITT.

Figure II-35: 2D View of collected in-situ XRD patterns for the global electrochemical reaction $LiVPO_4O$ ⬄ Li_2VPO_4O (left) and corresponding galvanostatic cycling data (right). The XRD patterns highlighted refer to $LiVPO_4O$ (blue), $Li_{1.5}VPO_4O$ (red), $Li_{1.75}VPO_4O$ (green) and Li_2VPO_4O (black).

Figure II-36: Selected 2θ regions showing the respective growths and disappearance of the phases involved in the $LiVPO_4O$ ⇨ Li_2VPO_4O reaction. The XRD patterns highlighted refer to $Li_{1.5}VPO_4O$ (red), $Li_{1.75}VPO_4O$ (green) and Li_2VPO_4O (black).

Figure II-37: Galvanostatic cycling of $Li/LiPF_6$ [1M] in EC:DMC (1:1)/$LiVPO_4O$ cell at C/50 from 3 V to 4.6 V

Figure II-38: Galvanostatic cycling of a Li/LP30/$LiVPO_4O$ cell cycled at C/50 up to 4.5 V (right) and in situ XRD patterns (left)

Figure II-39: Evolution (from charge to discharge) of the FWHM for $(200)_{P\bar{1}}$ peaks of $LiVPO_4O$.

Figure II-40: Different cycles (at a rate of C/20) for Li||$LiVPO_4O$ cell

Figure II-41: a) charge and discharge capacity of Li||$LiVPO_4O$ cell versus number of cycles b) polarization of each cycle

Figure II-42: Full pattern matching refinements of XRD data in Cc (left) and C2/c (right) space groups of VPO_4O obtained by chemical delithiation

Figure II-43: Representation of the structure of: a) $LiVPO_4O$ and b) ε-VPO_4O along the $(1\bar{1}0)_{C/c}$ and $(10\bar{1})_{P\bar{1}}$ directions.

Figure II-44: Different schematic densities of state of V^n/V^{n-1} encountered in $LiVPO_4F$ (left) and $LiVPO_4O$ (right)

Chapter III SYNTHESIS, CRYSTAL STRUCTURE AND ELECTROCHEMICAL PROPERTIES OF $LiFePO_4F$

Figure III-1: Respective positions of the Fe^{3+}/Fe^{2+} redox couple in iron phosphates/sulfates

Figure III-2: Full-pattern matching refinements of $LiFePO_4F$ synthesized using a) EMI-TFSI and b) Triflate

Figure III-3: XRD patterns of $LiFePO_4F$ preparations obtained after ceramic synthesis a) before washing and b) after washing with calculated Bragg positions. SEM images are included in the inserts.

Figure III-4: Calculated spectrum (blue line) and deconvolution (green line) of experimental data obtained
a) before washing (black dots) and b) after washing (red dots) for the $LiFePO_4F$ phase obtained by ceramic route

Figure III-5: Temperature dependence of the H/M ratio for the washed $LiFePO_4F$. Comparison of experimental and theoretical Curie constants is given and the temperature range used for its calculation.

Figure III-6: a) Rietveld refinement of neutron diffraction data (only Fe, P, O and F atoms are considered); b) 2D section of 3D Fourier difference maps at $y = 0.278$ with the maximum corresponding to the Li site in the crystal structure of $LiFePO_4F$

Figure III-7: Observed (red dots), calculated (black line), and difference (blue line) plots obtained for the Rietveld refinement of (a) X-ray diffraction data and (b) neutron diffraction data for $LiFePO_4F$

Figure III-8: Skeleton framework structure of Tavorite $LiFePO_4F$ with ellipsoid representation of atoms as obtained after thermal motion refinements

Figure III-9: Octahedral chains of FeO_4X_2 in $AFePO_4X$ (with A = H or Li and X = OH or F)

Figure III-10: a) Schematic representation of $[PO_4]$ tetrahedron local environment in $LiFePO_4F$ b) Schematic representation of LiO_4F local environment in $LiFePO_4F$.

Figure III-11:a) ^7Li MAS NMR and b) ^{31}P MAS NMR spectrum of $LiFePO_4F$ (spinning sidebands are shown by asterisks).

Figure III-12: ^7Li MAS NMR spectrum of $LiFePO_4F$ before (black) and after (red) washing.

Figure III-13: ^1H MAS NMR spectrum of $LiFePO_4F$ before
(black) and after (red) washing compared to the signal for $LiFePO_4OH$ (green).
Spinning sidebands are marked by asterisks.

Figure III-14: Rietveld Refinements of neutron diffraction data of the non-washed $LiFePO_4F$: Observed versus calculated (black line) powder neutron diffraction patterns collected at 2K (red dots) and 50 K (purple dots). The difference pattern (blue line) is displayed at the panel bottom. The positions of the Bragg reflections are shown as vertical bars below

Figure III-15: Illustration of the proposed magnetic structure of $LiFePO_4F$: a) 3D view of the magnetic structure b) 3D view of moment in isolated octahedra: [$Fe(1)O_4F_2$] octahedra (blue) and [$Fe(2)O_4F_2$] octahedra (red)

Figure III-16: The electrochemical signature of $LiFePO_4F$ as presented in literature by a) N. Recham et al. [7]; b) T.N. Ramesh et al. [8]

Figure III-17: Electrochemical behavior of $LiFePO_4F$ performed at different C rates a) C/10; b) C/100. The blue line is the first cycle.

***Figure III-18: XRD patterns (left) and the corresponding Mössbauer spectra (right) showing the degradation of a mixture of $LiFePO_4F$ and C_{sp} (85:15 wt %) after Spex milling and air exposure: a) initial $LiFePO_4F$ and C_{sp},
b) 15 min of Spex milling, c) air exposure during 3 months.***

Figure III-19: Mössbauer in situ study of $LiFePO_4F$: the galvanostatic data are surrounded by the spectra (from A to M)

Figure III-20: 2D View of collected in situ XRD patterns for the global electrochemical reaction $LiFePO_4F \Leftrightarrow Li_2FePO_4F$ (left) and corresponding galvanostatic cycling (right). The XRD patterns highlighted in blue refer to $LiFePO_4F$ and the red one to Li_2FePO_4F. The XRD pattern of the intermediate phase is presented in green.

Figure III-21: Selected 2θ regions showing the respective growth and disappearance of the phases involved in the $LiFePO_4F$ (blue) $\Leftrightarrow$ Li_2FePO_4F (red) reaction. The XRD pattern of the intermediate phase is presented in green.

Figure III-22: Relative peak intensities for the peak corresponding to an intermediate phase (green) and a fully lithiated phase Li_2FePO_4F (red)

Figure III-23: Fullpattern refinement of the XRD data n° 50 corresponding to a fully lithiated phase. Bragg positions are those taken from Ramesh et al. [8]

Chapter IV SYNTHESIS, CRYSTAL STRUCTURE AND ELECTROCHEMICAL PROPERTIES OF $LiTiPO_4F$

Figure IV-1: Electrochemical cycling of $LiTiPO_4F$ as reported by N. Recham et al. [16]. The inset shows the evolution of the capacity with the cycle numbers.

Figure IV-2: Full-pattern matching refinement of the XRD pattern recorded for the pristine (non-washed) $LiTiPO_4F$.

Figure IV-3: Temperature dependence of the H/M ratio for the pristine $LiTiPO_4F/LiF$ mixture. The calculated Curie constant is given in insert in comparison with the theoretical one considering a Ti^{3+}-only material.

Figure IV-4: a) Neutron diffraction data refinement considering only heaviest atoms (i.e. without Li) and b) Corresponding Fourier difference map.

Figure IV-5: Observed (red dots), calculated (black line), and difference (blue line) plots obtained for the Rietveld refinement of X-ray diffraction data for $LiTiPO_4F$. The presence of LiF is indicated by stars.

Figure IV-6: Representation of chains along the c axis in $LiTiPO_4F$ structure

Figure IV-7: ^7Li MAS NMR spectrum of $LiTiPO_4F$

Figure IV-8: ^{31}P MAS NMR spectrum of $LiTiPO_4F$

Figure IV-9: The XRD patterns of the "non-washed" sample (a) and the XRD patterns of the samples exposed to air during b) 15 hours, c) 9 months and d) 1 year. The simulated XRD pattern of $LiTiPO_4O$ is also given for comparison.

Figure IV-10: Full-pattern matching refinement of the XRD pattern obtained for the sample aged during 1 year in air, considering a) a unit cell described in the Cc space group for the main phase and b) a unit cell described in the C/2c space group for the main phase. The reliability factors are given in inserts.

Figure IV-11: Full-pattern matching refinement of the XRD patterns obtained for the samples aged in air during a) 15 hours and b) 9 months.

Figure IV-12: Temperature dependence of the H/M ratio for $LiTi^{III}PO_4F/LiF$ mixture (black), sample aged for 9 months (green) and the sample aged for 1 year (blue). The molar weight used for the calculation of the H/M ratio for both 9 months and 1 year aged samples was that of $TiPO_4F$

Figure IV-13: XRD patterns of different samples of "$LiTiPO_4F$":
a) "non-washed", b) "RT-washed" c) "CW-washed" and d) the "non-washed" aged during 15 hours in air

Figure IV-14: Full-pattern matching refinement of the XRD patterns collected for the samples washed with a) room temperature water: the XRD data were refined considering only one phase ($P\overline{1}$) and with b) cold water: the XRD data were refined considering two phases ($P\overline{1}$ and Cc).

Figure IV-15: Temperature dependence of the H/M ratio for $LiTiPO_4F/LiF$ mixture (black), sample aged for 9 months (green), the sample aged for 1 year (blue) and the sample washed with cold water (brown). The molar weight used for the calculation of the H/M ratio for the "CW-washed" sample was that of $TiPO_4F$.

Figure IV-16: Electrochemical behavior of:a-b) "non-washed" sample starting either by a) the extraction of Li^+ or b) the insertion of Li^+ c-d) "CW-washed" sample starting either by c) the extraction of Li^+ or d) the insertion of Li^+ The derivative curves are given in the inserts.

Figure IV-17: Electrochemical signature (starting in charge) of the $LiTiPO_4F/LiF$ sample aged during one year

GENERAL CONCLUSION, SUMMARY AND PERSPECTIVES

Figure 1: XRD patterns of different $LiMPO_4X$ obtained in this work

Figure 2: Temperature dependence of the H/M ratio for $LiMPO_4X$

Figure 3: Comparison of $[MO_4X_2]$ chains, dihedral angles, atomic radii of transition metal and V/Z in $LiMPO_4X$ (M = V, Fe, Ti and X = O or F)

Figure 4: Description of the three-dimensional structure of $Na_3V_2(PO_4)_2F_3$

Figure 5 a) Electrochemical curves obtained for $Li|LP30|Na_3V_2(PO_4)_2F_3$ cells cycled between 2.7–4.5 V vs. Li^+/Li at C/50 b) Electrochemical curves obtained for $Na|NaPF_6$ in PC $|Na_3V_2(PO_4)_2F_3$ cells cycled between 2.7–4.3 V vs. Na^+/Na.

Table Captions

General Introduction

Table1: Tavorite-like structures reported in the literature that adopt the space group $P\bar{1}$

Chapter I : SYNTHESIS AND CRYSTAL STRUCTURE OF LiVPO$_4$F AND LiVPO$_4$O

Table I-1: Comparison of the published LiVPO$_4$O lattice parameters (ICSD N°20537) with those obtained in this study

Table I-2: Magnetic moments (in μ_B) at 2 K, the components are given along the a, b and c axes. Propagation vector k = (½, ½, 0), Magnetic R-factor=19.5%

Table I-3: long (V-O) and short (V=O) distances (in Å) in LiVPO$_4$O and VPO$_4$O polymorphs.

Chapter II ELECTROCHEMICAL BEHAVIOR OF LiVPO$_4$X (X = O or F)

Table II-1: Average potentials, capacities and energy densities of vanadium phosphates reported in the literature.

Chapter III SYNTHESIS, CRYSTAL STRUCTURE AND ELECTROCHEMICAL PROPERTIES OF $LiFePO_4F$

Table III-1: recorded potential vs. Li of the Fe^{3+}/Fe^{2} redox couple, theoretical capacity, and energy density for reported Tavorite type compositions $AFeXO_4Y$ (with A= Li or H, X=P or S, Y = OH or F)

Table III-2: Lattice parameters and angles of different $LiFePO_4X$ (X = OH, F) obtained by iono-thermal syntheses and compared with those reported in literature

Table III-3: Anisotropic thermal motion parameters U_{ij} (in Å) for $LiFePO_4F$

Table III-4: Mössbauer parameters, distortions and Fe–X distances of the washed $LiFePO_4F$ ($LiFePO_4F_w$) and the non-washed $LiFePO_4F$ ($LiFePO_4F_{nw}$) in this study compared with the reported $LiFePO_4OH$ and $HFePO_4{\cdot}OH$ **[3].**

Table III-5: Magnetic moments (μ_B) at 2 K, the components (in μ_B) are given along the a, b and c axes. Propagation vector k = (½, ½, 0), G-type magnetic structure, Magnetic R-factor=4.80%

Chapter IV SYNTHESIS, CRYSTAL STRUCTURE AND ELECTROCHEMICAL PROPERTIES OF $LiTiPO_4F$

TableIV-1: Lattice parameters, unit cell volumes and V/Z values obtained after different aging time of $LiTiPO_4F$ in air. Comparison with those of $LiTiPO_4F$ and $LiTiPO_4O$.

TableIV-2: Lattice parameters, unit cell volumes and V/Z values determined for the different phases observed in samples washed with room temperature water and cold water. Comparison with those of $LiTi^{III}PO_4F$.

Résumé :

Nos efforts se sont portés sur des fluorophosphates de structure TAVORITE de formule $LiMPO_4F$ (M = V, Fe, Ti) et $LiVPO_4O$ qui, comparés à d'autres familles structurales de phosphates tels que $Li_3M_2(PO_4)_3$ (NASICON) ou $LiFePO_4(OH)$ (Tavorite) possèdent d'excellentes densités d'énergie théorique comme matériaux d'électrodes dans des accumulateurs au Li. Des méthodes de synthèse reproductibles, par voie céramique en tubes scellés et/ou ionothermale (synthèse à basse température), ont été mises au point dans ce travail. Les matériaux ainsi préparés ont été caractérisés en détail par magnétométrie, par RMN et surtout par diffraction des rayons X et des neutrons. Les structures cristallines ont ainsi pu être déterminées ainsi que les mécanismes d'insertion/extraction du Li^+, via de nombreuses études par diffraction X *insitu* lors de la charge/décharge des accumulateurs.

Mots-clés :

• Électrode positive pour batteries Li-ion	• Fluorophosphates	• Tavorite
• Diffraction des rayons X et des neutrons	• Diffraction X *in situ*	• Densités d'énergie

Abstract:

This work focused on TAVORITE-based fluorophosphates LiMPO4F (M = V, Fe, Ti) and LiVPO4O which, when compared with other phosphate structural families such as $Li_3V_2(PO_4)_3$ (NASICON) or $LiFePO_4(OH)$ (Tavorite), possess superior energy density as electrode materials for Li batteries. Reproducible synthesis procedures were developed through "classical" ceramic routes in sealed containers and/or low temperature ionothermal reaction. The obtained materials were characterized by magnetometry, solid state NMR and heavily by X-Ray and Neutron diffraction. The crystal structures of all the materials were determined, as well as the mechanisms of Li^+ insertion/extraction through *insitu* X-Ray diffraction during electrochemical charge/discharge of the batteries.

Keywords :

• Positive electrode for Li-ion batteries	• Fluorophosphate	• Tavorite
• X-ray and neutron diffraction	• In-situ X-ray diffraction	• Energy density